



# Supramolecular engineering of optoelectronic sensing devices

Marco Squillaci

## ► To cite this version:

Marco Squillaci. Supramolecular engineering of optoelectronic sensing devices. Theoretical and/or physical chemistry. Université de Strasbourg, 2017. English. NNT : 2017STRAF051 . tel-02003372

**HAL Id: tel-02003372**

**<https://theses.hal.science/tel-02003372>**

Submitted on 1 Feb 2019

**HAL** is a multi-disciplinary open access archive for the deposit and dissemination of scientific research documents, whether they are published or not. The documents may come from teaching and research institutions in France or abroad, or from public or private research centers.

L'archive ouverte pluridisciplinaire **HAL**, est destinée au dépôt et à la diffusion de documents scientifiques de niveau recherche, publiés ou non, émanant des établissements d'enseignement et de recherche français ou étrangers, des laboratoires publics ou privés.

**ÉCOLE DOCTORALE DES SCIENCES CHIMIQUES**

**UMR 7006 – Institut de Science et d'Ingénierie Supramoléculaires**

**(I.S.I.S.)**

# THÈSE

présentée par :

**Marco A. SQUILLACI**

soutenue le : **26 Septembre 2017**

pour obtenir le grade de : **Docteur de l'université de Strasbourg**

Discipline/ Spécialité : Chimie-Physique

## Supramolecular Engineering of Optoelectronic Sensing Devices

**THÈSE dirigée par :**

**M. SAMORÌ Paolo**

Professeur, université de Strasbourg

**RAPPORTEURS :**

**M. STELLACCI Francesco**

Professeur, Ecole polytechnique fédérale de Lausanne

**M. STEMMER Andreas C.**

Professeur, ETH Zurich

---

**AUTRES MEMBRES DU JURY :**

**M. ROGEZ Guillaume**

Chargé de recherches, université de Strasbourg



## *Résumé*

L'auto-organisation et l'auto-assemblage par le contrôle subtil des interactions adaptatives entre des blocs moléculaires adéquatement conçus permet le développement de matériaux (multi) fonctionnels.<sup>1,2</sup> L'utilisation d'interactions non covalentes pour générer des structures supramoléculaires sophistiquées permet d'exploiter la modification de leur environnement afin de précisément contrôler leur comportement d'auto-assemblage.<sup>3</sup> Une telle modification de la structure peut conduire à un accord précis des propriétés de l'ensemble. Lorsque l'assemblage est astucieusement conçu, des changements spécifiques subtiles dans l'environnement pourraient entraîner des changements spectaculaires d'une ou de plusieurs propriétés physico-chimiques.<sup>4</sup> En d'autres termes, si les interactions supramoléculaires entre un récepteur spécifique et un analyte (c'est-à-dire de petites molécules) présentes dans l'environnement sont optimisées, des capteurs extrêmement sensibles et sélectifs, s'appuyant sur de la reconnaissance, peuvent être fabriqués. En fonction des propriétés des composants, la lecture peut être un changement de masse,<sup>5</sup> des propriétés optiques<sup>6,7</sup> (par exemple une modification de l'absorbance et / ou de la fluorescence), ou des caractéristiques électriques<sup>8,9</sup> (comme une variation de la capacité électrique ou de la résistance). L'utilisation de la reconnaissance supramoléculaire s'est révélée être la clé pour la réalisation de la prochaine génération de capteurs présentant des limites de détection au niveau de ppm avec une vitesse de réponse élevée combinée à une sélectivité sans précédent. Ces caractéristiques sont le résultat d'interactions optimales au niveau non covalent, qui peuvent être très sélectives grâce à l'utilisation de groupes récepteurs possédant des caractéristiques ad hoc telles que la taille, la géométrie, le moment dipolaire, etc.

Les capteurs de gaz et en particulier les capteurs d'humidité sont d'une importance primordiale dans de nombreux domaines de la science et de la technologie et sont donc couramment utilisés dans les industries, les hôpitaux, le contrôle de l'environnement, etc.<sup>10</sup> Pour détecter l'eau (sous forme de vapeurs) dans l'environnement, de nombreux matériaux ont été utilisés comme composé actif tels que les polymers,<sup>11</sup> les matériaux à base de carbone,<sup>12</sup> et les composites.<sup>13</sup> L'ozone ( $O_3$ ) est un gaz extrêmement toxique,<sup>14,15</sup> naturellement généré dans l'atmosphère par l'interaction entre l'oxygène et la lumière UV. La surveillance de l' $O_3$  est fondamentale pour la sécurité des instruments et des opérateurs lorsque des sources UV (Hg,  $D_2$ , lampes etc.) sont utilisées.<sup>16</sup>

Puisque les processus de reconnaissance ont lieu à l'interface entre le matériau actif et le milieu environnant, une stratégie fructueuse pour améliorer la sensibilité et la vitesse de réponse est de maximiser le rapport surface / volume des matériaux de détection en construisant des architectures nanoscopiques entièrement décorées de récepteurs. A cet égard, les candidats les plus prometteurs à ce type de dispositifs sont les fibres 1D, les matériaux 2D ou les structures poreuses en forme d'éponge 3D, fonctionnalisées de manière covalente à leur surface avec les récepteurs choisis.

Le but de cette thèse est d'étudier et d'exploiter la puissance de la chimie supramoléculaire pour développer et construire de nouveaux capteurs optoélectroniques capables de répondre à des stimuli externes tels que de petites modifications de leur environnement. Pour atteindre cet objectif, différentes structures ont été explorées et, par conséquent, le manuscrit sera divisé en quatre chapitres principaux:

- Les structures plasmoniques dynamiques 2D de nanoparticules d'or réticulées comme capteurs d'humidité
- Les réseaux 3D poreux de nanoparticules d'or en tant que capteurs d'humidité micro-dimensionnés
- Les dyades  $\pi$ -conjuguées amphiphiles auto-assemblées en fibres en tant que capteur d'humidité ultrasensible et ultrasensible
- La réduction de l'oxyde de graphène pour les applications de détection de l'ozone

Les nanoparticules de métaux nobles présentent des propriétés optiques et électriques extrêmement intéressantes, du point de vue électrique, pour leur comportement dépendent de la taille: elles peuvent être isolantes, de diamètre inférieur à 2/3 nm ou conductrices, si elles sont plus grandes, en tant qu'électrodes métalliques nanoscopiques qui permettent de construire des milliers de jonction dans un espace extrêmement limité.<sup>17</sup> Les propriétés optiques sont données par la résonance de plasmon de surface localisée, due à l'oscillation collective des électrons sur la surface de la particule, en résonance avec le champ électrique oscillant de la lumière.<sup>18</sup>

Les plasmons de surface (SPs) sont essentiellement des ondes lumineuses qui sont piégées à la surface d'un métal noble en raison de leur interaction avec les électrons libres sur la surface du métal. Pendant ce processus, les électrons oscillent collectivement sur la surface du métal créant les SP.<sup>19</sup> Lorsque la surface métallique est confinée, comme dans le cas d'un nanocristal ou nanotrou dans un film, les électrons oscillent collectivement entre les bords, et les SPs résultants seront localisés (LSPs). La longueur d'onde caractéristique de la résonance plasmonique des NP métalliques nobles dépend de plusieurs paramètres tels que la résistivité du métal, la forme et la taille des nanoparticules. Lorsque plusieurs nanoparticules sont étroitement imbriquées et interagissent les unes avec les autres, les SP résultants seront un hybride entre des vibrations d'électrons localisées et collectives, avec un impact dramatique sur les propriétés optiques du système. Dans le premier projet présenté dans cette thèse, ces propriétés uniques seront utilisées pour construire des capteurs d'humidité à lecture optique induit par le changement des propriétés plasmoniques des réseaux 2D de nanoparticules d'or réticulées lors de l'absorption des molécules d'eau de l'atmosphère. Pour obtenir ce résultat, des nanoparticules d'or (AuNPs) de 8 nm de large ont été liées ensemble dans un empilement hexagonal 2D ordonné utilisant des chaînes de polyéthylèneglycol di-thiol (SH-PEG-SH). Les chaînes de PEG ont montré qu'elles étaient capables d'absorber de manière sélective et réversible les molécules d'eau de l'atmosphère subissant un gonflement. Le gonflement des chaînes PEG entraîne une augmentation de la distance entre les AuNPs au sein du réseau. En choisissant soigneusement la longueur du ligand du PEG utilisé, mesurant environ 7 nm, il a été possible d'utiliser l'humidité externe pour déplacer les AuNPs à l'intérieur et au-delà de la barrière tunnel et donc de passer de SPs localisés à collectifs en

utilisant l'humidité en tant que contrôleur externe, réalisant des capteurs d'humidité optique fonctionnant dans la plage visible entre 500 et 600 nm.

Le deuxième projet présenté dans ce travail de thèse tire profit des propriétés électriques des AuNP qui peuvent être décorées avec une molécule absorbant l'eau et utilisées pour construire des milliers de jonctions électriques dans un espace extrêmement limité. Ce résultat est obtenu en utilisant des chaînes d'oligoéthylène glycol di-thiol (OEG), semblables à celles utilisées dans le projet précédent, pour décorer et réticuler les AuNPs, mais dans ce cas, la longueur des chaînes est considérablement plus faible par rapport au cas précédent, étant d'environ 1.7 et 2.2 nm. L'utilisation ligand plus courtes affecte plusieurs propriétés du système résultant. Tout d'abord, les réseaux sont moins solubles (en raison de la coquille plus petite interagissant avec le solvant) et le ligand est plus rigide et réactif par rapport au cas précédent, ce qui signifie que la même réaction conduit à la précipitation de réseaux 3D poreux désordonnés en solution au lieu de monocouches ordonnées 2D. Du fait de l'utilisation de courtes chaînes de ligand, les structures poreuses 3D résultantes présentent une résistance électrique remarquablement faible, avec un transport de charge dominé par un mécanisme de tunneling direct, et des propriétés optiques typiques pour l'or massif (pas de LSP). Selon le modèle de tunneling direct, le courant électrique traversant le réseau 3D dépend exponentiellement de la distance inter-particules entre chaque jonction. Comme déjà décrit pour le premier projet, les chaînes OEG peuvent absorber de manière réversible des molécules d'eau de l'atmosphère, subissant un gonflement et, par conséquent, augmentant la distance inter-particules. En exploitant ce comportement, il a été possible d'utiliser ces systèmes 3D pour construire des dispositifs de détection d'humidité microscopiques à lecture électrique, présentant une dépendance exponentielle du courant tunnel mesuré sur une large plage d'humidité relative (HR de 5 % à 100 %) avec une vitesse de réponse remarquablement rapide  $< 13$  ms.

Le troisième projet rapporté dans cette thèse, vise à renforcer la performance des capteurs d'humidité résistifs à leur plus haut potentiel, pour atteindre des performances supérieures à l'état de l'art en termes de vitesse de réponse et de sensibilité. Ces résultats ont été obtenus en utilisant des nanofibres 1D supramoléculaires conçues avec des dyades moléculaires donneur-accepteur conjuguées (D-A), synthétisées par nos collaborateurs. Ces molécules, comportant des chaînes asymétriques et amphiphiles latérales, peuvent être auto-assemblés, dans des solutions aqueuses, combinant la précipitation induite par

le solvant et l'irradiation de lumière afin de croître des nano-fibres supramoléculaires. En utilisant l'interaction solvophobe comme force motrice et l'empilement  $\pi$ - $\pi$  comme stabilisant il était possible de déclencher la formation de longues structures 1D micrométriques. L'enveloppe externe des fibres supramoléculaires est entièrement fonctionnalisée par des chaînes latérales tétra éthylène glycol conduite (TEG) qui, comme on le voit dans les projets précédents, sont en mesure d'absorber de façon réversible des molécules d'eau de l'atmosphère. Dans les conditions de l'état solide et sec, l'encombrement stérique donné par les chaînes volumineuses secondaires, oblige les molécules à basculer, tourner le noyau de la nanofibres et, par conséquent, la diminution de l'empilement  $\pi$ - $\pi$  et le transport de charges le long des fibres. Lorsque l'humidité ambiante augmente, les molécules d'eau peuvent être absorbées dans les chaînes latérales, les connectant par l'intermédiaire d'une liaison hydrogène. La force collective des liaisons hydrogène, donnée par plusieurs molécules d'eau absorbées, est assez forte pour aligner les molécules et étirer les fibres, ce qui augmente le chevauchement entre les orbitales  $\pi$  intermoléculaires. Le chevauchement accru provoque une augmentation spectaculaire du courant électrique passant à travers les fibres. En tirant parti de ce comportement il est possible d'établir une corrélation entre le courant mesuré et la quantité de molécules d'eau absorbées. Ainsi on peut effectuer un étalonnage et déterminer la quantité de molécules d'eau dans l'environnement entourant le dispositif, par exemple avec l'humidité relative. En optimisant les processus de la croissance des fibres, il est possible de construire des capteurs humidité résistifs très sensibles, avec un changement de courant mesurée entre les deux électrodes de sept ordres de grandeur dans la plage comprise entre 5 et 75% HR avec une tendance exponentielle et un temps de réponse de 26 ms. En outre, grâce à la très petite structure des molécules d'eau (moins de 3 Å) et aux deux sites donneur et accepteur pour la formation de liaison hydrogène, les capteurs étudiés présentent également une grande sélectivité pour les molécules d'eau et aucune réponse n'a été mesurée lors de l'exposition des dispositifs à d'autres vapeurs de solvants tels que le méthanol, l'éthanol ou l'éther diéthylique.

Le quatrième et dernier projet rapporté dans cette thèse se concentre sur l'utilisation de l'oxyde de graphène réduit par laser (L-rGO) comme matière active pour les capteurs d'ozone résistifs. Le graphène est une monocouche de graphite, un matériau 2D constitué uniquement d'atomes de carbone disposés dans un réseau hexagonal, où tous les atomes



ont une hybridation  $sp^2$  et tous les électrons  $\pi$  de chaque atome sont libres de se déplacer le long de la couche 2D étant donné qu'ils n'ont pas de masse.<sup>20</sup> Cette caractéristique unique, avec son impressionnante résistance mécanique, a contribué à rendre le graphène célèbre comme le matériau miracle du futur. Les seuls inconvénients qui bloquent toujours le développement des technologies de la vie réelle basés sur des dispositifs de graphène sont la production et le traitement. Même si le graphite est extrêmement abondant dans la nature, la production de graphène haute qualité à partir de graphite peut être obtenue seulement en utilisant l'exfoliation mécanique avec l'approche de ruban adhésif. Cette approche repose sur l'utilisation de ruban adhésif pour séparer mécaniquement les flocons de graphène du graphite et de les transférer sur un substrat approprié. Cette approche est extrêmement longue et ne convient pas à grande échelle ou à la production industrielle de graphite. Une façon de surmonter ce problème consiste à oxyder chimiquement le graphène en oxyde de graphène (GO): un dérivé de graphène, où la conjugaison  $\pi$  est interrompue de façon aléatoire en raison de l'addition de groupes contenant de l'oxygène, lié de façon covalente aux atomes de carbone à l'intérieur du réseau. La présence de ces groupes rendent GO hautement soluble dans les solvants polaires tels que l'eau et permet la production de grandes quantités de ce produit en solution, directement à partir de graphite. Le GO peut être facilement préparé, stocké et traité en solution et réduit ensuite pour revenir à la forme GO réduite (rGO) en éliminant l'oxygène contenant des groupes et de restaurer partiellement les caractéristiques du graphène. La réduction de GO en rGO peut être réalisée avec plusieurs techniques, en solution, à l'état solide ou en couche mince. Jusqu'à présent, la technique la plus performante et étudiée de réduction est la réduction thermique sous vide ou environnement inerte à haute température, typiquement entre 800 et 1000° C pendant plusieurs heures. Ce processus est extrêmement consommateur d'énergie et non-adapté aux films plus épais que 20/30 nm en raison de la délamination du film en raison de la génération de bulles de gaz (typiquement de CO, CO<sub>2</sub> et H<sub>2</sub>O) en tant que produits de réduction. Une alternative intéressante repose sur l'utilisation d'un laser infrarouge à impulsions pour augmenter localement la température, favorisant la réduction. En irradiant une zone réduite, il est possible de réduire seulement quelques microns à chaque impulsion, permettant la diffusion des gaz produits sans engendrer de délaminage. De plus, cette technique permet d'écrire des espaces confinés de rGO sur une matrice de GO isolante, permettant de dessiner des contacts et les circuits électriques

directement sur GO. En utilisant cette technique, il est possible de produire des zones précises rGO de haute qualité comme matière active pour la détection de l'ozone ( $O_3$ ) à des concentrations extrêmement faibles. Les molécules d' $O_3$  ont une forte affinité avec la surface de matériaux à base de carbone, tels que rGO et peuvent être absorbées provoquant un fort dopage positif et, par conséquent, un changement brusque de la résistance électrique mesurée.

En conclusion, cette thèse vise à faire usage et rendre possible la programmation des processus supramoléculaires de reconnaissance dans des matériaux à faible dimension électriquement / optiquement actifs fonctionnalisés avec le récepteur d'un analyte donné. Le but ultime étant de développer de nouvelles architectures et des dispositifs avec des performances améliorées. Tous les différents systèmes utilisés pour les quatre projets présentés dans cette thèse ont été développées des premières étapes jusqu'aux dispositifs finaux compatibles avec la vie réelle, ce qui a permis d'acquérir des compétences et de l'expérience sur différentes techniques, systèmes et des instruments.

## *Abstract*

Self-organization and self-assembly through the subtle control of adaptive interactions between suitably designed molecular building blocks enables the development of (multi)functional materials.<sup>1,2</sup> The use of non-covalent interactions to generate sophisticated supramolecular structures makes it possible to exploit the modification of their environment in order to tune their self-assembly behavior.<sup>3</sup> Such modification of the structure can result in a precise tuning of the properties of the assembly. When the assembly is smartly engineered, subtle specific changes in the environment could lead to dramatic changes of one or more physico-chemical properties.<sup>4</sup> In other words, if the supramolecular interactions between a designed receptor and an analyte (i.e. small molecules) present in the environment are optimally engineered, extremely sensitive and selective sensors, relying on recognition events, can be fabricated. Depending on the properties of the components, the readout can be a change in the mass,<sup>5</sup> in the optical properties<sup>6,7</sup> (e.g. a modification of absorbance and/or fluorescence), or in the electrical characteristics<sup>8,9</sup> (like a variation of the electrical capacitance or of the resistance). The use of supramolecular recognition has proven to be the key for the realization of the next generation of sensors exhibiting detection limits at the ppm level with high response speed combined with unprecedented selectivity. These characteristics are the result of optimally designed interactions at the non-covalent level, which can be highly selective through the use of receptor groups possessing ad-hoc characteristic such as size, geometry, dipole moment, etc.

Gas and, in particular, moisture sensors are of paramount importance in numerous science and technology fields thus are commonly used in industries, hospitals, environmental monitoring, etc.<sup>10</sup> To detect water (vapors) in the environment, numerous materials have been employed as active components, including polymers,<sup>11</sup> carbon-based materials,<sup>12</sup> and

composites.<sup>13</sup> Ozone (O<sub>3</sub>) is an extremely toxic gas,<sup>14,15</sup> naturally generated in the atmosphere by the interaction between oxygen and UV light. O<sub>3</sub> monitoring is fundamental for the safety of instruments and operators whenever UV sources (Hg, D<sub>2</sub>, lamps ecc.) are involved.<sup>16</sup>

Since the recognition processes take place at the interface between the active material and the surrounding environment, a successful strategy to improve sensitivity and response speed is to maximize the surface to volume ratio of the sensing materials by building nanoscopic architectures fully decorated with receptors. On this view, the best and most promising candidates for this kind of devices are 1D fibers, 2D materials or 3D porous sponge-like structures, covalently functionalized on their surface with the chosen receptors.

The aim of this thesis is to study and harness the power of supramolecular chemistry to develop and build new optoelectronic sensing devices able to respond to external stimuli such as small modification of their surrounding environment. To achieve this goal, different scaffolds and structures have been explored and, therefore, the manuscript will be divided into four main chapters:

- 2D dynamic plasmonic structures of cross-linked gold nanoparticles as humidity sensors
- Porous 3D networks of gold nanoparticles as micro-sized humidity sensors
- Self-Assembled Amphiphilic  $\pi$ -Conjugated Dyads into Fibers as Ultrafast and Ultrasensitive Humidity Sensor
- Laser reduced graphene oxide for ozone sensing applications

Noble metal nanoparticles (NPs) exhibit extremely interesting optical and electrical properties, from the electrical point of view their behavior depends on the size: they could be insulating, with a diameter smaller than 2/3 nm or conducting, if bigger, behaving as nanoscopic metal electrodes that allow, allowing to build thousands of junction is an extremely limited space.<sup>17</sup> The optical properties are given by the so-called localized

surface plasmon resonance, due to the collective oscillation of the electrons on the particle's surface, in resonance with the oscillating electrical field of light.<sup>18</sup>

The surface plasmons (SPs) are, essentially, light waves that are trapped on the surface of a noble metal because of their interaction with the free electrons on the metal's surface. During this process the electrons will oscillate collectively on the metal's surface creating the SPs.<sup>19</sup> When the metal surface is confined, like in the case of a nanocrystals or nanoholes in a film, the electrons will oscillate collectively between the edges and the resulting SPs will be localized (LSPs). The characteristic wavelength of the plasmonic resonance of noble metal NPs depends on several parameter such as the resistivity of the metal, the shape and the size of the nanoparticles. When multiple nanoparticles are closely packed and interact between each other, the resulting SPs will be a hybrid between localized and collective electrons vibrations, with a dramatic impact on the optical properties of the system. In the first project presented in this thesis, these unique properties will be used to build humidity sensors with optical readout given by the change in the plasmonic properties in 2D networks of cross-linked gold nanoparticles, upon absorption of water molecules from the atmosphere. To achieve this result, 8 nm large gold nanoparticles (AuNPs) were linked together in ordered 2D hexagonal packing using polyethylene glycol di-thiol (SH-PEG-SH) chains. PEG chains have shown to be able of selectively and reversibly absorb water molecules from the atmosphere undergoing swelling. The swelling of the PEG chains causes an increase of the distance between the AuNPs within the network. By choosing carefully the length of used PEG ligand, measuring ca. 7 nm, it was possible to use the external humidity to move the AuNPs within and beyond the tunneling barrier and, therefore, to shift between localized and collective SPs using moisture as external controller, realizing optical humidity sensors operating in the visible range, between 500 and 600 nm.

The second project reported in this thesis work takes advantage of the electrical properties of AuNPs that can be decorated with water absorbing molecule and used to build thousands of electrical junction in an extremely limited space. This result is achieved by using oligoethylene glycol di-thiol (OEG) chains, similar to the ones used in the previous project, to decorate and cross-link the AuNPs, but, in this, case, the length of the chains is

drastically smaller, compared to the previous case, amounting to ca. 1.7 and 2.2 nm. The use of shorter ligand lengths affects several properties of the resulting system. First of all, the networks are less soluble (because of the smaller shell interacting with the solvent) and the ligand is more rigid and reactive, compared to the previous case, meaning that the same reaction leads to precipitation of disordered 3D porous networks in solution instead of 2D hexagonal and ordered packing monolayers. As a consequence of the short ligand chains, the resulting 3D porous structures exhibit remarkably low electrical resistance, with a charge transport dominated by direct tunneling mechanism, and optical properties typical for bulk gold (no LSPs). According to the direct tunneling model, the electrical current passing through the 3D network depends exponentially by the inter-particles distance between each junction. As already described for the first project, OEG chains can reversibly absorb water molecules from the atmosphere, undergoing swelling and, therefore, increasing the inter-particles distance. By taking advantage of this behavior it was possible to use these 3D systems to build microscopic moisture sensing devices with electrical readout, exhibiting exponential dependence of the measured tunneling current over a wide range of relative humidity (RH from 5% to 100%) and remarkably fast response speed  $< 13$  ms.

The third project reported in this thesis, aims at boosting the performance of electrical resistive moisture sensors at their highest potential, reaching state of the art performances in terms of response speed and sensitivity. This result was obtained by using smartly engineered 1D supramolecular nanofibers made by conjugated donor-acceptor (D-A) molecular dyads, synthesized by our collaborators. These molecules, featuring asymmetric and amphiphilic side chains, can be self-assembled, in water solutions, combining solvent induced precipitation and light irradiation, to grow supramolecular nano-fibers. By using the solvophobic interaction as driving force and the  $\pi$ - $\pi$  stacking as stabilizer it was possible to trigger the formation of micrometric long 1D structures. The external shell of the supramolecular fibers is fully decorated by tetra ethylene glycol (TEG) side chains that, as seen for the previous projects, are able to reversibly absorb water molecules from the atmosphere. In solid state and dry conditions, the steric hindrance given by the bulky side chains, forces the molecules to tilt, twisting the nanofiber's core and, therefore, decreasing the  $\pi$ - $\pi$  stacking and the charge transport along

the fibers. When the environmental humidity is increased, water molecules can be absorbed within the side chains bridging them by means of hydrogen bonding. The strength of the collective hydrogen bonding, given by multiple water molecules absorbed, is strong enough to align the molecules and stretch the fibers, increasing the overlap between the intermolecular  $\pi$  orbitals. The increased overlap causes a dramatic increase of the electrical current passing through the fibers. By taking advantage of this behaviour it was possible to correlate the measured current with the amount of absorbed water molecules and, performing a calibration, with the amount of water molecules in the environment surrounding the device, e.g. with the relative humidity. By optimizing the processes for the growth of the fibers and by proper engineering of the devices, it was possible to build extremely sensitive electrical resistive moisture sensors, featuring a change in the measured two-terminal current as big as seven orders of magnitude in the range between 5 and 75% RH with an exponential trend and a response speed of 26 ms. Moreover, thanks to the structure of water molecules being very small (less than 3 Å) and having two donor and acceptor sites for hydrogen bonding, the reported sensors exhibit also great selectivity for water molecules and no response was measured when exposing the devices to other solvent's vapours such as methanol, ethanol or diethyl ether.

The fourth and last project reported in this thesis is focussed on the use of laser-reduced graphene oxide (L-rGO) as active material for electrical resistive ozone sensors. Graphene is a monolayer of graphite, a 2D material made just by carbon atoms arranged in a hexagonal lattice, where all the atoms have a  $sp^2$  hybridization and all the  $\pi$  electrons of each atom are free to move along the 2D flake as they have no mass.<sup>20</sup> This unique characteristic, together with its impressive mechanical resistance, contributed to make graphene the wonder material of the future. The only drawbacks that is still blocking the development of real life technologies based on graphene devices are the production and the processing. Even though graphite is extremely abundant in nature, the production of high quality graphene from graphite can be only obtained using the mechanical exfoliation using the scotch tape approach. This approach relies on the use of scotch tape to mechanically separate the graphene flakes of graphite and to transfer them on an appropriate substrate. This approach is extremely time consuming and not suitable for large scale or industrial production of graphene. One way to overcome this problem is to

chemically oxidize the graphene into graphene oxide (GO): a derivative of graphene where the  $\pi$  conjugation is randomly broken because of the addition of oxygen containing groups, covalently bonded to the carbon atoms within the lattice. The presence of these group make the GO highly soluble in polar solvents such as water and allows the production of big amounts of this material in solution, directly from graphite. The GO can be easily prepared, stored and processed from solution and then reduced back to the so-called reduced GO (rGO) by removing the oxygen containing groups and partially restoring the characteristic of the graphene. The reduction of GO into rGO can be performed with several techniques, in solution, solid state or thin film. So far, the most performing and investigated reduction technique is the thermal reduction in vacuum or inert environment at high temperature, typically between 800 and 1000 °C for a few hours. This process is extremely energy consuming and is not suitable for films thicker than 20/30 nm because of the film's delamination due to the generation of gas bubbles (typically CO, CO<sub>2</sub> and H<sub>2</sub>O) as reduction's products. An interesting alternative relies on the use of a pulsed infrared laser to locally increase the temperature, promoting the reduction. Using a small spot it is possible to reduce just few  $\mu\text{m}$  for each pulse, allowing the diffusion of the produced gases without triggering the delamination. Moreover this technique allows to write confined areas of rGO onto a matrix of insulating GO, making it possible to pattern electrical contacts and circuits directly on GO. By using this technique it was possible to produce space confined areas of high quality rGO as active material for the detection of ozone (O<sub>3</sub>) at extremely low concentrations. O<sub>3</sub> molecules have as a strong affinity with the surface of carbon based materials, such as rGO and can be absorbed causing a strong positive doping and, therefore, a dramatic change in the measured electrical resistance.

In conclusion this thesis aims at making use and programming supramolecular recognition processes in electrically/optically active low dimensional materials suitably decorated with the receptor of a given analyte with the ultimate goal of developing new architectures and devices with enhanced performances. All the different systems used for the four projects reported in this thesis were followed and developed from the very first steps up to the final real life working devices, allowing to gain skills and experience with different techniques, systems and instruments.



- 1 Lehn, J. M. Toward self-organization and complex matter. *Science* **295**, 2400-2403, (2002).
- 2 Lehn, J. M. From supramolecular chemistry towards constitutional dynamic chemistry and adaptive chemistry. *Chem Soc Rev* **36**, 151-160, (2007).
- 3 Aida, T., Meijer, E. W. & Stupp, S. I. Functional Supramolecular Polymers. *Science* **335**, 813-817, (2012).
- 4 Stupp, S. I. *et al.* Supramolecular materials: Self-organized nanostructures. *Science* **276**, 384-389, (1997).
- 5 Xie, J., Wang, H., Lin, Y., Zhou, Y. & Wu, Y. Highly sensitive humidity sensor based on quartz crystal microbalance coated with ZnO colloid spheres. *Sensor Actuat B-Chem* **177**, 1083-1088, (2013).
- 6 Elghanian, R., Storhoff, J. J., Mucic, R. C., Letsinger, R. L. & Mirkin, C. A. Selective colorimetric detection of polynucleotides based on the distance-dependent optical properties of gold nanoparticles. *Science* **277**, 1078-1081, (1997).
- 7 Thomas, S. W., Joly, G. D. & Swager, T. M. Chemical sensors based on amplifying fluorescent conjugated polymers. *Chem Rev* **107**, 1339-1386, (2007).
- 8 Schedin, F. *et al.* Detection of individual gas molecules adsorbed on graphene. *Nat Mater* **6**, 652-655, (2007).
- 9 Chen, C. J., Smeu, M. & Ratner, M. A. Modeling ion sensing in molecular electronics. *J Chem Phys* **140**, 054709, (2014).
- 10 Fraden, J. *Handbook of Modern Sensors*. 4th edn, (Springer-Verlag New York, 2010).
- 11 Kulkarni, M. V., Apte, S. K., Naik, S. D., Ambekar, J. D. & Kale, B. B. Ink-jet printed conducting polyaniline based flexible humidity sensor. *Sensor Actuat B-Chem* **178**, 140-143, (2013).
- 12 Borini, S. *et al.* Ultrafast Graphene Oxide Humidity Sensors. *Acs Nano* **7**, 11166-11173, (2013).
- 13 Zilberman, Y., Ionescu, R., Feng, X., Mullen, K. & Haick, H. Nanoarray of polycyclic aromatic hydrocarbons and carbon nanotubes for accurate and predictive detection in real-world environmental humidity. *ACS Nano* **5**, 6743-6753, (2011).
- 14 Jerrett, M. *et al.* Long-Term Ozone Exposure and Mortality. *N Engl J Med* **360**, 1085-1095, (2009).
- 15 Turner, M. C. *et al.* Long-Term Ozone Exposure and Mortality in a Large Prospective Study. *Am J Respir Crit Care Med* **193**, 1134-1142, (2016).
- 16 Bocci, V. *OZONE. A new medical drug*. (Springer Dordrecht Heidelberg London New York, 2011).
- 17 Rao, C. N. R., Kulkarni, G. U., Thomas, P. J. & Edwards, P. P. Metal nanoparticles and their assemblies. *Chem Soc Rev* **29**, 27-35, (2000).
- 18 Sambles, J. R., Bradbery, G. W. & Yang, F. Z. Optical-Excitation of Surface-Plasmons - an Introduction. *Contemp Phys* **32**, 173-183, (1991).
- 19 Barnes, W. L., Dereux, A. & Ebbesen, T. W. Surface plasmon subwavelength optics. *Nature* **424**, 824-830, (2003).
- 20 Geim, A. K. & Novoselov, K. S. The rise of graphene. *Nat Mater* **6**, 183-191, (2007).

# Table of content

<b>RÉSUMÉ .....</b>	<b>I</b>
<b>ABSTRACT .....</b>	<b>VIII</b>
<b>TABLE OF CONTENT .....</b>	<b>XV</b>
<b>SYMBOLS AND ABBREVIATIONS .....</b>	<b>XVIII</b>
<b>CHAPTER 1 INTRODUCTION .....</b>	<b>1</b>
1 SENSING DEVICES .....	1
1.1 Gas sensors .....	4
1.1.1 Humidity sensors .....	7
1.1.2 Ozone sensors .....	10
2 SUPRAMOLECULAR INTERACTIONS .....	14
3 REFERENCES .....	17
<b>CHAPTER 2 LOW-DIMENSIONAL STRUCTURES FOR SENSING .....</b>	<b>19</b>
1 INTRODUCTION .....	19
2 OD: NANOPARTICLES .....	20
2.1 Metal nanoparticles .....	21
2.1.1 Electrical properties of metal nanoparticles .....	22
2.1.2 Optical properties of metal nanoparticles .....	28
3 1D: NANOFIBERS AND NANOTUBES .....	35
3.1 Electrical properties of 1D supramolecular structures .....	38
4 2D: GRAPHENE AND GRAPHENE OXIDE .....	43
4.1 Electrical properties of graphene and rgo .....	48
5 REFERENCES .....	54
<b>CHAPTER 3 METHODS .....</b>	<b>63</b>
1 INTRODUCTION .....	63
2 SYNTHESIS OF WATER-SOLUBLE GOLD NANOPARTICLES .....	63
2.1 Functionalization of gold nanoparticles .....	66
3 OPTICAL CHARACTERIZATIONS .....	68
3.1 UV-Vis absorbance spectroscopy .....	68
3.2 Dynamic light scattering (DLS). .....	70

4	MORPHOLOGICAL CHARACTERIZATION.....	72
4.1	<i>Atomic force microscopy (AFM)</i> .....	72
4.1.1	Conducting atomic force microscopy (C-AFM).....	77
4.2	<i>Scanning electron microscopy (SEM)</i> .....	78
5	COMPOSITIONAL CHARACTERIZATION .....	81
5.1	<i>X-ray photoelectron spectroscopy (XPS)</i> .....	81
6	ELECTRICAL CHARACTERIZATION .....	83
7	REFERENCES.....	86
<b>CHAPTER 4 FROM 0D TO DYNAMIC 2D MATERIALS – AuNPs PLASMONIC SENSORS .....</b>		<b>87</b>
1	INTRODUCTION .....	87
2	EXPERIMENTAL .....	88
2.1	<i>Materials</i> .....	88
2.2	<i>Sample preparation</i> .....	89
2.3	<i>Optical characterization</i> .....	89
3	RESULTS AND DISCUSSIONS .....	91
4	CONCLUSIONS .....	101
5	REFERENCES.....	102
<b>CHAPTER 5 USING 0D OBJECTS TO BUILD 3D MATERIALS: NANOPARTICLES 3D NETWORKS .....</b>		<b>104</b>
1	INTRODUCTION .....	104
2	EXPERIMENTAL .....	106
2.1	<i>Methods and samples preparation</i> .....	106
3	RESULTS AND DISCUSSIONS .....	107
4	CONCLUSIONS .....	118
5	REFERENCES.....	119
<b>CHAPTER 6 1D SUPRAMOLECULAR NANOFIBERS FOR ULTRASENSITIVE HUMIDITY SENSORS .....</b>		<b>120</b>
1	INTRODUCTION .....	120
2	EXPERIMENTAL .....	123
2.1	<i>Materials and samples preparation</i> .....	123
3	RESULTS AND DISCUSSIONS .....	124
4	CONCLUSIONS .....	132
5	REFERENCES.....	134
<b>CHAPTER 7 2D LASER REDUCED GRAPHENE OXIDE FILMS FOR OZONE SENSING .....</b>		<b>136</b>
1	INTRODUCTION .....	136
2	EXPERIMENTAL .....	138

2.1	<i>Materials and samples preparation</i> .....	138
3	RESULTS AND DISCUSSIONS.....	140
4	CONCLUSIONS .....	156
5	REFERENCES .....	157
<b>CHAPTER 8 CONCLUSIONS AND OUTLOOKS.....</b>		<b>160</b>
	CLOSING REMARKS .....	165
	ACKNOWLEDGEMENTS.....	166
	PUBLICATIONS IN INTERNATIONAL JOURNALS .....	168
	AWARDS .....	169
	CONTRIBUTIONS IN INTERNATIONAL CONFERENCES .....	170
	<i>Oral communications</i> .....	170
	<i>Poster presentations</i> .....	171

# Symbols and abbreviations

<b>4T</b> = Tetrathiophene	<b>PCB</b> = Printed board circuit
<b>AFM</b> = Atomic force microscopy	<b>PDI</b> = Perylene diimide
<b>C-AFM</b> = Conductive atomic force microscopy	<b>PEG</b> = Polyethylene glycol
<b>CH<sub>3</sub>Cl</b> = Chloroform	<b>PMT</b> = Photo-multiplier tube
<b>CNTs</b> = Carbon nanotubes	<b>ppb</b> = parts-per-billion
<b>CVD</b> = Chemical vapor deposition	<b>ppm</b> = parts-per-million
<b>D-A</b> = Donor-Acceptor	<b>PVA</b> = Polyvinyl alcohol
<b>DMF</b> = N,N-Dimethylformamide	<b>rGO</b> = Reduced graphene oxide
<b>DUT</b> = Device under test	<b>RH</b> = Relative humidity
<b>EtOH</b> = Ethanol	<b>SAM</b> = Self-assembled monolayer
<b>FET</b> = Field-effect transistor	<b>SE</b> = Secondary electrons
<b>FOG</b> = Forming gas (92 % N <sub>2</sub> + 8 % H <sub>2</sub> )	<b>SEM</b> = Scanning electron microscopy
<b>GIXRD</b> = Grazing incidence X-Ray diffraction	<b>SIP</b> = Solvent-induced precipitation
<b>GO</b> = Graphene oxide	<b>SP</b> = Surface plasmon
<b>HEG</b> = Hexaethylene glycol	<b>SPM</b> = Scanning probe microscopy
<b>IR</b> = Infrared	<b>SPR</b> = Surface plasmon resonance
<b>L-rGO</b> = Laser-reduced graphene oxide	<b>TEG</b> = Tetraethylene glycol
<b>LSPR</b> = Localized surface plasmon resonance	<b>THF</b> = Tetrahydrofuran
<b>MeOH</b> = Methanol	<b>UV</b> = Ultraviolet (10 nm < $\lambda$ < 400 nm)
<b>Mn</b> = Average molar mass	<b>Vis</b> = Visible (400 nm < $\lambda$ < 800 nm)
<b>n</b> = Refractive index	<b>VOCs</b> = Volatile organic compound
<b>NMP</b> = N-methyl-2-pyrrolidone	<b>XPS</b> = X-Ray photoelectron spectroscopy
<b>NPs</b> = Nanoparticles	<b>XRD</b> = X-Ray diffraction
<b>OEG</b> = Oligoethylene glycol	$\epsilon$ = Dielectrical permittivity
	$\lambda$ = Wavelength

# Chapter 1 Introduction

## 1 SENSING DEVICES

---

Sensors are as old as life. Any life being, from the simplest creatures to humans, use them to gain a perception of their surrounding environment. Over thousand years of evolution, nature has developed an impressive wide variety of sensors, employed from the live beings to adapt and survive in this mutable world. Thanks to these “devices” we have the possibility to see electromagnetic waves between  $\lambda = 400$  and  $700$  nm through our eyes, we can perceive air vibrations in the frequency range from  $20$  to  $20'000$  Hz as sounds through our ears, we can feel the pressure and the temperature along all our body through the skin, we have gyroscopes that allow us to move without falling down and we can recognize different chemical compounds in gas, liquid or solid state through our nose and mouth. Migratory birds and sea creatures are able to feel the magnetic field of the earth, bats are able to dodge obstacles in dark by using ultrasounds and so on. These are just few of the countless examples of sensors nature has developed and, for some of them, the working mechanism has not yet been completely unraveled.

In nature, the ability to perceive the external stimuli and to react to them are fundamental for the survival, meaning that not only the translation of the stimuli, but also the transmission of the related signals must be as fast as possible. For this reason, most of the natural sensors generate electrochemical signals, relying on transport of ions that can move quickly through the nerve fibers, reaching the brain in few milliseconds.

Artificial sensors have been developed by humans to assess qualitative and/or quantitative information that are not achievable by using our natural senses. An artificial sensor is often defined as “Something that reads and responds to a signal or a stimulus”. Obviously, this definition is broad and imprecise: a well-trained dog used to find truffles under the ground or drugs at the airport cannot be considered a truffle or a drug sensor, as well as a small bird in a cage, brought inside tunnels by miners, cannot be considered a methane detector.

Since all the current technology is based on the transmission of electrical signals, a more precise definition of sensor could be: “A sensor is a device that receives a stimulus and responds with an electrical signal”.<sup>1</sup> The electrical output signal generated from such devices, as a consequence of a specific input, may be in the form of voltage, current, or charge. These may be further described in terms of amplitude, polarity, frequency, phase, or digital code. Therefore, a sensor has input properties (of any kind) and electrical output properties. This means that an artificial sensor could be seen as a translator of a generally non-electrical input into an electrical value, compatible with other devices based on the same technology (e.g. amplifiers, analyzers, computers etc.). In a more general vision we can consider these devices as the bridge between man-made object and the external world. Nowadays, many sensing devices are already in our homes and offices as commodities and are considered indispensable for our safety (like smoke detectors) or to capture pictures and frames of our lives (like digital optical cameras) and so on, improving the quality of our lives. At the current stage, sensing devices are employed for routine applications or to continuously monitor specific analytes for sensitive processes but, in a near future, they will be exploited to allow electrical devices and artificial intelligences to gain a perception of their environment and to interact with it, mimicking life being. Some prototype humanoid robots like the EU funded “Icub” project are, already, driven by a cognitive system, connected to a set of sensors that provides the senses of touch, temperature and sight, allowing them to discover and understand their surrounding world. These technologies can also be exploited in medical applications, helping patients to restore partially lost senses or to improve the usability of prosthetic body parts.

At this point it is important to distinguish between sensors and transducers, the first ones, as discussed above are employed to convert an input into an electrical output while the latter are employed to convert an input into any kind of non-electrical output. If a

transducer is used to convert an electrical input into a non-electrical output, like motion (in the case of electric motors) or sounds (in the case of speakers), they are called actuators and can be imagined as the opposite of a sensor. Complex sensors consist in multiple transduction processes and may include several transducers to convert the initial input into a different kind of non-electrical output that can be finally converted by a sensor to produce the electrical output. An example of complex sensor which is well-known by any chemist is the phenolphthalein pH indicator: when this molecule is in the acid form ( $\text{pH} < 8.2$ ) its water solutions are colorless, while, when it is in the basic form ( $\text{pH} > 8.2$ ), it is strongly colored in pink/fuchsia. Diluted water solutions of this molecule can then be used as a translator of a chemical input (pH) into an optical output (change of color). Finally, by using a UV-Vis spectrophotometer is then possible to convert the optical color change into an electrical signal (**Figure 1.1**).

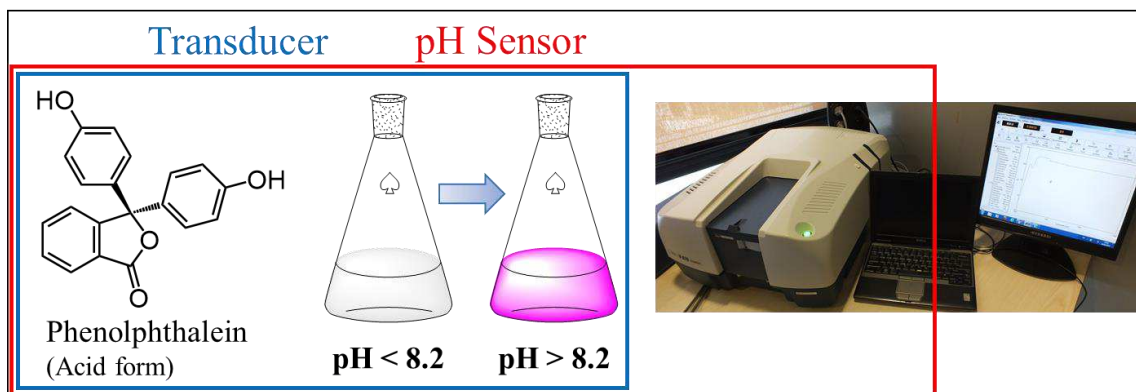


**Figure 1.1:** Example of a complex pH sensor made phenolphthalein transducer and a UV-Vis spectrophotometer as optical sensor.

In this example a complex pH sensor is composed by the combination of a phenolphthalein transducer and spectrophotometer optical sensor. Another example of complex sensors can be found in chapter 4 of this thesis, where 2D networks of gold nanoparticles are used as transducers for humidity sensors featuring an optical readout.

This thesis must be intended as a fundamental work, focused on the understanding and mastering the recognition processes involved in sensing. The experimental sections aims at the exploitation of such processes for the development of new active materials for gas sensing by using the principles of supramolecular chemistry to trigger specific recognition



mechanisms and to improve the performances of the fabricated devices. The devices fabricated and the data reported are the result of a strong statistic but are mostly proofs-of-concepts built with standards geometries and devices configurations, because the engineering and optimization of the device performances are far from the scope of this work.

## 1.1 GAS SENSORS

Gas sensors are devices employed to detect specific gaseous analytes. They are currently employed to monitor the exhausts gases in any industrial process involving a production and release of gaseous molecules in the atmosphere, they are employed in our cars, to constantly provide the right air/fuel ratio in the combustion chamber, but can also be used to monitor the levels of humidity or oxygen for the manufacturing of sensitive equipment or to monitor the concentration of harmful gas species in working and living places. The atmosphere in which we live in contains indeed numerous kinds of chemical species, both natural and artificial, some of which are vital to our life while many others are, more or less, harmful.

**Figure 1.2** illustrates the nature and concentration levels of typical gas components in atmospheric air. The vital gases like  $O_2$  and humidity should be kept at adequate levels in living atmospheres, while the concentration of hazardous gases should be controlled to be below the safety levels. Flammable gases such as short hydrocarbons (e.g. methane and GPL) and  $H_2$ , which are used as fuels, can explode upon leakage in the atmosphere with dramatic consequences, for this reason, gas sensors targeting such compounds must be capable of detecting concentrations below 1/10 of the lower explosion limit for the targeted gas as an alarming level.

For toxic gases, volatile organic compounds (VOCs), offensive odors and other air pollutants, their standards have been legislated by various laws based on the strength of toxicity or offensiveness of each gas, those values are indicated as star marks in **Figure 1.2**.<sup>2</sup>

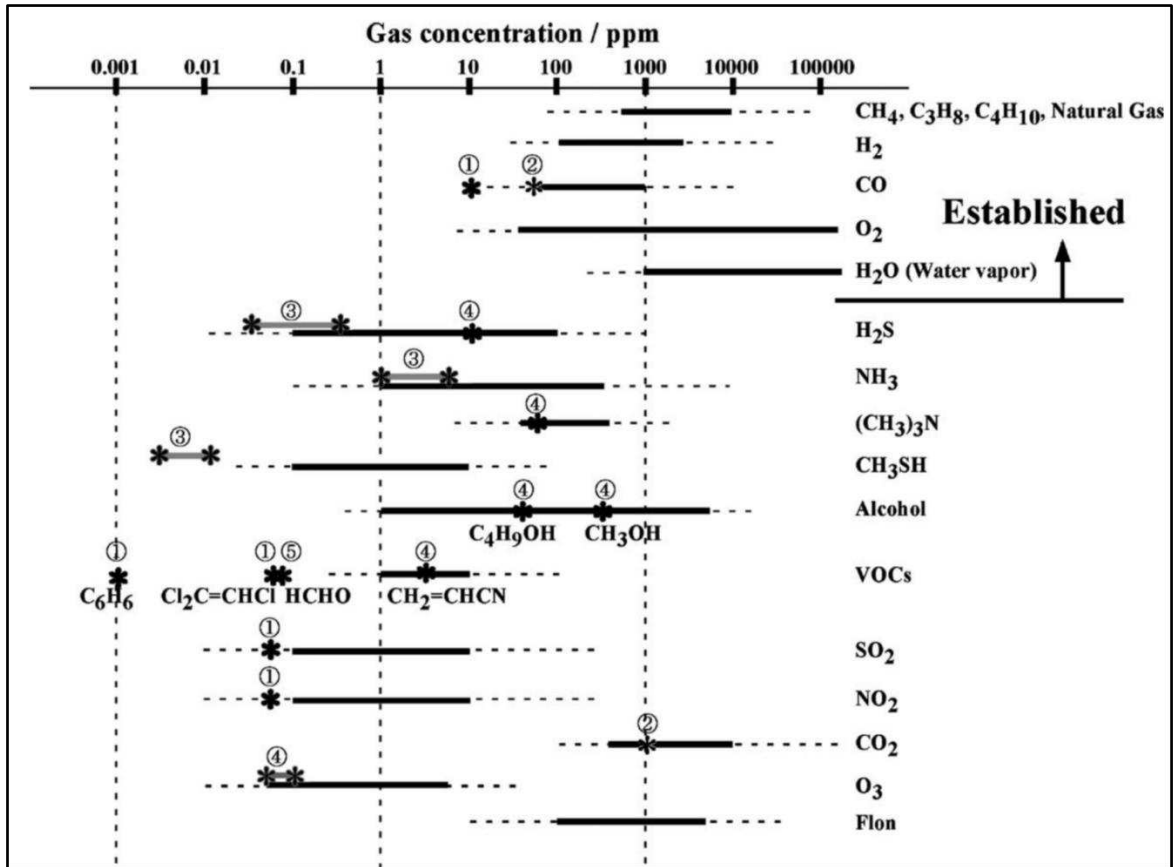


**Figure 1.2:** Concentration levels of typical gas components concerned. Star marks indicate the standards of the gases legislated in Japan by (1) Environmental Standard, (2) Ordinance on Health Standards in the Office, (3) Offensive Odor Control Law, (4) Working Environment Measurement Law, and (5) Ordinance by Ministry of Health, Labour and Welfare. (Image reprinted with permission from Ref.<sup>2</sup>).

The full lines in **Figure 1.2** shown for each gas indicates the range of concentration safely covered by currently commercial gas sensors, while the broken lines indicates the range covered in laboratory tests.<sup>2</sup>

To be employed in real world applications, a gas sensing device should fulfill many requirements depending on the purposes, locations and the operative conditions to which the device will be exposed. Among these requirements, the most stringent are directly related to the sensing performances (e.g. sensitivity, selectivity and response speed) and to the reliability (e.g. drift, stability and interfering gases). These characteristics are strongly dependent on the active materials used to detect the gas molecules and on the translation mechanism used to generate the output.

The cheapest, easiest and, therefore, the most diffused sensors to detect gas molecules are the electrical resistive ones, usually called “Chemiresistive sensors”. In such devices, the quantitative information on the concentration of the targeted compound in the environment is directly translated into a change in the electrical resistance of the device.

Electrical resistive gas sensors were introduced for the first time more than sixty years ago. In the early 1950s, when Brattain and Bardeen, two scientists working at Bell Laboratories, demonstrated that some bulky semiconductor materials, such as Ge, change their resistance depending on the atmosphere they are in contact with.<sup>3</sup> At the beginning of the 1960s, Seyama and co-workers, were able to demonstrate that gas sensing is possible with simple electrical devices, using ZnO thin films as a sensing layer. To do it, they have employed a simple chemiresistive device based on ZnO thin films operating at the temperature of 485 °C that, upon interaction with propane vapors, exhibited a response almost 100 times higher, compared to the thermal conductivity detectors usually employed at that time.<sup>4</sup> These devices displayed interesting sensitivity but very low selectivity. Just 10 years after, Taguchi N. fabricated and patented the first selective gas sensor based on SnO<sub>2</sub>. After investigating many metal oxides, he found that SnO<sub>2</sub> exhibited advantageous properties such as higher sensitivity, low operating temperature and high thermal resistance. The first generation of these devices were based on a mixture of tin chloride (SnCl<sub>4</sub>) and stearic acid that was painted on the substrate and fired at 700 °C in air. Firing process was used to burn off the organic component, leaving behind a porous SnO<sub>2</sub> layer, in order to increase the sensitivity, selectivity and stability.<sup>5</sup> The main application of these devices commercialized by Figaro Inc. was as detectors to prevent accidents and fire in domestic residences by monitoring the presence of hazardous levels of explosive gases. Intense efforts in this direction resulted in widespread application of semiconductor gas sensors. After this, the real expansion of the “gas sensors era” started in 1980s with the advent of new techniques for nanofabrication and characterization that allowed the development of new devices based on low-dimensional structures with high surface-to-volume ratio, featuring higher performances and lower energy consumption.

Nowadays, the combination of nanostructured materials and *ad-hoc* receptors has allowed the fabrication of multi-sensor arrays able to detect selectively and simultaneously the different components of a gas mixture in lab tests. Such devices, called “artificial noses”, are currently studied for different applications such as food control,<sup>6</sup> detection of pathogen

microbial on the skin<sup>7</sup> or to monitor the quality of indoor air<sup>8</sup> by measuring the simultaneous presence and the relative amounts of different specific gaseous compounds.

### 1.1.1 Humidity sensors

Atmospheric air is mainly composed by N<sub>2</sub>, O<sub>2</sub> and water vapor. While the amount of the first two components is, more or less, uniformly distributed in the atmosphere and constant over time, the percentage of water content can be dramatically different between different areas, altitudes and seasons, ranging from ~ 0% to ~ 2%. The water content in air is called humidity and its presence is fundamental for the well-being of animals and plants. Moreover, controlled humidity levels are an important factor for operating certain equipment, for instance, high impedance electronic circuits, electrostatic sensitive components, high voltage devices, fine mechanisms, etc.<sup>1</sup>

The real content of water vapor in air is called “Absolute humidity” and is usually expressed in grams of water per cubic meter of air. It can be measured by forcing the wet air to pass by a hygroscopic material, such as a salt, and measuring the weight difference before and after the absorption. The absolute humidity measured in this way is obviously dependent on the pressure and is not convenient for engineering purposes. A more convenient way to quantify the amount of water in air is by using the so-called “Relative humidity” (RH). The relative humidity is given by the ratio between the actual vapor pressure of water in air at any temperature and the maximum vapor pressure at the same temperature (e.g. the vapor tension at the same temperature). This value is usually reported in percentage and is defined as:

$$RH(\%) = 100 \frac{P_w}{P_s}$$

Where  $P_w$  = Actual pressure of water vapor (at any temperature) and  $P_s$  = Saturation vapor pressure (at the same temperature).

When  $RH = 100\%$  e.g. the actual vapor pressure is equal to the vapor tension, the water in the atmosphere is in equilibrium between vapor and liquid form, meaning that, under these conditions, condensation of water droplets will occur (these conditions are called “Dew point”).

To calibrate the fabricated humidity sensors, a reference source of humidity is required. There are several methods for producing a known humidity level. For instance it could be possible to generate dry ( $0\% RH$ ) and saturated ( $100\% RH$ ) air separately and mix them in a known ratio to obtain the desired humidity value.

Yet, the easiest and most popular method is by using saturated salt solutions in water. With this method, a controlled and stable humidity level can be obtained by placing a dish containing a saturated solution of a specific salt in a closed box which is tightly sealed from the atmosphere. After a certain amount of time, depending on the size of the box and on the exposed solution surface, the water in the salt solution will reach an equilibrium with the one in the box's atmosphere, modifying and controlling the relative humidity in the free space above the dish with good accuracy. By changing the salts, this approach allows to generate atmospheres ranging from  $RH = 9.32\%$  (using a  $KOH$  solution) up to  $RH = 97.59\%$  (Using a  $K_2SO_4$  solution) at  $20^\circ C$  with a very small dependency on the temperature.<sup>9</sup> An example application of this method to produce controlled humid air can be found in chapter 4 where saturated salt solutions were used to control the humidity inside a spectroscopy cuvette.

Devices able to detect and quantify the humidity levels in the atmosphere are usually called “Hygrometers”.

Such devices should, ideally, be selective for water vapor and their response should be proportional to the amount of water vapor in the atmosphere.

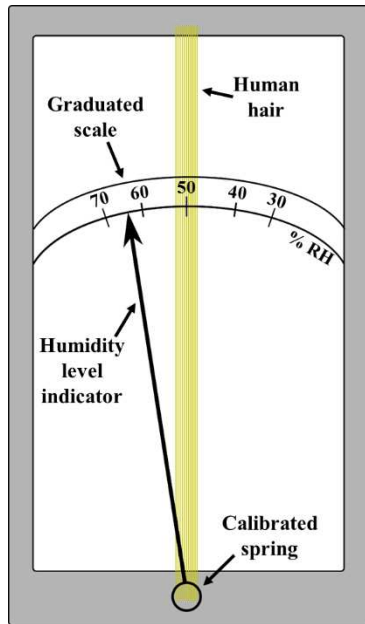


*Figure 1.3: Scheme of a hair hygrometer (Horace Bénédict de Saussure, late 1700s)*

The first rudimental working hygrometer was invented by Horace Bénédict de Saussure in late 1700s and was based on the use of a strand of human (blond) hair set under tensile stress and connected to a calibrated spring to read the environmental humidity (**Figure 1.3**).

In these devices the hair were blocked on one side, the other side was connected to a spring to apply a certain tension. Since hair are made of keratin, their structure and mechanical strength are given by the contemporary presence of covalent cross-link between cysteine and weaker hydrogen bonds. The presence of this protein makes their surface hygroscopic e.g. able to absorb water from the atmosphere.

Upon absorption of water, the hydrogen bonding between the amino-acids on the hair's surface are broken and the tensile stress is released. The change in the tension is proportional to the amount of water absorbed and causes a displacement of the spring that is amplified by using a long indicator arm, pointing at a calibrated scale (**Figure 1.3**).

Nowadays the control of the humidity is of paramount importance in numerous field and applications, in science and technology but also to guarantee the comfort of working and living places. As a “rule of thumb”, the humidity level should be kept around 50% with a temperature of 20-25° C to ensure the well-being in living and working environments but these values may vary for the different applications. For instance relative humidity must be constantly set at 38% for class-10 clean rooms and 60% in hospital operating rooms.<sup>1</sup> The growing demand of ways to control and monitor the humidity levels has pushed the field over the last decades for the development of more performing and reliable humidity sensing devices that can be included in other components such as air conditioners, humidifiers and so on, without affecting the price and the size of the equipment. Hitherto, different transduction mechanisms have been explored in order to improve sensitivity, response speed, and recovery time, by exploiting different properties as read-out, including optical<sup>10</sup> and electrical characteristics (capacitance,<sup>11</sup> resistance,<sup>12</sup> and gate effect in field-effect transistors<sup>13</sup>) as well as small mass changes.<sup>14</sup> To detect water in the environment, numerous

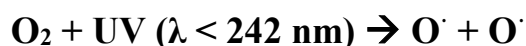
materials have been employed as active components, including polymers,<sup>15</sup> carbon based materials,<sup>16</sup> and composites.<sup>17</sup>

Since the sensing processes occur via molecular recognition, the sensitivity of such devices can, in principle, be harnessed by using low dimensional structures exhibiting a high surface area fully decorated with receptors. The importance of low-dimensional structures for the improvement of sensing performances will be deeply discussed in the next chapter.

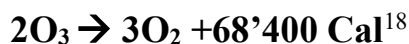
### 1.1.2 Ozone sensors

Ozone (O<sub>3</sub>) is a strongly oxidant and toxic allotropic form of oxygen. It has been known since 1785, the year in which van Marum observed the formation of this gas in an electric spark discharge in oxygen. Schoenbein recognized ozone in 1840 as a new substance. Soret showed in 1866 that the chemical composition of ozone is that of triatomic oxygen. Under normal conditions, ozone is a gas with a light blue color, and has a characteristic pungent smell. Its name derives from the Greek word “*ozein*”, that means, indeed, “smell”. The characteristic odor of this molecule can be easily detected by human nose and permits the recognition of ozone in concentrations as low as about 1 ppm.<sup>18</sup>

Ozone is naturally present in earth's atmosphere. It is generated in the stratosphere, ~22 km above the level of sea, from the light-induced reaction of oxygen molecules upon exposure to the deep UV light  $\lambda < 242$  nm coming from the sun.<sup>19</sup>



Gaseous ozone is a highly active, irritating, oxidizing substance. Among oxidant agents, ozone is the third strongest, after fluorine and persulfate, a fact that explains its high reactivity. It is characterized by its strong oxidizing power and by the tendency to revert to molecular oxygen according to the reaction



The rate of reaction depends upon temperature, pressure, and concentration of the ozone. The reaction proceeds slowly at ordinary temperatures but fairly quickly, even to the velocity of thermal explosion, at elevated temperatures. In addition, the reaction is catalyzed by many sensitizers.

Naturally, ozone is generated and accumulated in the most external shell of the atmosphere but, within the last centuries, human activities such as industrial processes, vehicular traffic, etc. have led to a dangerous environmental pollution of the air present in the troposphere, which extends 8–17 km from the earth's surface. Exaggerated emissions of pollutants such as nitrogen oxides (NO and NO<sub>2</sub>), carbon oxides (CO and CO<sub>2</sub>), methane (CH<sub>4</sub>), acids, such as hydrochloric (HCl) and sulfuric (H<sub>2</sub>SO<sub>4</sub>) and other minor compounds, have catalyzed the formation of ozone, increasing its concentration in those areas up to 0.3 µg/l or even more.

In large metropolis, ozone, mixed with the other pollutants, composes the photochemical smog and has become the main toxicant for the lungs, eyes, noses and, to a lesser extent, the skin. In particular, respiratory mucosa suffers the most severe damages because it does not contain enough buffer substances to neutralize this dangerous acid mixture. Indeed the respiratory tract lining fluids, that amounts to only 20–40 ml covering as an aqueous film layer the alveolar space of about 70 m<sup>2</sup>, is easily overwhelmed by this acidic mixture of strong oxidants.<sup>19</sup> Particularly children, asthmatic and other broncho-pulmonary patients are at high risk, justifying the necessity of more careful investigation on the behavior of this compound.<sup>20,21</sup> Recent studies have shown that, after prolonged breathing of air contaminated with ozone, the seriousness of symptoms and pathological changes are in relation to the ozone concentration and the exposure time, as reported in **Table 1.1**. These effects can be also amplified if the ozone-containing air is contaminated with NO<sub>2</sub>, acidic compounds, CO, etc.



O <sub>3</sub> concentration in air (ppm)	Toxic effects
0.1	Lachrymation and irritation of upper respiratory airways
1.0-2.0	Rhinitis, cough, headache, occasionally nausea and retching. (Predisposed subjects may develop asthma)
2.0-5.0 (10-20 min)	Progressively increasing dyspnoea, bronchial spasm, retrosternal pain
5.0 (60 min)	Acute pulmonary oedema and occasionally respiratory paralysis
10.0	Death within 4 h
50.0	Death within minutes

**Table 1.1:** Table reporting the effect of exposure to ozone gas on humans. (Data taken from ref.<sup>19</sup>)

From the data reported in **Table 1.1** it is clear how important could be to constantly monitor the amount of ozone in the air we breathe, especially inside big and polluted cities.

The standard method currently employed to detect and quantify environmental ozone is to use UV absorbance measurements, targeting the characteristic features of such molecule. Although this method is reliable and has a high sensitivity, it exhibit several drawbacks given by the complexity of the measurement apparatus, the high cost and the large size of the used detectors.<sup>22</sup> On the other hand, the use of inorganic metal oxide thin films, relying on an electrochemical transduction methods, ensures compact sizes and high sensitivity. In 1993 Takada et al. reported on the use of a semiconducting layer of In<sub>2</sub>O<sub>3</sub> with different metal catalyzers to improve the performances of the previously reported electrochemical resistive ozone sensors (**Figure 1.4**).<sup>23</sup> In such kind of devices, the readout is given by the selective decomposition of ozone, catalyzed by the metal oxide active layer. The Oxygen radical formed during the reaction are absorbed within the semiconducting layer increasing the resistance of the devices

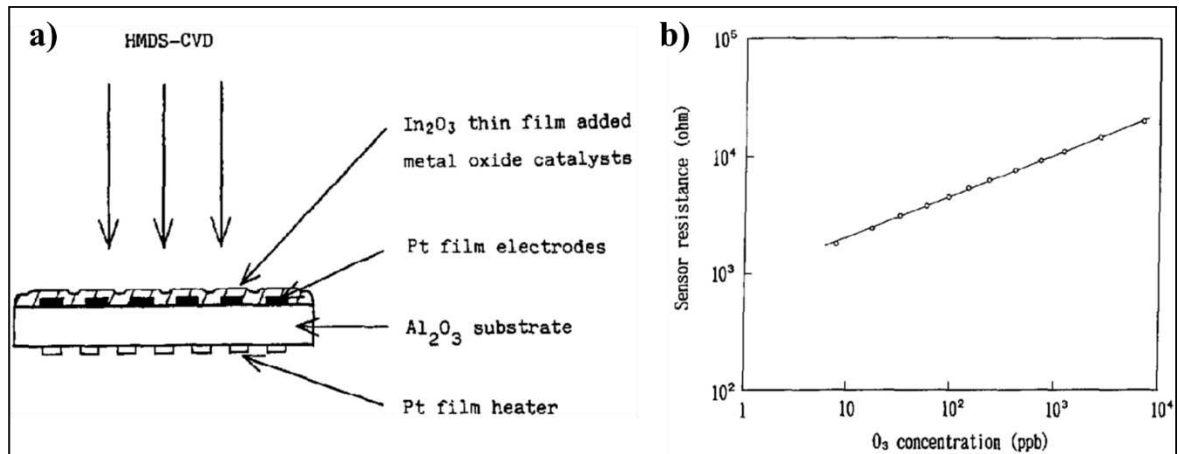


**Figure 1.4:**  $\text{In}_2\text{O}_3$  resistive ozone sensor reported by Takada et al in 1993. a) Design of the device. b) resistance response at different ozone concentrations. (Images reprinted with permission from Ref.<sup>23</sup>)

These devices exhibited extremely low detection limits of  $\sim 8$  ppb and good sensitivity but required high operating temperature to trigger the decomposition of ozone into radical oxygen (between  $350^\circ\text{C}$  and  $500^\circ\text{C}$ , depending on the metal catalyzer employed).

Conductive carbon based materials, such as carbon nanotubes (CNTs), graphene and graphene oxide can be reversibly doped, changing their electrical properties upon exposure to ozone at room temperature. Since, in this case, the recognition is given by absorption and doping at room temperature, this characteristic has been exploited for the realization new ozone sensing devices operating at room temperature and featuring high performances and low costs.

## 2 SUPRAMOLECULAR INTERACTIONS

---

As already mentioned, this manuscript is a PhD thesis in physical chemistry and aims at exploiting the principles of supramolecular chemistry for the development of new active materials for gas (humidity and ozone) sensing. This paragraph is meant to provide a general and brief understanding on the principles and on the processes involved in the supramolecular chemistry. The concept of supramolecular chemistry was introduced for the first time in 1979 by Jean-Marie Lehn as “the chemistry of molecular assemblies and of the intermolecular bonds”,<sup>24</sup> Although the term “supramolecule” appeared for the first time 76 years earlier in Webster dictionary.<sup>25</sup> This field started, indeed, officially in 1960s as the chemistry of the *host-guest* interactions with the studies on the formation of “supramolecules” made by a selective binding of alkali metal cations by natural<sup>26</sup> or synthetic macrocyclic ligands known as crown ethers<sup>27</sup> and cryptands.<sup>24,28</sup> Such preliminary studies paved the way for the expansion of the horizons of supramolecular chemistry towards the study of self-organization processes.

Self-organization consists in a reversible and spontaneous organization of single molecular entities into ordered supramolecular structures stabilized by weak non-covalent bonds.<sup>29</sup> The main advantage of supramolecular self-assembly, compared to the conventional covalent chemistry, is given by the presence of a fully thermodynamic control of the processes involved, providing unprecedented predictability of the resulting structures and reaction's yields. The exploitation of the non-covalent interactions rapidly became an outstanding and powerful tool for the realization of supramolecular functional architectures with precise structures up to the nanometer scale<sup>30</sup> and, since the interactions are based on precise and controlled recognition events, for the realization of the new generation of selective sensing devices. By using this approach it was possible, for the first time, to use classic covalent chemistry to synthesize and engineer the functional and structural building blocks, featuring *ad-hoc* geometries and functionalities, to self-assemble into 1, 2 and 3D complex structures.<sup>31</sup>

As aforementioned, supramolecular self-assemblies are grown by bottom-up approaches under thermodynamic control by exploiting non-covalent interactions. The non-covalent interaction, featuring energies between ~2 kJ/mol to 300 kJ/mol, are generally weaker than

the covalent ones (e.g. a single C-C bond features an energy of  $\sim 347$  kJ/mol) and are always in equilibrium between associated and non-associated forms.

Depending on the nature of the interactions, the diverse non-covalent bonds can exhibit completely different energies and properties such as geometry and range of the interaction.

**Table 1.2** reports the typical non-covalent interaction energies and properties.<sup>25</sup>

Interaction	Typical energy (kJ/mol)	Directionality
Ion-Ion	200-300	Low
Ion-Dipole	50-200	High
Hydrogen bond	4-120	Very high
Dipole-Dipole	5-50	High
$\pi$ - $\pi$	1-50	High
Van der Waals (Weak)	0-5	High
Solvophobic interactions	Depending on the species	Low

**Table 1.2:** Overview on the different non-covalent interaction exploited in supramolecular chemistry. (Data taken from Ref.<sup>25</sup>)

Electrostatic interactions, such as the ion-ion and the ion-dipole, are the strongest ones and feature the longest interaction range among the non-covalent bonds. These interactions can be used to build extremely robust and rigid structures such as supramolecular wires and metal organic framework and can be employed in the field of sensing for the trapping and recognition of metal ions in water solutions.<sup>32</sup>

Among the non-covalent interactions, the key role for the realization of complex and controlled supramolecular structures is played by hydrogen bonding. Such interactions are a special kind of dipole-dipole interactions in which an hydrogen atom behave as a bridge between a donor and an acceptor, generating a strong and highly directional bond.<sup>33</sup> The requirement for the formation of a hydrogen bond is to have a donor group in which a hydrogen atom is directly connected to an electronegative atom (such as N or O), generating a permanent dipole with a partial positive charge localized on the Hydrogen atom. On the other hand the hydrogen bond acceptor should expose an electron-withdrawing group, generating a second permanent dipole, as shown in **Figure 1.5**.

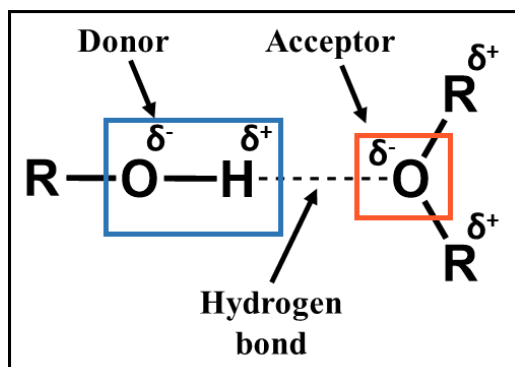


Figure 1.5: Example of a hydrogen bond between an alcohol donor and an ether acceptor.

Hydrogen bonding represents the main non-covalent forces stabilizing biological compounds and systems but can be exploited for several different applications. In the specific case of this thesis, hydrogen bonding was used to reversibly catch water molecules in the gas state for the realization of humidity sensors in chapters 4, 5 and 6.

$\pi$ - $\pi$  interactions are weak non-covalent forces taking place between the  $\pi$  electrons of adjacent aromatic molecules. These interactions can have two different geometries: the face-to-face, where the molecules lie parallel between each other and the face-to-edge, where the aromatic cores of the molecules are perpendicular between each other. The former kind of interaction generates the so-called J-aggregates where the  $\pi$  electrons are delocalized over several adjacent molecules. Those aggregates are extremely important especially in the field of organic electronics, where the overlapping between  $\pi$  orbitals is used to transport charge carriers over long distances, for the realization of electrical devices such as transistors, solar cells, light-emitting diode etc. In this thesis,  $\pi$ - $\pi$  interactions are employed in chapter 6 to form J-aggregates between PDI-4T molecules, growing conductive supramolecular nanofibers.

Solvophobic interactions are long range forces occurring in solution between a solvent and a solute. Depending on the solvent-solute couple, these forces can be a powerful tool to trigger the aggregation of supramolecular structures. These interactions can be exploited, for instance, to form micelles of surfactants such as soaps or to grow supramolecular structures with the solvent-induced precipitation (SIP) technique (more details on the use of solvophobic interactions and SIP are provided in Chapter 6).

### 3 REFERENCES

---

- 1 Fraden, J. *Handbook of Modern Sensors*. 4th edn, (Springer-Verlag New York, 2010).
- 2 Yamazoe, N. Toward innovations of gas sensor technology. *Sensor Actuat B-Chem* **108**, 2-14, (2005).
- 3 Brattain, W. H. & Bardeen, J. Surface Properties of Germanium. *Bell System Technical Journal* **32**, 1-41, (1953).
- 4 Seiyama, T., Kato, A., Fujiishi, K. & Nagatani, M. A New Detector for Gaseous Components Using Semiconductive Thin Films. *Anal Chem* **34**, 1502-1503, (1962).
- 5 Taguchi, N. Gas-detecting device; U.S. patent 3631436 A. (1971).
- 6 Efremenko, Y. & Mirsky, V. M. Virtual sensor array consisting of a single sensor element with variable affinity: An application for analysis of fish freshness. *Sensor Actuat B-Chem* **241**, 652-657, (2017).
- 7 Carmona, E. N. *et al.* Detection of food and skin pathogen microbiota by means of an electronic nose based on metal oxide chemiresistors. *Sensor Actuat B-Chem* **238**, 1224-1230, (2017).
- 8 Caron, A., Redon, N., Thevenet, F., Hanoune, B. & Coddeville, P. Performances and limitations of electronic gas sensors to investigate an indoor air quality event. *Build Environ* **107**, 19-28, (2016).
- 9 Greenspan, L. Humidity Fixed-Points of Binary Saturated Aqueous-Solutions. *J Res Nbs a Phys Ch* **81**, 89-96, (1977).
- 10 Wong, W. C. *et al.* Polyvinyl alcohol coated photonic crystal optical fiber sensor for humidity measurement. *Sensor Actuat B-Chem* **174**, 563-569, (2012).
- 11 Hong, H. P. *et al.* Percolated pore networks of oxygen plasma-activated multi-walled carbon nanotubes for fast response, high sensitivity capacitive humidity sensors. *Nanotechnology* **24**, 085501, (2013).
- 12 Tang, Q.-Y., Chan, Y. C. & Zhang, K. Fast response resistive humidity sensitivity of polyimide/multiwall carbon nanotube composite films. *Sensor Actuat B-Chem* **152**, 99-106, (2011).
- 13 Liang, F. *et al.* TiO<sub>2</sub> nanotube-based field effect transistors and their application as humidity sensors. *Mater Res Bull* **47**, 54-58, (2012).
- 14 Xie, J., Wang, H., Lin, Y., Zhou, Y. & Wu, Y. Highly sensitive humidity sensor based on quartz crystal microbalance coated with ZnO colloid spheres. *Sensor Actuat B-Chem* **177**, 1083-1088, (2013).
- 15 Kulkarni, M. V., Apte, S. K., Naik, S. D., Ambekar, J. D. & Kale, B. B. Ink-jet printed conducting polyaniline based flexible humidity sensor. *Sensor Actuat B-Chem* **178**, 140-143, (2013).
- 16 Borini, S. *et al.* Ultrafast Graphene Oxide Humidity Sensors. *ACS Nano* **7**, 11166-11173, (2013).
- 17 Zilberman, Y., Ionescu, R., Feng, X., Mullen, K. & Haick, H. Nanoarray of polycyclic aromatic hydrocarbons and carbon nanotubes for accurate and predictive detection in real-world environmental humidity. *ACS Nano* **5**, 6743-6753, (2011).
- 18 Streng, A. G. Tables of Ozone Properties. *J Chem Eng Data* **6**, 431-436, (1961).

- 19 Bocci, V. *OZONE. A new medical drug*. (Springer Dordrecht Heidelberg London New York, 2011).
- 20 Turner, M. C. *et al.* Long-Term Ozone Exposure and Mortality in a Large Prospective Study. *Am J Respir Crit Care Med* **193**, 1134-1142, (2016).
- 21 Jerrett, M. *et al.* Long-Term Ozone Exposure and Mortality. *N Engl J Med* **360**, 1085-1095, (2009).
- 22 Lodge, J. J. *Methods of Air Sampling and Analysis*, 3rd ed. Vol. 23 (American Chemical Society, 1989).
- 23 Takada, T., Suzuki, K. & Nakane, M. Highly Sensitive Ozone Sensor. *Sensor Actuat B-Chem* **13**, 404-407, (1993).
- 24 Lehn, J. M. Cryptates - Inclusion Complexes of Macropolycyclic Receptor Molecules. *Pure Appl Chem* **50**, 871-892, (1978).
- 25 Steed, J. W., Turner, D. R. & Wallace, K. *Core Concepts in Supramolecular Chemistry and Nanochemistry*. (John Wiley & Sons, 2007).
- 26 Ovchinnikov, Y. A. Second FEBS-Ferdinand Springer lecture: Membrane active complexones. Chemistry and biological function. *FEBS Lett* **44**, 1-21, (1974).
- 27 Pedersen, C. J. & Frensdorff, H. K. Macrocyclic polyethers and their complexes. *Angew Chem Int Ed Engl* **11**, 16-25, (1972).
- 28 Lehn, J. M. Cryptates: the chemistry of macropolycyclic inclusion complexes. *Acc Chem Res* **11**, 49-57, (2002).
- 29 Whitesides, G. M. & Grzybowski, B. Self-assembly at all scales. *Science* **295**, 2418-2421, (2002).
- 30 Reinhoudt, D. N. *Perspectives in Supramolecular Chemistry: Supramolecular Materials and Technologies*. Vol. 4 (John Wiley & Sons, 2007).
- 31 Dietrich-Buchecker, C. O., Sauvage, J.-P. & Kintzinger, J.-P. Une Nouvelle Famille de Molecules: Les Metallo-Catenanes. *Tetrahedron Lett* **24**, 5095-5098, (1983).
- 32 Cho, E. S. *et al.* Ultrasensitive detection of toxic cations through changes in the tunnelling current across films of striped nanoparticles. *Nat Mater* **11**, 978-985, (2012).
- 33 Jeffrey, G. A. *An Introduction to Hydrogen Bonding*. (Oxford University Press, 1997).

# Chapter 2

## Low-dimensional structures for sensing

### 1 INTRODUCTION

---

As briefly mentioned in the previous chapter, all the recognition and transduction processes involved in sensing take place on the surface of the device's active material. For this reason, a viable strategy to harness high sensing performances in terms of sensitivity and response speed is to employ low-dimensional architectures exhibiting extremely high surface/volume ratio. By decorating the surface of such low-dimensional structures with *ad-hoc* receptors it is also possible to gain improved detection limit and selectivity for specific target analytes.

In order to provide a basic knowledge on the processes and on the phenomena exploited in the experimental section of this thesis, this chapter is meant to explore the use of nanoscopic structures such as 0D nanoparticles, 1D supramolecular nanowires and nanotubes and 2D carbon-based materials in the field of sensing, providing also the theoretical background essential to understand the transduction mechanisms for such diverse scaffolds. Every section includes also a short connection with one or more experimental chapters of this manuscript and a brief overview on the state-of-the-art for low-dimensional chemical sensors based on the aforementioned architectures.



## 2 0D: NANOPARTICLES

---

Nanoparticles are nanoscale objects featuring all their dimensions within the nanometer scale. Such objects could be stable clusters composed of just a few atoms or bigger entities featuring sizes up to hundreds nanometers and geometrically regular shapes, such as spheres, cubes, rods, stars, prisms etc.

Depending on the materials nature, such objects can be fabricated with either top-down or bottom-up approaches but, usually, the latter is preferred, if applicable, because it enables reaching a greater control over shapes and sizes. The optical and electrical characteristics of such objects can be extremely diverse and strongly related on the materials of which the nanoparticles are made. In general, it is possible to distinguish between three classes of materials: pure metals (such as Au, Cu, Ag, etc.) which feature electrical conducting behavior and localized surface plasmon resonance (LSPR), metal chalcogenides (also called “quantum dots”, such as CdSe, PbS, InAs, etc.) which are semiconductors with size-dependent band gap and optical properties and oxides (such as TiO<sub>2</sub>, ZnO, SiO<sub>2</sub>, etc.) which can be wide band gap semiconductors or insulators. The strategy and the architectures for the development of nanoparticles-based sensing devices are countless and depends on the target molecules, on its medium, on the desired transduction mechanism and on collateral interaction with the environment in which the sensor will be placed. For instance gold nanoparticles have shown great performances for sensing biological relevant moieties<sup>1</sup> but also toxicity if injected *in vivo* at high concentrations.<sup>2</sup>

An in-depth discussion on the sensing strategies and performances for all the mentioned classes of materials would require a dedicated book and is far beyond the scope of this chapter. The attention is therefore focused on the use of metal nanoparticles to provide an exhaustive overview on the possible different strategies to exploit such materials in chemical sensing.

## 2.1 METAL NANOPARTICLES

Metal nanoparticles exhibit interesting and unique physicochemical properties that can be exploited for the realization of sensing devices featuring different transduction mechanisms and readouts. For this reason such materials rapidly became the most used scaffold for the realization of chemical sensors.

Among the metals which can be shaped in the form of nanoparticles, the most widely used are certainly Au and Ag. These two materials possess a special affinity for sulfur, in particular in the form of thiols. The reaction between such metals and thiolated molecules leads to the formation of an ordered self-assembled monolayer (SAM) covering uniformly the whole metal surface.

The molecular self-assembled monolayer can be employed with a double function: it can be used as a template to grow ordered nanostructure by modifying the reactivity and the solubility of the particles or to covalently decorate the nanoparticle's surface with specific receptors.

Sensing devices with metal nanoparticles-based active materials can rely on different transduction mechanism depending on the target molecules and on the operative condition in which the device will be exposed. In particular, the interaction between metal nanoparticles decorated with *ad-hoc* receptors and a target analyte can generate electrical signal, such as changes in resistance and/or capacitance, changes in the optical plasmonic properties due to changes in the refractive index or aggregation/disaggregation, changes in the Raman and fluorescence signal of the target molecule due to the proximity with the metallic particles and so on,<sup>1</sup> as summarized in **Figure 2.1**.

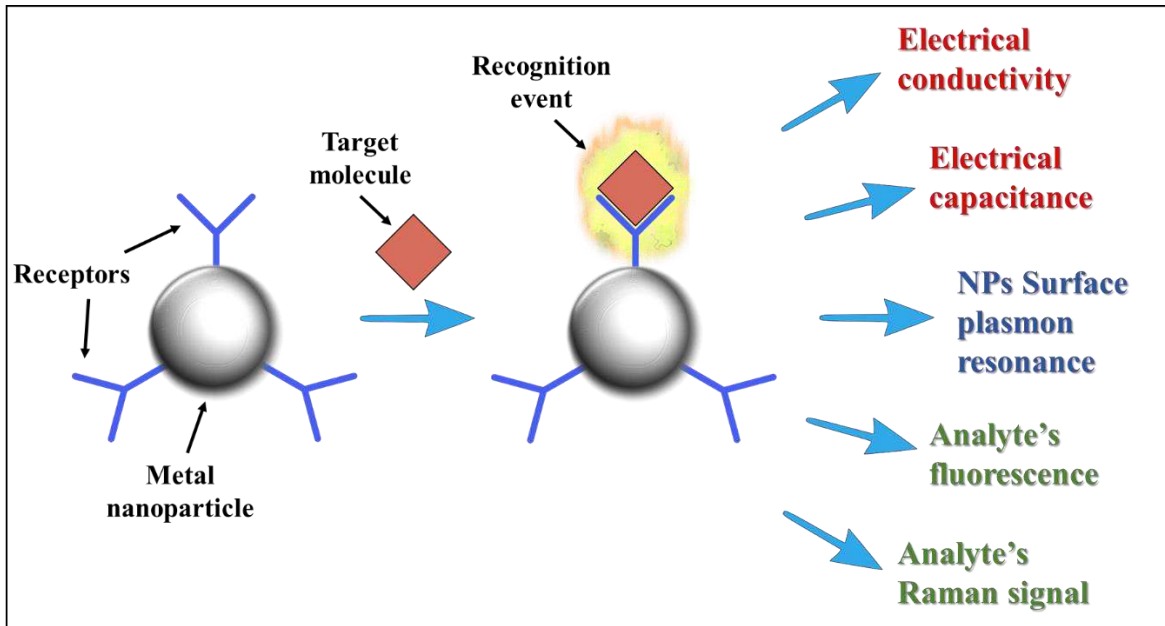


**Figure 2.1:** Schematic summarizing the metal nanoparticles-based sensing methods (Red = electrical readout. Blue = Optical readout monitoring the NPs features. Green = Optical readout monitoring the analytes features).

### 2.1.1 Electrical properties of metal nanoparticles

As aforementioned, the nanoparticles can feature different dimensions and all their characteristics are affected by this aspect. From the electrical point of view, the behavior of metal nanoparticles is strongly correlated to the amount of atoms forming the clusters, as emphasized by the equation of the Kubo gap ( $\delta$ ):

$$\delta = \frac{E_F}{N}$$

Where  $E_F$  = Fermi energy of the material and  $N$  = Number of atoms within the cluster.

According to this simple equation with decreasing the amount of atoms forming the particles, the energy levels are discretized opening a gap which makes the material insulating, as schematized in **Figure 2.2**.<sup>3</sup>

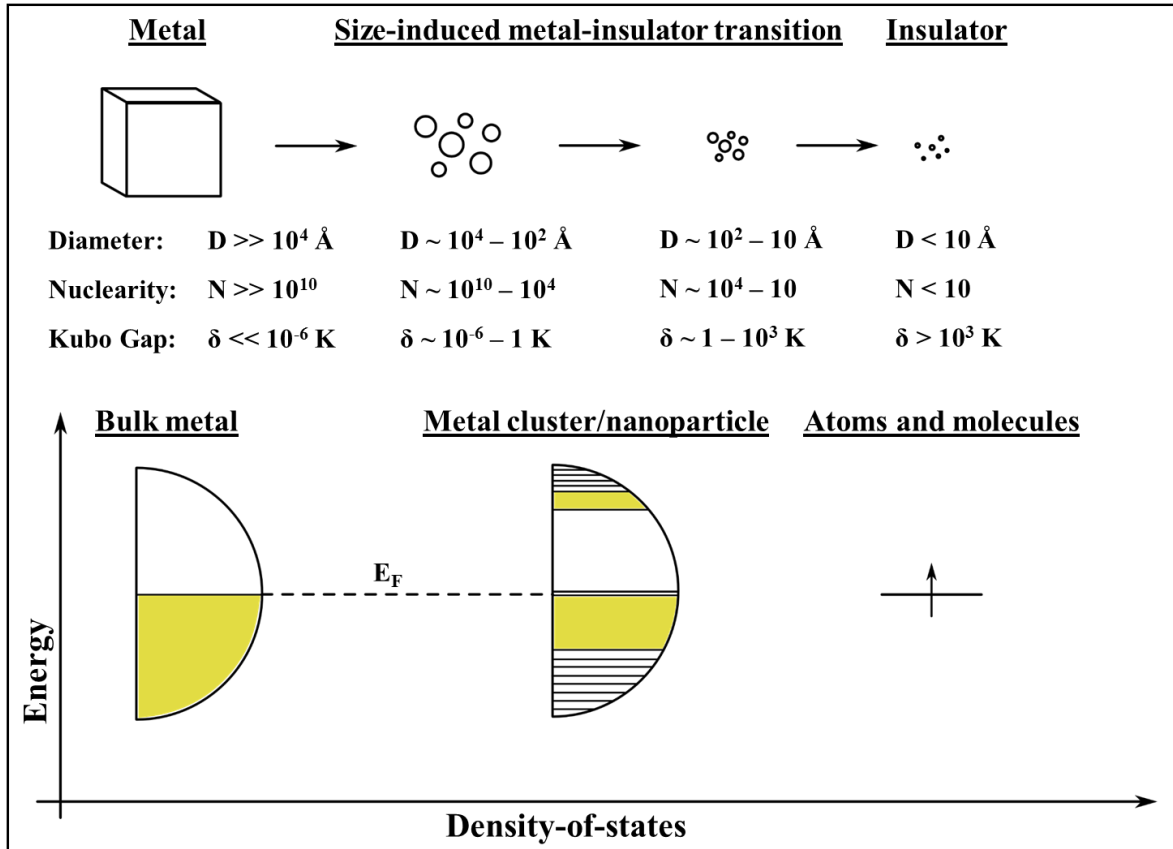
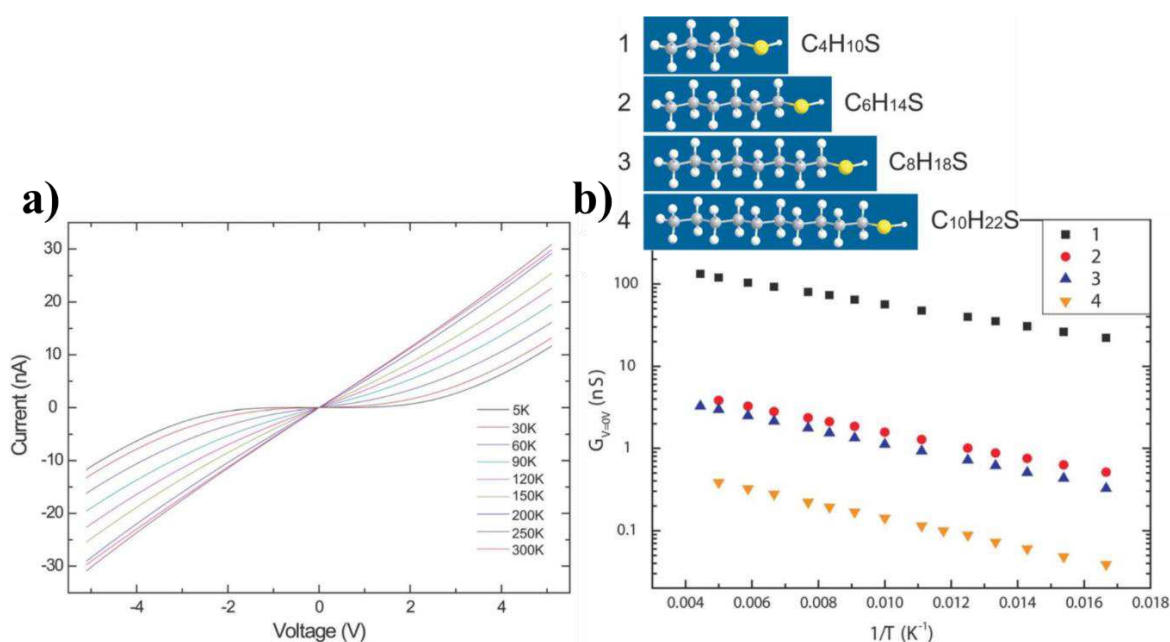


Figure 2.2: Schematic diagram showing the size-dependent evolution of the energy level of metals. (Adapted from Ref.<sup>3</sup>).

According to the Kubo model, for materials like Au and Ag, if the cluster are bigger than  $\sim 2 \text{ nm}$ , they behave electrically as bulk and can be employed as nanoscopic electrical conductors following the Ohm's law.

A viable strategy to efficiently exploit the advantages of such small metal conductors, is to generate thousands of electrical molecular junctions with controlled nanoscopic gaps by employing the nanoparticles as electrodes and the SAMs as spacer to define the gaps.<sup>4</sup> These architectures can be adjusted and optimized by changing the nanoparticles size and the nature of the organic linkers. Such bi-component architectures can be used as versatile test bed to test the unique properties brought into play by the use of functional molecules.<sup>5</sup> The strategy to deposit such materials depends on the purpose: by drop casting it is possible to obtain thick and relatively disordered films with great exposed surfaces that are advantageous for the fabrication of sensing devices,<sup>6,7</sup> while, more sophisticated techniques such as drying mediated assembly<sup>8-12</sup> and Langmuir-Blodgett,<sup>13,14</sup> can be employed to make ordered 2D arrays holding even more defined physical properties. The electrical transport properties of

metal nanoparticles films are governed by the different energy scales and geometrical parameters characterizing their architectures. The properties can vary from insulating layers, when the nanoparticles are widely spaced between each other, to a metallic behavior when the particles are arranged in a close packed structure. The organic matrix surrounding the nanoparticles plays the key role in controlling the electronic coupling between neighboring particles but, some minor parameters such as particles size, geometrical defects and quenched charged disorder in the arrays and/or the substrate can also influence the electrical transport properties of the arrays.<sup>5</sup> To investigate the electrical properties of such complex systems, where the charge carriers can move following different pathways and different transport mechanism, it is not enough to perform simple I-V electrical measurements but it is also necessary to perform low temperature studies of hybrid structures featuring different inter-particles distances. In 2013 C. Duan et al. reported a study on the electrical properties of gold nanoparticles films of different thickness and inter-particles spacing, in a temperature range ranging from 5 to 300 K (**Figure 2.3**).<sup>15</sup>



**Figure 2.3:** Temperature dependent charge transport. a) I-V curves of interlinked 2D nanoparticles arrays measured at variable temperatures from 5K to 300K. b) Zero-voltage conductance of the nanoparticle arrays as a function of inverse temperature for nanoparticle arrays with different inter-particle distances. Adapted from Ref.<sup>15</sup> with permission of the Royal Society of Chemistry.

From the I-V curves in **Figure 2.3a** it is visible that the relationship between measured current and applied bias becomes less and less linear upon decreasing the temperature. When the temperature is low enough, the current at low bias is suppressed due to Coulomb blockade. Such phenomenon relates to the Coulomb charging energy of a nanoparticle, which is defined as the energy needed to add an excess electron onto a neutral nanoparticle.<sup>5</sup>

Theoretically, in the I-V curves of nanoparticle arrays at low temperature, a threshold voltage should exist below which the current is completely suppressed.<sup>16,17</sup> **Figure 2.3b** portrays the zero-voltage conductance of the nanoparticle arrays as a function of inverse temperature. This study was performed using nanoparticle arrays functionalized with alkanethiols featuring different chain lengths (particles diameter 9.25 nm). It reveals a strong dependence of the conductivity on the inter-particles distance.<sup>15</sup> Similar results have been reported also from Reissner et al. who shed light on the effect of solvents on 2D monolayers of gold nanoparticles functionalized with 1-dodecanethiol. Immersion of such films in solvents such as ethanol or THF caused an increased interdigitation of the aliphatic chains with a subsequent decrease of the inter-particles distance and therefore an increase in the measured current by a factor of 36 (ethanol) and 22 (THF), which is not reversible and accompanied by structural changes.<sup>18</sup>

By looking at such results it appears evident how metal nanoparticles films respond to the environment, thus they could be exploited for the realization of reliable sensing devices and, in particular, of chemiresistors.<sup>19-21</sup> As described in the previous chapter, such devices can change their electrical resistivity upon interaction with a targeted chemical species.

Metal nanoparticles-based chemiresistors are usually fabricated by depositing films of ligand-capped or inter-linked particles onto an appropriate substrate.<sup>22</sup> In such devices the organic components attached on the particle's surface provide stabilization of the structure and sites for the analyte absorption while enabling sufficient electrical conductivity through the film, as schematized in **Figure 2.4**.

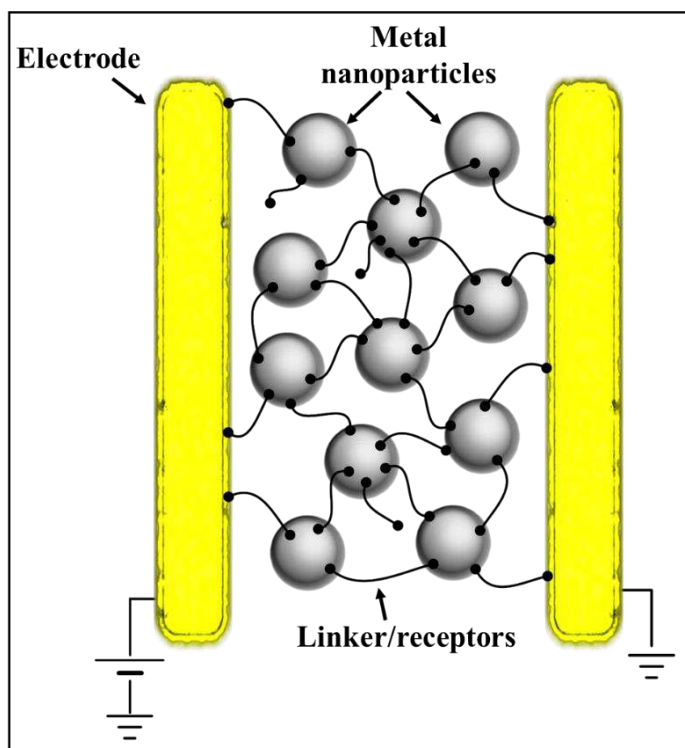


**Figure 2.4:** Schematic of a generic chemiresistor device based on metal nanoparticles and organic di-thiols.

In such versatile configuration it is possible to modulate the electrical transport through a junction just by controlling the nature and/or the conformation of the organic molecular linkers.<sup>23</sup> Changes in the bridge's effective length and in its conformation, due to the interaction with a targeted analyte, will then lead to substantial changes in the conductance through the active materials.

For instance, polar molecular bridges such as peptides can be used to bind charged analytes such as ions, increasing the conductance of the system.<sup>24,25</sup> By preparing contact electrodes using a head-to-head pyridine dimer, Bui et al. have also shown that the coordination of a single metal ion such as  $\text{Zn}^{2+}$  can lead to a facilitated electron transfer in sandwich-type molecular-junctions.<sup>26</sup> An interesting application of such concepts for the realization of actual ion sensing devices was reported in 2012 by Cho et al. where drop-cast films of AuNPs were employed for the quantitative and selective detection of toxic  $\text{CH}_3\text{Hg}^+$  ions in water with attomolar detection limit.<sup>6</sup> These outstanding results were achieved by using *ad-hoc* self-assembled monolayers covering the particles and forming a striped shell capable of selectively bind the targeted ions. The absorption of the targeted ions creates a percolative path for the charge carriers to travel across the electrodes, resulting in an increased current output which is proportional to the amount of ions absorbed.<sup>6</sup>

In the case of gas and vapor sensing, the exposure of the nanoparticles arrays to such analytes causes the diffusion of the targeted molecule inside the film with a subsequent swelling of the structure, commonly leading to an increase of the measured resistance through the

devices.<sup>27</sup> The correlation between vapor response-sensitivity and inter-particles spacing properties was demonstrated by Wang et al. for the detection of volatile organic compounds using AuNPs capped with di-thiolated alkyl chains featuring different chain lengths.<sup>28</sup> This approach has also been exploited by Joseph et al. for the realization of sensors for organic volatile solvents such as toluene, 4-methyl-2-pentanone, 1-propanol by employing networks of AuNPs (4 nm diameter), cross-linked with organic non-polar di-thiolated ligands such as 1,12-dodecanedithiol, 4,4'-terphenyldithiol or 4-staffane-3,3-dithiol.<sup>22</sup> Similar result for organic compound have also been reported by Wohltjen et al, reaching a detection limit of ~1 ppm for toluene<sup>29</sup> and, later, by Vossmeier et al. who performed a systematic study exploring the use of C<sub>6</sub>, C<sub>9</sub>, C<sub>12</sub> and C<sub>16</sub> alkane di-thiols, demonstrating that the sensitivity can be exponentially increased by the presence of an higher amount of -CH<sub>2</sub> units.<sup>19</sup> Mixed self-assembled monolayers on AuNPs surface have been used to fabricate “electronic-tongue”<sup>30</sup> sensor arrays just by changing the ratios between the different components in the monolayer mixture.<sup>31</sup> By using this approach Kim et al. showed that with different ratios of chlorobenzene methanethiol and n-octanethiol SAMs on the particle's surface it was possible to tune the response towards the selective sensing of 1-propanol, acetone or ciclohexane.<sup>32</sup>

For the realization of devices capable of sensing vapors of polar solvents, such as water, the use of hygroscopic organic linkers capable of interacting efficiently with water molecules would be required. However, only very few examples of such devices are present in literature. In 2010 Yao et al. reported on the use of AuNPs-polyvinyl alcohol (PVA) based active materials for the realization of humidity sensors. In such devices the PVA water absorbing shell was too thick to let the current flow through the devices and the electrical readout was based on changes in the capacitance of the system, resulting in a poor sensitivity of the devices, exhibiting a change < 2 nF in the range between 0 and 90% RH.<sup>33</sup> An example of highly sensitive humidity sensors has been reported by Lee et al. in 2014. In their work, the authors exploited thick films of AuNPs (4-6 nm diameter) coated with a layer of dopamine as water absorbing material and transducer of the amount of absorbed water. Such devices display a remarkable decrease of the recorded resistance up to 4 orders of magnitude upon increasing the humidity from 10 to 90% because of the interaction between water and dopamine that generates OH<sup>-</sup> ions as charge carriers embedded within the films. However, such process requires time to equilibrate, leading to slow response speed (5 s absorption and 10 s desorption).<sup>34</sup>



The use of metal nanoparticles networks cross-linked with strongly hygroscopic polyethylene glycol di-thiol can allow the realization of ultra-fast (<13 ms) humidity sensing devices, as described in the experimental section in chapter 5.

### 2.1.2 Optical properties of metal nanoparticles

The optical properties of metal nanoparticles are a consequence of the interaction between the oscillating electrical field of light in the visible range and a collective oscillation of the free electrons on the particle's surface, also called "localized surface plasmons" (LSPs) and, for this reason, are strongly correlated with the amount of free electron given by the Kubo model. If the metal clusters are smaller than  $\sim 2$  nm the Kubo gap is too big and the particles will exhibit insulating behavior, meaning that the electrons are not free to move on the cluster's surface, preventing the existence of surface plasmons and therefore of any optical property. On the other hand, if the particles are too big (diameter  $> 10^4$  Å) they will behave as a bulk material, exhibiting not localized surface plasmons and the typical high optical reflectivity of metal bulks. For this reason, from now on the term "nanoparticle" is meant to include just objects featuring a size between  $\sim 2$  nm and  $\sim 1$   $\mu$ m.

This section of the chapter aims to provide a general understanding on the world of plasmonic properties of metal nano-objects, focusing the attention on how such phenomena can be exploited for the realization of chemical sensing devices.

As already mentioned, the optical properties of metal nanoparticles are a consequence of the presence of surface plasmons confined on a finite surface, to explain this phenomena is therefore necessary to introduce first the general concept of surface plasmon on an infinite surface e.g. on bulk metals.

Surface Plasmons (SPs) are waves that propagate along the surface of a conductor, usually a metal. These are essentially light waves that are trapped on the surface because of their interaction with the free electrons of the conductor.<sup>35</sup> During this interaction with an external oscillating electrical field, the free electrons moves collectively on the metal's surface, oscillating in resonance with the external field, generating the SPs (**Figure 2.5**).<sup>36</sup>

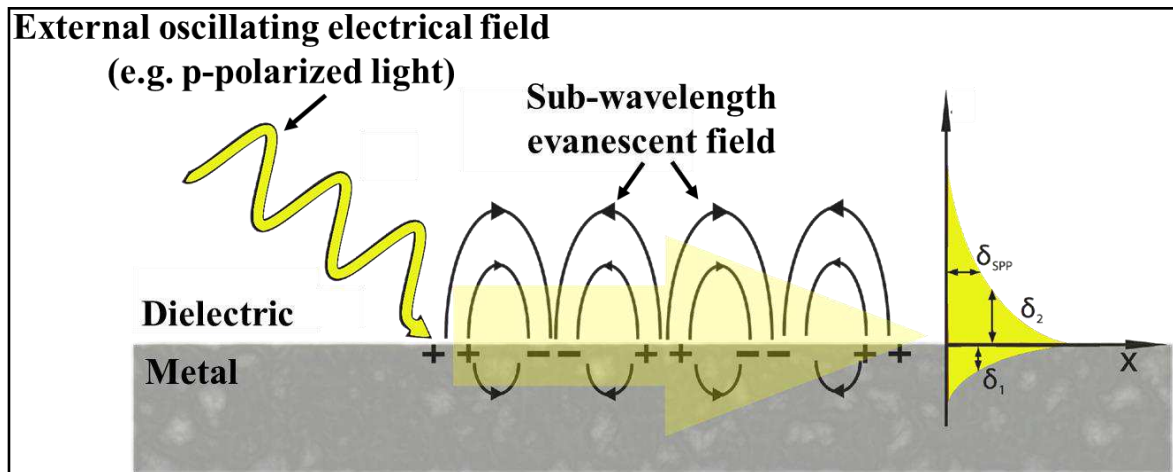


*Figure 2.5: Schematic of the formation and propagation of SPs at the metal/dielectric interface.*

In an ideal metal conductor the free electrons should be capable of moving at any velocity and without energy losses, resonating with the external electrical field at any frequency, meaning that, in an ideal case, relative permittivity should be equal to  $-\infty$  at any wavelength and, in other words, that these surfaces should feature perfect reflectivity of light at any wavelength. This is obviously not realistic because the free electrons have a finite mass and suffer scattering from the lattice vibrations and defects, meaning that by increasing the frequency of the external field, the free electrons progressively find it harder to respond and, ultimately, at high enough frequency, the metal becomes transparent for the electrical field, behaving as a dielectric.

From this simplistic treatment it is easy to understand the existence of a limit frequency (in the range of UV for many metals) above which it is not possible to generate plasmons. Another requirement for the generation of SPs that propagate along the metal surface at the interface with a dielectric, is that the electromagnetic wave equation for the p-polarized light (electric vector perpendicular to the surface) is satisfied in both medium (metal and dielectric).

By solving the Maxwell's equations and applying the boundary conditions for such systems it is possible to obtain that:

$$k_{SP} = k_0 \left( \frac{\varepsilon_d \varepsilon_m}{\varepsilon_d + \varepsilon_m} \right)^{\frac{1}{2}}$$

Where  $k_{SP}$  = SP wave vector along the metal surface,  $k_0$  = wave vector of external oscillating field (p-polarized photon),  $\varepsilon_d$  = permittivity of the dielectric layer  $\varepsilon_m$  = permittivity of the metal.

The exhaustive theoretical development of such model can be found in Ref.<sup>37</sup> but from this simple equation it is already possible to understand that the generation of the SPs is a direct consequence of the contrast in the wavelength-relative permittivity at the interface between the metal surface and the adjacent dielectric material.<sup>37</sup> After being generated, the SPs propagate onto the surface generating an electric field, perpendicular to the metal's surface, which is strongly confined in the space and decays exponentially with the distance. For this reason, such field is said to be “evanescent” or “near field” and is a consequence of the bound, non-radiative nature of SPs, which prevents power from propagating away from the surface.<sup>35</sup>

The strong enhancement of the electrical field in close proximity to the metal/dielectric interface generated by the SPs was exploited for the first time in 1988 by Rothenhäusler and Knoll for the realization of the first microscope capable of visualizing with high spatial resolution low contrast heterogeneously-organized lipid monolayer, transferred from the water surface to a solid substrate without addition of fluorescent labels.<sup>38</sup> Such achievement was a game changer in the fields of optical microscopy and, in particular of sensing and bio-sensing, leading to the realization of the first surface plasmon resonance based immunosensor in 1991<sup>39</sup> and paving the way for the future development of higher sensitivity and low-costs devices to be implemented in lab-on-chip setups that nowadays can even be coupled and run with a smartphone.<sup>40</sup>

As aforementioned, when the metal surface features finite dimensions (e.g in the case of nanoparticles or nanoholes) which are comparable or smaller than the external wavelength, the free electrons are confined forced to collectively vibrate forming the so-called localized surface plasmons (LSPs) **Figure 2.6**.

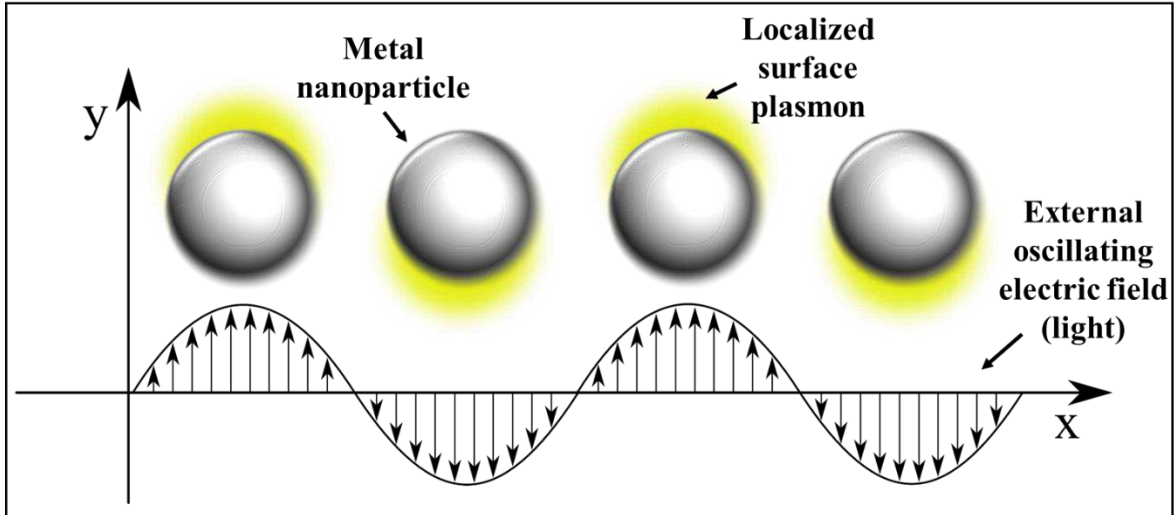


**Figure 2.6:** Schematic of the localized surface plasmons formation.

These highly confined and localized SPs exhibit some special and interesting features: on one hand they allow to concentrate the evanescent near field into an extremely smaller area, compared to non-localized SPs, causing a dramatic enhancement of all the above mentioned effects. On the other hand, the LSPs on the particle's surface oscillate at a certain frequency and can resonate with light, leading to an optical extinction band which has a maximum corresponding to the surface plasmon resonant (SPR) frequency, which, for noble metal nanoparticles, occurs in the visible range.

The extinction cross section given by SPR in metal nanoparticles was described for the first time in details by Mie in 1908<sup>41</sup> as a combination of scattering and absorbance:

$$\sigma_{abs} = \sigma_{ext} - \sigma_{sca}$$

Where the cross sections of extinction ( $\sigma_{ext}$ ) and scattering ( $\sigma_{sca}$ ) are respectively:

$$\sigma_{ext} = \frac{18\pi\epsilon_m^{\frac{3}{2}} V}{\lambda} \frac{\epsilon_2(\lambda)}{[\epsilon_1(\lambda) + 2\epsilon_m]^2 + \epsilon_2(\lambda)^2}$$

$$\sigma_{sca} = \frac{32\pi^4 \varepsilon_m^2 V^2}{\lambda^4} \frac{(\varepsilon_1 - \varepsilon_m)^2 + (\varepsilon_2)^2}{(\varepsilon_1 + 2\varepsilon_m)^2 + (\varepsilon_2)^2}$$

Where  $\varepsilon_m$  = permittivity of the medium surrounding the nanoparticle,  $V$  = Volume of the nanoparticle,  $\varepsilon_1$  and  $\varepsilon_2$  = respectively real and imaginary component of the complex permittivity for the metal nanoparticle and  $\lambda$  = incident wavelength.

The one reported above is a simplified version of the Mie model which takes into account just the dipolar contributions inside the particles, considering as negligible all the superior order. Such approximation is valid only for small spherical particles featuring a diameter < 20 nm. From this model it appears evident how the extinction spectra of metal nanoparticles could be affected and, therefore be sensitive to changes in the permittivity (e.g. in the refractive index) of their environment. This characteristic can be exploited for the realization of highly sensitive sensors, featuring an optical readout which rely on the shift of the SPR band in solutions as well as in solid-state.<sup>42</sup>

The simplest and more immediate way to exploit LSPR-active particles is to detect changes in the bulk refractive index of their environment through the shift in the LSPR wavelength peak. Such measurements are typically performed by acquiring UV-Vis extinction spectra on dense nanoparticles films immobilized on a transparent substrate. As expected from the Drude model and from the more precise Mie approximation reported above, by changing the medium e.g. the solvent in which the metal NPs films are immersed, the LSPR peak wavelength shift linearly with the bulk refractive index of the medium.<sup>43</sup>

The use of metal nanostructure to detect changes in the bulk refractive index is extremely straightforward but does not fully exploit the potentials given by the strong confinement of the near field surrounding the nanoparticles. Indeed, since the evanescent near field of the LSPR decays completely within few nanometers, such systems are extremely powerful to probe nanoscale regions around the particles. The highly localized sensing volume allows to observe molecular interactions near the particle's surface as a result of the modification in the local refractive index.<sup>42</sup>

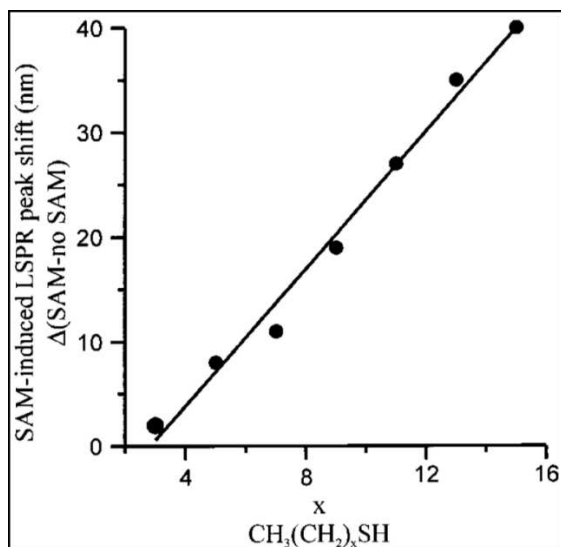


**Figure 2.7:** Alkanethiol chain length dependence on the LSPR spectral. (reprinted with permission from Ref.<sup>44</sup> Copyright 2001 American Chemical Society).

One example demonstrating the power and the sensitivity of such systems was reported by Malinsky et al. by reporting the shift in the LSPR wavelength of 30 nm large AgNPs covered with SAM of alkanethiols featuring different chain lengths. In this study they managed to measure the refractive index shift given by the presence of a different amount of CH<sub>2</sub> groups (**Figure 2.7**).<sup>44</sup> Similar results have been obtained also with other metal and nanoparticles shapes confirming the versatility of such approach.<sup>45</sup>

The same principles can be exploited for the realization of LSPR-based optical sensing devices functionalized with *ad-hoc* receptors to bind and detect specific molecular systems.

During the last two decades gold nanoparticles have become one of the most exploited scaffold for the realization of chemical and biosensors. In particular such approach has been successfully applied for the detection and quantification of anions,<sup>46</sup> dopamine,<sup>47</sup> serum albumin,<sup>48,49</sup> antibodies,<sup>50</sup> insulin<sup>51</sup> and even explosives.<sup>52</sup>

Another interesting application for the LSPR of metal nanoparticles consists in the so-called “colorimetric sensing”. The latter is a mostly qualitative sensing technique that relies on the LSPR wavelength shift (e.g. a macroscopic and visible change of color) due to the surface plasmon coupling caused by the aggregation of nanoparticles in solutions.

In the case of AuNPs such process causes a strong and evident change of color from red (insulated particles) to blue (aggregated particles), which is detectable up to nanomolar concentration (**Figure 2.8**).<sup>53</sup>

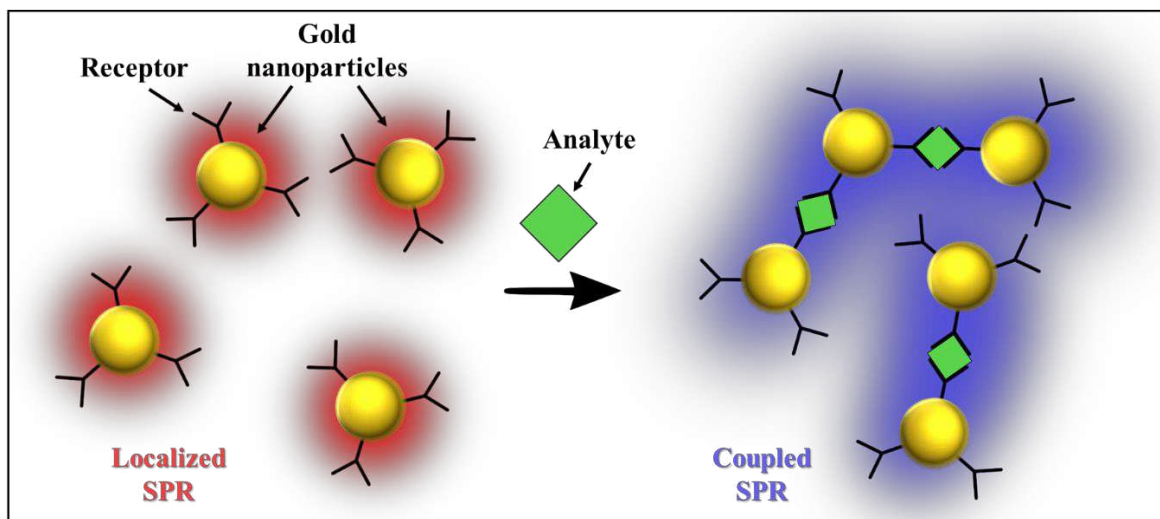


Figure 2.8: Schematic representing the working principle of colorimetric chemical sensors based on AuNPs LSPR.

One of the greatest advantage of such approach is that the detection process can be performed just by mixing the AuNPs with complex matrices of different analytes in solutions. The color change can be visually detected by naked eyes and no expensive nor electrically powered instrumentations are required. These characteristic made AuNPs sensor particularly appealing for the *in-situ* detection of toxic metal ions in water samples. One of the first examples in this field was reported by Lin et al with the selective detection of micromolar concentration of  $K^+$  ions in complex matrixes including  $Li^+$ ,  $Cs^+$ ,  $NH_4^+$ ,  $Mg^{2+}$ ,  $Ca^{2+}$  and excess of  $Na^+$ , using AuNPs functionalized with 15-crown-5 moieties.<sup>54</sup> For heavy metal, which pose significant public health hazards, the tolerated concentrations in water are significantly lower and the systems must be properly engineered to meet the requirements. In 2009 Kalluri et al. developed a colorimetric sensor to detect the presence of  $As^{3+}$  ions in groundwater with a detection limit of 5 ppb by using glutathione, dithiothreitol and cysteine as receptors, exploiting the strong affinity of the targeted ions with sulfur containing groups.<sup>55</sup> This value of detection limit was improved in 2014 by zhan et al. who reached a remarkable value of 1.26 ppb using *ad-hoc* aptamers to induce the aggregation of AuNPs in presence of  $As^{3+}$ .<sup>56</sup> Similar approaches have been reported also for the detection of  $Hg^{2+}$ ,<sup>57-59</sup>  $Cr^{3+}$ ,<sup>60</sup>  $Cu^{2+}$ ,<sup>61,62</sup>  $Pb^{2+}$ ,<sup>63,64</sup>  $Cd^{2+}$ ,<sup>65</sup> and, recently, also for toxic organic compounds such as bisphenol A.<sup>66</sup>

A novel version of a solid state colorimetric sensor based on gold nanoparticles can be found in chapter 4 where 2D networks of AuNPs cross-linked with polyethylene glycol di-thiol are



used to fabricate humidity sensors with enhanced LSPR wavelength shift given by the contemporary changes in the refractive index and in the inter-particles distance upon absorption of water molecules.

The LSPR shift induced by local changes in the refractive index or by coupling between particles above discussed are the simplest and more immediate approaches to exploit metal nanoparticles as active materials or transducers in chemical sensing but the evanescent near field surrounding metal nanoparticles can be also exploited to strongly amplify the optical signals (including, fluorescence, IR absorption and Raman) of molecules which are located in close proximity to the particle's surface. These techniques, called Surface enhanced fluorescence (SEF),<sup>67,68</sup> IR absorption (SEIRA)<sup>69</sup> and, Raman spectroscopy (SERS),<sup>70</sup> have shown great potential in the field of sensing and, in particular SERS can allow increased sensitivity up to single molecule detection<sup>71,72</sup> but their working principles and their detailed description are far beyond the scope of this chapter.

### 3 1D: NANOFIBERS AND NANOTUBES

---

One-dimensional structures such as nanowires, nanofibers and nanotubes, have attracted great interest in the field of sensing to be employed in particular as chemiresistors due to their high aspect ratio.

It is indeed possible to use such architectures to bridge electrodes through micrometric channels, providing an easier and more reproducible devices fabrication respect to the above discussed 0D nanoparticles.<sup>73</sup> 1D structures may be formed via different approaches with virtually any material including noble metals,<sup>74,75</sup> oxides,<sup>76,77</sup> carbon materials,<sup>78</sup> conventional organic polymers<sup>79</sup> and supramolecular polymers.<sup>80</sup>

As evident, the fabrication techniques, the processing and the transduction mechanism of such materials as chemiresistors are completely different, depending on the chosen material and on its characteristics. This section focuses on the use of organic supramolecular polymers which are the most versatile organic scaffold due to the non-covalent nature of their backbone.



While the synthetic covalent polymers which extensively employed in technology and everyday life are macromolecules, in which small structural units are connected by covalent bonds, in a supramolecular polymer the building blocks of any size are connected through non-covalent “weak” bonds, such as hydrogen bonds or electrostatic interactions, to create coiled chains, ordered filament or tubes with nanoscopic inner channels. Such an approach is intensively exploited and almost ubiquitous in living systems and, more generally, in nature. For instance, the cytoskeleton cells form long ordered filaments of protein monomers which continuously assemble and disassemble to ensure the vital cell functions.

As already discussed in chapter 1, supramolecular interactions can be employed as a toolbox to design and engineer molecules to trigger the formation of ordered structures.

In polymer chemistry, these controlled interactions have been exploited to create liquid crystalline materials<sup>81</sup> and intriguing architectures in block copolymer assemblies.<sup>82</sup> The use of strong unidirectional interactions among molecules can, not only recreate some of the key properties of covalent polymers, but also add functionality based on two basic principles: (I) shape persistence and order within one-dimensional assemblies and (II) the dynamics of non-covalent bonds.<sup>80</sup>

The first example of a linear supramolecular polymer based on hydrogen bonding among small molecules was designed and reported in 1990 by Fouquey et al.<sup>83</sup> such system was behaving as a covalent polymer and was characterized by a random coil structure and high polydispersity.

A viable strategy to achieve high degree of internal order between the molecular units is to use cooperative nucleation-elongation self-assembly of the monomers, as reported by Hartgerink et al. in 1996 for the formation of assemblies of peptide into ordered nanotubes.<sup>84</sup> By using such approach it is possible to trigger the aggregation of the monomers into different kind of 1D architecture, including nanotubes, coils and twisted nanoribbons, engineered to feature the desired mechanical (**Figure 2.9 A and B**), biological (**Figure 2.9 C and D**), and optical (**Figure 2.9 E and F**) or electronic (**Figure 2.9 G and H**) functionalities.

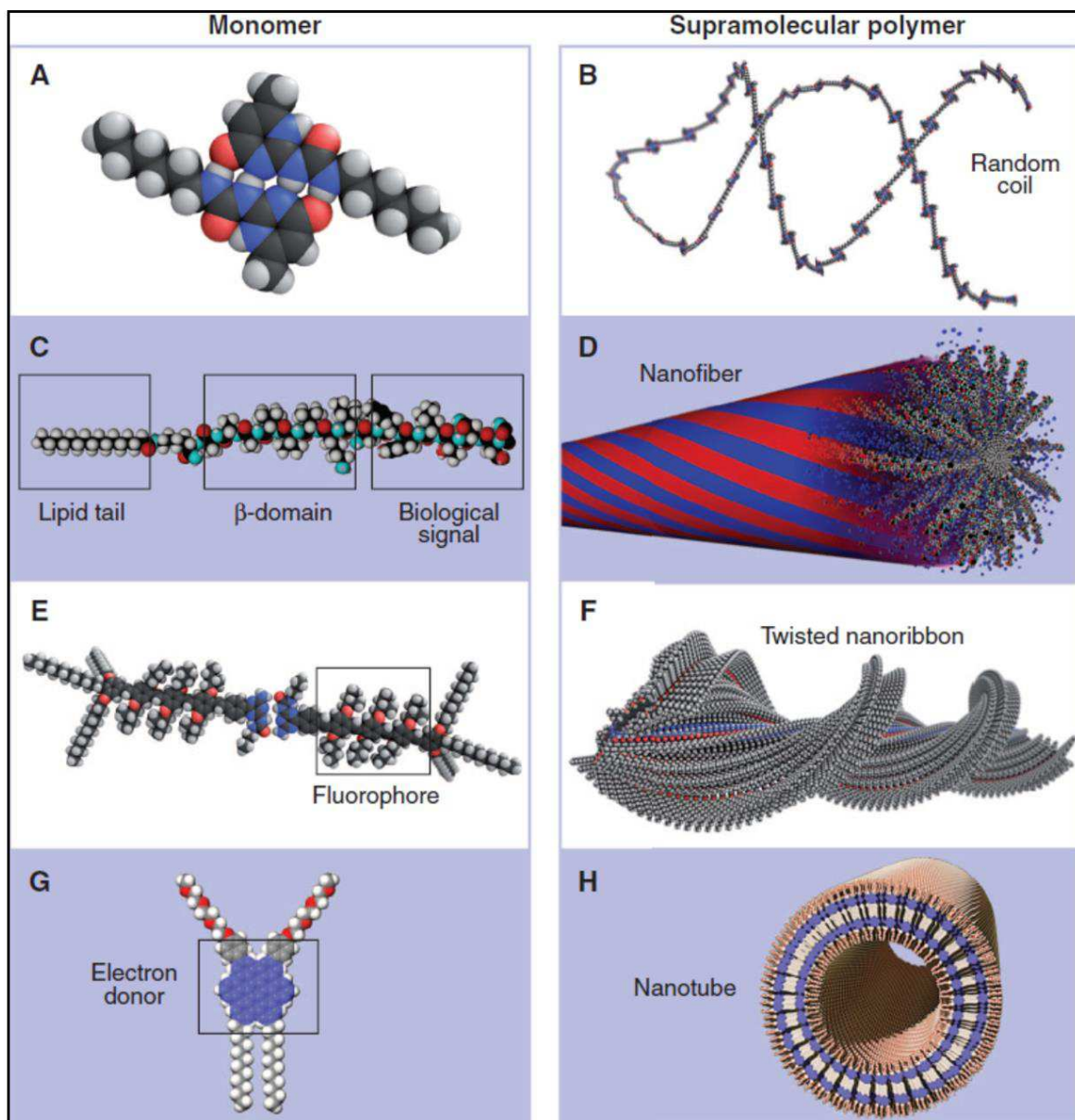


**Figure 2.9:** Molecular representation of four different monomers and the corresponding supramolecular architecture formed by their aggregation through specific interactions. (A,B) ureidopyrimidinone monomer aggregating into random coils through hydrogen bonds. (C,D) peptide amphiphile monomer composed of three segmental domains: a sequence bearing a biological signal, a domain containing amino acids with a strong tendency to form  $\beta$  sheets, and a hydrophobic alkyl tail, assembled into nanofibers through hydrophobic interactions. (E,F) fluorophore oligo (phenylene vinylene), substituted by alkyl groups and chiral centers aggregating through quadruple hydrogen bonds into stable dyads and, finally, into ordered supramolecular twisted ribbons with defined chirality. (G,H) hexabenzocoronene core substituted by phenyl triethylene glycol and dodecyl chains forming supramolecular nanotubes with a well-defined wall thickness growth through solvophobic interactions. Reproduced From Ref.<sup>80</sup>. Reprinted with permission from AAAS.

**Figure 2.9** displays different ordered supramolecular 1D structures that can be obtained by careful engineering the starting monomers. Depending on the nature of the building blocks and on their arrangement, it is possible to trigger desired optical, electrical and mechanical properties. Since the final structure is the result of an interplay of different forces among the

building blocks but also with the solvent and any other specimen in solution, such systems are particularly sensitive to specific analytes in solution, therefore acting as chemical sensors. Since electrical devices, relying on supramolecular nanostructures, would not be stable upon immersion in solutions, the most typical readout for such kind of sensors is the optical one. Depending on the employed scaffold and on the nature of the interactions with the analytes, the recognition event could trigger changes in the position of the absorbance peak or dramatic intensity changes in the fluorescence on the supramolecular active materials. For instance, rotaxanes with different backbones have been successfully employed for the selective sensing of charged species like metal cations, pH ( $H^+$  ions) and anions, by probing the changes in their fluorescence or in their electrochemical emission upon interaction with such analytes.<sup>85</sup> However, the most straightforward and exploited approach to use 1D supramolecular polymers for the realization of chemical sensing devices, relies on the use of such structures in thin films as chemiresistors for gaseous analytes. In such case, the supramolecular polymers can be engineered and designed to undergo changes in their internal arrangement upon interaction with the targeted molecular species, leading to a dramatic impact on their electrical properties.

### 3.1 ELECTRICAL PROPERTIES OF 1D SUPRAMOLECULAR STRUCTURES

In the field of organic electronics, supramolecular systems are considered to be the bridge between single molecules and macroscopic crystals-based devices, allowing to design devices based on ordered and controlled structures in the nanometer range. This new branch of organic electronics is called “supramolecular electronics”.<sup>86</sup> 1D structures employed for supramolecular electronics usually comprise building blocks possessing rigid aromatic cores, such as rylenes,<sup>87</sup> hexabenzocoronenes,<sup>88</sup> anthracenes,<sup>89</sup> fluorenes,<sup>90</sup> oligothiophenes<sup>91</sup> etc. capable of driving the aggregation through the stacking of their  $\pi$  orbitals.<sup>92</sup> In addition to the  $\pi$ - $\pi$  stacking interactions, the use of side chains interacting with the solvent to trigger solvophobic interactions can be exploited to drive the aggregation towards more complicated structures.<sup>93</sup> By using different and incompatible side chains in amphiphilic building blocks it is also possible to prevent undesired aggregation to achieve phase-segregated

architectures, particularly interesting in organic photovoltaic to build nanoscopic heterojunctions between electron donor and acceptors.<sup>94-97</sup>

From the electrical point of view, such architectures usually features either n-type or p-type semiconducting behavior, given by the electron-rich conjugated core as main channel for the charge carriers<sup>98,99</sup> and exhibit similar or better field-effect characteristics respect to spin coated films of the unassembled building blocks, as showed in **Figure 2.10**. However, different behaviors such as ambipolar nature or absence of field-effect are also possible due to the presence of functional side-chains and permanent or self-doping of the assemblies.<sup>100,101</sup>

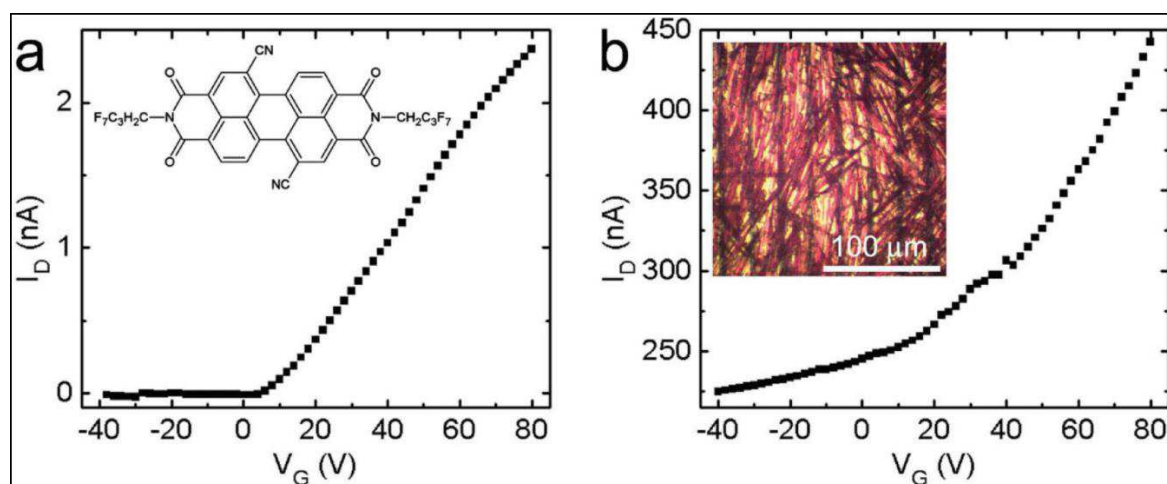


**Figure 2.10:** Electrical characteristics of rylene-based transistors. Transfer characteristics for (a) a spun-cast thin film transistor (molecular structure shown in inset), and (b) a fibers transistor based on the same molecule (optical micrograph of the supramolecular fibers on interdigitated source-drain electrodes shown in inset). Channel length = 10  $\mu m$ ,  $V_d = 10$  V. Reprinted with permission from Ref.<sup>99</sup>

The use of non-covalent interactions to produce sophisticated supramolecular structures makes it possible to exploit the modification of their environment in order to tune their self-assembly behavior. Such a modification of the supramolecular arrangement between the building blocks can result in a precise tuning of the characteristics of the assembly.

When the scaffold is smartly engineered, subtle specific changes in the environment could lead to dramatic changes of one or more physico-chemical properties. In other words, if the supramolecular interactions between a designed receptor and its target analyte (i.e. small

molecules or ions) present in the environment are optimally engineered, extremely sensitive and selective sensors relying on recognition events can be fabricated.

As already deeply discussed in the previous section, metal nanoparticles can be exploited as scaffold for the detection of different analytes which can be present in gas or in solutions, with very low limitations on the working environments because of the remarkable chemical and structural stability of functionalized metal nanoparticles. On the other hand supramolecular structures offer extreme versatility on the geometries and on the functionalization, allowing the realization of more specific receptors and higher sensitive devices but, due to the non-covalent nature of the structural bonds, those scaffold suffer of a lower stability in solution. For this reason very few examples of supramolecular chemiresistors targeting analytes in solution have been reported and the majority of this field have been developed towards the detection of gaseous molecules.<sup>102,103</sup>

For instance Kumar et al. reported on the use of self-assembled phthalocyanine-based nanobelts as active materials for chemiresistors capable of selectively detect Cl<sub>2</sub> gas with a detection limit of 5 ppb. The sensitivity is tunable by changing the nature of the side chains.<sup>104,105</sup> Similar approach have been recently employed by Zhu et al. for the fabrication of supramolecular 1D nanobelts, based on ferrocene-porphyrin derivative, as chemiresistive sensors targeting NO<sub>2</sub> molecules in atmosphere, featuring detection limit of 1 ppm and response speed of 120 s.<sup>106</sup> In both case the sensing mechanism relies on the reversible doping effect due to the absorption of the electron-withdrawing target gases (Cl<sub>2</sub> or NO<sub>2</sub>) on the nanobelt's surface, resulting in a reversible increase in the measured current flowing through the aggregates.

In the case of humidity sensing, where the target gaseous analyte does not behave as a dopant for the supramolecular aggregates, the sensing and transduction mechanisms are different from the ones reported above and must rely on structural rather than electrical changes within the aggregates. An example of such mechanism has been reported by Mogera et al. in 2014 employing a supramolecular donor-acceptor system made by coronene tetracarboxylate and dodecyl methyl viologen respectively. Such system can be self-assembled in solution into 1D supramolecular fibers, characterized by long range  $\pi$ - $\pi$  stacking between the components (**Figure 2.11**).<sup>107</sup>



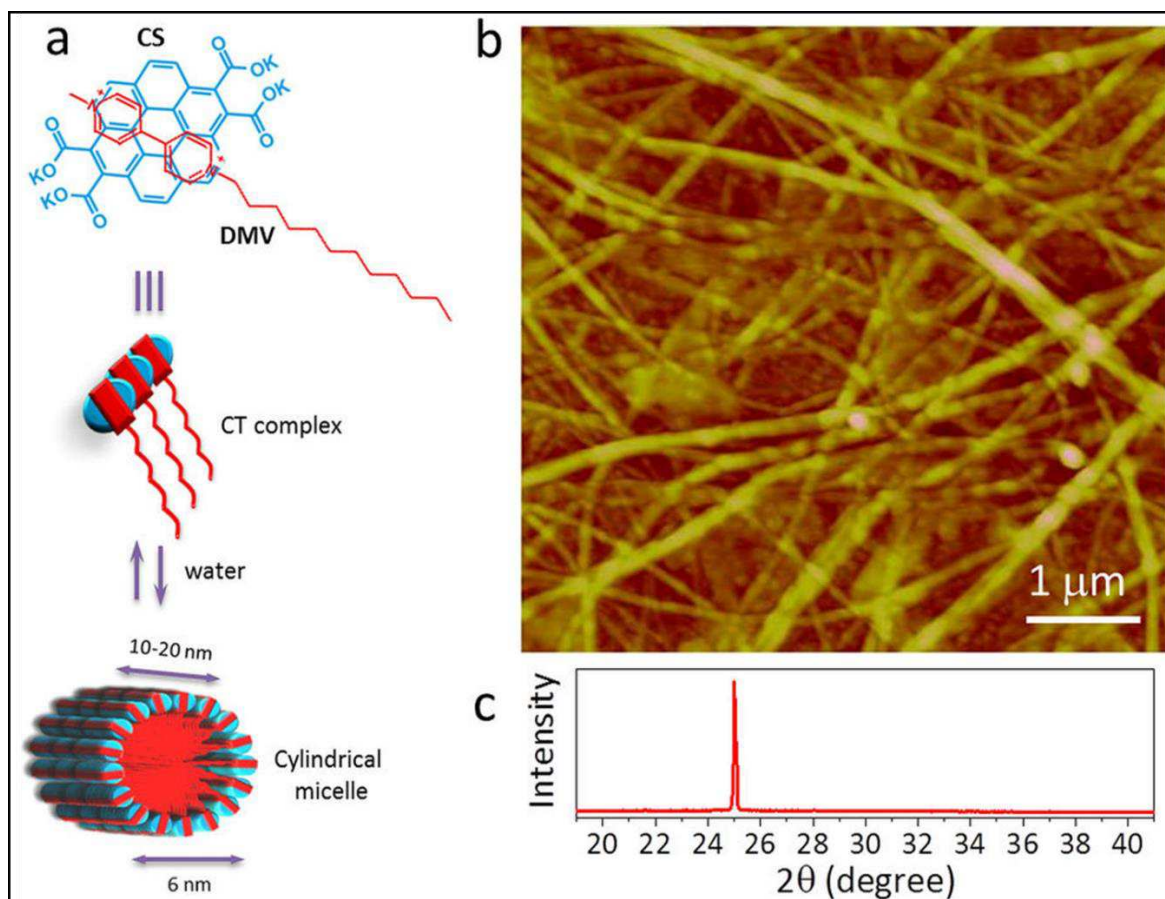


**Figure 2.11:** (a) Molecular structure and schematic of the aromatic donor, coronene tetracarboxylate (CS) and the acceptor, dodecyl methyl viologen derivative (DMV). (b) Tapping mode AFM image of a nanofibre carpet film. (Z scale = 20 nm). (c) XRD pattern of the film measured in ambient conditions (26°C, 35% RH). The peak at  $2\theta \approx 25.031^\circ$  corresponds to d-spacing of 3.5545 Å rising from the  $\pi$ - $\pi$  stacking in nanofibers. Reprinted with permission from Ref.<sup>107</sup>

Upon interaction with moisture, these supramolecular fiber can reversibly absorb water molecules in their external shell.

By performing *in-situ* XRD measurements at different humidity levels, the author demonstrated that the absorption of water molecules can decrease the  $\pi$ - $\pi$  stacking distances between the components of the assembly, resulting in an increased overlap between  $\pi$  orbitals and, as a consequence, a dramatic increase in the measured current flowing through the device (**Figure 2.12**).<sup>108</sup>

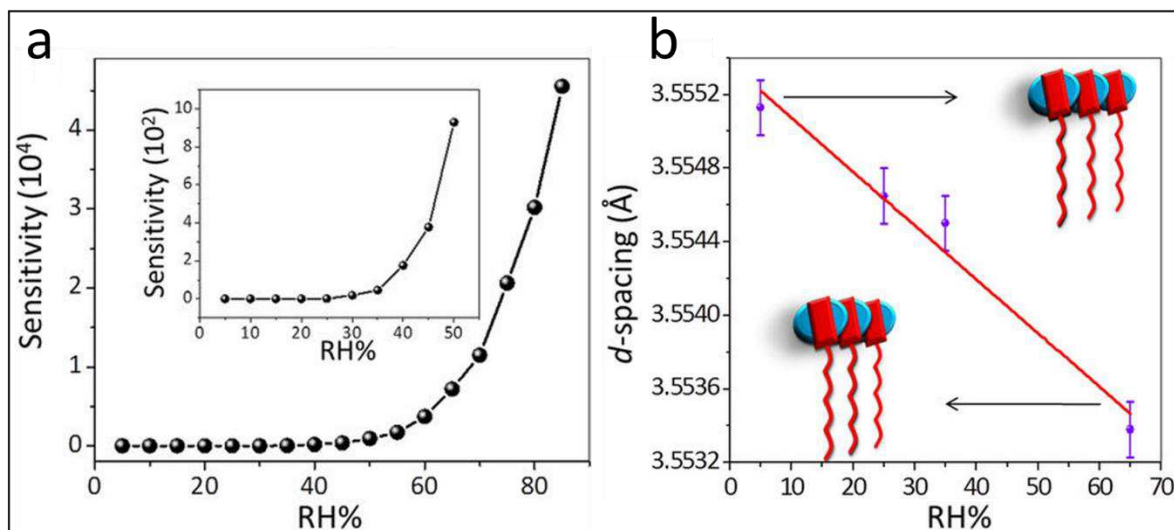


**Figure 2.12:** Effect of water absorption on CS-DMV nanofibers. (a) Electrical sensitivity response of the chemiresistive humidity sensors. (b) Change in the  $\pi$ - $\pi$  stacking distances between the building blocks as a consequence of water absorption (probed by performing XRD measurements at different RH). Adapted with permission from Ref.<sup>107</sup>

An application of a similar approach for the realization of 1D supramolecular chemiresistors targeting humidity, can be found in chapter 6 where conjugated donor-acceptor dyads are self-assembled into supramolecular nanofibers which are employed as active materials for humidity sensors featuring extremely high sensitivity and response speed.

## 4 2D: GRAPHENE AND GRAPHENE OXIDE

---

Since 2004, when Novoselov and Geim for the first time reported on the isolation and experimental electrical characterization of graphene,<sup>109</sup> this material attracted great

worldwide interest among the scientific community and is now one of the most studied and investigated materials of all time with > 110'000 scientific papers published so far and a still growing interest, as highlighted in **Figure 2.13** (Source: web of knowledge). Graphene is a single-atom thick single layer of  $sp^2$  carbon atoms arranged in a hexagonal honeycomb crystal lattice featuring a

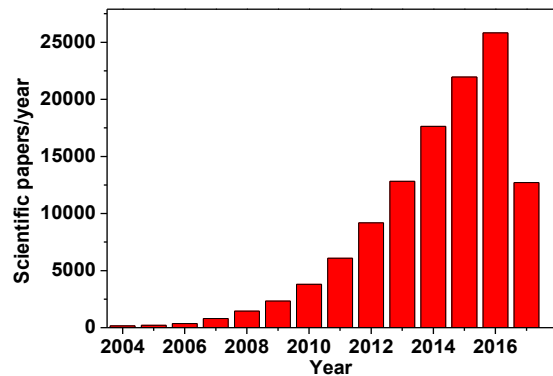


*Figure 2.13: Amount of scientific paper published every year on graphene (source: web of knowledge).*

C-C distance of 1.42 Å.<sup>110</sup> This material possesses unique electrical and mechanical properties such as high carrier mobility,<sup>111,112</sup> room temperature quantum Hall effect,<sup>112</sup> ballistic charge carriers conduction,<sup>109</sup> high electricity and mechanical resistance.<sup>113</sup>

In the first experiments on single and few layer graphene, the samples were prepared by micromechanical cleavage of highly oriented pyrolytic graphite crystals using common scotch tape. Such an approach is extremely straightforward and does not require any dedicated equipment, allowing, at the same time, the deposition of high quality graphene flakes featuring lateral size up to several tens on  $\mu\text{m}$ , which are large enough to be used as single-flake devices for the electrical characterizations.<sup>109</sup>

The scotch-tape approach allowed the facile fabrication of devices to unravel most of the interesting properties of graphene which could have countless applications in various technological field. The major drawback which is still preventing the appearance of graphene-based devices on the market is the lack of large scale industrial processes for the cost-effective production of such material.



So far, several different approaches, both bottom-up and top-down have been developed to solve this issue. Among the two, bottom-up approaches, in which small molecular precursors are bond together into the desired structure, are the most controlled and reproducible ones. Small graphene nanoribbons can also be grown in solution by chemical reaction between small aromatic precursors such as benzene, resulting in molecular-like graphene with controlled size, shape and characteristics.<sup>114-117</sup>

A more technologically relevant bottom-up approach is the chemical vapor deposition (CVD) which allow the fabrication of large area single layer graphene by using organic small molecules as precursors to be decomposed into graphene lattices on a catalytic metallic substrate.

The first example reported on CVD graphene in 2008 relies on the use on ethylene precursor on Ir [111] but the high costs of the substrate and the difficulty in transferring the grown materials limited the application of this approach.<sup>118</sup> The field rapidly moved towards the use of different precursors and substrates to increase the efficiency of the processes and the quality of the final materials and nowadays, less than 10 years after, wafer-scale high quality CVD graphene layers grown on Cu foils and transferable on different substrates are already commercially available from several companies around the world.

This material features low density of defects and high reproducibility but the high costs, the difficulty to pattern and the relatively high sheet resistance ( $360 \pm 30 \text{ } \Omega/\text{sq}$  according to Graphenea website) are still limiting the application of such materials.

On the other hand, top-down approaches, including dry processes such as micromechanical cleavage, anodic bonding<sup>119</sup> and laser ablation/photoexfoliation<sup>120,121</sup> as well as wet processes such as liquid phase exfoliation<sup>122</sup> and electrochemical exfoliation<sup>123</sup> consist on the production of single and few layer graphene starting from bulk graphite.<sup>124</sup>

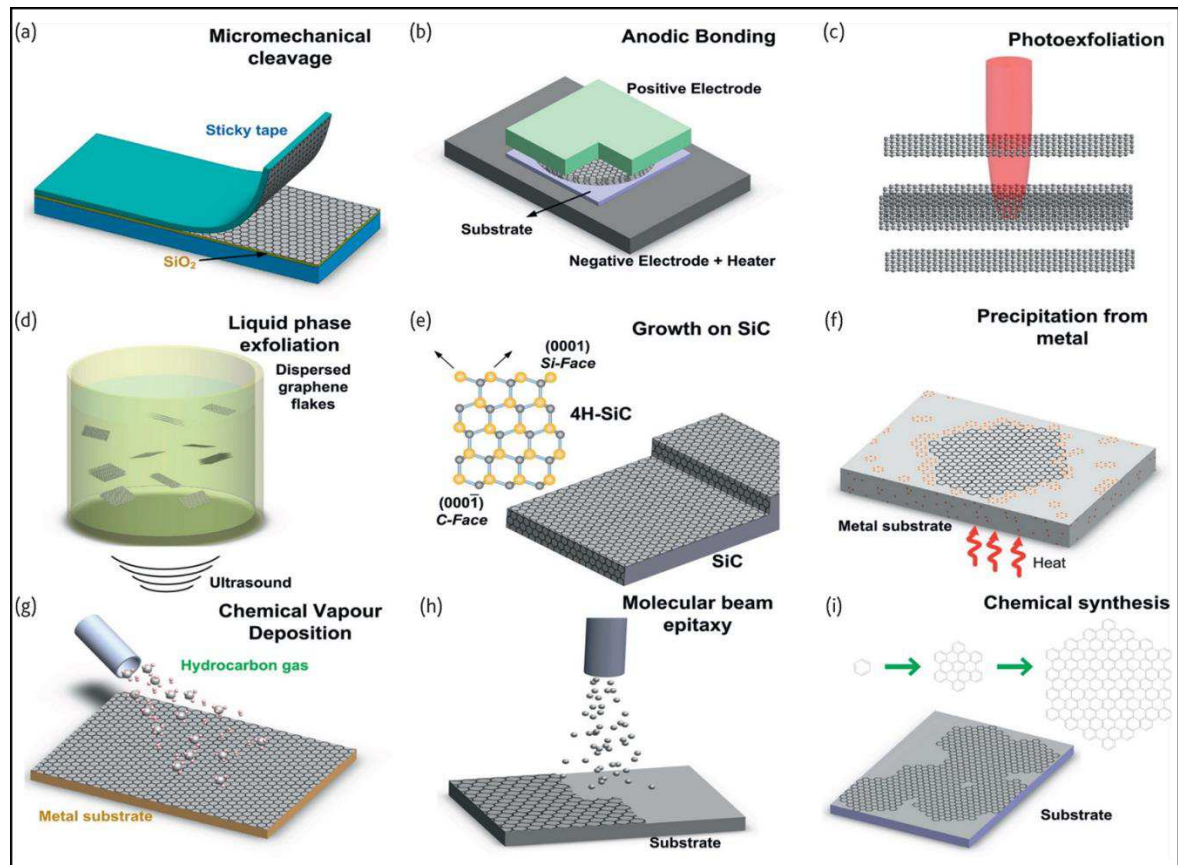


**Figure 2.14:** Schematic illustration of the main graphene production techniques. (a) Micromechanical cleavage. (b) Anodic bonding. (c) Photoexfoliation. (d) Liquid phase exfoliation. (e) Growth on SiC. (f) Segregation/precipitation from carbon containing metal substrate. (g) Chemical vapor deposition. (h) Molecular Beam epitaxy. (i) Chemical synthesis using benzene as building block. Reprinted with permission from Ref.<sup>124</sup>

Among the top-down approaches, the liquid phase and, in particular, the electrochemical exfoliations represent a viable strategy for the large-scale industrial production of few layers (1-7) graphene dispersions which are solution processable.<sup>125</sup>

The major drawbacks for this approach arise from the low dispersibility of graphene which require the presence of lattice defects such as oxygen containing groups and the use of organic solvents such as NMP and DMF which are pollutant and difficult to be removed after processing.<sup>122-125</sup>

Extreme oxidation of graphene flakes into the so-called graphene oxide (GO) could render them dispersible in environmental friendly water solution and, since the surface of this material is negatively charged in neutral water solutions, the electrostatic repulsion prevent the aggregation between the flakes allowing a high monolayer yield ( $> 90\%$ ) even at extremely high concentrations (up to 4 mg/ml).<sup>126</sup>

Synthesis of GO can be achieved by placing graphite in concentrated acids in the presence of oxidizing agents. GO was first prepared almost 150 years ago by Brodie, who made it by treating bulk graphite repeatedly with potassium chlorate and nitric acid.<sup>127</sup> This method was modified over time by several investigators but the major contributions were given by Staudenmaier<sup>128</sup> and Hamdi<sup>129</sup> who used a mixture of sulfuric acid and nitric acid with potassium chlorate.

Hummers and Offeman<sup>130</sup> later demonstrated a less hazardous and more efficient method, which involves a mixture of sodium nitrate, potassium permanganate, and concentrated sulfuric acid. These and their modified versions are still the most commonly used methods for the oxidation of graphite in laboratory as well as in industrial scale.<sup>131</sup>

The presence of the oxygen containing groups, as defect on the graphene lattice, have a dramatic impact on the characteristic of GO which lack most of the aforementioned properties of pristine graphene. For this reason, one of the most viable strategy to fully exploit such material is to take advantage of the superior dispersibility of GO to process it into thin films with controlled thickness and then remove the oxygen containing groups, forming the so-called “reduced GO” (rGO) and partially restoring the lattice and the properties typical of graphene (**Figure 2.15**).<sup>132-134</sup>

As reported by Erickson et al. reduction of GO can effectively restore the graphitic lattice making rGO equivalent to pristine graphene at extremely small scales. On the other hand, by looking at larger scale TEM images, reprinted from ref.<sup>134</sup> in **Figure 2.15**, it appears evident that, even though the reduction process can increase the size of the ordered graphitic domains, such domains are still separated by amorphous regions which can be considered as grain borders and which are responsible for the lower electrical characteristics of rGO compared to pristine graphene.

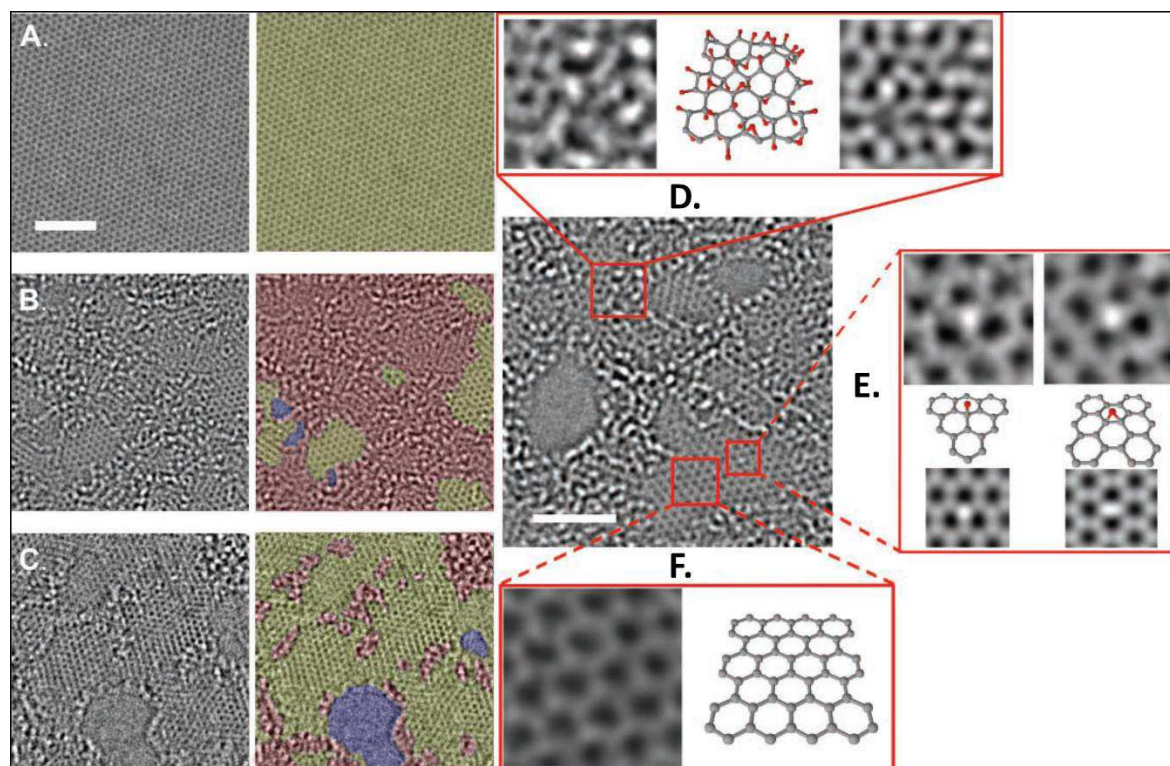


**Figure 2.15:** Aberration corrected TEM images (scale bar = 2 nm). (A) Single suspended sheet of graphene. On the right, graphitic area indicated in yellow. (B) Single suspended sheet of GO. On the right, holes are indicated in blue, graphitic areas in yellow, and high contrast, disordered regions, indicating oxygen functionalities, in red. (C) Suspended monolayer of rGO. On the right, holes indicated in blue, graphitic regions in yellow, and areas with remaining functionalities in red. Expansion (D) shows, from left to right, a 1 nm<sup>2</sup> enlarged oxidized region of the material, then a proposed possible atomic structure of this region and finally the average of a simulated TEM image of the proposed structure. Expansion (E) focuses on the white spot on the graphitic region, the ball-and-stick figures below the microscopy images represent the proposed atomic structure for such functionalities. The simulated TEM image for the suggested structure agrees well with the TEM data. Expansion (F) shows a 1 nm<sup>2</sup> graphitic portion and the atomic structure of this region. Adapted with permission from Ref.<sup>134</sup>

Within the last decades, numerous routes for reduction of GO have been reported and summarized in several reviews.<sup>135-137</sup> Chemical methods are usually wet processes involving exposure of GO to reducing agents such as hydrazine,<sup>138</sup> sodium borohydride<sup>139</sup> etc in solutions. Chemical reduction of GO has also been reported in strongly alkaline environments<sup>140</sup> and in supercritical water.<sup>141</sup> Dry approaches, including thermal treatment in inert or reducing environments,<sup>142,143</sup> hydrogen plasma treatment,<sup>144</sup> photo-reduction,<sup>145</sup> flash conversion,<sup>146</sup> and microwave reduction<sup>132</sup> are usually cleaner and more efficient, proving a higher degree of reduction and resulting in better optoelectronic characteristics of the materials. In this view, chapter 7 describes a novel photo-thermal approach employing a focused IR ( $\lambda = 1064$  nm) laser to pattern high quality conductive rGO paths over insulating films of GO.

## 4.1 ELECTRICAL PROPERTIES OF GRAPHENE AND RGO

As already mentioned, graphene is a single layer of  $sp^2$  hybridized carbon atom arranged in a honeycomb lattice, which is generated by the superposition of 2s with  $2p_x$  and  $2p_z$  orbitals. Such planar orbitals generates the energetically stable and localized  $\sigma$ -bonds with the three nearest-neighbor carbon atoms within the lattice and are the responsible for most of the binding energy and for the mechanical elastic properties of graphene sheet. The remaining  $2p_z$  orbitals are orthogonal with respect to the lattice and their overlap and delocalization between neighboring atoms plays the major role in the appearance of the electronic properties of this material. Because of this configuration, the electronic band structure of graphene can be described by an orthogonal nearest-neighbor tight-binding approximation, assuming that its electronic states can be represented by a linear combination of the  $2p_z$  orbitals. By solving the Schrödinger equation, it is then possible to obtain the energy dispersion relation of  $\pi$  (bonding)  $\pi^*$  (antibonding) bands:<sup>147,148</sup>

$$E(k_x, k_y) = \pm \gamma \sqrt{1 + 4 \cos\left(\frac{\sqrt{3}k_x a}{2}\right) \cos\left(\frac{k_x a}{2}\right) + 4 \left[\cos\left(\frac{k_y a}{2}\right)\right]^2}$$

Where  $k_x$  and  $k_y$  = components of the  $k$  vector folded onto the first hexagonal Brillouin zone (**Figure 2.16c**).  $\gamma$  = hopping energy (2.75 eV) and  $a$  = C-C distance (1.42 Å).

In condensed matter physics, the Schrödinger equation rules the world, usually being quite sufficient to describe electronic properties of materials. Graphene is an exception, its charge carriers mimic relativistic particles and are more easily and naturally described starting with the Dirac equation rather than the Schrödinger equation.<sup>149</sup>

The electronic structure of graphene, in a wider energy spectrum, could then be better represented by closed-form expressions obtained analytically for the single electron propagators on a real space (more details on the mathematical methods and calculations can



be found in Ref.<sup>150</sup>). From this model it is possible to obtain the band structure of graphene which yields conduction and valence bands which are symmetric respect to the Fermi energy (also called *Dirac point* or *Charge neutrality point*) which is set at 0 eV.<sup>151</sup>

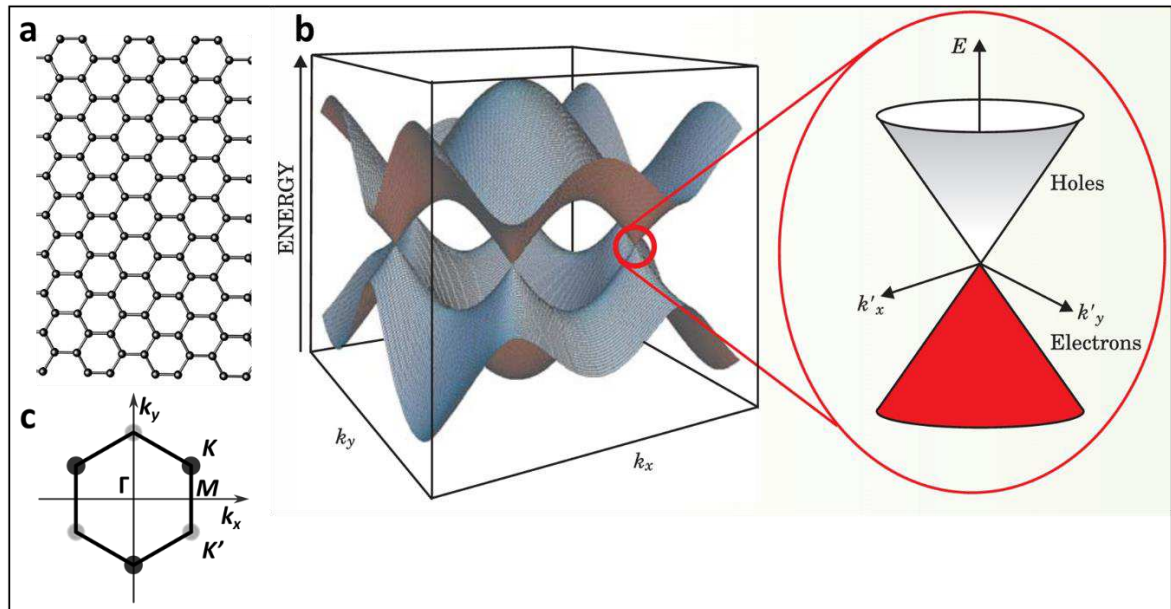


**Figure 2.16:** (a) Graphene's honeycomb structure. (b) Band energy dispersions calculated via tight binding approximations (inset highlights the conical-shape dispersion around the Dirac point). (c) First Brillouin zone. Adapted from Ref.<sup>151</sup>

Graphene valence and conduction bands are degenerated in 6 points, located at the corner of the Brillouin zone and are also called  $K$  and  $K'$  valleys, delineating the Fermi surface of this material.

This theoretical introduction may have been hard to digest but is necessary to understand the macroscopic electrical properties of graphene and rGO and their potential application as active material in electrical resistive sensing devices.

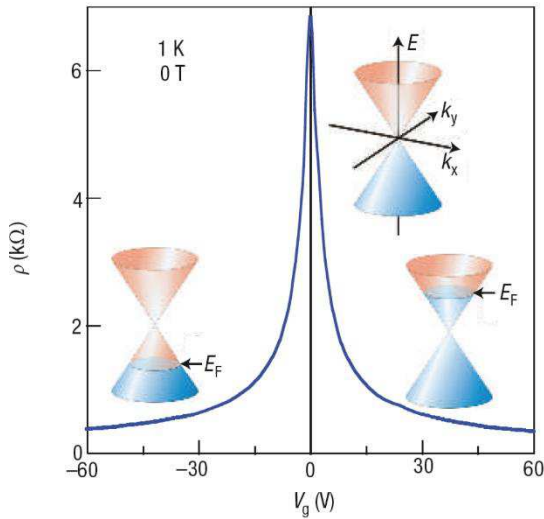
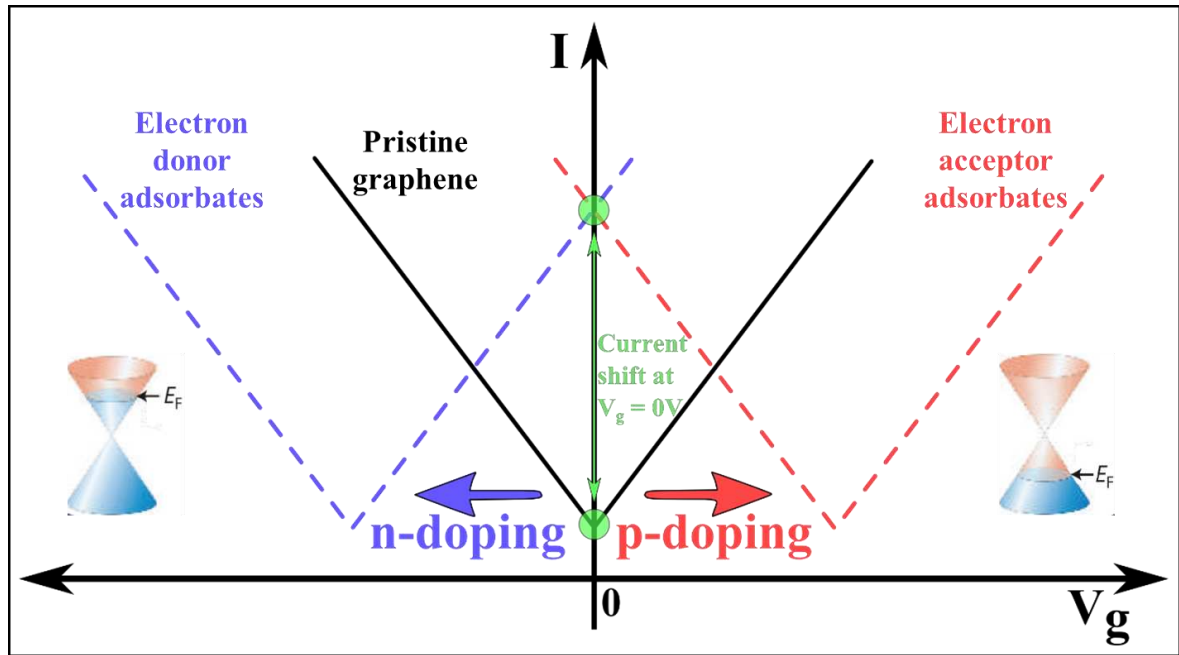


Figure 2. 17: Ambipolar electric field-effect in single-layer graphene on 300 nm SiO<sub>2</sub> dielectric layer. The insets show its conical low-energy spectrum  $E(k)$ , indicating changes in the position of the Fermi energy  $E_F$  with changing gate voltage  $V_g$ . Positive (negative)  $V_g$  induce electrons (holes). Reproduced with permission from Ref.<sup>149</sup>

Indeed, because of its peculiar band structure, graphene exhibit remarkably pronounced ambipolar electric field-effect (**Figure 2.17**) such that charge carriers can be tuned continuously between electrons and holes in concentrations as high as  $n = 10^{13} \text{ cm}^{-2}$  and their mobilities can exceed  $\mu = 15,000 \text{ cm}^2 \text{ V}^{-1} \text{ s}^{-1}$ , even under ambient conditions.<sup>111,152</sup> Moreover, the observed mobility weakly depend on temperature, which means that at 300 K is still limited by impurity scattering, and therefore can be improved significantly.

Interestingly, similar shift of the Dirac point given by the application of an external bias can be triggered by absorption of certain species on the graphene surface, resulting in a “doping” effect.<sup>153</sup> This characteristic of the two dimensional structure of graphene and rGO makes the electron transport through graphene highly sensitive to the adsorption of gas molecules.<sup>154</sup>

The adsorption of gas molecules on graphene’s surface leads to a shift of the Dirac point which corresponds to changes in the electrical conductivity measured at  $V_g = 0 \text{ V}$ . Depending on the nature of the absorbed molecules the Dirac point could be shifted to either negative (n-doping) or positive (p-doping) gate biases, as schematized in **Figure 2.18**. This effect can be attributed to the change in the local carrier concentration induced by the adsorbates on the surface which act as electron donors or acceptors.<sup>155</sup> Since the shift in the Dirac point is proportional to the amount of absorbed molecules, such devices can be calibrated and employed as active materials for quantitative gas sensors.



**Figure 2.18:** Schematic of the current shift given by the presence of adsorbates on graphene and rGO surface.

The intensity but also the direction of the measured drain current at  $V_g = 0$  V depends not only from the nature of the absorbed molecules but also from the nature of the employed graphene material. The schematic reported in **Figure 2.18**, for instance is an ideal case which is valid for pristine graphene prepared by micromechanical cleavage with the scotch tape approach but is not valid in the case of electrochemically exfoliated graphene or reduced graphene oxide, which normally exhibit strong p-doping given by the production processing.<sup>125,153</sup> In such case, for instance, the interaction of the graphene materials with an n-dopant will correspond to a decrease of the initial p-doping, leading to a lower zero gate current while the interaction with a p-dopant will still lead to higher measured current.

The first experimental example on a graphene-based gas sensor has been reported by Schedin et al. in 2007. In such study, the authors demonstrated that a micrometer-sized sensor made from mechanically exfoliated few-layer pristine graphene, was capable of detecting even a single molecule of  $\text{NO}_2$  in high vacuum environment.<sup>155</sup> Similar behavior have been reported also by Ko et al. who developed chemiresistive graphene-based  $\text{NO}_2$  detectors by employing mechanically exfoliated graphene layers with thickness in the range of 3.5–5 nm on a  $\text{SiO}_2/\text{Si}$  substrates. Such sensors showed fast response, good reproducibility, reversibility and high sensitivity, exhibiting a change in resistance, upon  $\text{NO}_2$  exposure in air, of  $\sim 9\%$



in response to 100 ppm NO<sub>2</sub> at RT.<sup>156</sup> By continuous in situ cleaning of CVD graphene-based 2-terminal devices with UV light, Chen et al. reported detection limits of ppq (part-per-quadrillion) for a wide range of gas molecules in controlled environment.<sup>157</sup>

Thanks to its higher hydrophilicity, GO has shown higher sensitivity for water vapor compared to pristine graphene. In 2013 Bi et al. exploited this characteristic to fabricate a micro-scale capacitive humidity sensor that featured a sensitivity more than 10 times higher, compared with conventional capacitive humidity sensors, within the range 15-95 % RH.<sup>158</sup> The same approach and similar results have been reported at the same time also by Borini et al. who also achieved remarkably fast response and recovery time of just ~ 30 ms. Such devices must rely on an electrical capacity readout because of the extremely high electrical resistance of GO flakes. By reducing GO into rGO it is possible to partially restore the electrical conductivity of the flakes while keeping a certain amount of defects and oxygen containing groups which can act as receptor, increasing the affinity for certain analytes. This characteristic, combined with the advantages of low costs and processability in solution, made rGO one of the most exploited platform for the realization of gas sensing devices.<sup>159</sup> In 2009 Lu et al. developed high performance gas sensors based on partially reduced GO by multi-step, low-temperature thermal treatments. Such rGO-based devices exhibited high sensitivity of ~1.56 to 100 ppm NO<sub>2</sub> and fast response.<sup>154</sup> As aforementioned, rGO is capable of interacting with a wide range of gaseous analytes and exhibited interesting sensing capability also for the detection of NH<sub>3</sub>,<sup>160</sup> H<sub>2</sub><sup>161</sup> and, SO<sub>2</sub>.<sup>162</sup>

Another example of a novel rGO-based gas sensing devices can be found in chapter 7 where films of laser reduced GO (LrGO) are used as active material in chemiresistors for ozone sensing. Such devices exhibited increased drain current upon interaction with the target analyte which is known to behave as a p-dopant for carbon-based materials.

To fabricate sensors which are both qualitative and quantitative for certain species, Rumyantsev et al. employed low frequency noise spectrum measurements of pristine graphene-based devices for selective detection of vapors of different organic solvents.<sup>163</sup> Upon exposure of the devices transistor to such vapors, distinctive bulges with different characteristic frequencies appear in the low frequency noise spectra of the transistors, whereas others introduce only change in resistance with no change in noise spectra. They found that some vapors such as ethanol, methanol, THF, CH<sub>3</sub>Cl and acetonitrile induce

Lorentzian components with distinct characteristic frequencies in the low frequency noise spectrum, thereby modifying the spectra, which serve as unique gas signatures.<sup>164</sup>

Such an approach represents an interesting strategy to overcome the lack of selectivity exhibited by 2D carbon-based sensing devices. However, the only route towards selectivity for such materials is considered to be the chemical functionalization, which can be exploited to covalently attach *ad-hoc* receptors, engineered to interact selectively with specific analytes. The presence of covalently attached receptors could preclude the interaction between the device surface and any other gas component that could dope the active materials, causing a change in drain current.

## 5 REFERENCES

---

- 1 Saha, K., Agasti, S. S., Kim, C., Li, X. & Rotello, V. M. Gold nanoparticles in chemical and biological sensing. *Chem Rev* **112**, 2739-2779, (2012).
- 2 Chen, Y. S., Hung, Y. C., Liao, I. & Huang, G. S. Assessment of the In Vivo Toxicity of Gold Nanoparticles. *Nanoscale Res Lett* **4**, 858-864, (2009).
- 3 Rao, C. N. R., Kulkarni, G. U., Thomas, P. J. & Edwards, P. P. Metal nanoparticles and their assemblies. *Chem Soc Rev* **29**, 27-35, (2000).
- 4 Liao, J., Bernard, L., Langer, M., Schonenberger, C. & Calame, M. Reversible formation of molecular junctions in 2D nanoparticle arrays. *Adv Mater* **18**, 2444-2447, (2006).
- 5 Liao, J. H. *et al.* Ordered nanoparticle arrays interconnected by molecular linkers: electronic and optoelectronic properties. *Chem Soc Rev* **44**, 999-1014, (2015).
- 6 Cho, E. S. *et al.* Ultrasensitive detection of toxic cations through changes in the tunnelling current across films of striped nanoparticles. *Nat Mater* **11**, 978-985, (2012).
- 7 Han, L. *et al.* Porous gold cluster film prepared from Au@BSA microspheres for electrochemical nonenzymatic glucose sensor. *Electrochim Acta* **138**, 109-114, (2014).
- 8 Kiely, C. J., Fink, J., Brust, M., Bethell, D. & Schiffrin, D. J. Spontaneous ordering of bimodal ensembles of nanoscopic gold clusters. *Nature* **396**, 444-446, (1998).
- 9 Narayanan, S., Wang, J. & Lin, X. M. Dynamical self-assembly of nanocrystal superlattices during colloidal droplet evaporation by in situ small angle x-ray scattering. *Phys Rev Lett* **93**, 4, (2004).
- 10 Andres, R. P. *et al.* Self-assembly of a two-dimensional superlattice of molecularly linked metal clusters. *Science* **273**, 1690-1693, (1996).
- 11 Black, C. T., Murray, C. B., Sandstrom, R. L. & Sun, S. H. Spin-dependent tunneling in self-assembled cobalt-nanocrystal superlattices. *Science* **290**, 1131-1134, (2000).
- 12 Bigioni, T. P. *et al.* Kinetically driven self assembly of highly ordered nanoparticle monolayers. *Nat Mater* **5**, 265-270, (2006).
- 13 Tao, A., Sinsermsuksakul, P. & Yang, P. Tunable plasmonic lattices of silver nanocrystals. *Nat Nanotechnol* **2**, 435-440, (2007).
- 14 Markovich, G., Collier, C. P. & Heath, J. R. Reversible metal-insulator transition in ordered metal nanocrystal monolayers observed by impedance spectroscopy. *Phys Rev Lett* **80**, 3807-3810, (1998).
- 15 Duan, C. *et al.* Controllability of the Coulomb charging energy in close-packed nanoparticle arrays. *Nanoscale* **5**, 10258-10266, (2013).
- 16 Zabet-Khosousi, A. & Dhirani, A. A. Charge transport in nanoparticle assemblies. *Chem Rev* **108**, 4072-4124, (2008).
- 17 Middleton, A. A. & Wingreen, N. S. Collective transport in arrays of small metallic dots. *Phys Rev Lett* **71**, 3198-3201, (1993).
- 18 Reissner, P. A., Tisserant, J. N., Sanchez-Ferrer, A., Mezzenga, R. & Stemmer, A. Solvent-mediated conductance increase of dodecanethiol-stabilized gold nanoparticle monolayers. *Beilstein J Nanotechnol* **7**, 2057-2064, (2016).

- 19 Joseph, Y. *et al.* Self-assembled gold nanoparticle/alkanedithiol films: Preparation, electron microscopy, XPS-analysis, charge transport, and vapor-sensing properties. *J Phys Chem B* **107**, 7406-7413, (2003).
- 20 Joseph, Y., Guse, B., Yasuda, A. & Vossmeier, T. Chemiresistor coatings from Pt- and Au-nanoparticle/nonanedithiol films: sensitivity to gases and solvent vapors. *Sensor Actuat B-Chem* **98**, 188-195, (2004).
- 21 Krasteva, N. *et al.* Self-assembled gold nanoparticle/dendrimer composite films for vapor sensing applications. *Nano Lett* **2**, 551-555, (2002).
- 22 Joseph, Y. *et al.* Vapor sensitivity of networked gold nanoparticle chemiresistors: Importance of flexibility and resistivity of the interlinkage. *J Phys Chem C* **111**, 12855-12859, (2007).
- 23 Ghane, T. *et al.* Interplay between Mechanical and Electronic Degrees of Freedom in pi-Stacked Molecular Junctions: From Single Molecules to Mesoscopic Nanoparticle Networks. *J Phys Chem C* **119**, 6344-6355, (2015).
- 24 Chen, C. J., Smeu, M. & Ratner, M. A. Modeling ion sensing in molecular electronics. *J Chem Phys* **140**, 054709, (2014).
- 25 Xiao, X. Y., Xu, B. Q. & Tao, N. J. Changes in the conductance of single peptide molecules upon metal-ion binding. *Angew Chem Int Ed* **43**, 6148-6152, (2004).
- 26 Bui, P. T. & Nishino, T. Electron transfer through coordination bond interaction between single molecules: conductance switching by a metal ion. *Phys Chem Chem Phys* **16**, 5490-5494, (2014).
- 27 Ibanez, F. J. & Zamborini, F. P. Chemiresistive Sensing with Chemically Modified Metal and Alloy Nanoparticles. *Small* **8**, 174-202, (2012).
- 28 Wang, L. Y. *et al.* Array of molecularly mediated thin film assemblies of nanoparticles: Correlation of vapor sensing with interparticle spatial properties. *J Am Chem Soc* **129**, 2161-2170, (2007).
- 29 Wohltjen, H. & Snow, A. W. Colloidal Metal-Insulator-Metal Ensemble Chemiresistor Sensor. *Anal Chem* **70**, 2856-2859, (1998).
- 30 Guerrini, L., Garcia-Rico, E., Pazos-Perez, N. & Alvarez-Puebla, R. A. Smelling, Seeing, Tasting-Old Senses for New Sensing. *ACS Nano* **11**, 5217-5222, (2017).
- 31 Chow, E., Gengenbach, T. R., Wieczorek, L. & Raguse, B. Detection of organics in aqueous solution using gold nanoparticles modified with mixed monolayers of 1-hexanethiol and 4-mercaptophenol. *Sensor Actuat B-Chem* **143**, 704-711, (2010).
- 32 Kim, Y. J. *et al.* Mixed-ligand nanoparticles of chlorobenzenemethanethiol and n-octanethiol as chemical sensors. *Sensor Actuat B-Chem* **106**, 189-198, (2005).
- 33 Yao, W., Chen, X. & Zhang, J. A capacitive humidity sensor based on gold-PVA core-shell nanocomposites. *Sensor Actuat B-Chem* **145**, 327-333, (2010).
- 34 Lee, H. C., Wang, C. Y. & Lin, C. H. High-performance humidity sensors utilizing dopamine biomolecule-coated gold nanoparticles. *Sensor Actuat B-Chem* **191**, 204-210, (2014).
- 35 Barnes, W. L., Dereux, A. & Ebbesen, T. W. Surface plasmon subwavelength optics. *Nature* **424**, 824-830, (2003).
- 36 D., B. & D., P. A Collective Description of Electron Interactions. *Phys Rev* **82**, 625-634, (1951).
- 37 Sambles, J. R., Bradbery, G. W. & Yang, F. Z. Optical-Excitation of Surface-Plasmons - an Introduction. *Contemp Phys* **32**, 173-183, (1991).
- 38 Rothenhausler, B. & Knoll, W. Surface-plasmon microscopy. *Nature* **332**, 615-617, (1988).

- 39 Attridge, J. W., Daniels, P. B., Deacon, J. K., Robinson, G. A. & Davidson, G. P. Sensitivity Enhancement of Optical Immunosensors by the Use of a Surface-Plasmon Resonance Fluoroimmunoassay. *Biosens Bioelectron* **6**, 201-214, (1991).
- 40 Zhang, D. M. & Liu, Q. J. Biosensors and bioelectronics on smartphone for portable biochemical detection. *Biosens Bioelectron* **75**, 273-284, (2016).
- 41 Mie, G. Beiträge zur Optik trüber Medien, speziell kolloidaler Metallösungen. *Ann Phys* **330**, 377-445, (1908).
- 42 Mayer, K. M. & Hafner, J. H. Localized surface plasmon resonance sensors. *Chem Rev* **111**, 3828-3857, (2011).
- 43 Link, S., Mohamed, M. B. & El-Sayed, M. A. Simulation of the optical absorption spectra of gold nanorods as a function of their aspect ratio and the effect of the medium dielectric constant. *J Phys Chem B* **103**, 3073-3077, (1999).
- 44 Malinsky, M. D., Kelly, K. L., Schatz, G. C. & Van Duyne, R. P. Chain length dependence and sensing capabilities of the localized surface plasmon resonance of silver nanoparticles chemically modified with alkanethiol self-assembled monolayers. *J Am Chem Soc* **123**, 1471-1482, (2001).
- 45 Haes, A. J., Zou, S. L., Schatz, G. C. & Van Duyne, R. P. A nanoscale optical biosensor: The long range distance dependence of the localized surface plasmon resonance of noble metal nanoparticles. *J Phys Chem B* **108**, 109-116, (2004).
- 46 Watanabe, S. *et al.* Enhanced optical sensing of anions with amide-functionalized gold nanoparticles. *Chem Commun*, 2866-2867, (2002).
- 47 Matsui, J. *et al.* SPR sensor chip for detection of small molecules using molecularly imprinted polymer with embedded gold nanoparticles. *Anal Chem* **77**, 4282-4285, (2005).
- 48 Frederix, F. *et al.* Biosensing based on light absorption of nanoscaled gold and silver particles. *Anal Chem* **75**, 6894-6900, (2003).
- 49 Yang, H. W. *et al.* Fabrication of a Nanogold-Dot Array for Rapid and Sensitive Detection of Vascular Endothelial Growth Factor in Human Serum. *ACS Appl Mater Interfaces* **8**, 30845-30852, (2016).
- 50 Zhang, J. *et al.* A protein A modified Au-graphene oxide composite as an enhanced sensing platform for SPR-based immunoassay. *Analyst* **138**, 7175-7181, (2013).
- 51 Frasconi, M., Tortolini, C., Botre, F. & Mazzei, F. Multifunctional au nanoparticle dendrimer-based surface plasmon resonance biosensor and its application for improved insulin detection. *Anal Chem* **82**, 7335-7342, (2010).
- 52 Cennamo, N. *et al.* Sensitive detection of 2,4,6-trinitrotoluene by tridimensional monitoring of molecularly imprinted polymer with optical fiber and five-branched gold nanostars. *Sensor Actuat B-Chem* **208**, 291-298, (2015).
- 53 Srivastava, S., Frankamp, B. L. & Rotello, V. M. Controlled plasmon resonance of gold nanoparticles self-assembled with PAMAM dendrimers. *Chem Mater* **17**, 487-490, (2005).
- 54 Lin, S. Y., Liu, S. W., Lin, C. M. & Chen, C. H. Recognition of potassium ion in water by 15-crown-5 functionalized gold nanoparticles. *Anal Chem* **74**, 330-335, (2002).
- 55 Kalluri, J. R. *et al.* Use of Gold Nanoparticles in a Simple Colorimetric and Ultrasensitive Dynamic Light Scattering Assay: Selective Detection of Arsenic in Groundwater. *Angew Chem Int Ed* **48**, 9668-9671, (2009).

- 56 Zhan, S. S., Yu, M. L., Lv, J., Wang, L. M. & Zhou, P. Colorimetric Detection of Trace Arsenic(III) in Aqueous Solution Using Arsenic Aptamer and Gold Nanoparticles. *Aust J Chem* **67**, 813-818, (2014).
- 57 Si, S., Kotal, A. & Mandal, T. K. One-dimensional assembly of peptide-functionalized gold nanoparticles: An approach toward mercury ion sensing. *J Phys Chem C* **111**, 1248-1255, (2007).
- 58 Kim, Y. R., Mahajan, R. K., Kim, J. S. & Kim, H. Highly sensitive gold nanoparticle-based colorimetric sensing of mercury(II) through simple ligand exchange reaction in aqueous media. *ACS Appl Mater Interfaces* **2**, 292-295, (2010).
- 59 Su, D. Y. *et al.* Colorimetric detection of Hg<sub>2</sub><sup>+</sup> using thioctic acid functionalized gold nanoparticles. *Rsc Advances* **3**, 24618-24624, (2013).
- 60 Dong, C. *et al.* Selective colorimetric detection of Cr(III) and Cr(VI) using gallic acid capped gold nanoparticles. *Dalton Trans* **45**, 8347-8354, (2016).
- 61 Zhou, Y., Wang, S., Zhang, K. & Jiang, X. Visual detection of copper(II) by azide- and alkyne-functionalized gold nanoparticles using click chemistry. *Angew Chem Int Ed* **47**, 7454-7456, (2008).
- 62 Gunupuru, R. *et al.* Colorimetric detection of Cu<sup>2+</sup> and Pb<sup>2+</sup> ions using calix[4]arene functionalized gold nanoparticles. *J Chem Sci* **126**, 627-635, (2014).
- 63 Chai, F., Wang, C., Wang, T., Li, L. & Su, Z. Colorimetric detection of Pb<sup>2+</sup> using glutathione functionalized gold nanoparticles. *ACS Appl Mater Interfaces* **2**, 1466-1470, (2010).
- 64 Liu, J. & Lu, Y. Accelerated color change of gold nanoparticles assembled by DNazymes for simple and fast colorimetric Pb<sup>2+</sup> detection. *J Am Chem Soc* **126**, 12298-12305, (2004).
- 65 Sung, Y.-M. & Wu, S.-P. Colorimetric detection of Cd(II) ions based on di-(1H-pyrrol-2-yl)methanethione functionalized gold nanoparticles. *Sensor Actuat B-Chem* **201**, 86-91, (2014).
- 66 Ma, Y., You, F., Promthaveepong, K. & Li, N. Ultrasensitive Bisphenol A sensing based on responsive plasmonic nanoparticles. *Sensor Actuat B-Chem* **245**, 369-374, (2017).
- 67 Mulpur, P., Yadavilli, S., Rao, A. M., Kamiseti, V. & Podila, R. MoS<sub>2</sub>/WS<sub>2</sub>/BN-Silver Thin-Film Hybrid Architectures Displaying Enhanced Fluorescence via Surface Plasmon Coupled Emission for Sensing Applications. *ACS Sens* **1**, 826-833, (2016).
- 68 Li, X. M., Wang, Y., Luo, J. & Ai, S. Y. Sensitive detection of adenosine triphosphate by exonuclease III-assisted cyclic amplification coupled with surface plasmon resonance enhanced fluorescence based on nanopore. *Sensor Actuat B-Chem* **228**, 509-514, (2016).
- 69 Inokuchi, Y. *et al.* New insights into metal ion-crown ether complexes revealed by SEIRA spectroscopy. *New J Chem* **39**, 8673-8680, (2015).
- 70 Nie, S. M. & Emery, S. R. Probing single molecules and single nanoparticles by surface-enhanced Raman scattering. *Science* **275**, 1102-1106, (1997).
- 71 Homola, J., Yee, S. S. & Gauglitz, G. Surface plasmon resonance sensors: review. *Sensor Actuat B-Chem* **54**, 3-15, (1999).
- 72 Sugano, K., Aiba, K., Ikegami, K. & Isono, Y. Single-molecule surface-enhanced Raman spectroscopy of 4,4'-bipyridine on a prefabricated substrate with directionally arrayed gold nanoparticle dimers. *Jpn J Appl Phys* **56**, 5, (2017).



- 73 Shalev, G. The Electrostatically Formed Nanowire: A Novel Platform for Gas-Sensing Applications. *Sensors* **17**, (2017).
- 74 Wang, W. *et al.* Tuning Nanowires and Nanotubes for Efficient Fuel-Cell Electrocatalysis. *Adv Mater* **28**, 10117-10141, (2016).
- 75 Abbasi, N. M. *et al.* Preparation of silver nanowires and their application in conducting polymer nanocomposites. *Mater Chem Phys* **166**, 1-15, (2015).
- 76 Hainey, M. F. & Redwing, J. M. Aluminum-catalyzed silicon nanowires: Growth methods, properties, and applications. *Appl Phys Rev* **3**, 10, (2016).
- 77 Wang, B., Cancilla, J. C., Torrecilla, J. S. & Haick, H. Artificial Sensing Intelligence with Silicon Nanowires for Ultrasensitive Detection in the Gas Phase. *Nano Lett* **14**, 933-938, (2014).
- 78 Zhang, R. F., Zhang, Y. Y. & Wei, F. Controlled Synthesis of Ultralong Carbon Nanotubes with Perfect Structures and Extraordinary Properties. *Accounts Chem Res* **50**, 179-189, (2017).
- 79 Chandran, G. T., Li, X., Ogata, A. & Penner, R. M. Electrically Transduced Sensors Based on Nanomaterials (2012-2016). *Anal Chem* **89**, 249-275, (2017).
- 80 Aida, T., Meijer, E. W. & Stupp, S. I. Functional Supramolecular Polymers. *Science* **335**, 813-817, (2012).
- 81 Kato, T. & Frechet, J. M. J. New Approach to Mesophase Stabilization through Hydrogen-Bonding Molecular-Interactions in Binary-Mixtures. *J Am Chem Soc* **111**, 8533-8534, (1989).
- 82 Lohmeijer, B. G. G. & Schubert, U. S. Supramolecular engineering with macromolecules: An alternative concept for block copolymers. *Angew Chem Int Ed* **41**, 3825-3829, (2002).
- 83 Fouquey, C., Lehn, J.-M. & Levelut, A.-M. Molecular recognition directed self-assembly of supramolecular liquid crystalline polymers from complementary chiral components. *Adv Mater* **2**, 254-257, (1990).
- 84 Hartgerink, J. D., Granja, J. R., Milligan, R. A. & Ghadiri, M. R. Self-assembling peptide nanotubes. *J Am Chem Soc* **118**, 43-50, (1996).
- 85 Langton, M. J. & Beer, P. D. Rotaxane and catenane host structures for sensing charged guest species. *Acc Chem Res* **47**, 1935-1949, (2014).
- 86 Meijer, E. W. & Schenning, A. Chemistry - Material marriage in electronics. *Nature* **419**, 353-354, (2002).
- 87 De Luca, G. *et al.* Nucleation-governed reversible self-assembly of an organic semiconductor at surfaces: Long-range mass transport forming giant functional fibers. *Adv Funct Mater* **17**, 3791-3798, (2007).
- 88 Samorì, P. *et al.* Self-Assembly of Perylene Monoimide Substituted Hexa-peri-hexabenzocoronenes: Dyads and Triads at Surfaces. *Adv Mater* **18**, 1317-1321, (2006).
- 89 Sun, Y. *et al.* Semiconductive, One-Dimensional, Self-Assembled Nanostructures Based on Oligopeptides with pi-Conjugated Segments. *Chem Eur J* **17**, 4746-4749, (2011).
- 90 Xu, H. *et al.* An investigation of the conductivity of peptide nanotube networks prepared by enzyme-triggered self-assembly. *Nanoscale* **2**, 960-966, (2010).
- 91 Crivillers, N. *et al.* Self-assembly and electrical properties of a novel heptameric thiophene-benzothiadiazole based architectures. *Chem Commun* **48**, 12162-12164, (2012).

- 92 Moulin, E., Cid, J. J. & Giuseppone, N. Advances in Supramolecular Electronics - From Randomly Self-assembled Nanostructures to Addressable Self-Organized Interconnects. *Adv Mater* **25**, 477-487, (2013).
- 93 Cacialli, F., Samorì, P. & Silva, C. Supramolecular architectures. *Mater Today* **7**, 24-32, (2004).
- 94 Chen, L. *et al.* Assembly and fiber formation of a gemini-type hexathienocoronene amphiphile for electrical conduction. *J Am Chem Soc* **135**, 13531-13537, (2013).
- 95 Li, W. S. *et al.* Use of side-chain incompatibility for tailoring long-range p/n heterojunctions: photoconductive nanofibers formed by self-assembly of an amphiphilic donor-acceptor dyad consisting of oligothiophene and perylenediimide. *Chem Asian J* **5**, 1566-1572, (2010).
- 96 Ponnuswamy, N., Pantos, G. D., Smulders, M. M. J. & Sanders, J. K. M. Thermodynamics of Supramolecular Naphthalenediimide Nanotube Formation: The Influence of Solvents, Side Chains, and Guest Templates. *J Am Chem Soc* **134**, 566-573, (2012).
- 97 Sakurai, T. *et al.* Electron- or hole-transporting nature selected by side-chain-directed pi-stacking geometry: liquid crystalline fused metalloporphyrin dimers. *J Am Chem Soc* **133**, 6537-6540, (2011).
- 98 Rekab, W. *et al.* High-Performance Phototransistors Based on PDIF-CN2 Solution-Processed Single Fiber and Multifiber Assembly. *ACS Appl Mater Interfaces* **8**, 9829-9838, (2016).
- 99 Mativetsky, J. M., Orgiu, E., Lieberwirth, I., Pisula, W. & Samorì, P. Charge Transport Over Multiple Length Scales in Supramolecular Fiber Transistors: Single Fiber Versus Ensemble Performance. *Adv Mater* **26**, 430-435, (2014).
- 100 Squillaci, M. A. *et al.* Self-Assembly of an Amphiphilic pi-Conjugated Dyad into Fibers: Ultrafast and Ultrasensitive Humidity Sensor. *Adv Mater* **27**, 3170-3174, (2015).
- 101 Mativetsky, J. M. *et al.* Self-Assembly of a Donor-Acceptor Dyad Across Multiple Length Scales: Functional Architectures for Organic Electronics. *Adv Funct Mater* **19**, 2486-2494, (2009).
- 102 Tonezzer, M., Maggioni, G. & Dalcanale, E. Production of novel microporous porphyrin materials with superior sensing capabilities. *J Mater Chem* **22**, 5647-5655, (2012).
- 103 Garg, K. *et al.* Room temperature ammonia sensor based on jaw like bis-porphyrin molecules. *Org Electron* **14**, 1189-1196, (2013).
- 104 Kumar, A. *et al.* Room temperature ppb level Cl<sub>2</sub> sensing using sulphonated copper phthalocyanine films. *Talanta* **82**, 1485-1489, (2010).
- 105 Saini, R., Mahajan, A., Bedi, R. K., Aswal, D. K. & Debnath, A. K. Solution processed films and nanobelts of substituted zinc phthalocyanine as room temperature ppb level Cl<sub>2</sub> sensors. *Sensor Actuat B-Chem* **198**, 164-172, (2014).
- 106 Zhu, P. *et al.* Morphology-controlled self-assembly of a ferrocene-porphyrin based NO<sub>2</sub> gas sensor: tuning the semiconducting nature via solvent-solute interaction. *J Mater Chem C* **4**, 10471-10478, (2016).
- 107 Mogera, U., Sagade, A. A., George, S. J. & Kulkarni, G. U. Ultrafast response humidity sensor using supramolecular nanofibre and its application in monitoring breath humidity and flow. *Sci Rep* **4**, 4103, (2014).
- 108 Bhattacharyya, A. *et al.* In-Situ GISAXS Study of Supramolecular Nanofibers having Ultrafast Humidity Sensitivity. *Sci Rep* **7**, 246-246, (2017).



- 109 Novoselov, K. S. *et al.* Electric field effect in atomically thin carbon films. *Science* **306**, 666-669, (2004).
- 110 Castro Neto, A. H., Guinea, F., Peres, N. M. R., Novoselov, K. S. & Geim, A. K. The electronic properties of graphene. *Rev Mod Phys* **81**, 109-162, (2009).
- 111 Novoselov, K. S. *et al.* Two-dimensional gas of massless Dirac fermions in graphene. *Nature* **438**, 197-200, (2005).
- 112 Chen, J. H., Jang, C., Xiao, S., Ishigami, M. & Fuhrer, M. S. Intrinsic and extrinsic performance limits of graphene devices on SiO<sub>2</sub>. *Nat Nanotechnol* **3**, 206-209, (2008).
- 113 Lee, C., Wei, X. D., Kysar, J. W. & Hone, J. Measurement of the elastic properties and intrinsic strength of monolayer graphene. *Science* **321**, 385-388, (2008).
- 114 Cai, J. *et al.* Atomically precise bottom-up fabrication of graphene nanoribbons. *Nature* **466**, 470-473, (2010).
- 115 Cai, W. *et al.* Synthesis and solid-state NMR structural characterization of (13)C-labeled graphite oxide. *Science* **321**, 1815-1817, (2008).
- 116 Narita, A. *et al.* Bottom-Up Synthesis of Liquid-Phase-Processable Graphene Nanoribbons with Near-Infrared Absorption. *ACS Nano* **8**, 11622-11630, (2014).
- 117 Osella, S. *et al.* Graphene Nanoribbons as Low Band Gap Donor Materials for Organic Photovoltaics: Quantum Chemical Aided Design. *ACS Nano* **6**, 5539-5548, (2012).
- 118 Coraux, J., N'Diaye, A. T., Busse, C. & Michely, T. Structural coherency of graphene on Ir(111). *Nano Lett* **8**, 565-570, (2008).
- 119 Shukla, A., Kumar, R., Mazher, J. & Balan, A. Graphene made easy: High quality, large-area samples. *Solid State Commun* **149**, 718-721, (2009).
- 120 Lee, S. *et al.* Laser-Synthesized Epitaxial Graphene. *ACS Nano* **4**, 7524-7530, (2010).
- 121 Dhar, S. *et al.* A new route to graphene layers by selective laser ablation. *Aip Advances* **1**, 8, (2011).
- 122 Hernandez, Y. *et al.* High-yield production of graphene by liquid-phase exfoliation of graphite. *Nat Nanotechnol* **3**, 563-568, (2008).
- 123 Parvez, K. *et al.* Electrochemically Exfoliated Graphene as Solution-Processable, Highly Conductive Electrodes for Organic Electronics. *ACS Nano* **7**, 3598-3606, (2013).
- 124 Bonaccorso, F. *et al.* Production and processing of graphene and 2d crystals. *Mater Today* **15**, 564-589, (2012).
- 125 Yang, S. *et al.* Ultrafast Delamination of Graphite into High-Quality Graphene Using Alternating Currents. *Angew Chem Int Ed* **56**, 6669-6675, (2017).
- 126 Eda, G. & Chhowalla, M. Chemically derived graphene oxide: towards large-area thin-film electronics and optoelectronics. *Adv Mater* **22**, 2392-2415, (2010).
- 127 Brodie, B. C. On the Atomic Weight of Graphite. *Philos Trans R Soc London* **149**, 249-259, (1859).
- 128 Staudenmaier, L. Verfahren zur Darstellung der Graphitsäure. *Ber Dtsch Chem Ges* **31**, 1481-1487, (1898).
- 129 Hamdi, H. Zur Kenntnis der kolloidchemischen Eigenschaften des Humus. *Kolloid Beih* **54**, 554-634, (1943).
- 130 Hummers, W. S. & Offeman, R. E. Preparation of Graphitic Oxide. *J Am Chem Soc* **80**, 1339-1339, (1958).

- 131 Niyogi, S. *et al.* Solution properties of graphite and graphene. *J Am Chem Soc* **128**, 7720-7721, (2006).
- 132 Voiry, D. *et al.* High-quality graphene via microwave reduction of solution-exfoliated graphene oxide. *Science* **353**, 1413-1416, (2016).
- 133 Yung, W. K. C., Li, G. J., Liem, H. M., Choy, H. S. & Cai, Z. X. Eye-friendly reduced graphene oxide circuits with nonlinear optical transparency on flexible poly(ethylene terephthalate) substrates. *J Mater Chem C* **3**, 11294-11299, (2015).
- 134 Erickson, K. *et al.* Determination of the local chemical structure of graphene oxide and reduced graphene oxide. *Adv Mater* **22**, 4467-4472, (2010).
- 135 Park, S. & Ruoff, R. S. Chemical methods for the production of graphenes. *Nat Nanotechnol* **4**, 217-224, (2009).
- 136 Rao, C. N. R., Biswas, K., Subrahmanyam, K. S. & Govindaraj, A. Graphene, the new nanocarbon. *J Mater Chem* **19**, 2457-2469, (2009).
- 137 Rao, C. N. R., Sood, A. K., Subrahmanyam, K. S. & Govindaraj, A. Graphene: The New Two-Dimensional Nanomaterial. *Angew Chem Int Ed* **48**, 7752-7777, (2009).
- 138 Tung, V. C., Allen, M. J., Yang, Y. & Kaner, R. B. High-throughput solution processing of large-scale graphene. *Nat Nanotechnol* **4**, 25-29, (2009).
- 139 Si, Y. & Samulski, E. T. Synthesis of water soluble graphene. *Nano Lett* **8**, 1679-1682, (2008).
- 140 Fan, X. B. *et al.* Deoxygenation of Exfoliated Graphite Oxide under Alkaline Conditions: A Green Route to Graphene Preparation. *Adv Mater* **20**, 4490-4493, (2008).
- 141 Zhou, Y., Bao, Q. L., Tang, L. A. L., Zhong, Y. L. & Loh, K. P. Hydrothermal Dehydration for the "Green" Reduction of Exfoliated Graphene Oxide to Graphene and Demonstration of Tunable Optical Limiting Properties. *Chem Mater* **21**, 2950-2956, (2009).
- 142 Wang, X., Zhi, L. J. & Mullen, K. Transparent, conductive graphene electrodes for dye-sensitized solar cells. *Nano Lett* **8**, 323-327, (2008).
- 143 Becerril, H. A. *et al.* Evaluation of solution-processed reduced graphene oxide films as transparent conductors. *ACS Nano* **2**, 463-470, (2008).
- 144 Gomez-Navarro, C. *et al.* Electronic transport properties of individual chemically reduced graphene oxide sheets. *Nano Lett* **7**, 3499-3503, (2007).
- 145 Zhang, Y. L. *et al.* Photoreduction of Graphene Oxides: Methods, Properties, and Applications. *Adv Opt Mater* **2**, 10-28, (2014).
- 146 Cote, L. J., Cruz-Silva, R. & Huang, J. Flash reduction and patterning of graphite oxide and its polymer composite. *J Am Chem Soc* **131**, 11027-11032, (2009).
- 147 Wallace, P. R. The Band Theory of Graphite. *Phys Rev* **71**, 622-634, (1947).
- 148 Dubois, S. M. M., Zanolli, Z., Declerck, X. & Charlier, J. C. Electronic properties and quantum transport in Graphene-based nanostructures. *Eur Phys J B* **72**, 1-24, (2009).
- 149 Geim, A. K. & Novoselov, K. S. The rise of graphene. *Nat Mater* **6**, 183-191, (2007).
- 150 Power, S. R. & Ferreira, M. S. Electronic structure of graphene beyond the linear dispersion regime. *Phys Rev B* **83**, (2011).
- 151 Wilson, M. Electrons in atomically thin carbon sheets behave like massless particles. *Phys Today* **59**, 21-23, (2006).
- 152 Novoselov, K. S. *et al.* Two-dimensional atomic crystals. *Proc Natl Acad Sci USA* **102**, 10451-10453, (2005).

- 153 Varghese, S. S., Lonkar, S., Singh, K. K., Swaminathan, S. & Abdala, A. Recent advances in graphene based gas sensors. *Sensor Actuat B-Chem* **218**, 160-183, (2015).
- 154 Lu, G., Ocola, L. E. & Chen, J. Reduced graphene oxide for room-temperature gas sensors. *Nanotechnology* **20**, (2009).
- 155 Schedin, F. *et al.* Detection of individual gas molecules adsorbed on graphene. *Nat Mater* **6**, 652-655, (2007).
- 156 Ko, G. *et al.* Graphene-based nitrogen dioxide gas sensors. *Curr Appl Phys* **10**, 1002-1004, (2010).
- 157 Chen, G., Paronyan, T. M. & Harutyunyan, A. R. Sub-ppt gas detection with pristine graphene. *Appl Phys Lett* **101**, (2012).
- 158 Bi, H. *et al.* Ultrahigh humidity sensitivity of graphene oxide. *Sci Rep* **3**, 2714, (2013).
- 159 Fowler, J. D. *et al.* Practical Chemical Sensors from Chemically Derived Graphene. *ACS Nano* **3**, 301-306, (2009).
- 160 Lu, G., Yu, K., Ocola, L. E. & Chen, J. Ultrafast room temperature NH<sub>3</sub> sensing with positively gated reduced graphene oxide field-effect transistors. *Chem Commun* **47**, 7761-7763, (2011).
- 161 Wang, J., Kwak, Y., Lee, I. Y., Maeng, S. & Kim, G. H. Highly responsive hydrogen gas sensing by partially reduced graphite oxide thin films at room temperature. *Carbon* **50**, 4061-4067, (2012).
- 162 Kumar, R., Avasthi, D. K. & Kaur, A. Fabrication of chemiresistive gas sensors based on multistep reduced graphene oxide for low parts per million monitoring of sulfur dioxide at room temperature. *Sensor Actuat B-Chem* **242**, 461-468, (2017).
- 163 Rumyantsev, S., Liu, G., Shur, M. S., Potyrailo, R. A. & Balandin, A. A. Selective Gas Sensing with a Single Pristine Graphene Transistor. *Nano Lett* **12**, 2294-2298, (2012).
- 164 Huang, B. *et al.* Adsorption of gas molecules on graphene nanoribbons and its implication for nanoscale molecule sensor. *J Phys Chem C* **112**, 13442-13446, (2008).

# Chapter 3                      Methods

## 1 INTRODUCTION

---

This section of the manuscript is dedicated at briefly explaining the sample's preparation methods and the working principle of the characterization techniques employed for the reported projects. It also provides details on the experimental conditions and on the instruments that were employed. Due to the multidisciplinary nature of this thesis, it involves the use of several different methods and experimental techniques, in solutions as well in solid-state, ranging from basic chemical synthesis and analysis to multiscale characterization and electrical device testing.

## 2 SYNTHESIS OF WATER-SOLUBLE GOLD NANOPARTICLES

---

The first section of this chapter explains the synthetic procedures that were employed for the preparation of the water-soluble gold nanoparticles (AuNPs) that were employed as starting material for the realization of the 2D and 3D networks described in chapters 4 and 5, respectively.

Metal nano-objects such as nanoparticles, nanorods, nanocubes, etc. are commonly produced by using bottom-up approaches in solutions, starting from a soluble metal precursor which

is, usually, a water-soluble salt of the chosen metal. The general chemical route for the realization of such objects involves the use of a reducing agent to reduce the metal ions in solution to the “0” oxidation state, e.g. to their metallic state. During the reaction, such unstable metal atoms tend to aggregate between each other into bigger cluster and then into nanoscopic objects. By using *ad-hoc* stabilizing agents and optimized strategies, it is possible to achieve a great control over the aggregation processes, allowing to finely tune the size and shape of the aggregates.<sup>1</sup>

In the case of gold nanoparticles, the synthesis can be performed at the interface between water and toluene using chloroauric acid ( $\text{HAuCl}_4$ ) as source of gold, sodium borohydride as reducing agent and alkanethiols as stabilizers and size-controllers.<sup>2</sup> By using this approach it is possible to grow small gold nanoparticles ( $\sim 2\text{-}3\text{ nm}$ ), which are dispersible in organic solvents such as toluene. Since the scope of this thesis is to decorate the AuNPs with water soluble thiolated ligands as receptors for moisture, this approach was discarded. The chosen procedure to grow water-soluble AuNPs was reported for the first time by John Turkevich in 1953 and involves the use of chloroauric acid as source of gold and sodium citrate as reducing and particles stabilizing agent. Such reaction is performed at high temperature ( $\sim 100\text{ }^\circ\text{C}$ ) and is complete within few minutes.<sup>3</sup>

The AuNPs employed for the experiments in chapters 4 and 5 of this thesis, were synthesized with the aforementioned Turkevich method by placing a 150 ml of a 2.2 mM water solution of sodium citrate in a 3-neck round-bottom flask. The flask was kept under Ar atmosphere using a balloon and heated up to  $100\text{ }^\circ\text{C}$ . At this point 1 ml of a 25 mM water solution of  $\text{HAuCl}_4$  was added rapidly in the flask under stirring (the solution turns yellow because of the presence of the  $\text{HAuCl}_4$ ). The solution was kept at  $100\text{ }^\circ\text{C}$  under continuous stirring for 3.5 min before being left to cool down at room temperature.<sup>4</sup> During the reaction the color of the solution slowly turns from yellow to red because of the localized plasmonic resonance of the growing AuNPs. The volume of the solution was kept constant during the whole reaction by using a reflux condenser (**Figure 3.1**).

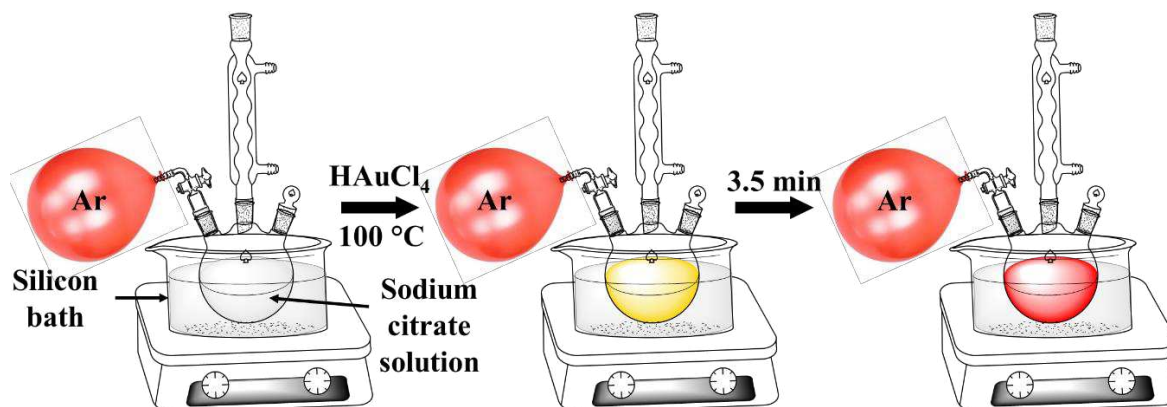


Figure 3.1: Schematic of the synthesis for the water-soluble gold nanoparticles.

The AuNPs synthesized with this method exhibit great stability over time (at least 1 year at room temperature) thanks to the strong non-covalent bond between the gold surface and the sodium citrate in solution.<sup>5</sup>

Dynamic light scattering (DLS) investigations of the as-synthesized AuNPs solutions revealed a narrow size distribution and an average nanoparticle radius of  $\sim 4.5$  nm (Figure 3.2a). In accordance with the size information obtained by DLS characterization, such nanoparticles exhibit a strong localized plasmon resonance at  $\lambda = 519$  nm, as reported in Figure 3.2b.

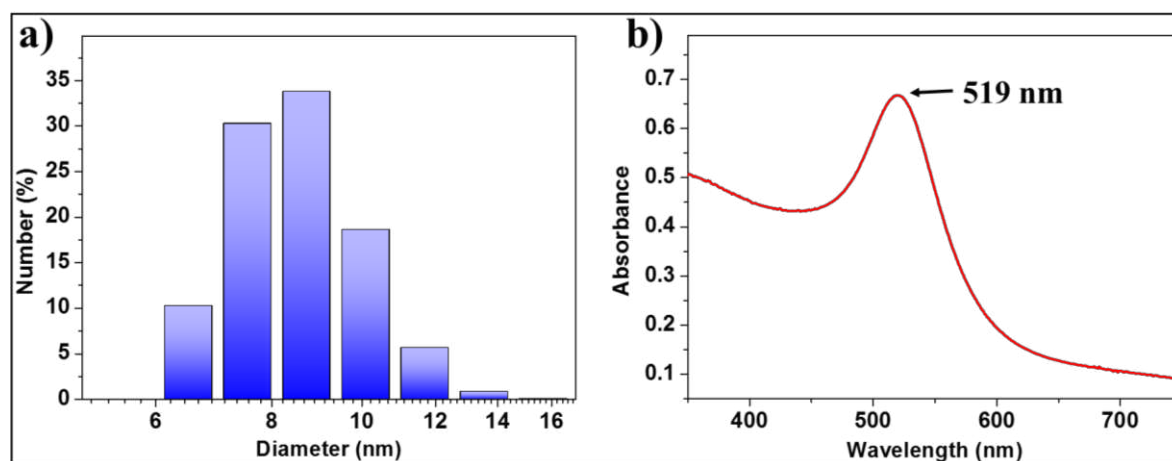


Figure 3.2: Characterization of the water-soluble AuNPs. a) Dynamic light scattering. b) UV-Vis absorbance spectra.

## 2.1 FUNCTIONALIZATION OF GOLD NANOPARTICLES

The water-soluble AuNPs synthesized with the Turkevich method, as described in the previous section, were employed in the experimental chapters 4 and 5 for the realization of 2D and 3D networks capable of absorbing water molecules from the atmosphere.

The AuNPs within such networks are connected between each other by using di-thiolated polyethylene glycol (PEG) or shorter di-thiolated oligoethylene glycols (OEG). The functionalization can be achieved by exploiting the affinity between the gold surface and the sulfur atoms of the thiol groups. The reaction between the gold surface and thiolated molecules leads to the formation of the so-called “self-assembled monolayers” (SAMs) on the gold surface, which consists into a single layer of highly ordered and tightly packed molecules covering the metal through covalent sulfur-gold bonds.<sup>6</sup>

The reaction of di-thiolated molecules to connect and cross-link multiple AuNPs together into a covalent and robust network, is an extremely delicate process in which the stoichiometric ratio between the AuNPs and the linkers is a fundamental parameter for the success of the reaction. The major complication, on this regard, is given by the unknown amount of binding sites in a certain volume of the synthesized AuNPs solutions. Since the size of the AuNPs is not monodispersed and the synthesis yield is not precisely known, it is necessary to introduce some approximations and to perform numerous control experiments to define such parameters.

The preliminary calculations to find the right stoichiometric ratio between the reactive sites on the nanoparticles and di-thiolated ligands, were based on purely geometrical considerations: by knowing the initial amount of gold precursor used for the synthesis of the nanoparticles, the volume of water used for the synthesis and considering a reaction yield close to 100%, it is possible to know the amount of gold atoms in the starting solution. Then, by exploiting dynamic light scattering (DLS) measurements, it was possible to know the average size and size distribution of the nanoparticles. By combining such information it is possible to estimate the amount of nanoparticles in solution. From this rough calculation it was possible to estimate an initial concentration of AuNPs of  $\sim 1.02 \times 10^{-8}$  M. By recording UV-Vis absorbance spectra of the obtained AuNPs solutions it was found that the SPR peak



absorbance of such solutions was equal to 0.6674 ( $\lambda = 519$  nm). By considering the Lambert-Beer law:

$$A = \varepsilon cd$$

Where  $A$  = peak absorbance,  $\varepsilon$  = extinction coefficient and  $d$  = optical path.

By knowing that the optical path of the used cuvettes is 1 cm and that the extinction coefficient of AuNPs is equal to  $5.14 \times 10^7 \text{ M}^{-1}\text{cm}^{-1}$  (for AuNPs in water, stabilized with sodium citrate and featuring a diameter of 8.55 nm)<sup>7</sup>, it is possible to conclude that the optically determined concentration of the synthesized AuNPs is equal to  $1.3 \times 10^{-8} \text{ M}$ , strongly in accordance with the values obtained by purely geometrical considerations. At this point, by knowing the amount of particles in solution, their size and their shape, it was possible to determine the total exposed gold surface accessible for the chemical reaction with the thiolated ligands in a fixed volume of the AuNPs solution.

From theoretical and experimental studies on Au/thiolated SAMs, reported in literature, it is known that the maximum molecular density of alkanethiol SAMs, on flat Au [111], amounts  $\sim 4.5 \text{ molecules/nm}^2$ .<sup>8</sup> By considering the higher steric hindrance of PEG backbone, compared to aliphatic chains, and that for particles bigger than 5.2 nm the curvature radius is negligible at molecular scales,<sup>6,9</sup> it is possible to conclude that the upper limit for the density of molecules in the AuNPs-PEG SAM is equal  $4.5 \text{ molecules/nm}^2$ . Therefore each nanoparticle cannot react with more than 900 thiol groups. This model is obviously based on strong approximations and was used in the preliminary steps of the projects as a starting point to experimentally determine the optimal AuNPs/PEG ratio for the formation of stable 2D and 3D networks, as described also in chapters 4 and 5.



### 3 OPTICAL CHARACTERIZATIONS

#### 3.1 UV-VIS ABSORBANCE SPECTROSCOPY

UV-Vis spectroscopy is a technique used to record the extinction spectra of samples in solution or solid-state, by measuring the difference in the light intensity between a beam passing through the sample and one passing through a reference, while scanning a wide spectrum of monochromatic wavelengths. These measurements are usually performed with a double beam UV-Vis spectrophotometer which is schematized in **Figure 3.3**.

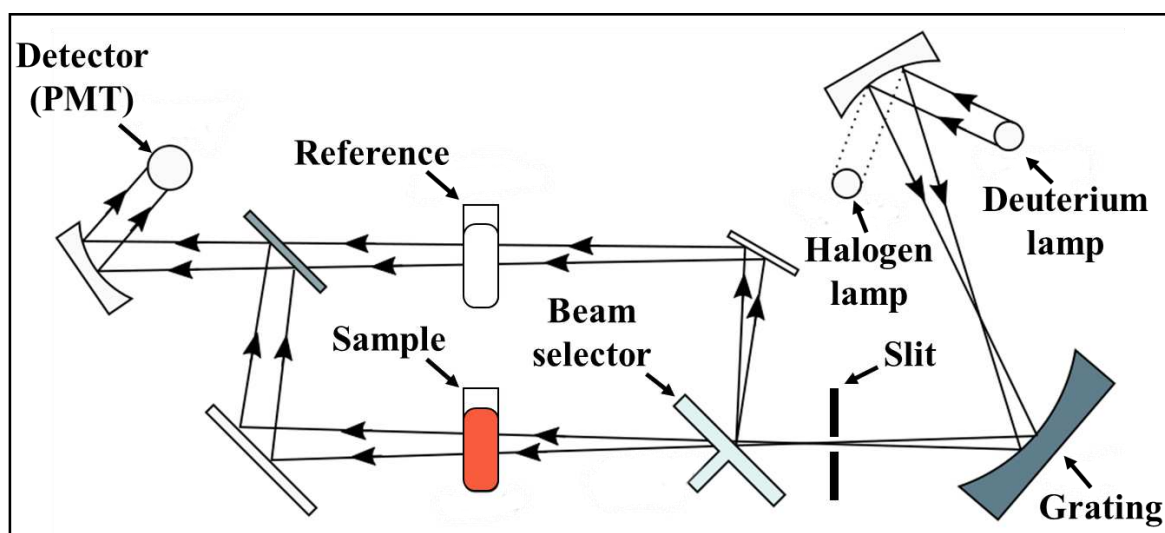


*Figure 3.3: Scheme of a double beam UV-Vis spectrophotometer.*

The instrument employed for such measurements in this thesis is a Jasco “V-670” UV-Vis-NIR spectrophotometer. This instrument is equipped with two light sources: a deuterium lamp which produces UV light (covering from  $\lambda = 200$  to 400 nm) and a halogen lamp which produces visible and near-infrared (NIR) light (from 400 to  $\sim 2700$  nm). The light produced by the sources is focused with a parabolic mirror into the monochromator, which is made by a grating and a slit. By moving the grating it is possible to choose which wavelength will pass through the slit and, by changing the size of the slit, it is possible to find the best

compromise between wavelength resolution and light intensity for each sample. The light is then focused on a beam selector, which consists in a rotating disc with alternating mirrors and holes that alternatively sends the monochromatic light through the sample and through the reference. In the case of samples in solutions (liquid phase), the reference consist in a cuvette identical to the one used for the sample, filled with the same solvent used to prepare the sample's solution. In the case of thin films deposited on a substrate, the reference is just a clean substrate featuring identical material and thickness compared to the one used to prepare the sample. The light passing through the sample is then collected with a parabolic mirror and sent to the photodetector, which usually is a photo-multiplier tube (PMT). The detector translates the optical signal into an electrical one which is then amplified and sent to the computer, to be corrected with the signal given from the reference. The data is then reported as a plot of optical absorbance (or transmittance) of the sample as a function of the wavelength, as for example displayed in **Figure 3.2b** of this chapter.

UV-Vis spectroscopy was employed in chapter 4 to study the plasmonic extinction spectra of gold nanoparticles in solutions as well as in 2D solid-state films, in which it also allowed to quantify the shift of the SPR band upon exposure to humid air. In chapter 5 it was used to follow the cross-link reaction between AuNPs and short di-thiolated OEG, by probing the LSPR band of the AuNPs over time during the reaction.

In chapter 6 such technique was employed to follow the aggregation of the PDI-4T building blocks into supramolecular nanofibers, by probing the decrease in the UV-Vis extinction bands upon aggregation in solution. In chapter 7 It was exploited to quantify the optical transmittance of GO and L-rGO films over a wide wavelength spectrum.

For samples in solution it is also possible to gain quantitative insight into the concentration of the samples by applying the Lambert-Beer law, as already explained in the previous section for determining the concentration of the synthesized AuNPs solutions.

### 3.2 DYNAMIC LIGHT SCATTERING (DLS).

Dynamic light scattering is a non-invasive optical characterization technique commonly used to determine the molecular weights of polymers or the diameter of dispersed nanoparticles (usually smaller than 1  $\mu\text{m}$ ) in solutions. This kind of measurements are performed with a size analyzer like the one schematized in **Figure 3.4**.

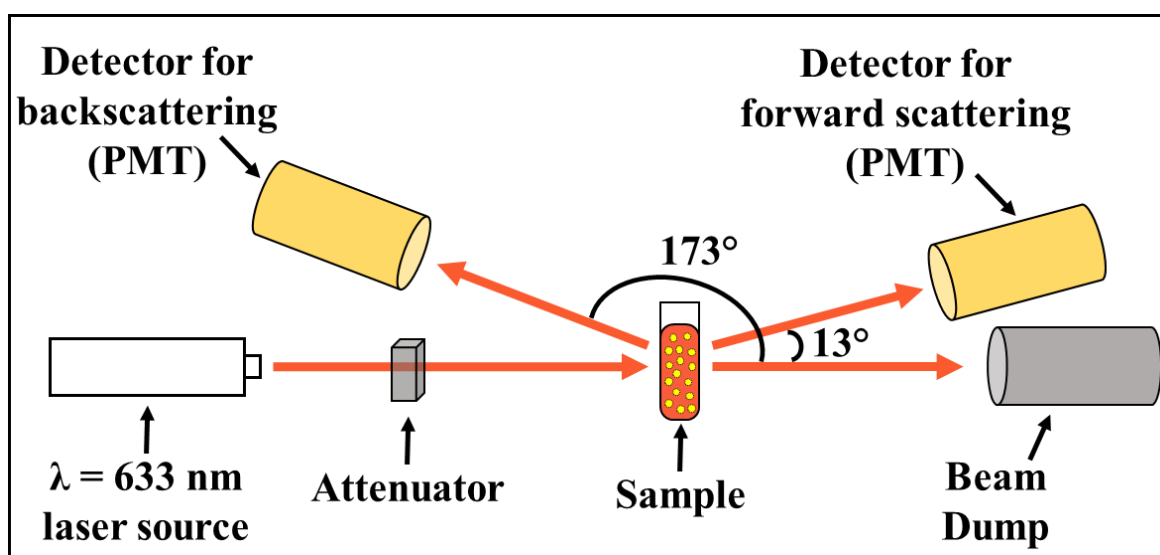


*Figure 3.4: Scheme of a DLS size analyzer.*

In a DLS measurement, the monochromatic light, produced by a laser source, passes through an attenuator, which is employed to finely tune the initial light intensity before hitting the sample solution. During the interaction with the sample, the intensity of the scattered light is not constant over time but undergoes fluctuations induced by the Brownian motion of the particles in solution.

The frequencies of such fluctuations depend on the size of the particles scattering the light, in general, smaller particles move faster, generating fast variations in the scattering intensity while bigger particles move slower, generating slow variations.

By measuring the speed of the fluctuations it is possible to calculate the diffusion coefficient by mean of a correlation function. Since the diffusion coefficient is a function of several

parameters, including: Viscosity of the media, temperature and hydrodynamic radius of the particles, by knowing the physical properties of the media it is possible to use the Stokes-Einstein equation to determine the size of the particles in solution as:

$$D = \frac{k_B T}{6\pi\eta r}$$

Where D = diffusion constant,  $k_B$  = Boltzmann's constant, T = temperature (K),  $\eta$  = dynamic viscosity, and r = particle's hydrodynamic radius.

The light scattered from the sample is then collected and focused in a PMT detector. The instrument employed for the DLS experiments in this thesis is a Malvern "Zetasizer Nano ZS" which is equipped with a 4 W  $\lambda = 633$  nm laser source and two PMT detectors, placed at  $13^\circ$  and  $173^\circ$  respect to the beam dump. The choice of the detector to be employed, depends on the concentration and on the extinction coefficient of the solution at  $\lambda = 633$  nm: for diluted solutions with a low extinction the forward scattered light ( $13^\circ$ ) is preferred while the backscattering detector ( $173^\circ$ ) is mostly used for big objects or highly concentrated solutions.

The light intensity collected from the detector is then translated into an electric signal, amplified and processed by a dedicated software. The data output can be reported in different ways: it is possible to check the average raw correlation function or to directly plot the size distribution as histograms, as showed in **Figure 3.2a**, at the beginning of this chapter.

DLS was mainly used for the characterizations of gold nanoparticles solutions in chapters 4 and 5.

## 4 MORPHOLOGICAL CHARACTERIZATION

---

### 4.1 ATOMIC FORCE MICROSCOPY (AFM)

Atomic force microscopy (AFM) is one of the most famous and widely used scanning probe microscopy (SPM) techniques developed to assess a wide variety of surface information on solid samples. As for all the SPM techniques it involve the use of a “probe” which interacts with the surface to be analyzed. By performing a raster scan with the probe over a certain area of the sample it is possible to build distribution a map of the probed characteristic in that area. In the specific case of the AFM, the probed characteristic is the mechanical tip-sample interaction, providing information over topography and viscoelastic properties of the sample’s surface, which are obtained by scanning the sample with a sharp (radius < 10 nm) conical tip mounted at the end of a flexible cantilever.

During the AFM measurements, the close proximity between the sample and the tip generates a large amount of forces, which can be both attractive and repulsive and that strongly depends on the tip-sample distance. In a first approximation it is possible to attribute the deflection of the cantilever to a combination of Van der Waals attractive forces and interatomic repulsion forces. Those two contributions have an extremely different dependence with the tip-sample distance and their combination can be described by using the Lennard-Jones potential model ( $V_{LJ}$ ):

$$V_{LJ}(r) = 4\varepsilon \left[ \left( \frac{\sigma}{r} \right)^{12} - \left( \frac{\sigma}{r} \right)^6 \right]$$

Where  $V_{LJ}$  = Lennard-Jones potential,  $\varepsilon$  = Minimum potential energy,  $\sigma$  = Minimum center-to-center distance and  $r$  = Distance.

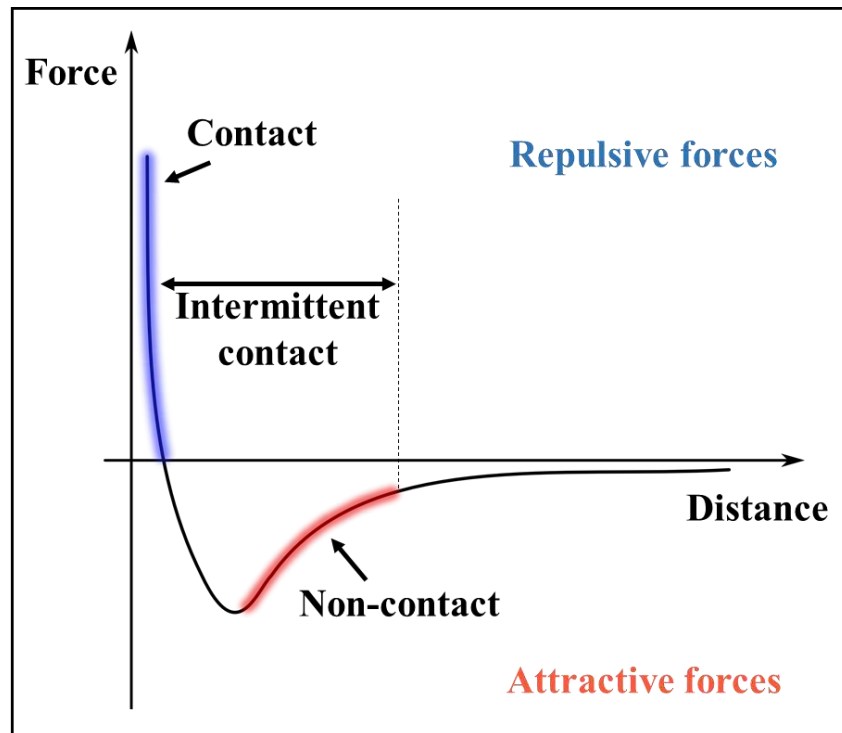


*Figure 3.5: Lennard-Jones potential model of interatomic forces vs. distance.*

AFM provides extremely high lateral ( $\leq 1$  nm) and vertical ( $\leq 0.1$  nm) resolutions, given by extremely short range of the forces involved and allows a non-invasive characterization of samples in air or at solid-liquid interfaces, regardless their composition (organic, inorganic, conductors, insulators etc.).

While scanning the sample, the tip precisely follows the surface topography with interaction forces of few piconewtons that cause the deflection of the cantilever. The movement of the tip following the sample's features, such as the roughness or the presence of nanostructured architectures, is read by using a laser beam that is focused on the reflecting backside of the cantilever and, finally collected by a position sensitive detector, as schematized in **Figure 3.6**.

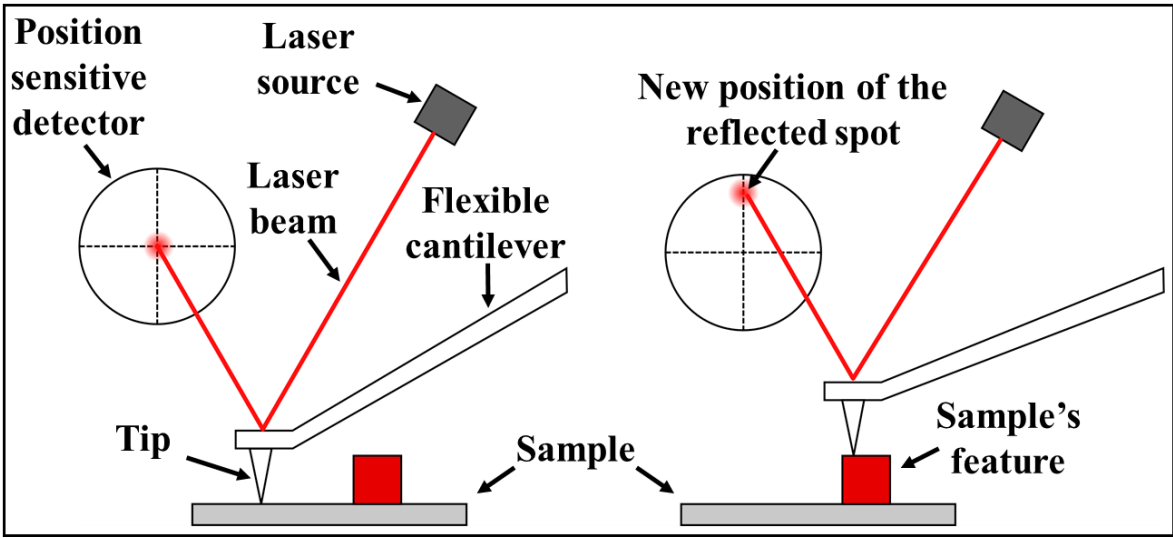


Figure 3.6: Schematic representation of the AFM setup.

The precisely controlled Z movements of the tip and the XY raster scans of the probed area are obtained by employing a scanner made out of five piezoelectric elements that work simultaneously. The scanner features 2 piezoelectric modules for the X movements, 2 for the Y movement and 1 for the Z movement of the tip, like shown in **Figure 3.7**.

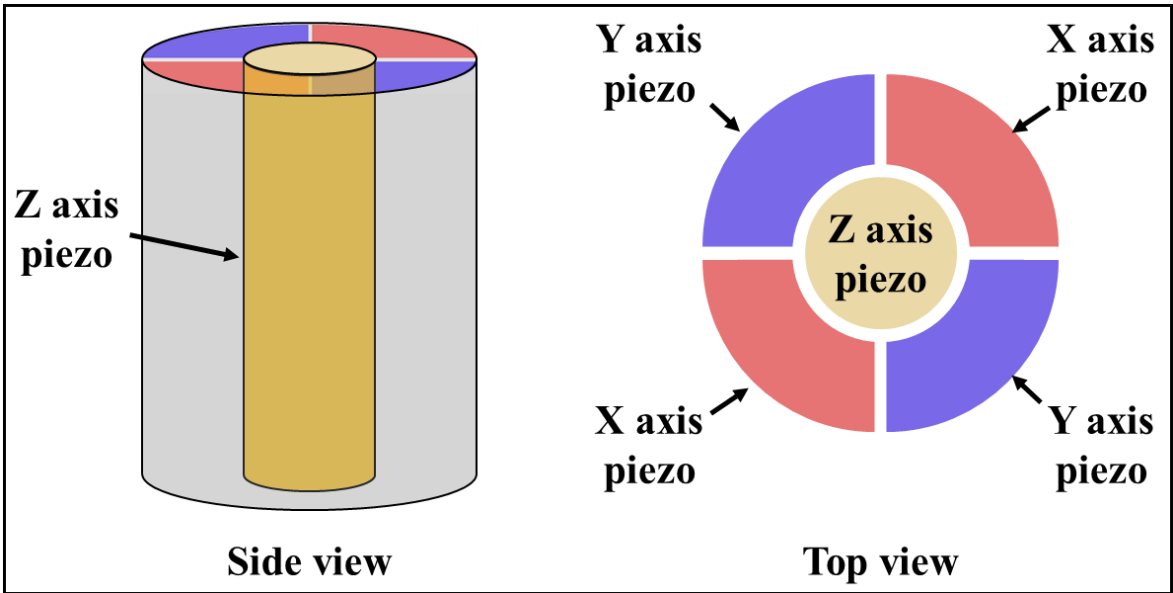


Figure 3.7: Schematic of a XYZ piezoelectric scanner tube.



The AFM topographic characterizations can be performed in three different regimes, highlighted in **Figure 3.5** in blue (contact regime), in red (non-contact regime) and with a double arrow (intermittent contact regime).

When operating in contact mode the tip is always in contact and therefore in a repulsion regime with the sample. This technique can be operated in two modes: constant height or constant force. In constant height mode, no feedback is applied and the topographic map is directly generated from the movement of the laser spot on the position sensitive detector. In constant force mode, the deflection of the cantilever is kept constant during the scan. This is obtained by using a feedback system: when the tip encounters a feature, either positive (e.g. an adsorbate) or negative (e.g. a hole) on the surface, the movement of the tip, that causes a displacement of the reflected beam on the photodetector, is translated from a feedback system acting on the Z piezoelectric. The Z piezoelectric is controlled to physically move the tip towards or away from the sample to remove the displacement, restoring the initial deflection of the tip. The topographic map is then generated by using the amplitude of the shift of the Z piezoelectric component used to keep the deflection constant. Both operating modes exhibit advantages and disadvantages and are commonly used for different kind of samples and experimental conditions: constant height mode provides a real image of the surfaces and, since it does not involve any feedback of Z movement, allows faster acquisition rates and higher resolutions. On the other hand, it does not allow any control over the applied forces on rough samples and can be employed only on atomically flat and ultra-clean surfaces. Constant force mode can be safely employed for rough samples but the resulting images are filtered from the feedback system and require slower scan rates. In both cases, the interaction forces between the tip and the sample depends of the spring constant of the employed cantilever and on the settings, but are usually kept between  $10^{-6}$  and  $10^{-9}$  N. Those forces are obviously very small but, when applied with a nanoscopic tip, the generated pressure can be sufficient to scratch and damage fragile samples, such as organic or biological thin films and nano-structures. To perform AFM characterizations of such delicate systems it is possible to operate AFM scans in non-contact regime, by keeping the tip far from the surface and probing the morphology with the long range attractive Van der Waals forces. This technique must be performed using stiff cantilevers to keep the distance constant but it provides a very low lateral resolution and is not commonly used.

A good compromise combining the advantages of both contact and non-contact operating modes relies in the use of the so-called “Tapping mode” or intermittent contact. This mode is operated with very short and stiff cantilevers connected to a supplementary piezoelectric component which makes the tip vibrate close to its resonance frequency, usually around 200 to 400 kHz. During this oscillation the tip experience both contact and non-contact regimes and the interaction with the sample’s surface can affect the amplitude and the frequency of the vibration. Since the best performances, in terms of resolution and accuracy, are achieved while operating at frequencies  $\sim 5\%$  below the resonance frequency peak of the tip, tapping mode is usually operated in constant frequency mode. This means that an external feedback control is used to move the tip towards or away from the surface when the frequency changes during the scan, as a consequence of the interaction between the tip and the sample’s features. Imaging in tapping mode obviously require lower scan rate, compared with contact mode, but provides high spatial resolution and extremely low damages to samples and tips during the scans, allowing to map high aspect ratio features, up to few  $\mu\text{m}$  in the Z direction.

Another advantage in using the tapping mode is given by the phase information. The phase map can be recorded simultaneously with the normal topographic map and probes the viscoelastic properties of the materials on the sample’s surface, providing useful information over the phase distribution and segregation of the different components. Such map are not affected by the topography of the surface and the contrast is given only by the shift in the phase of the cantilever’s vibration due to attractive or repulsive forces between the tip and the phase-segregated components on the surface. A comparison between topographic and phase AFM images can be found in **Figure 7.1** where few layer of graphene oxide, deposited on flat  $\text{SiO}_2$  exhibit great phase contrast with the exposed substrate.

Since all the topographic information given by the AFM are generated by purely mechanical interactions, this technique exhibit great versatility, allowing the characterization of different materials such as electrical conductors, semiconductors or insulators, regardless their composition.

AFM was employed in this thesis to assess information over the self-assembly of the supramolecular fibers in chapter 6 and to study topography and thickness of GO and L-rGO films in chapter 7.

All the reported AFM images were recorded in tapping mode using Bruker “Multimode V” or “Dimension 3100” microscopes equipped with Bruker “TESPA-V2” tips (nominal spring constant = 37 N/m; nominal tip radius = 7 nm)

#### 4.1.1 Conducting atomic force microscopy (C-AFM)

Conducting atomic force microscopy (C-AFM) is a special application mode of AFM, used to simultaneously acquire electrical conductance maps together with the common topographic AFM maps. The conductance maps are obtained by applying a bias between the sample and a metal coated AFM tip and by continuously measuring the electrical current flowing through such junction during AFM scans in contact mode. Since the measured electrical current through the tip-sample junction is strongly affected by the contact resistance between the tip and the sample, these measurements are always performed in constant force contact mode, to keep the applied pressure and therefore the contact resistance, constant over the whole scanned area.

The tips employed for such kind of measurements feature the same mechanical properties as the ones used for regular contact mode AFM (very long cantilevers with small spring constants) but are made conductive by the presence of a continuous 20 nm thick layer of Pt/Ir, deposited on the whole tip surface by thermal evaporation. A special electrical insulating tip holder, usually made of quartz, enables the electrical connection between the tip and the instrument controller. The circuit is then closed by mounting the conducting sample on a metal disc using conductive adhesives (e.g. silver paste), and by connecting it to the source of the controller.

C-AFM was employed, in this thesis, to perform the electrical characterization at the micro-scale of conducting reduced graphene oxide paths in an electrical insulating graphene oxide matrix deposited on insulating SiO<sub>2</sub> substrates (an example of such current maps can be found in **Figure 7.12**). Under this conditions, it is not possible to perform electrical measurements in a vertical junction configuration, as mentioned above, and it is necessary to directly connect the conductive area to be characterized with the metallic sample holder by using electrical conducting wires, as schematized in **Figure 3.8**.

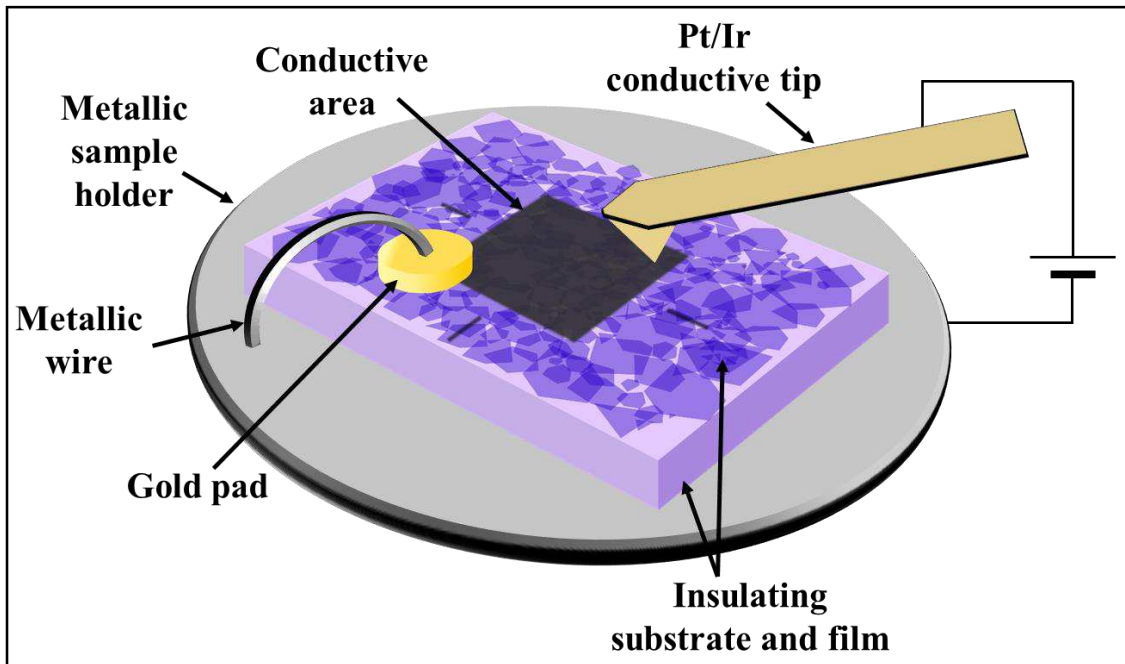


*Figure 3.8: Experimental configuration employed for the C-AFM characterization of L-rGO in chapter 7.*

## 4.2 SCANNING ELECTRON MICROSCOPY (SEM)

Scanning electron microscopy (SEM) is a non-destructive microscopy technique widely used to perform morphological characterizations on virtually any kind of sample: from inorganic materials to biological tissues, with high lateral resolution (from  $\sim 1\text{-}2\text{ nm}$  to micrometer scale, depending on the samples and on the operative conditions). The high resolution of the SEM, compared to optical microscopy techniques, is given by the use of a high energy electron beam which can be focused beyond the diffraction limits of light. The electron beam is generated by a field emission electron gun which consist in a sharp single crystal of tungsten on which is applied a negative bias of several kV relative to a nearby acceleration anode grid. The electron beam is then collimated using electromagnetic condenser lenses. The collimated beam passes through an adjustable slit that determines the nominal spot size and is then focused by electromagnetic focusing lenses. A series of deflection coils is employed to scan the sample's surface in a raster pattern (**Figure 3.9**).

The microscope is, usually, divided into two sections: the tube, where the electron beam is generated and the sample chamber, where the sample is placed. While the tube is always

kept in ultra-high vacuum ( $P \sim 10^{-7}$  Pa), the pressure inside the chamber can be modulated depending on the sample, from high vacuum ( $P \sim 10^{-4}$  Pa) up to atmospheric pressure, by filling the chamber with water vapor. Such operating mode is called “environmental SEM” (ESEM) and is particularly useful for imaging of electrical insulating or biological samples.

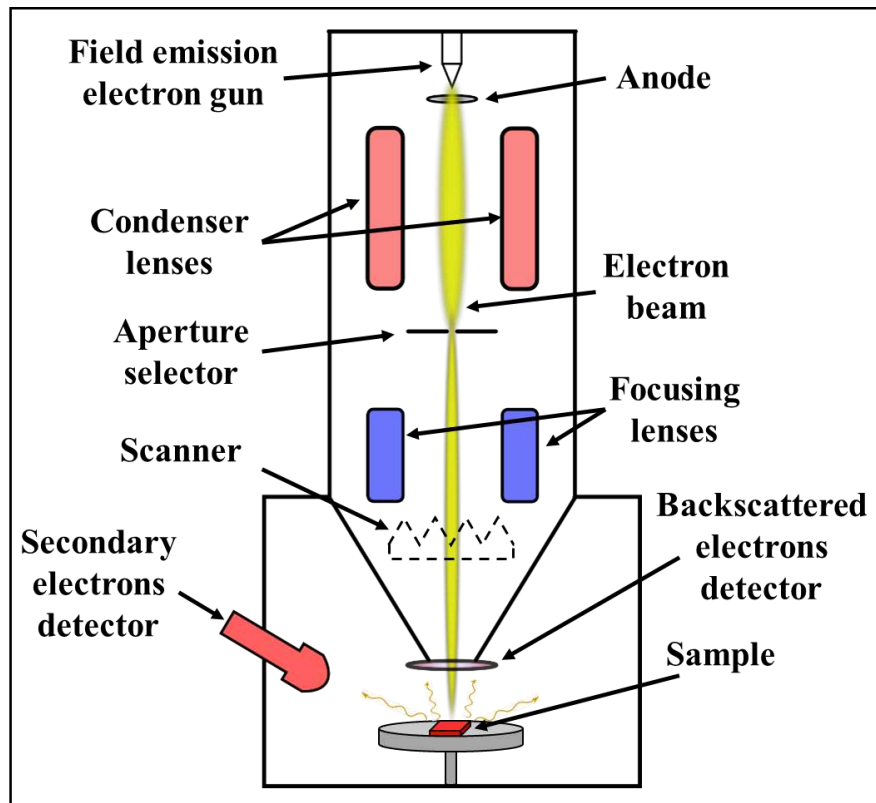


*Figure 3.9: Structure of a scanning electron microscope.*

When the electrons reach the sample's surface, they can interact with it in two ways depending on the acceleration energy of the beam and on the material of which the sample is made. If the energy of the beam is small (e.g. the electrons move slowly) and the sample is made of heavy elements (like transition metals), the primary electrons coming from the beam will undergo elastic scattering close to the surface. The backscattered electrons can be collected using a dedicated detector placed normally to the surface and, since the amount of backscattered electrons at each spot of the raster pattern depends on the morphology of the surface and on its composition, it is possible to employ such electrons to generate an image of the scanned area.

When higher beam energies are used, the electrons that reach the surface are too fast to interact elastically with it and lose part of their energy by extracting secondary electrons from the atoms they come in contact with. Such extracted electrons are called “Secondary” and possess lower energies compared to the primary and the backscattered ones. The secondary electrons that escape from the sample’s surface can be collected with a dedicated detector to generate a map of the scanned area. In both operative modes the obtained images consist in false color maps where the contrast is given by the morphology of the surface and on its composition (brighter areas corresponds to higher amounts of backscattered or extracted secondary electrons).

SEM was employed in this thesis to characterize the morphology of the 2D and 3D AuNPs networks, discussed in chapters 4 and 5, and to study the supramolecular PDI-4T fibrillary bundles reported in chapter 6. All the SEM images reported in this manuscript were recorded using a FEI Quanta 250 FEG microscope in high vacuum. The used spot size is 3 nm while the acceleration voltages are: 20 kV for the AuNPs systems in chapters 4-5 and 5kV for the organic PDI-4T fibers in chapter 6.

## 5 COMPOSITIONAL CHARACTERIZATION

---

### 5.1 X-RAY PHOTOELECTRON SPECTROSCOPY (XPS)

X-Ray photoelectron spectroscopy (XPS) is a compositional characterization technique used to gain insight into the superficial (few nanometers penetration sampling) chemical composition of solid samples, either in the form of thin films or powders. This technique is based on the use of a soft X-ray beam, usually monochromatic Al K $\alpha$  ( $E = 1486$  eV), to excite and extract the core electrons from the atoms on the sample's surface. The kinetic energy of the extracted electrons will be equal to the difference between the energy of the incident X photons and the binding energy of the extracted electrons. Since the binding energies of such electrons are different for the different elements, by scanning the kinetic energies of the extracted electrons reaching the detector, it is possible to obtain a survey of the surface composition of the probed area.

The characteristic binding energy of the core electrons of each element could be shifted by the environment surrounding the atoms. For instance, if a carbon atom is covalently bonded to oxygen, like in the case of a carboxylic acid, its core electrons (C1s) will be partially attracted by the oxygen atoms and will exhibit a slightly higher binding energy, compared for instance, to the C1s electrons extracted from alkyl chains. An example of this effect can be found by comparing GO and rGO XPS spectra **Figure 7.6** or oxidized PDI-4T in **Figure 6.7**. By combining the information obtained by the elemental survey with the binding energy shifts, it is then possible to achieve useful information on the oxidation states or, more generally on the chemical environment of the elements on the sample's surfaces.

From the above reported discussions, it looks evident that the working principle of the XPS is based on the precise measurement of the kinetic energy of the extracted electrons. This means that the extracted electrons should reach the energy analyzer without any energy loss given by possible interactions with external elements, such as air or other gaseous compounds. For such reason it is crucial to constantly keep the analysis chamber under ultra-high vacuum ( $\sim 10^{-9}$  mBar).



In the instrument used for the XPS measurements reported in this thesis (**Figure 3.10**) the high vacuum is ensured by the use of two independent chambers connected with two turbomolecular pumps, for the insertion and analysis of the samples. The instrument is also equipped with a flood gun which generates a low energy unfocused electron beam over the sample's surface to discharge it, allowing to perform XPS analysis on electrical insulating samples.

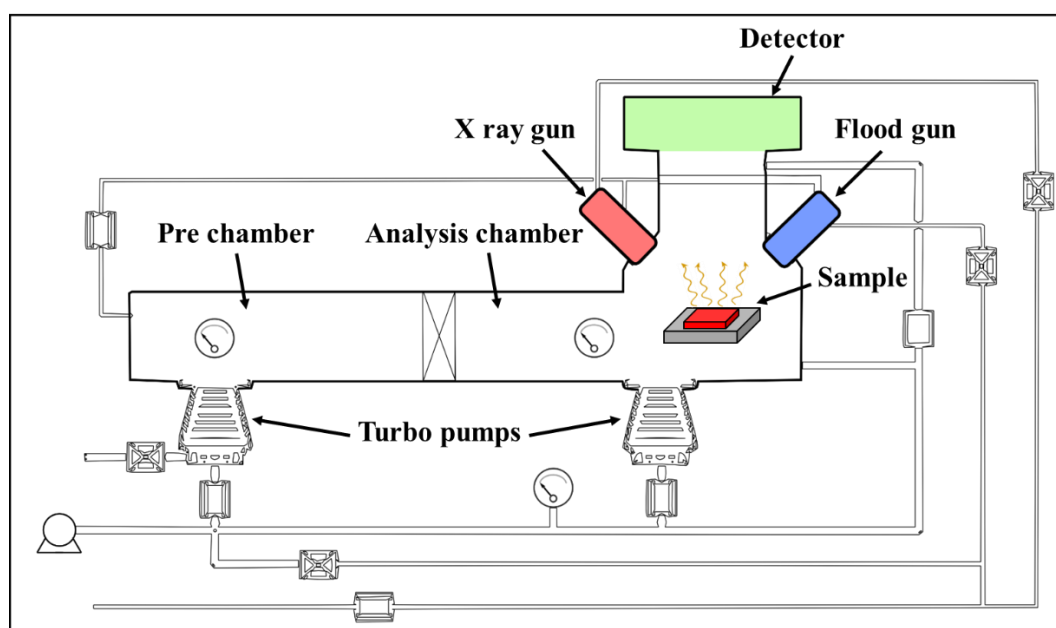


**Figure 3.10:** Structure of the Thermo Scientific "K-Alpha" X-Ray spectrometer used to record the XPS spectra reported in this thesis.

XPS analysis were performed in this thesis to check the chemical state of the thiophene core of PDI-4T upon exposure to the light irradiation used to trigger the formation of the supramolecular aggregates reported in chapter 6 and to quantify the effect of the laser-induced reduction of graphene oxide using high energy IR lasers, in chapter 7.

All the XPS spectra reported in this thesis were recorded using a Thermo Scientific "K-Alpha" X-Ray spectrometer, at a pressure of  $P \sim 10^{-9}$  mBar, using a 400  $\mu\text{m}$  wide elliptical beam spot and the flood gun active.

## 6 ELECTRICAL CHARACTERIZATION

---

This manuscript is made by four experimental chapters reporting on as many projects. Out of them, three of such projects reports on the development and fabrication of new sensing devices featuring electrical resistive readout. For such reason, the electrical characterization played the most crucial role and consist into the biggest amount of data collected for the realization of this work.

As aforementioned, most of the devices fabricated among the different projects feature an electrical resistive type readout, meaning that the interaction between the samples and the analytes (moisture or ozone) can reversibly modify the measured electrical resistance of the systems.

The electrical resistance of a material is defined as the quantitative measure of the difficulty to pass an electric current through that material. In the international system of units it is measured in Ohms ( $\Omega$ ) and, for electrical conductive material (e.g. a metal), its value is given by the Ohm law:

$$R = \frac{V}{I}$$

Where  $R$  = Electrical resistance,  $V$  = Applied bias and  $I$  = Measured current.

For a given material the measured resistance is also strongly influenced by its geometrical characteristics according to the equation:

$$R = \rho \frac{l}{A}$$

Where  $l$  = Length of the conductor,  $A$  = Section of the conductor and  $\rho$  = Resistivity of the material.

In certain systems the electrical resistance can also be affected by the environmental conditions. Depending on the specific cases, external temperature or specific gaseous compound in the atmosphere can dramatically affect such characteristic, for instance in the 3D AuNPs networks presented in chapter 5 the measured resistance can be modulated with the environmental humidity and decrease linearly with the temperature, while for conductors, such as the L-rGO presented in chapter 7, it can be increased by higher temperatures and reduced upon exposure to ozone.

Organic materials, such as the PDI-4T supramolecular nanofibers presented in chapter 6, usually show semiconducting behavior and their resistance does not follow Ohm's law, exhibiting a non-linear dependence on the applied bias. In such materials, the current, and therefore the resistance, are also strongly affected by external electric fields that can be used to rapidly open and close the circuits, creating the so-called field effect transistors (FET) and the, more complicated, logic gates.

As evident from what mentioned above, the systems explored in this thesis are dramatically different between each other in terms of conduction mechanism, electrical behavior and properties and it wouldn't be possible, nor useful, to explain in this section the theoretical background for each of them. For this reason, more details on this topic and general discussion on the transduction mechanisms are provided in the "Results and discussions" section of each chapter.

All the electrical data recorded for the experimental chapters of this thesis were acquired in direct current using a Keithley 2636B source meter connected to a custom made printed circuit board (PCB).

The use of PCB instead of a regular probe station was preferred because of the necessity to measure the electrical performances of the sensing devices in a small and sealed chamber kept under controlled atmosphere.

For such characterizations the use of a dedicated glovebox, big enough to fit a probe station inside, would be disadvantageous because of the huge latency upon atmospheric changes

given by the high internal volume of the box which would require long modification times, implying a poor control over the environment

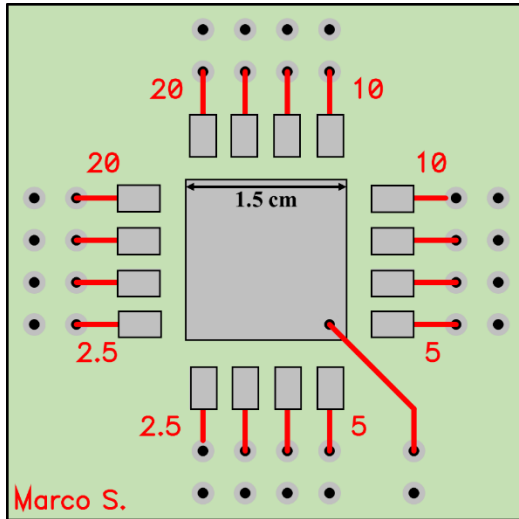


**Figure 3.11:** Layout of the shadow mask drawn to build the measurement board.

The employed measurement board was built by transferring the pattern in **Figure 3.11** onto a commercial pre-sensitized board (35  $\mu\text{m}$  thick Cu film on 1.6 mm thick epoxy glass fabric laminate) with photolithography, by using a shadow mask. After exposure with white light for 7 min, the board was developed by dipping it in a development agent for 4 min. After development the board was annealed at 120° C for 2 min to harden the unexposed photoresist before the wet etching step.

The exposed Cu was etched by dipping the board in a  $\text{FeCl}_3$  30% etching solution for 5 min. After this step the board was rinsed in water and acetone to remove all the traces of etching agent and unexposed photoresist. The board was then completed by drilling holes and welding copper wires to electrically connect it to the source meter. The samples were mounted on the central square of the board by using double side conductive copper tape and connected to the pads by cold welding with In wires.

This setup was used for the characterization of all the electrical sensing devices reported in this thesis and was modified with the addition of a 20 W resistive heater and a temperature sensor, on the back side, for the characterization L-rGO based ozone sensors reported in chapter 7, because of the necessity to heat up the sample up to 70° C to trigger the ozone desorption.

## 7 REFERENCES

---

- 1 Grzelczak, M., Perez-Juste, J., Mulvaney, P. & Liz-Marzan, L. M. Shape control in gold nanoparticle synthesis. *Chem Soc Rev* **37**, 1783-1791, (2008).
- 2 Brust, M., Walker, M., Bethell, D., Schiffrin, D. J. & Whyman, R. Synthesis of Thiol-Derivatized Gold Nanoparticles in a 2-Phase Liquid-Liquid System. *J Chem Soc Chem Comm*, 801-802, (1994).
- 3 Turkevich, J., Stevenson, P. C. & Hillier, J. The Formation of colloidal gold. *J Phys Chem* **57**, 670-673, (1953).
- 4 Ojea-Jimenez, I., Romero, F. M., Bastus, N. G. & Puentes, V. Small Gold Nanoparticles Synthesized with Sodium Citrate and Heavy Water: Insights into the Reaction Mechanism. *J Phys Chem C* **114**, 1800-1804, (2010).
- 5 Al-Johani, H. *et al.* The structure and binding mode of citrate in the stabilization of gold nanoparticles. *Nat Chem* **advance online publication**, (2017).
- 6 Love, J. C., Estroff, L. A., Kriebel, J. K., Nuzzo, R. G. & Whitesides, G. M. Self-assembled monolayers of thiolates on metals as a form of nanotechnology. *Chem Rev* **105**, 1103-1169, (2005).
- 7 Liu, X., Atwater, M., Wang, J. & Huo, Q. Extinction coefficient of gold nanoparticles with different sizes and different capping ligands. *Colloids Surf B Biointerfaces* **58**, 3-7, (2007).
- 8 Dubois, L. H. & Nuzzo, R. G. Synthesis, Structure, and Properties of Model Organic-Surfaces. *Annu Rev Phys Chem* **43**, 437-463, (1992).
- 9 Hostetler, M. J. *et al.* Alkanethiolate gold cluster molecules with core diameters from 1.5 to 5.2 nm: Core and monolayer properties as a function of core size. *Langmuir* **14**, 17-30, (1998).

# Chapter 4

## From 0D to dynamic 2D materials – AuNPs plasmonic sensors

### 1 INTRODUCTION

---

This first experimental chapter reports on the use of 2-dimensional gold nanoparticles arrays as colorimetric humidity sensors. As thoroughly explained in chapter 2, such kind of devices rely on the unique optical properties of metallic nano-objects which exhibit localized surface plasmon resonance (LSPR) and undergo dramatic changes in the optical extinction wavelength upon modification of the media refractive index or of their aggregation state.<sup>1</sup> Metal NPs-based colorimetric sensors are usually employed in solutions to gain qualitative insight into the composition of a solution by detecting the presence of specific analytes. The presence of the target analyte in solution can trigger the aggregation of the receptors-functionalized metal NPs, causing the coupling of their LSPR and the subsequent macroscopic color change.<sup>2,3</sup> Such process is usually not reversible and leads to the formation of random NPs aggregates. The possibility to gain control over the NPs superstructure and finely tune the inter-particles distance could pave the way towards the development of plasmonic materials exhibiting interesting and unique collective properties.<sup>4-7</sup> On this view, in 2007 Tao et Al. reported on the realization of tuneable plasmonic lattices of silver nanocrystals on the water's surface. By changing the surface pressure in a

Langmuir-Blodgett setup, the authors showed that they could control the spacing and therefore the optical characteristics of such system.<sup>8</sup> However, the realization of tuneable and dynamic plasmonic structures, with stable and predictable optical properties in solid films, still remains elusive.<sup>9</sup> Here, we demonstrate how gold NPs (AuNPs), cross-linked with a self-assembled monolayer of di-thiolated molecules,<sup>10,11</sup> can be exploited to generate thin films of robust dynamic plasmonic superlattices featuring precisely tuneable optical properties. The solid-state 2D lattices of AuNPs were cross-linked into ordered hexagonal networks by using flexible and hygroscopic Poly ethylene glycol di-thiol (SH-PEG-SH) chains ( $M_n = 1$  kDa). PEG backbone is able to reversibly absorb water molecules from the atmosphere<sup>12</sup> and, upon modification of the environmental humidity, it allows to swell or shrink the 2D networks, therefore modifying the inter-particles distances. When fully elongated, the employed ligand exhibit a nominal chain length of  $\sim 8$  nm, allowing the AuNPs to move within or beyond the threshold distance for the inter-particles coupling of the surface plasmons. Such effect can be obtained just by the absorption and desorption of water molecules, triggered by changing the environmental humidity.<sup>13</sup> The change of humidity cause an overall shift of the SPR band as big as 35 nm, corresponding to a macroscopic color change from blue to red in the range between 0% and 100% relative humidity (RH), also accompanied by a change in the SPR band broadening.

## 2 EXPERIMENTAL

---

### 2.1 MATERIALS

Gold nanoparticles, featuring  $8.6 \pm 1.4$  nm diameter, were synthesized in Milli-Q water by using the Turkevitch method described in chapter 3. Towards this end, commercial chloroauric acid ( $\text{HAuCl}_4 \cdot 3\text{H}_2\text{O}$ ) and sodium citrate ( $\text{HOC}(\text{COONa})(\text{CH}_2\text{COONa})_2 \cdot 2\text{H}_2\text{O}$ ) purchased from Sigma-Aldrich and used as received. The functionalization of the AuNPs to



form 2D networks was obtained by combining them with commercial polyethylene glycol dithiol (SH-PEG-SH),  $M_n = 1\text{kDa}$ , purchased from Sigma-Aldrich and used as received.

## 2.2 SAMPLE PREPARATION

2D AuNPs networks were assembled directly on the substrates, as an effect of the solvent evaporation during the drop-casting of water solutions containing AuNPs and PEG ligands in the appropriate ratio. Different substrates were used for the different characterizations: quartz for the optical measurements, conducting silicon ([100]  $p^{++}$  doping) for SEM and AFM images, insulating 100 nm thick silicon oxide on doped silicon ( $\text{SiO}_2/\text{Si } p^{++}$ ) with pre-patterned gold electrodes (channel length = 100 nm, contact area =  $5\text{ }\mu\text{m}^2$ ) for the two-terminal electrical characterizations. Prior the deposition all the substrates were washed by sonication in acetone (20 minutes) and isopropanol (20 minutes) before treatment in a UV-ozone cleaner (20 minutes) to increase the surface's wettability to water. The UV-Ozone cleaning was found to be crucial for the realization of the 2D networks which cannot be obtained on hydrophobic substrates. After complete evaporation of the water, the samples were intensively rinsed in DI water to remove the sodium citrate and the excess of gold nanoparticles. The rinsing process is invasive enough to remove all the AuNPs which are not connected to the main network, including all the particles which haven't react with the PEG and the ones in which the folding of the (back-folded) PEG chain made both thiol groups react within the same particle.

## 2.3 OPTICAL CHARACTERIZATION

The optical characterization is the main part of this chapter and in this project it represents an extremely powerful tool allowing to track changes in the inter-particles distance and in 2D assembly with sub-nanometer resolution. In particular, thanks to the special nature of the system, it was possible to translate sub-nanometer changes of inter-particles distance into

macroscopic changes in the sample's color and therefore in the UV-Vis absorbance spectra, by using the plasmonic properties of the AuNPs as extremely sensitive probes.

The UV-Vis absorbance spectra were recorded with a Jasco V670 spectrophotometer, equipped with a Peltier stage and internal thermocouples to gain control over the temperature of the samples during the measurements. UV-Vis extinction spectra at different humidity conditions were recorded by placing the quartz substrates, covered by the 2D AuNPs networks, inside quartz cuvettes (optical path = 1 cm), sealed in a nitrogen-filled glovebox (as “zero” humidity), in air (changing between 25 and 40%) or in presence of 1 ml of saturated salt solution, which gives precisely controlled humidity by using different salts and temperatures (**Figure 4.1**).

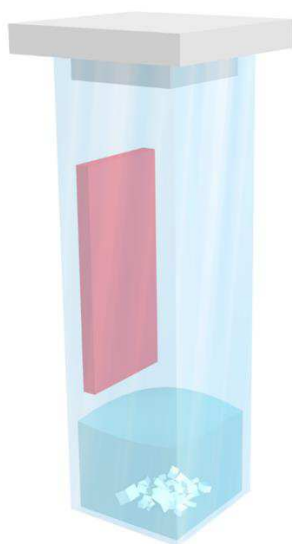


**Figure 4.1:** Sketch of the setup used to record UV-Vis spectra at different humidity conditions.

Employed salt	Relative humidity (20°C)
Lithium chloride (LiCl)	11.3 %
Magnesium chloride (MgCl <sub>2</sub> )	32.6 %
Sodium chloride (NaCl)	75.3 %
Potassium chloride (KCl)	84.3 %
Potassium sulfate (K <sub>2</sub> SO <sub>4</sub> )	97.3 %

**Table 4.1:** List of the saturated salt solutions used for the experiments and their given equilibrium relative humidity.

The presence of a salt at saturation concentration in water solution, can dramatically affect several physical properties of the solution, including the vapor pressure. When placed in a sealed environment, saturated salt solutions tend to establish an equilibrium between the evaporated (e.g. the humidity) and the condensed water. The equilibrium point and, as a consequence the relative humidity inside the chamber, depends on the nature of the employed salt and on the temperature but is not affected by the volume of the solution.<sup>14</sup> By

choosing properly the salts to be used, it was possible to explore a wide range of relative humidity, as shown in **Table 4.1**. After the addition of each saturated solution, the cuvette was sealed and kept at 20°C for 20 minutes to reach the equilibrium point. After each measurement the cuvette was emptied from the solution and rinsed with Milli-Q water several times to remove any trace of the salt, without moving or wetting the sample, before adding the new salt solutions. The last points, labelled as “water” were recorded by direct immersion of the samples in Milli-Q water, by filling completely the cuvette.

### 3 RESULTS AND DISCUSSIONS

---

Water-soluble gold nanoparticles (AuNPs) were synthesized with the Turkevich method,<sup>15</sup> as explained in detail in chapter 3. The cross-link of the AuNPs into 2D network was performed directly in the growth solution of the AuNPs, without any further purification or separation, just by addition of water solutions containing controlled amounts of commercial SH-PEG-SH. The correct stoichiometric ratio to be used to obtain the desired packing was initially roughly estimated by geometrical considerations, as explained in details in the methods section in chapter 3, and then optimized experimentally to gain full control over the system.

Upon addition of the ligands, the solution retains its red color given by the LSPR of AuNPs but the characteristic UV-Vis extinction band undergoes a slight red shift from 519 to 522 nm (**Figure 4.2**), because of the different refractive index of the media in close proximity to the particle's surface, meaning that the functionalization is taking place and that sodium citrate shell around the particles

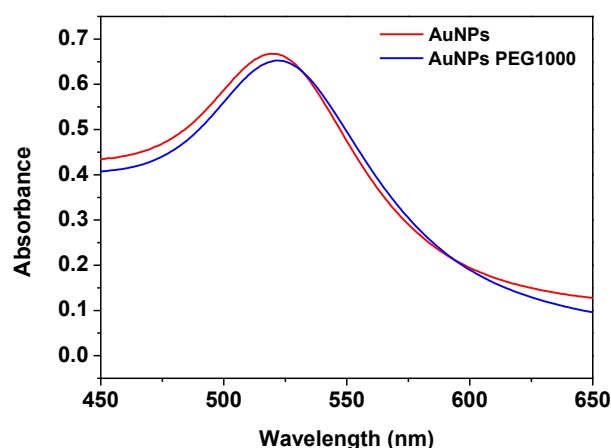


*Figure 4.2: UV-Vis extinction spectra of AuNPs solution before and after reaction with di-thiolated PEG linkers.*

has been replaced by the thiolated ligands.<sup>1</sup>

Deposition of the solution containing the AuNPs/PEG networks by drop casting on hydrophilic substrates, such as quartz, glass or silicon (freshly ozone cleaned), results into large area monolayers of 2D networks exhibiting high degree of order and a tight hexagonal packing, as shown in **Figure 4.3**.

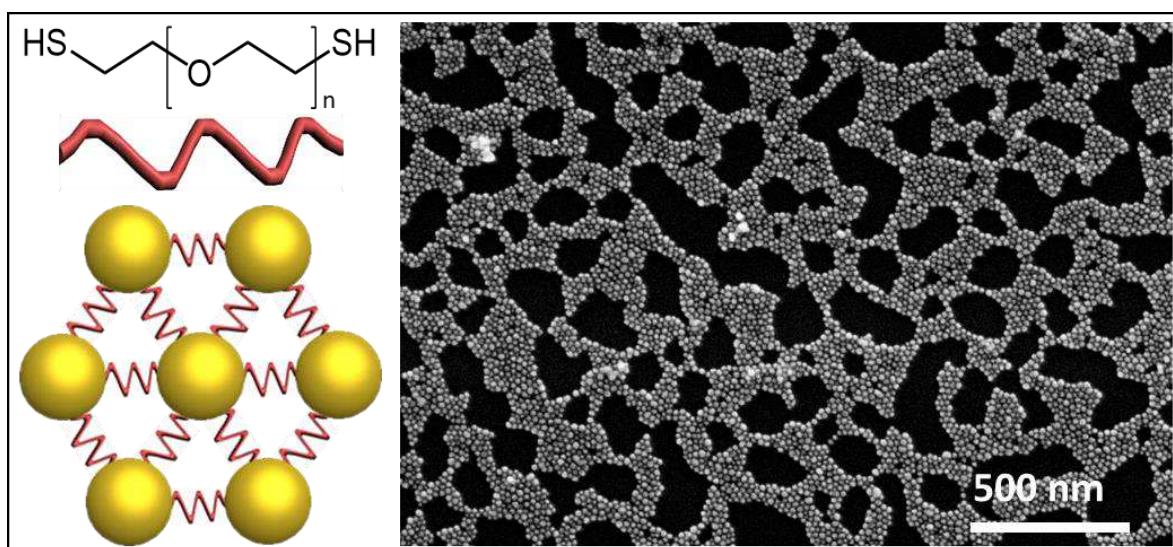


**Figure 4.3:** Schematic of AuNPs di-thiolated PEG 2D networks and SEM image of drop-cast AuNPs/SH-PEG-SH solution on Si substrate. The deposition results into robust and ordered 2D networks of cross-linked AuNPs with tight hexagonal packing.

SEM investigations, like the one displayed in **Figure 4.3**, revealed that the AuNPs/PEG networks are arranged as a single layer of interconnected domains made by several hundreds of nanoparticles each, covering uniformly the whole centimeter-scale substrates. Such domains are separated between each other by “holes” e.g. uncovered areas of exposed substrate featuring a width of few hundred of nanometers.

By depositing the 2D AuNPs networks onto  $\text{SiO}_2$  substrates, pre-patterned with extremely short channel length (channel length = 100 nm) gold electrodes, it was possible to measure the electrical properties of the single AuNPs closely-packed domains with a two terminals geometry, as showed in **Figure 4.4**.

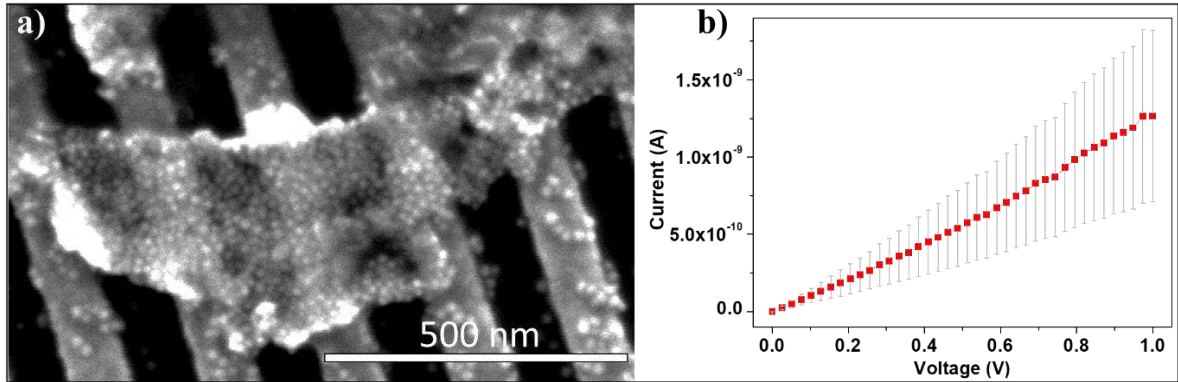


**Figure 4.4:** Electrical characterization of AuNPs 2D networks. a) SEM image of a single domain bridging the gold electrodes. b) I-V characteristics recorded in a two-terminal device configuration.

Electrical characterization of such devices employing short 100 nm channels, has shown an average resistance of 772 M $\Omega$ , indicating an extremely short percolative paths for the charge carriers, due to the insulating nature of PEG chains and to the large inter-particles distances within the network. This result is extremely important to demonstrate that the surface of the AuNPs has been functionalized by the organic linkers and that such functionalization can prevent any metal-metal contact between the particles.

The choice of using PEG chains as linkers to bridge the particles has a strategic reason: these chains exhibit high flexibility and tendency to absorb water molecules from the atmosphere.<sup>12,16</sup> As a result, upon increasing the humidity in the atmosphere, the water molecules can be absorbed by the PEG chains connecting the AuNPs. Absorption of water molecules causes a swelling of the PEG chains, yielding an increase of the inter-particles distance and therefore a smaller diffusion length for the electrical charge carriers.

The increased inter-particles distance can dramatically affect the electrical resistance of the system. Such statement can be confirmed by performing electrical characterizations in which the current flowing through the network is measured as a function of the environmental humidity, while applying a constant bias (source-drain bias applied for such measurements = 1 V) (**Figure 4.5**)

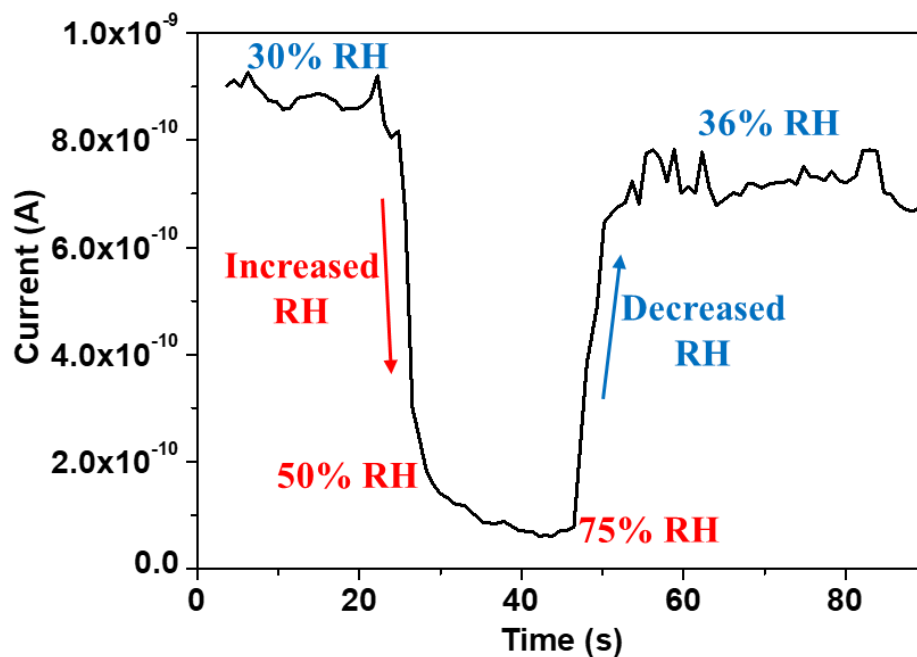


**Figure 4.5:** Effect of environmental humidity on the electrical characteristics of single domains of 2D AuNPs networks (constant bias applied = 1 V)

As displayed in **Figure 4.5**, the swelling of the networks, induced by the amount of absorbed water molecules, has a dramatic impact on the electrical characteristics of the system, causing an important, yet reversible, drop of the measured current,

From the optical point of view, the films of 2D AuNPs networks exhibit different optical properties compared with the starting AuNPs in solutions, featuring a broad UV-vis extinction band at  $\lambda \sim 595$  nm, ascribed to the collective plasmonic resonance of the 2D assembly of closely packed particles.<sup>8,13</sup> Upon increase of the environmental humidity, such collective SPR band undergoes a strong blue-shift, reaching a  $\lambda \sim 560$  nm, and a sharpening of the peak. This shift of the SPR band causes a macroscopic change of color from blue to red which is easily visible by naked eye, similar to what displayed in the optical pictures in **Figure 4.6a,b**.

As already discussed for the electrical characteristics, such modification of the optical properties is fully reversible and can be ascribed to an increased inter-particles distance within the network. The swelling of the system, caused by the absorption of water molecules, is enough to move the AuNPs beyond the range of surface plasmons coupling, making them behave as insulated objects, when placed in high humidity environments. By increasing the



environmental humidity surrounding the AuNPs networks, the limit of the subsequent blue-shift would correspond to a configuration in which all the particles are completely insulated and decoupled between each other. In such configuration, the films would exhibit a fully localized SPR, featuring a sharp band at  $\lambda = 535$  nm, this limit is reported as a red dashed line in **Figure 4.6c**

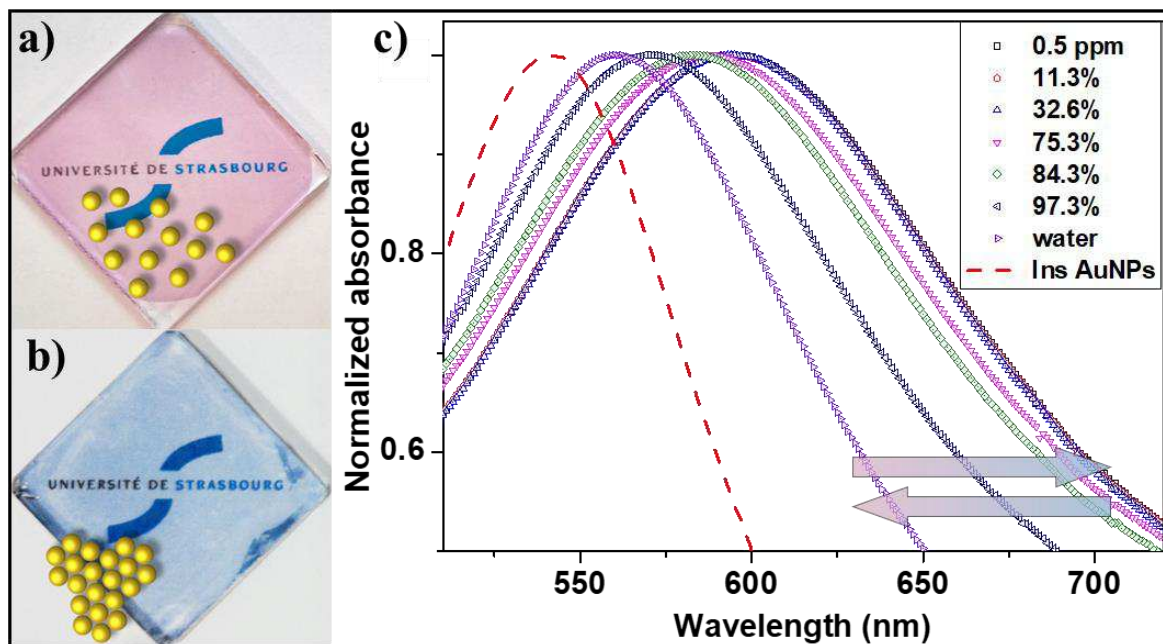


**Figure 4.6:** Optical properties of 2D AuNPs networks. The increased environmental humidity causes a visible and reversible change of color from blue (b) towards red (a). This change of color is given by a gradual shift and sharpening of the UV-Vis extinction band which moves gradually from 595 to 560 nm, towards a state of completely insulated AuNPs (c).

The reference sample portrayed in the optical picture in **Figure 4.6a** and employed as “limit case” (dashed red line in **Figure 4.6c**), was prepared by using the same AuNPs solutions and the same di-thiolated PEG linkers. Indeed, by using on purpose a wrong stoichiometric ratio between AuNPs and PEG linkers, it was possible to deposit, by drop-casting, highly disordered monolayers of AuNPs/PEG featuring a great inter-particles distance, as displayed in the SEM picture in **Figure 4.7**.



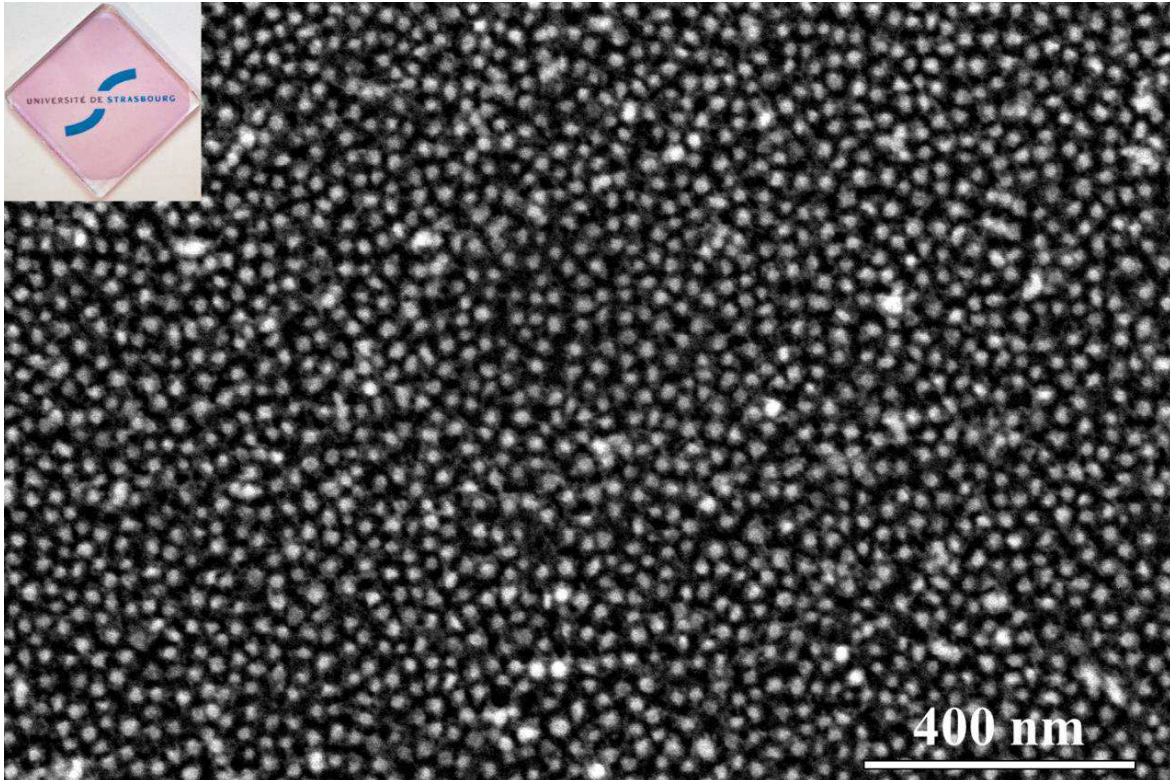


**Figure 4.7:** SEM image of highly disordered AuNPs/PEG monolayer on Si substrate. Inset showing an optical picture of a similar film on quartz substrate.

As already mentioned before, the disordered AuNPs/PEG films reported in **Figure 4.7** are obtained from the same AuNPs and PEG linkers employed for the ordered 2D networks, therefore the refractive index and the extinction of the nanoparticles must be the same in the two cases, meaning that the dramatically different optical characteristics between such films can be just ascribed to the different packing of the particles.

As aforementioned, absorption of water molecules from the atmosphere can modify such arrangement by changing the inter-particles distance. By using the optical characteristic as a macroscopic probe to measure such sub-nanometer changes of arrangement, it was possible to demonstrate that the moisture absorption and the subsequent shift of the SPR band are fully reversible and depend exponentially by the environmental humidity surrounding the films, as displayed in **Figure 4.7**.

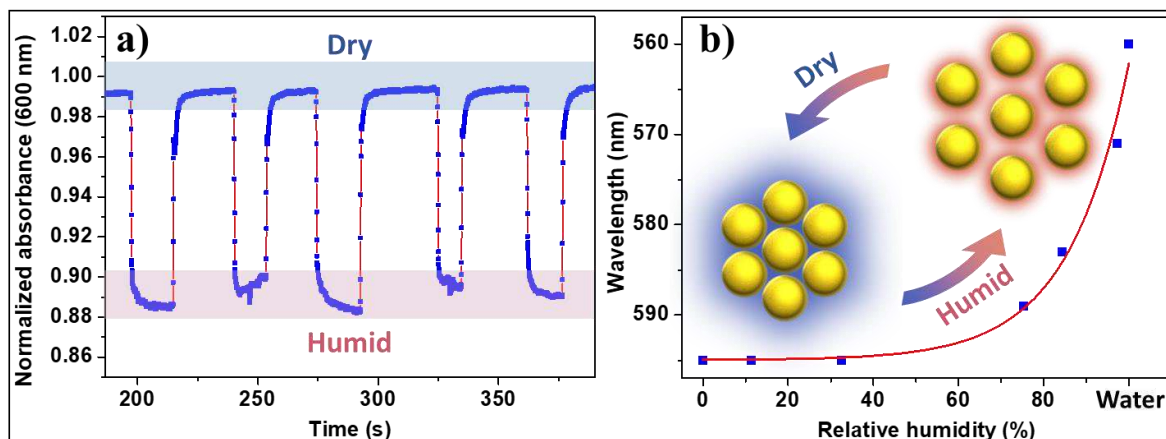


**Figure 4.8:** Increased environmental humidity from dry ( $RH \sim 32\%$ ) to humid ( $RH \sim 75\%$ ) results in a sharp, fast and fully reversible blue shift in the UV-Vis absorbance peak. By monitoring the UV-Vis absorbance at a fixed wavelength of 600 nm over time, while sending pulses of humid air on the sample's surface, it is possible to record the blue shift as a decrease of the normalized extinction measured at that wavelength (a). On the other hand, by recording the whole spectra at different RH it is possible to plot the evolution of the peak wavelength versus the environmental RH, finding an extremely precise exponential dependency given by the contemporary contribution of changes in refractive index and inter-particles distance (b).

Moreover, by sending short pulses of humid air on the sample's surface while measuring the optical response, it was possible to demonstrate that the absorption/desorption processes are extremely fast, featuring a response speed of  $\sim 200$  ms. Moreover, such process is reproducible over undefined amount of cycles without suffering any hysteresis effect neither stress nor modification of the optical characteristics, as displayed in **Figure 4.9**.

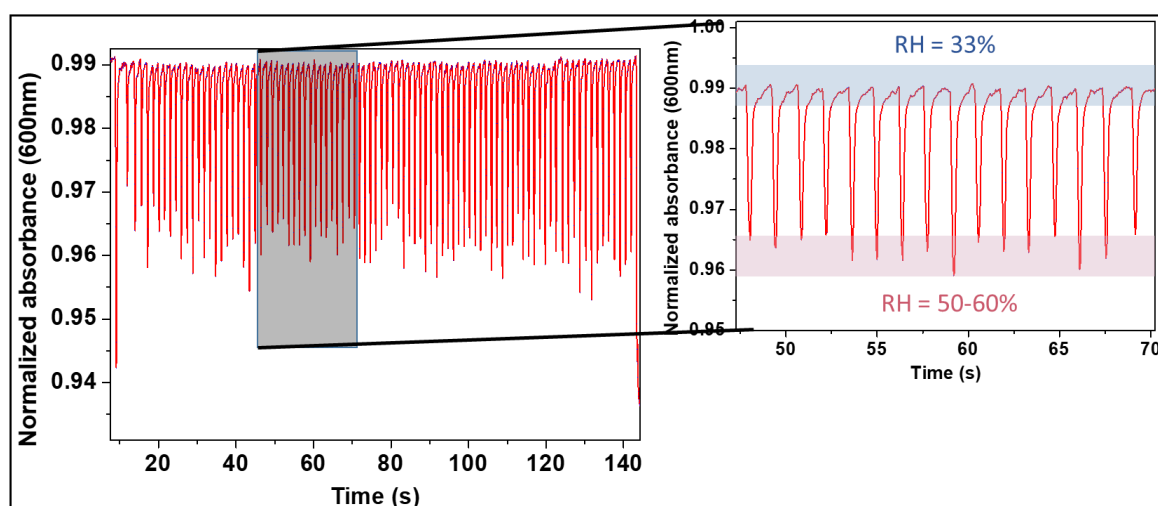


**Figure 4.9:** Optical response of AuNPs networks exposed to short pulses of humid air (pulses frequency = 2 Hz). Inset showing a zoom-is of the highlighted region of the plot.

The use of di-thiolated ligands and cross-linked networks guarantees an extreme robustness to the 2D structure, making it possible to achieve a perfect control and predictability over the optical properties. External humidity can be employed as a controller to finely tune such characteristics, by affecting the inter-particles distance without damaging the films. This aspect is essential to gain fast control over the optical properties with outstanding precision. Noteworthy, the shift of the SPR versus the relative humidity follows an exponential trend within the whole range of humidity: from 0.5 ppm up to 98% and, even upon complete immersion of the films in water, as displayed in **Figure 4.8b**. As previously anticipated, this interesting behavior cannot be ascribed to a mere modification of the refractive index surrounding the particles upon absorption of water molecules within the PEG linkers, which would lead to a linear rather than exponential dependence of the LSPR wavelength,<sup>17</sup> as usually reported for AuNPs based sensors.<sup>1,18</sup> With the aim of explaining such unusual finding we have performed discrete dipole approximation (DDA) simulations on hexagonal AuNPs lattices of 9 nm large particles. We have implemented such method in order to calculate the extinction spectra of hexagonal clusters made of 7 AuNPs. The calculating resolution (i.e. minimum distance between 2 discretizing dipoles) is set to 1 nm and the radius of each AuNP is fixed at 4.5 nm. In the experiments, the AuNPs are cross-linked into 2D networks with a self-assembled monolayer of di-thiolated linkers (see **Figure 4.3**) which swells as the humidity increases. In the simulations, we account for such a PEG backbone through a background refractive index that evolves as a function of the adsorbed humidity as

$$n_{back} = (1 - \alpha)n_{PEG} + \alpha n_{H_2O}$$

Where  $n_{PEG} \sim 1.78$  is the refractive index of PEG (taken from tabulated data in standard conditions of pressure and temperature) and  $n_{H_2O} = 1.33$  the refractive index of pure water.

The critical point is to evaluate the impact of an increase in humidity on the  $\alpha$  coefficient which corresponds to the water uptake within the PEG chains around the particles. The amount of water absorbed at different RH conditions was extracted by experimental literature data on water sorption isotherms in bulk PEGs, reported in Ref. <sup>19</sup> and reprinted in **Figure 4.10**.

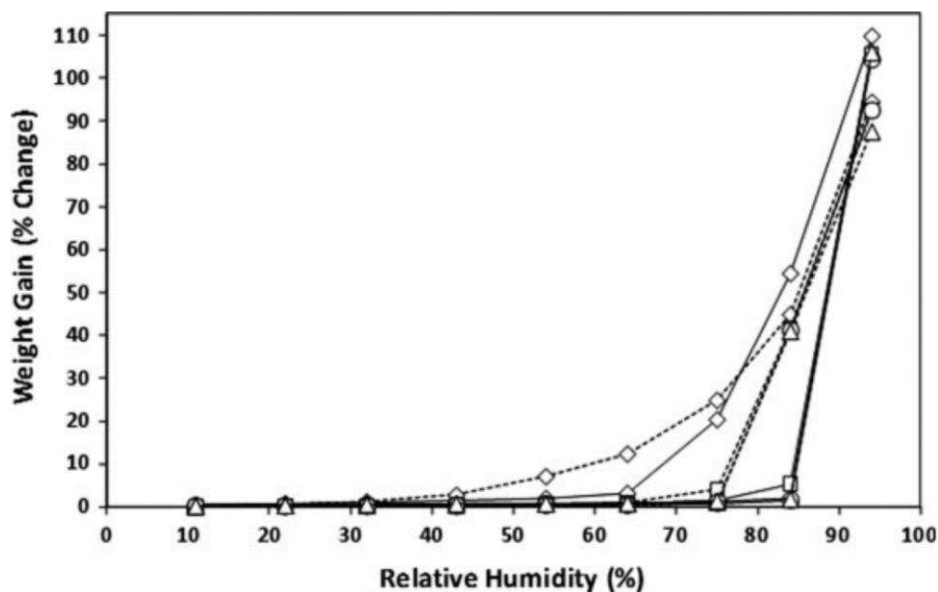


**Figure 4.10:** Vapor sorption isotherms of various MW PEGs measured by automated gravimetric moisture analysis at each relative humidity. ( $\diamond$ ) PEG 1450, ( $\square$ ) PEG 3350, ( $\circ$ ) PEG 6000, ( $\Delta$ ) PEG 8000. Solid lines (—) and dashed lines (---) are isotherms measured at 25° C and 40° C respectively. Reprinted with permission from Ref. <sup>19</sup>

The plot displayed in **Figure 4.10** contains useful information over the water uptake (in weight) of PEG bulks featuring different molecular weight at 25° C and 40° C. Among the different polymers explored in this study, the closest to the one we employed for our AuNPs 2D networks is the  $M_n = 1450$  Da at 25° C, represented as “ $\diamond$ ” with a solid line in **Figure 4.10**. Such data directly yields the  $\alpha/(1 - \alpha)$  water “weight gain” ratio as a function of the relative humidity between the PEG and water refractive indices, which can be nicely fitted by an exponential function. The resulting background refractive index is then injected in the simulation that now yields a relation between the relative humidity  $R$  and the spectral position  $\lambda$  of the cluster’s optical absorption peak as:

$$R = -0.077 * \exp(-\lambda / -15.58) + 596.19$$

This fit immediately reveals that merely accounting for the influence of the relative humidity on background refractive index changes is not sufficient in order to reproduce the actual spectral evolutions gathered in **Figure 4.8b**. In order to fit such spectral evolution, it is also necessary to progressively increase the inter-particle distances as the relative humidity

increases, in relation with the progressive swelling of the PEG 2D network, as clearly showed by our best fit result displayed in **Figure 4.11**. Combined with the modification of the background refractive index changes, the progressive increase of the inter-particles distance turns out to be an essential spectral parameter, starting from a minimal distance of 4 nm up to the maximally allowed distance of 8 nm (**Figure 4.11**).

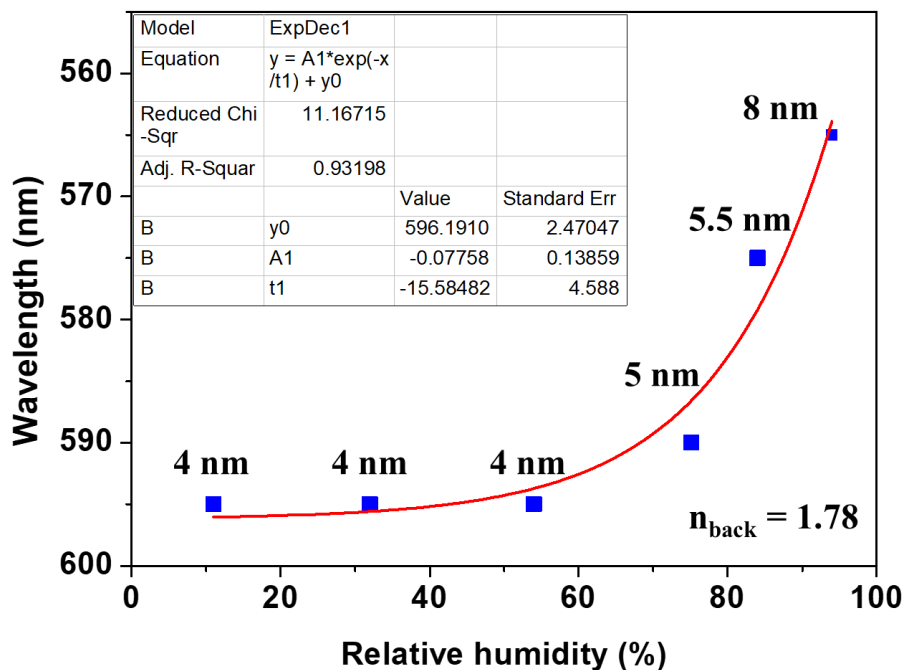


**Figure 4.11:** Evolution of the absorption peak of a 7 AuNPs hexagonal cluster simulated by a DDA approach and accounting for changes in both (i) the background refractive index and (ii) the ligand chain length (i.e. inter-particle distances) as the relative humidity increases. This simulated curve is to be compared with the experimental data shown in **Figure 4.8b**.

By using such simulations we prove that the only way to justify the experimental extinction shift recorded and its exponential evolution, is to assume a change of the inter-particles distance of almost 3 nm between dry (0 % RH) and immersion in water, where the inter-particle distance is set to a maximal value of 8 nm, consistently with a calculated fully elongated ligand chain length (see above). Moreover, the experimental data can be fitted by assuming values of  $n_{\text{back}} \geq 1.78$ , which cannot be given by a linear combination of the refractive indexes of PEG ( $n_{\text{PEG}} \sim 1.45$ ) and water ( $n_{\text{H}_2\text{O}} = 1.33$ ), confirming the non-metallic optical properties of the gold nanoparticles within the network, which retains their individual characteristics and plays a crucial role in defining the background refractive index of the

films, as already reported in literature with ellipsometric investigations on AuNPs thin films.<sup>20</sup>

## 4 CONCLUSIONS

---

In conclusion, we have reported on a new approach to fabricate centimeter-scale single-layer dynamic plasmonic nanostructures that enables a fine and precise control over the optical properties by using the environmental humidity as a remote controller. In such structures, the maximum recorded shift of the absorbance band was as big as 35 nm in the visible range, being also accompanied by a change of the band broadening. Such shift is clearly visible by naked eye and it is highly reproducible. Indeed the structures exhibit remarkable stability for an undefined amount of cycles with an excellent response speed of 200 ms and full recovery. Moreover, the whole system is solution processed and synthesized from water. Such processing of the AuNPs/PEG networks is suitable for deposition onto any kind of hydrophilic substrate, allowing fabrication of electrical devices on silicon as well as optical devices on glass and quartz. After deposition, our cross-linked networks are not soluble and can be put in contact and immersed in any organic or inorganic solvent without damages or modifications of the optical properties. Our test also showed remarkable mechanical robustness, allowing also to build layered structures with 2D materials, such as graphene or metal dichalcogenides, using the scotch tape depositions directly over the plasmonic nanostructures without damaging them.



## 5 REFERENCES

---

- 1 Saha, K., Agasti, S. S., Kim, C., Li, X. & Rotello, V. M. Gold nanoparticles in chemical and biological sensing. *Chem Rev* **112**, 2739-2779, (2012).
- 2 Elghanian, R., Storhoff, J. J., Mucic, R. C., Letsinger, R. L. & Mirkin, C. A. Selective colorimetric detection of polynucleotides based on the distance-dependent optical properties of gold nanoparticles. *Science* **277**, 1078-1081, (1997).
- 3 Kim, Y. R., Mahajan, R. K., Kim, J. S. & Kim, H. Highly sensitive gold nanoparticle-based colorimetric sensing of mercury(II) through simple ligand exchange reaction in aqueous media. *ACS Appl Mater Interfaces* **2**, 292-295, (2010).
- 4 Nie, Z., Petukhova, A. & Kumacheva, E. Properties and emerging applications of self-assembled structures made from inorganic nanoparticles. *Nat Nanotechnol* **5**, 15-25, (2010).
- 5 Hamon, C., Novikov, S., Scarabelli, L., Basabe-Desmonts, L. & Liz-Marzan, L. M. Hierarchical self-assembly of gold nanoparticles into patterned plasmonic nanostructures. *ACS Nano* **8**, 10694-10703, (2014).
- 6 Hamon, C. & Liz-Marzan, L. M. Hierarchical Assembly of Plasmonic Nanoparticles. *Chem Eur J* **21**, 9956-9963, (2015).
- 7 Klinkova, A., Choueiri, R. M. & Kumacheva, E. Self-assembled plasmonic nanostructures. *Chem Soc Rev* **43**, 3976-3991, (2014).
- 8 Tao, A., Sinsermsuksakul, P. & Yang, P. Tunable plasmonic lattices of silver nanocrystals. *Nat Nanotechnol* **2**, 435-440, (2007).
- 9 Kunstmann-Olsen, C., Belic, D., Bradley, D. F., Grzelczak, M. P. & Brust, M. Humidity-Dependent Reversible Transitions in Gold Nanoparticle Superlattices. *Chem Mater* **28**, 2970-2980, (2016).
- 10 Love, J. C., Estroff, L. A., Kriebel, J. K., Nuzzo, R. G. & Whitesides, G. M. Self-assembled monolayers of thiolates on metals as a form of nanotechnology. *Chem Rev* **105**, 1103-1169, (2005).
- 11 DeVries, G. A. *et al.* Divalent metal nanoparticles. *Science* **315**, 358-361, (2007).
- 12 Squillaci, M. A. *et al.* Self-Assembly of an Amphiphilic pi-Conjugated Dyad into Fibers: Ultrafast and Ultrasensitive Humidity Sensor. *Adv Mater* **27**, 3170-3174, (2015).
- 13 Amendola, V., Bakr, O. M. & Stellacci, F. A Study of the Surface Plasmon Resonance of Silver Nanoparticles by the Discrete Dipole Approximation Method: Effect of Shape, Size, Structure, and Assembly. *Plasmonics* **5**, 85-97, (2010).
- 14 Greenspan, L. Humidity Fixed-Points of Binary Saturated Aqueous-Solutions. *J Res Nbs a Phys Ch* **81**, 89-96, (1977).
- 15 Turkevich, J., Stevenson, P. C. & Hillier, J. The Formation of colloidal gold. *J Phys Chem* **57**, 670-673, (1953).
- 16 Thijs, H. M. L. *et al.* Water uptake of hydrophilic polymers determined by a thermal gravimetric analyzer with a controlled humidity chamber. *J Mater Chem* **17**, 4864-4871, (2007).
- 17 Antosiewicz, T. J., Apell, S. P., Claudio, V. & Kall, M. A simple model for the resonance shift of localized plasmons due to dielectric particle adhesion. *Optics Express* **20**, 524-533, (2012).

- 18 Antosiewicz, T. J. & Kall, M. A Multiscale Approach to Modeling Plasmonic Nanorod Biosensors. *J Phys Chem C* **120**, 20692-20701, (2016).
- 19 Baird, J. A., Olayo-Valles, R., Rinaldi, C. & Taylor, L. S. Effect of molecular weight, temperature, and additives on the moisture sorption properties of polyethylene glycol. *J Pharm Sci* **99**, 154-168, (2010).
- 20 Brust, M., Bethell, D., Kiely, C. J. & Schiffrin, D. J. Self-assembled gold nanoparticle thin films with nonmetallic optical and electronic properties. *Langmuir* **14**, 5425-5429, (1998).



# Chapter 5

## Using 0D objects to build 3D materials: nanoparticles 3D networks

### 1 INTRODUCTION

---

The previous chapter reported on the use of 2D networks of cross-linked gold nanoparticles to study and develop humidity sensors with an optical readout relying on the plasmonic properties of such objects. Those sensors are extremely interesting from the fundamental point of view to study the optical phenomena taking place in such complex systems. However, from a purely technological point of view, the optical readout is not well suitable with the current sensors technology which is based on the use of electrical signal, being easier to handle, process and amplify with standard equipment.

In this view, this chapter reports on the fabrication and use of 3D AuNPs networks, made by using the same concepts and AuNPs already employed in the previous chapter, but using shorter di-thiolated PEG cross-linkers, featuring 4 (TEG) and 6 (HEG) repetitive units. The use of such short chains dramatically changes all the characteristic of the networks, enabling electronic cross-talk among adjacent nanoparticles within the network. Moreover, such short molecules are more rigid, more reactive and less soluble in water compared to the PEG 1000 previously described, such characteristics enables the formation of porous and amorphous

3D structures that grow and precipitate during the cross-link reaction, rather than generating ordered 2D assemblies.

As already discussed, upon absorption of water from the atmosphere, the AuNPs networks undergo swelling via the increasing of the inter-particles distances therefore, dramatically changing the measured electrical resistance. These structures were then implemented in electrical devices and used as active materials for the realization of high performance humidity sensors with electrical resistive readout.

Thanks to their all-covalent structure and to their purely geometrical-induced translation mechanism, our devices feature a state of the art response time  $< 13$  ms and a minimum sensitivity of  $678 \Omega/\text{RH} (\%)$  over a wide 0-100% RH working range. Moreover, such devices showed high mechanical robustness and require extremely small sizes, exposing an active area  $< 0.23 \text{ mm}^2$ .

## 2 EXPERIMENTAL

---

### 2.1 METHODS AND SAMPLES PREPARATION

UV-Vis absorbance spectra of the solutions were recorded in standard 1 cm optical path quartz cuvettes using a JASCO V670 UV-Vis-NIR spectrophotometer. Optical images were taken with an Olympus BX51 optical microscope. All scanning electron microscopy imaging was conducted using a FEI Quanta 250 FEG Scanning Electron Microscope (SEM), operated in high vacuum mode (pressure in  $10^{-4}$  Pa range). The electrical characterizations were performed by using a Keithley double channel source meter model 2636B, connecting the samples through to a custom made PCB board. Two commercial humidity sensors: SENSIRION SHT21 and Radio Spares 1364 Humidity-Temperature Meter, were employed as reference for the calibration during the electrical measurements. Low temperature electrical characterizations were carried out in an Oxford Instruments Optistat DN-V cryostat operating in the range between 80 and 300 K (liquid N<sub>2</sub>).

As for the previous chapter, the gold nanoparticles used in this project, featuring an average diameter of  $8.6 \pm 1.4$  nm, were synthesized in water employing the Turkevich method.<sup>5</sup> The functionalization was performed using tetraethylene glycol dithiol (Molecular weight = 226.36 Da) and hexaethylene glycol dithiol (Molecular weight = 314.36 Da). Both reactants were purchased from Sigma-Aldrich and were used upon dilution 1:10'000 in MilliQ water.

### 3 RESULTS AND DISCUSSIONS

The cross-link reactions between the AuNPs and the OEG dithiols were performed by addition of the diluted ligand solutions directly in the growth solution of the AuNPs, without further purification, as already explained in the previous chapter. The ligands solutions were added in stoichiometric ratio with respect to the amount of gold nanoparticles in solution. A proper stoichiometric ratio between the particles and the ligands is fundamental for such kind of systems because, to achieve the formation of stable cross-linked networks, is necessary to have equal amount of binding sites on the particle's surface and free thiol groups in solution. The use of an excess of ligands would bring to a saturation of the nanoparticle's surface precluding the cross-link, while the use of too small ligands amounts, would ensure the cross-link between the particles but with just few bridges stabilizing the structures. Both of the situations described would lead to weak and unstable networks which cannot be employed for the purpose of this project (**Figure 5.1**).

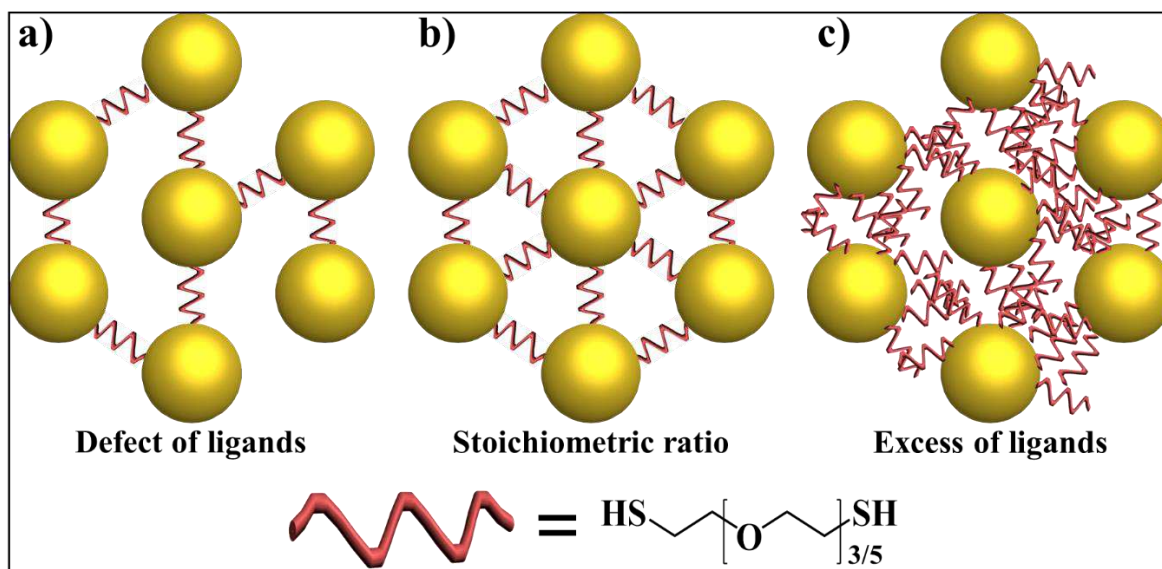


**Figure 5.1:** Cartoon explaining the importance of the use of proper stoichiometric ratio between AuNPs binding sites and free thiol groups in solution. a) Effect of a defect of the ligands in solution. b) Effect of proper stoichiometric ratio. c) Effect of excess of ligands in solution.

A rough estimation of the needed amount of thiol groups can be obtained by purely geometrical considerations, as described in detail in the methods section in chapter 3.2. According to these approximation, the cross-link reaction should be achieved by adding  $\sim 450$  di-thiolated OEGs per each nanoparticle in solution. Such values were used to perform the preliminary optical studies on the functionalization of the AuNPs with the chosen di-thiolated OEG ligands (**Figure 5.2**).

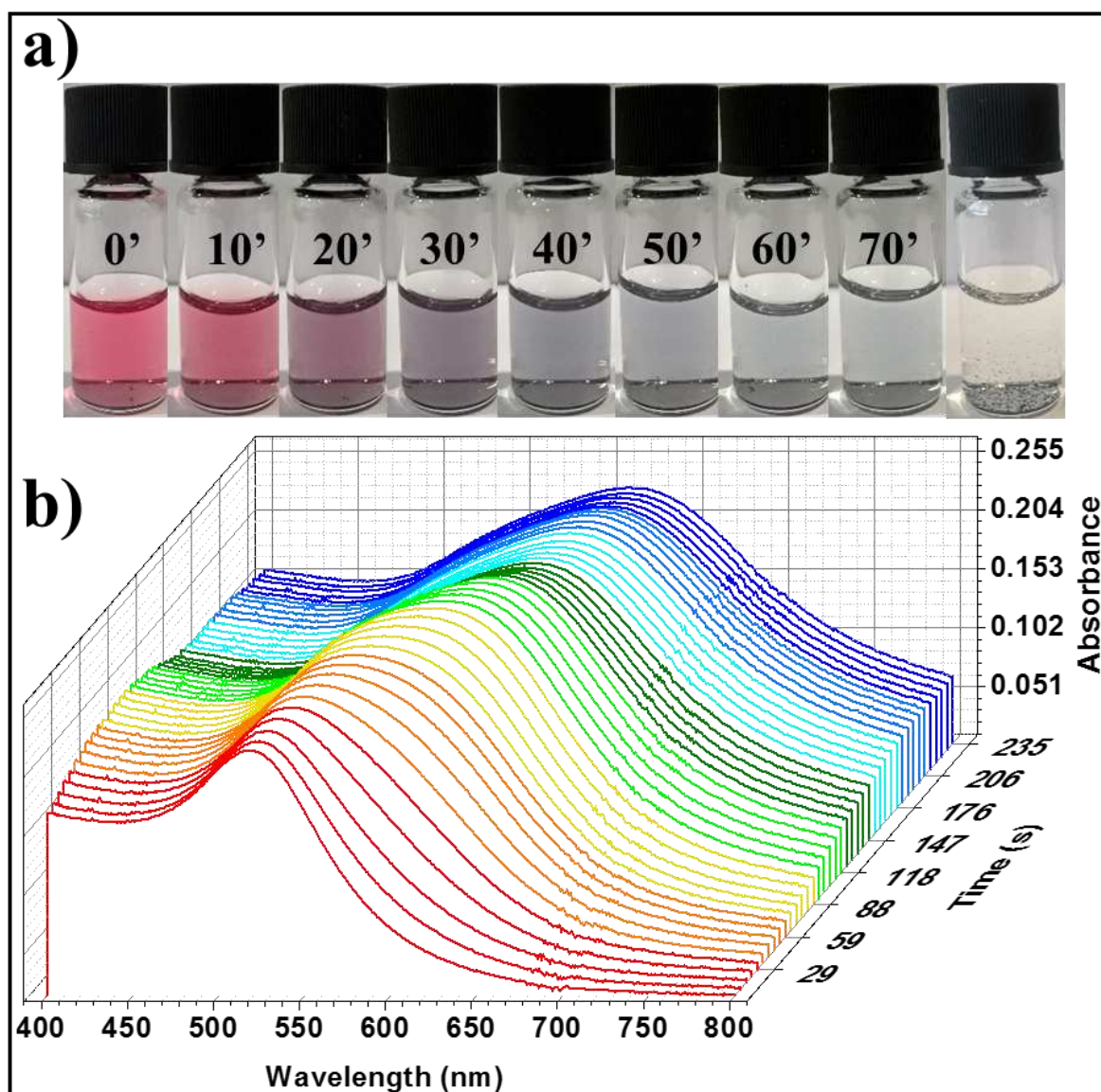


**Figure 5.2:** Optical evolution of AuNPs solutions upon addition of stoichiometric amounts of di-thiolated TEG. a) Series of optical photographs of the solution recorded with steps of 10 minutes and after one day (last picture). b) Evolution of the UV-Vis absorbance spectra within the first 4 minutes upon addition of the ligand solution.

**Figure 5.2** portrays the evolution in the optical properties of the AuNPs solutions upon addition of di-thiolated TEG at room temperature. Such measurements reveal several crucial information: (I) the red shift of the AuNPs SPR band, accompanied by a broadening of the signal and by an increase of the background signal given by scattered light, represent clear evidences of aggregation, meaning that the cross-link reaction is taking place under the chosen condition. (II) The dramatic changes in the optical properties, observed during the reaction, are strongly different compared to the ones observed with the use of longer ( $\sim 20$  repetitive units) PEG chains reported in the previous chapter. Such finding means that by employing short ligands, such as TEG, the inter-particles distance is so small that ensures the electrical contact and therefore the loss of the SPR band of the particles even in water solution, where the ligand chains are expected to be fully elongated. (III) The clear and colourless supernatant the solution, obtained after completion of the reaction, proves that the employed ratio between particles and ligands for the reaction, was correct. Several control experiments have shown that the use of either excess or defect of ligands would lead to the contemporary presence of precipitate and detectable SPR band in the supernatant after completion of the reaction. In such case, the presence of detectable SPR band in the supernatant solution could be given by unreacted AuNPs (in the case of defect of ligands) or by ligands saturated AuNPs which are not connected to the networks (in the case of an excess of ligands). (IV) The same experiment, performed using a slightly longer ligand (HEG instead of TEG), leads to the same optical evolution and final results but features a lower kinetic, requiring six days instead of 20 hours to reach the final stage under the same conditions.

The different kinetics of the cross-link reaction, observed by comparing TEG and HEG, could be ascribed to a lower reactivity of the thiol groups connected to longer linear chains or, more probably, to an higher solubility of the resulting networks which need to grow bigger in order to trigger the precipitation of the aggregate, when longer ligands are employed.

The dark precipitate found at the bottom of the vials after completion of the cross-link reaction and visible in the last vial picture in **Figure 5.2a**, was deposited by drop casting on the basal plane of silicon substrate and characterized by SEM (**Figure 5.3**).



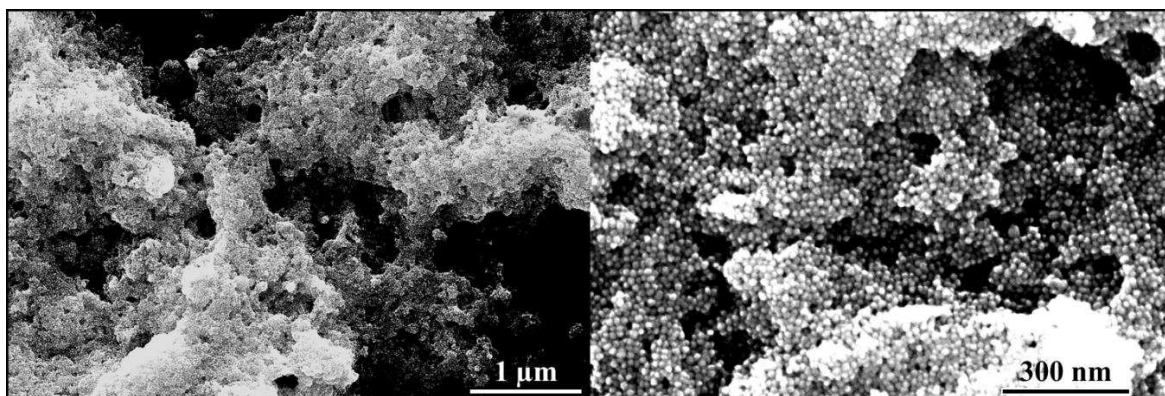


*Figure 5.3: SEM images of AuNPs/TEG porous 3D networks.*

SEM images reported in **Figure 5.3**, show that the precipitate resulting from the reaction between AuNPs and di-thiolated TEG or HEG possesses an amorphous 3D architecture, in which the AuNPs are interconnected between each other forming porous structures, exhibiting high surface development. Due to their size, the AuNPs/OEG networks are not soluble in any solvent. By exploiting such characteristic, it is possible to rinse the substrates in water (or in any other solvent) after the drop-casting process, to remove the residuals of sodium citrate, present as stabilizer for the AuNPs in the growth solution. This step has been found to be crucial, not only for the removal of the insulating layer covering the networks during the SEM imaging but also because sodium ions could get trapped inside the OEG chains surrounding the particles, behaving as bridges for the electrical charges between the particles and affecting the measured electrical current through the devices.

The first preliminary electrical devices based on such systems, were fabricated by directly drop-casting the grown 3D AuNPs networks on SiO<sub>2</sub>/Si substrates, pre-patterned with interdigitated gold electrodes featuring a channel length ranging from 2.5 to 20 μm. This approach provides a poor control over the deposition and lead to an extremely low uniformity of the coverage, making it impossible to perform any statistical study on the resulting devices. This drawback has been removed by performing the cross-link reaction directly on the substrate's surface instead of depositing the AuNPs/OEG precipitate after the reaction. By drop-casting the AuNPs solutions mixed with the ligands immediately after the OEG addition, it was possible to achieve a more uniform deposition of the 3D networks all over the substrate's surface, improving the reproducibility of the device fabrication. Such procedure requires that the cross-link reaction between AuNPs and OEGs takes place

directly on the substrate's surface and in contact with the electrodes. During the reaction, the free thiols could also react with the gold surface of the interdigitated electrodes, precluding the growth of the networks, for this reason the substrates need to be passivated before the reaction. The electrodes passivation was performed by growing a self-assembled monolayer (SAM) of di-thiolated TEG ligands on the gold electrodes, before proceeding with the deposition. The SAMs were grown by immersing the substrates into highly concentrated ( $5 \times 10^{-3}$  M) TEG solutions at room temperature for 48 hours. TEG was chosen as a passivation layer for the electrodes because, featuring a short nominal length of 1.5 nm, it is more rigid than HEG and, under the employed conditions, only one of the two thiol groups of each molecule should react with the electrode, preventing the back-folding. The result is the formation of a monolayer of pending thiols on the electrode's surface.<sup>10</sup> This procedure allows to passivate the electrodes from the di-thiolated OEGs needed for the reaction with the AuNPs and to concentrate the AuNPs/OEG networks on the electrodes, further increasing the coverage inside the channel. Moreover, such procedure creates a covalent link between the electrodes and the nanoparticles networks, dramatically improving the electrical contact, the stability and the mechanical robustness of the final devices (**Figure 5.4**).

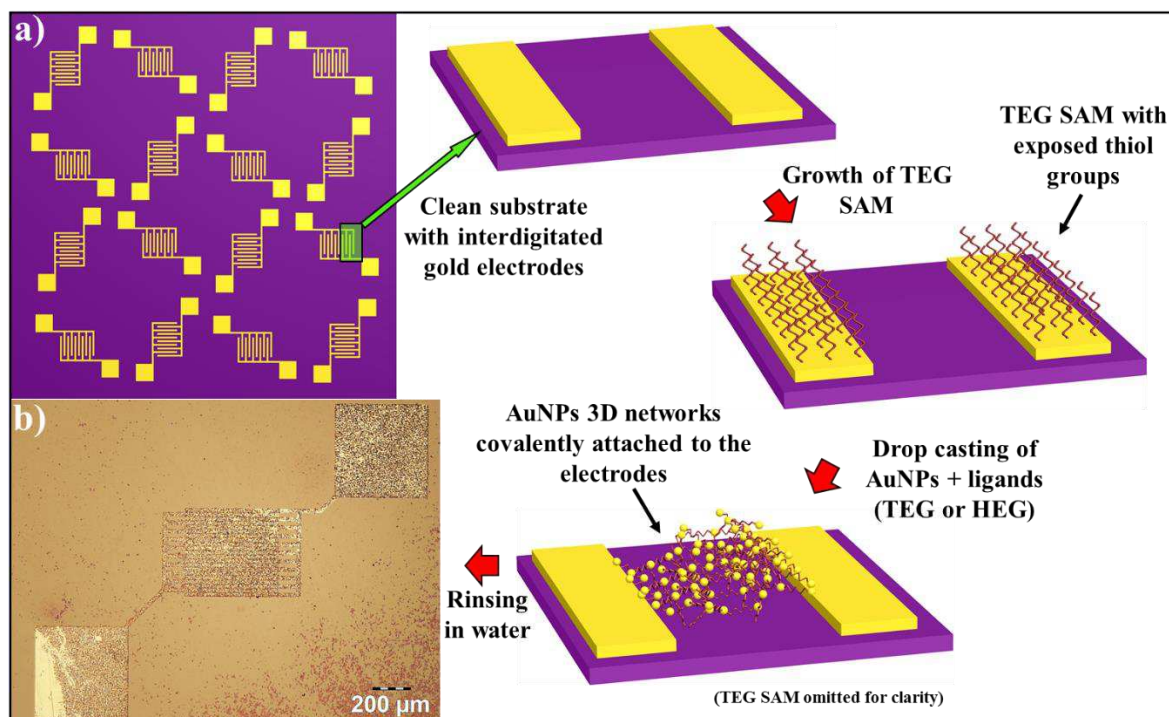


**Figure 5.4:** Optimized procedure for the fabrication on 3D AuNPs/OEG based electrical devices. a) Flowchart of the process. b) Optical micrograph of the resulting device.



From the optical micrograph in **Figure 5.4b**, it is possible to see that such optimized procedure employed for the devices fabrication, allows to increase and concentrate the deposition of the AuNPs/OEG networks on the interdigitated electrodes, bridging them inside the channel. This observation was also confirmed at smaller scales, by performing SEM characterizations, reported in **Figure 5.5**. The high coverage and the stability of the devices fabricated with the aforementioned optimized procedure, have a dramatic impact on the reproducibility of the deposition, as confirmed by the remarkably small error bars in the electrical measurements reported in **Figure 5.6**.

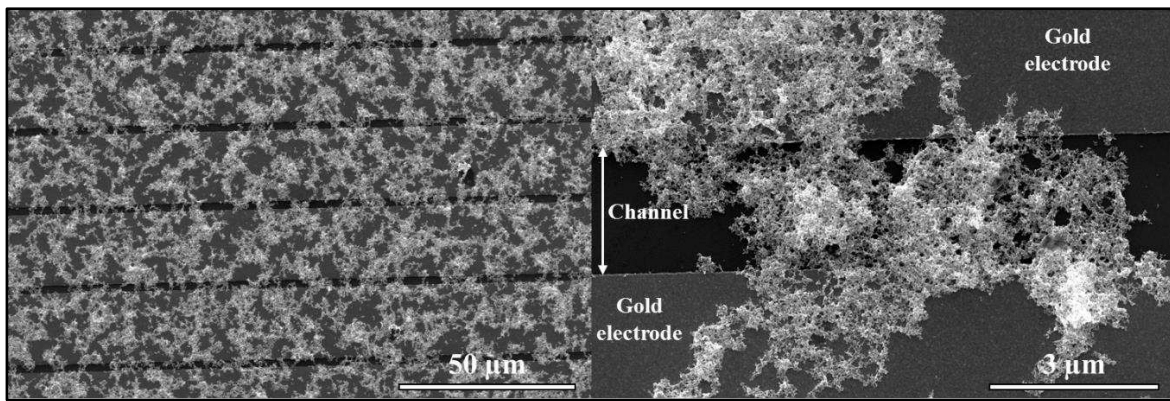


*Figure 5.5: SEM images of AuNPs/OEG electrical devices obtained with optimized procedure.*

As displayed in **Figure 5.5**, the films of AuNPs/OEG 3D networks resulting from the deposition are composed by small cluster which feature an average size of just few  $\mu\text{m}$ , meaning that a uniform coverage can be ensured just for the shortest channels measuring 2.5 and 5  $\mu\text{m}$ . Two terminal electrical resistance measurements of such devices at room temperature, showed an ohmic behaviour with a linear dependence of the measured current respect to the applied bias (**Figure 5.6a**).

The statistical analysis on the electrical resistance of such devices was performed by preparing series of at least 4 samples (32 devices) per each employed ligand (TEG or HEG). The same study was also performed on films of bare AuNPs (e.g without any ligand or bridge connecting the AuNPs), prepared under the same conditions and on the same substrates, to be used as reference to evaluate the intrinsic resistivity and contact resistance of such systems

when the particles are in direct contact between each other. The obtained results are summarized in **Figure 5.6** and show an average resistance of  $34 \pm 9 \text{ k}\Omega$  for the AuNPs TEG networks and  $430 \pm 90 \text{ k}\Omega$  for the AuNPs HEG devices, while the resistance of the bare AuNPs films was found to be  $105 \pm 7 \text{ }\Omega$ . The latter, being extremely low, can be considered as the “zero resistance” value for such series of devices. Interestingly, such device resistance have shown to be exponentially dependent by the nominal chain length of the employed di-thiolated OEG. By plotting the measured 2-terminal electrical resistance versus the nominal length of the ligands, it is also possible to fit the experimental data using a general exponential equation (**Figure 5.6b**):

$$R = R_0^{\beta L}$$

Where R = Resistance and L = Nominal ligand length.

The proportionality factor “ $\beta$ ”, extracted from the fitting, amounts to  $3.8 \text{ nm}^{-1}$ , indicating a strong dependence of the resistance with the inter-particles distance. Such value of  $\beta$  is too big for an hopping-like charge transport mechanism, where usually  $\beta \sim 1$  and strongly suggest the presence of a tunnelling transport of the charge carriers through the networks.<sup>11</sup>

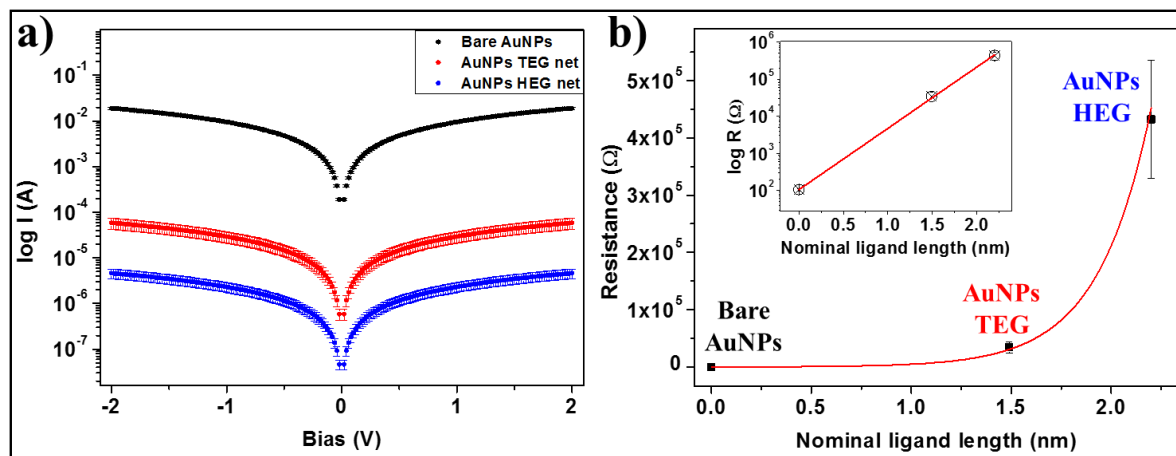


**Figure 5.6:** Electrical behavior and average resistance of AuNPs-based electrical devices (channel length =  $2.5 \text{ }\mu\text{m}$ ). a) Average I-V curve of bare AuNPs (used as reference), AuNPs networks with TEG and HEG ligands. b) Plot of average device resistance versus the nominal length of the fully extended ligands.

The tunnelling charge transport mechanism was confirmed by performing electrical characterization of the devices at low temperatures. Electrical I-V measurements, performed inside a cryostat ranging from 80 to 300 K (**Figure 5.7a**), revealed an extremely small dependency of the electrical resistance from the temperature. Moreover, the I-V curve retain their linearity over the whole range of explored temperatures, confirming that the charge carriers are transported through a direct tunnelling mechanism.<sup>12</sup> As shown in **Figure 5.7a**, the same behaviour (e.g. very small dependency between electrical properties and temperature) was also found for the reference device made of bare nanoparticles, in which all the particles are in ohmic contact between each other. By comparing the evolution of the measured devices resistance at different temperature for bare AuNPs and AuNPs/OEG networks, it is also possible to see that the trend is reversed, as highlighted in **Figure 5.7b**. Such finding can be easily explained: Direct tunnelling is a moderate thermally-activated process thus the resistance decreases with increasing temperature; on the other hand, in an ohmic metal-metal junction the resistivity is given by the scattering of the charge carriers hitting the metal lattice and higher temperatures increase the amplitude of such lattice vibrational modes, increasing the electrical resistance.

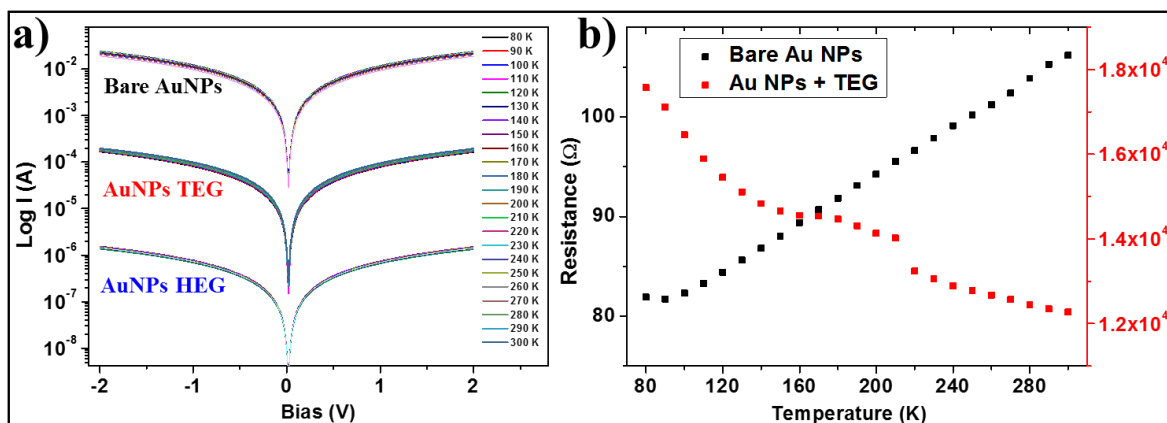


**Figure 5.7:** Electrical behaviour of AuNPs based devices at different temperatures. a) Comparison of the I-V curve for bare AuNPs, and AuNPs networks with TEG and HEG. b) Plot of electrical resistance for bare AuNPs and AuNPs/TEG networks.

The resistance measurements of the AuNPs/TEG networks performed inside the cryostat and reported as red squares in **Figure 5.7b**, show the presence of a “bump” between 170 and 220 K where the resistance undergoes a slight increase and then decreases back following the

initial trend. Careful investigations of the employed setup, have shown that even if the cryostat is purged with nitrogen and constantly kept under vacuum ( $10^{-3}$  mBar) during the measurements, it is subject to small increase of inner humidity in the 170-220 K range of temperatures. Such small increase of humidity was detected by the AuNPs/TEG networks but did not affect the measurements on bare AuNPs, which does not have any receptor to interact with moisture. As already seen in the previous chapter, PEG backbone can absorb water molecules from the atmosphere and, upon absorption it undergoes swelling. In the case of 3D AuNPs/OEG networks, being the tunnelling current exponentially dependent by the inter-particles distance, the swelling of the networks causes a dramatic decrease of the tunnelling current and, as a consequence, an increase in the resistance. This process is schematized in **Figure 5.8a**. The actual humidity sensing performances were characterized by connecting the AuNPs/OEG based devices with a custom made printed board circuit (PCB). This setup allows to perform electrical measurements in sealed chambers, does not requires the use of probes or micro-manipulators and features multiple individual electrical connections to characterize multiple TEG and HEG devices at the same time (**Figure 5.8b**).

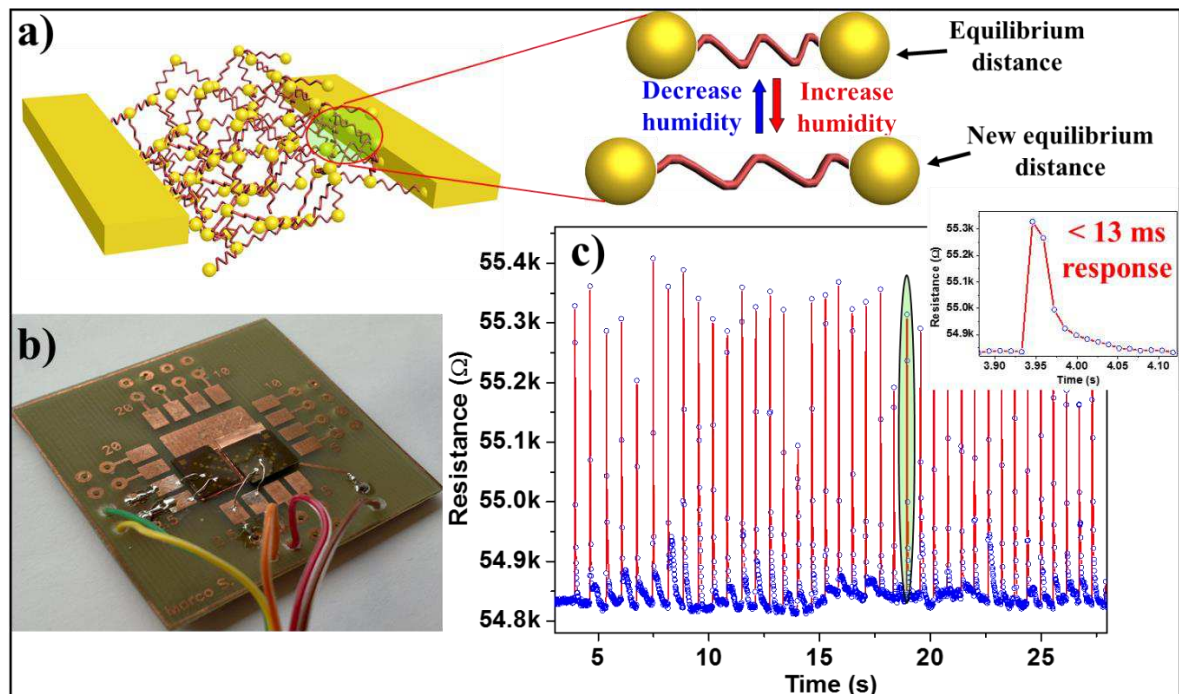


**Figure 5.8:** Electrical resistive humidity sensors based on AuNPs/OEG 3D porous networks. a) Schematic of the sensing process. b) Picture of the device setup used for the sensor's characterization. c) Measurements of response speed, reversibility and stability of the final devices (constant bias applied = 500 mV).

The data reported in **Figure 5.8b** shows the electrical response of AuNPs/TEG networks over time, while applying a constant bias of 500 mV. During the measurement, short pulses of humid air were sent on the device's surface with a frequency of 2 Hz.

The obtained results, displayed in **Figure 5.8**, highlight 3 major features of such devices: (I) the devices are stable for an indefinite amount of cycles, certainly more than hundreds, and allow to continuously measure the response without suffering any loss of performances or bias stress (e.g. feature a stable baseline). (II) The absorption of water molecules and the subsequent increase of the electrical resistance is a totally reversible process, allowing the resistance to go back to its initial value in  $\sim 100$  ms. (III) The response to humid air is extremely fast and requires less than 13 ms to take place.

Unfortunately, a precise evaluation of the actual response speed of such devices cannot be provided because, as highlighted in the inset in **Figure 5.8b**, the sampling time e.g. the time delay between two measured points, visible as blue circles in the plot, is limited to 13 ms. Such limitation is intrinsic of the source meter employed to perform the electrical characterization and cannot be overcome without changing the setups.

A more precise evaluation of the response speed could be obtained by performing impedance measurements using a frequency higher than 100 Hz, on which we are currently working.

By taking advantages of their interesting features, the fabricated device could be employed as resistive humidity sensors for real word applications. Such step obviously requires a calibration of the device's resistance at different humidity and a model providing a predictable and unambiguous trend to correlate such parameters.

The devices calibration was performed by recording the evolution of the devices electrical resistance upon exposure to different conditions, by sealing the samples inside a chamber with controlled humidity and constant temperature, in presence of a commercial humidity meter to be used as a reference.

An example of calibration curves for AuNPs TEG and HEG networks-based devices, in the relative humidity range between 5% and 85%, can be found in **Figure 5.9**.

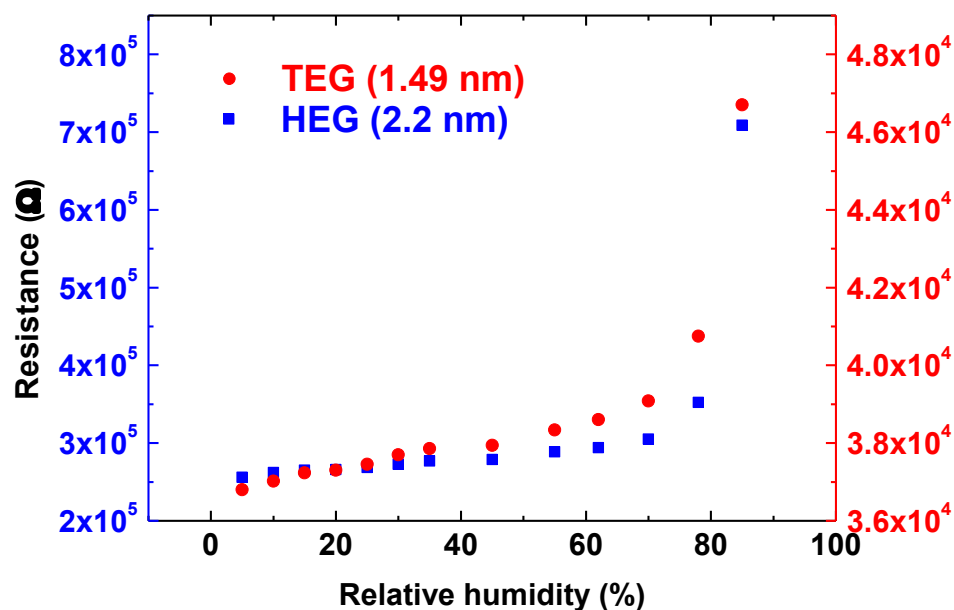


Figure 5.9: Calibration curves of AuNPs TEG and HEG-based humidity sensors.

The calibration curves reported in **Figure 5.9**, were recorded by connecting the AuNPs TEG and HEG based devices with two separated electrical channels, to apply a constant bias (20 mV for TEG and 500 mV for HEG based devices) and to continuously recording their electrical resistance at the constant temperature of 22°C. Both devices showed linear dependency of the measured electrical resistance with the environmental humidity in the range 0-70% RH with a dramatic change of slope above 70% RH. Such finding is in a strong agreement with the literature and it is due to the not linear hygroscopic behaviour of PEG backbone which exhibit a strong increase of the absorbed content of moisture at humidity levels higher than 60/70%.<sup>13,14</sup>

Interestingly, the calibration plot reported in **Figure 5.9**, show similar behaviour and humidity threshold for the two systems but, with a more careful look at the resistance values of such devices, it is clear that the sensitivity (e.g. the slope of the resistance versus RH) of the HEG based networks is extremely higher, amounting to 678 Ω/RH(%) versus 32 Ω/RH(%) of TEG based devices under the same conditions, in the range between 0 and 70% RH (low sensitivity range). This values grows exponentially above the threshold of RH > 70% reaching the remarkable value of 51 kΩ/RH (%) for HEG based devices.



## 4 CONCLUSIONS

---

This chapter described a new approach to fabricate humidity sensors based on gold nanoparticles networks, by using short di-thiolated oligoethylene glycols featuring 4 and 6 repetitive units. Thanks to the shorter and more rigid backbone respect to the PEG 1000, employed and discussed in the previous chapter, such networks exhibit 3D porous structures and direct tunnelling-based electrical charge transport. Such AuNPs/OEG 3D networks were implemented in electrical devices by covalently connecting them to short channels gold interdigitated electrodes using a novel approach which dramatically improved reproducibility, electrical performances, stability and mechanical strength of the resulting devices.

The AuNPs/OEG 3D networks have shown great response upon exposure to moisture and have been characterized as humidity sensors exhibiting state of the art response speed<sup>15,16</sup> (response time < 13 ms), no hysteresis effect and great sensitivity of 678  $\Omega$ /RH(%), in the range between 0 and 70% RH, which grows exponentially to 51 k $\Omega$ /RH(%) above this threshold. Moreover, the direct tunnelling transport mechanism of the charge carriers through the networks makes the electrical response almost independent from the temperature and, thanks to their all covalent structure, our devices are extremely versatile, featuring a wide operative range: from 0% RH to immersion in water without any modification in the sensing performances.

## 5 REFERENCES

---

- 1 Joseph, Y., Guse, B., Yasuda, A. & Vossmeier, T. Chemiresistor coatings from Pt- and Au-nanoparticle/nonanedithiol films: sensitivity to gases and solvent vapors. *Sensor Actuat B-Chem* **98**, 188-195, (2004).
- 2 Konvalina, G. & Haick, H. Effect of humidity on nanoparticle-based chemiresistors: a comparison between synthetic and real-world samples. *ACS Appl Mater Interfaces* **4**, 317-325, (2012).
- 3 Joseph, Y. *et al.* Vapor sensitivity of networked gold nanoparticle chemiresistors: Importance of flexibility and resistivity of the interlinkage. *J Phys Chem C* **111**, 12855-12859, (2007).
- 4 Garg, N. *et al.* Robust gold nanoparticles stabilized by trithiol for application in chemiresistive sensors. *Nanotechnology* **21**, (2010).
- 5 Turkevich, J., Stevenson, P. C. & Hillier, J. The Formation of colloidal gold. *J Phys Chem* **57**, 670-673, (1953).
- 6 Liu, X., Atwater, M., Wang, J. & Huo, Q. Extinction coefficient of gold nanoparticles with different sizes and different capping ligands. *Colloids Surf B Biointerfaces* **58**, 3-7, (2007).
- 7 Dubois, L. H. & Nuzzo, R. G. Synthesis, Structure, and Properties of Model Organic-Surfaces. *Annu Rev Phys Chem* **43**, 437-463, (1992).
- 8 Love, J. C., Estroff, L. A., Kriebel, J. K., Nuzzo, R. G. & Whitesides, G. M. Self-assembled monolayers of thiolates on metals as a form of nanotechnology. *Chem Rev* **105**, 1103-1169, (2005).
- 9 Hostetler, M. J. *et al.* Alkanethiolate gold cluster molecules with core diameters from 1.5 to 5.2 nm: Core and monolayer properties as a function of core size. *Langmuir* **14**, 17-30, (1998).
- 10 Akkerman, H. B. *et al.* Self-assembled-monolayer formation of long alkanedithiols in molecular junctions. *Small* **4**, 100-104, (2008).
- 11 Choi, S. H., Kim, B. & Frisbie, C. D. Electrical resistance of long conjugated molecular wires. *Science* **320**, 1482-1486, (2008).
- 12 Zheng, T. H., Choy, W. C. H. & Sun, Y. X. Hybrid Nanoparticle/Organic Devices with Strong Resonant Tunneling Behaviors. *Adv Funct Mater* **19**, 2648-2653, (2009).
- 13 Baird, J. A., Olayo-Valles, R., Rinaldi, C. & Taylor, L. S. Effect of molecular weight, temperature, and additives on the moisture sorption properties of polyethylene glycol. *J Pharm Sci* **99**, 154-168, (2010).
- 14 Thijs, H. M. L. *et al.* Water uptake of hydrophilic polymers determined by a thermal gravimetric analyzer with a controlled humidity chamber. *J Mater Chem* **17**, 4864-4871, (2007).
- 15 Mogera, U., Sagade, A. A., George, S. J. & Kulkarni, G. U. Ultrafast response humidity sensor using supramolecular nanofibre and its application in monitoring breath humidity and flow. *Sci Rep* **4**, 4103, (2014).
- 16 Borini, S. *et al.* Ultrafast Graphene Oxide Humidity Sensors. *ACS Nano* **7**, 11166-11173, (2013).



# Chapter 6

## 1D supramolecular nanofibers for ultrasensitive humidity sensors

### 1 INTRODUCTION

---

The project described in this chapter reports on the use of one-dimensional supramolecular nanofibers, made by self-assembled molecular dyad, as building blocks, to be employed as active material for novel electrical resistive humidity sensors. Such result was achieved by decorating the surface of the 1D nanofibers with water absorbing TEG derivatives. The key to obtain the desired supramolecular architecture was to employ amphiphilic molecular building blocks, featuring asymmetric and incompatible side chains. The word “Amphiphile” (from the Greek *αμφίς*, *amphis*: both and *φιλία*, *philia*: love), means that the molecule can interact with both polar and non-polar solvents. This behavior is given by the asymmetric polar and non-polar pending groups within each molecule, which are able to interact selectively with the different environments surrounding them, enabling the formation of well-defined and ordered supramolecular architectures. The most known and studied class of amphiphilic molecules are surfactants, the basic components of soaps. Surfactants are usually made by a long alkyl chain, which is hydrophobic, terminated with a polar or ionic head, which is hydrophilic. As already explained in chapter 1.2 and 2.3, when well-engineered molecular building blocks are placed in solutions, the non-covalent

interactions play a fundamental role in driving their aggregation into supramolecular objects. In the case of surfactants, such process can lead to the formation of supramolecular architectures such as bilayer membranes, fibers, micelles etc. The final supramolecular structure is the result of an interplay of several different forces and corresponds to the most thermodynamically stable configuration. In the case of amphiphilic molecules, since solvophobic interactions usually provide the strongest contribution in defining the self-assembled structure, the molecules tend to arrange within the aggregates in order to expose the most compatible groups to the solvent and to shield the others. In polar solvents, such as water, usually all the polar heads lie on the surface of the supramolecular structure, interacting with the environment, while the aliphatic chains are hidden inside the aggregates and thus are protected from the solvent, in order to minimize the overall energy of the system (**Fig.6.1**). When the solvent is non-polar, the structure of the aggregates can be reversed.<sup>1</sup>

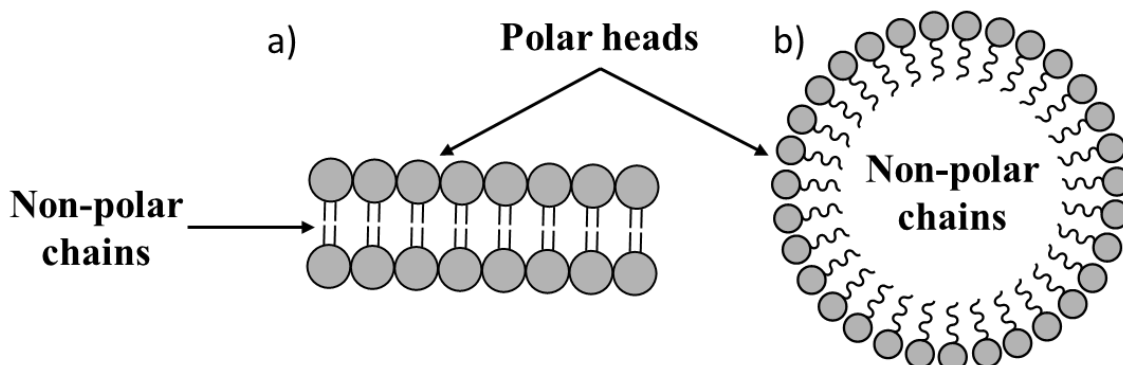


*Figure 6.1: Supramolecular self-assembled structures of surfactants in water. a) Bilayer membrane. b) Micelle.*

As introduced in chapter 2.3, in donor-acceptor (D-A) systems the electronic affinity would drive the aggregation of the molecular building blocks towards the formation of D-A stacking, leading to high disorder degree due to mixed A-A, A-D and D-D stacking phases. In the field of organic (opto)electronics as, for instance, in bulk heterojunction solar cells, phase segregation of the D-A components is fundamental to trigger the excitons separation and, therefore, photo-current. In this view, amphiphilic molecular design is considered a viable strategy to prevent the D-A stacking, by exploiting the incompatibility of the side-chains, to achieve high degree of order at the supramolecular level, via sub-nanometer phase segregation, and to ultimately modulate the properties of the resulting materials.<sup>2,3</sup>

Amphiphilic molecules with large  $\pi$ -conjugated cores have been employed to obtain excellent optoelectronic properties (e.g., charge transport, light emission, etc.), associated with characteristic nanostructures. Typical examples include hexa-peri-hexabenzocoronene,<sup>4</sup> perylene diimide,<sup>5-7</sup> porphyrin,<sup>8,9</sup> and fullerene<sup>10</sup> based amphiphiles, which tend to possess high charge carriers mobility when are organized in ordered self-assembled nanostructures. Donor-acceptor dyads are well known molecular systems that can undergo self-assembly, forming fibers or nanotubes, which exhibit good (photo)electrical characteristics.<sup>11-13</sup> This self-assembly capability renders them interesting components to be integrated in technologically advanced devices for (opto)electronics, such as field effect transistors,<sup>14</sup> photovoltaic solar cells,<sup>15,16</sup> and light-emitting diodes.<sup>17</sup> In this chapter we investigate on the self-assembly of an amphiphilic electron donor-acceptor (D-A) molecular dyad, based on a conjugated backbone, containing a tetrathiophene (4T) and a perylenediimide (PDI), connected by a conformationally rigid ethynylene bridge (**Figure 6.2**).<sup>18</sup> The aggregation of such molecule into supramolecular nanofibers is triggered by the combination of solvophobic (hydrophobic) interactions and exposure to white light. These architectures, exposing ethylene glycol in their external shell, are able to selectively interact with the water molecules from the atmosphere. Water trapping induces a dramatic change in their electrical properties and, for this reason, such materials were employed as active components in electrical resistive humidity sensors, exhibiting remarkably high sensitivity and fast response.<sup>18</sup>

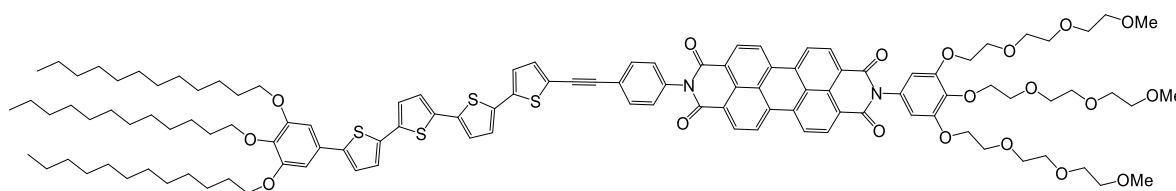


**Figure 6.2:** Molecular structure of PDI-4T dyad used in this chapter.

## 2 EXPERIMENTAL

---

### 2.1 MATERIALS AND SAMPLES PREPARATION

The PDI-4T molecular dyads were synthesized by our collaborators (Dr. Prof. Klaus Müllen group, Max Planck Institute for Polymer Research in Mainz, Germany) by using a Sonogashira coupling of an ethynyl-group-terminated 4T derivative with the corresponding iodophenyl-group-appended PDI derivatives, respectively, as described in literature.<sup>19</sup> The samples for AFM, SEM and electrical characterizations were prepared by drop casting 120  $\mu\text{l}$  of the fibers-containing solutions on thermally grown  $\text{SiO}_2/\text{Si n}^{++}$  substrates ( $230 \pm 10$ ) nm thick  $\text{SiO}_2$  (Fraunhofer Institute for Photonic Microsystems IPMS, Dresden, Germany), pre-patterned with interdigitated gold electrodes, featuring channel lengths ranging from 2.5 to 20  $\mu\text{m}$ . The substrates were sonicated in acetone (20 minutes) and isopropanol (20 minutes) and freshly cleaned with UV-ozone (10 minutes) prior use. The supramolecular aggregation was triggered in solution with a Newport solar simulator using a power density of 100  $\text{mW}/\text{cm}^2$ . The electrical characterizations were performed using a Keithley double channel source meter model 2636B connected to a micromanipulator probes station or to a custom made PCB board. The AFM images were recorded in intermittent contact mode using a Veeco/Bruker Dimension 3100 AFM, equipped with Nanoscope 4 controller and with a Bruker Multimode V AFM, equipped with Nanoscope 5 controller. SEM micrographs were recorded with a Quanta FEG 250 ESEM employing SE detector with an acceleration voltage of 5kV and a spot size of 3.5 nm. The structural investigation was performed by our collaborators (Dr. Laura Ferlauto and Dr. Silvia Milita, Istituto per la Microelettronica e Microsistemi (IMM)–CNR, Bologna, Italy) at the XRD1 beamline of the ELETTRA synchrotron facility of Trieste (Italy) by using a X-ray beam energy of 8 keV (corresponding to a wavelength of 1.55 Å) and a beam size of 200 x 200  $\mu\text{m}^2$ . The grazing incidence angle  $\alpha_i$  was fixed at 0.18° to allow the detection of the diffraction coming from the topmost surface of the sample. The 2D-GIXRD diffraction pattern was recorded using a 2D Pilatus detector. Due to the large dimensions of the sample (1.5 x 1.5  $\text{cm}^2$ ), the diffraction pattern is affected by the footprint of the X-ray beam, which reflects itself in a broadening of the

Bragg reflection. Optical and fluorescence microscopy images were taken with an Olympus BX51 optical microscope equipped with an X-Cite series 120 fluorescence cube 37088 U-MWBS3 (excitation wavelength from 450 to 490 nm). The XPS measurements were carried on using a Thermo Scientific K-Alpha X-ray photoelectron spectrometer with a basic chamber pressure of  $\sim 10^{-8}$  mbar and an Al anode as the X-ray source (x-ray radiation of 1486 eV). Spot sizes between 30  $\mu\text{m}$  and 400  $\mu\text{m}$  were used. The high-resolution spectra are an average of 60 scans. The XPS samples were deposited via drop-casting on  $\text{SiO}_2$ , using the solutions kept in dark for 6 months and the solutions exposed to white light for 20 hours. UV-Vis absorbance spectra were recorded in 1 cm optical path quartz cuvettes using a JASCO V670 UV-Vis-NIR spectrophotometer.

### 3 RESULTS AND DISCUSSIONS

---

The PDI-4T dyads were self-assembled into fibers in solution, by using a modified version of the solvent-induced precipitation (SIP) technique. This technique consists into boosting the aggregation of the building blocks, upon modification of their environment, by mixing a solution containing the molecules to be assembled with a second solvent. The key for this technique to be successful is to start from a concentrated solution of the chosen molecules in a proper good solvent and to employ a bad solvent, which is mixable with the starting one, to force the aggregation. Depending on the procedure it is possible to control the kinetic of the process going from a slow SIP, when the bad solvent is slowly added into the molecules-containing solution, to a fast SIP, when the molecules in solution are injected into the bad solvent.<sup>20</sup> In the case of our PDI-4T dyads, it was not possible to apply the classic SIP technique because of the amphiphilicity of the molecules, which can interact efficiently with both polar and non-polar solvents. This problem was solved by employing a procedure which is different from the one reported in literature by Li et al. on the same system.<sup>19</sup> In particular, 0.5 mg of the dyads were dissolved in 1 ml of tetrahydrofuran (THF). After complete dissolution, 200  $\mu\text{L}$  of such THF solution were added to 1 mL of deionized water. Differently from the procedure previously reported for generating fibers, using a THF/Methanol (MeOH) 9:1 solution, and resulting in extremely small aggregates, featuring a length of just

a few hundreds of nanometers, our approach relies on the use of a H<sub>2</sub>O/THF solution which is stable in environmental condition for several months. In particular, upon storage under dark condition, our H<sub>2</sub>O/THF solution showed high stability and retention of its optical properties, without exhibiting traces of precipitation (**Figure 6.3**).

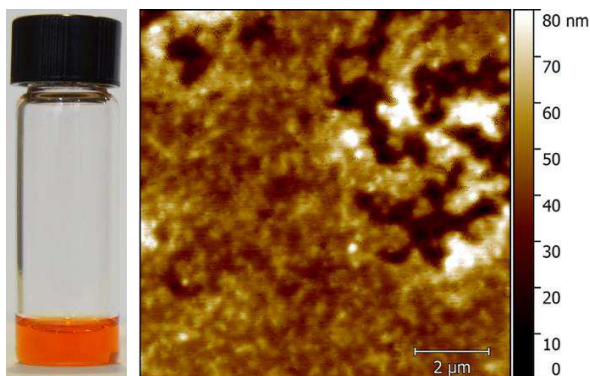


**Figure 6.3:** Optical and AFM pictures of PDI-4T in THF/H<sub>2</sub>O (kept in dark).

When such solution is applied to the basal plane of a SiO<sub>2</sub> substrate by drop-casting, amorphous films are obtained. By keeping the solution in a sealed glass vial on the lab bench, thus under daily light for at least one week, a color transition to light pink was observed. Such a color transition of the solution can be accelerated upon exposure to the white light of a solar

simulator (power density: 100 mW cm<sup>-2</sup>). After at least 10h of exposure, the solution slowly turns from orange to light pink. Such modification of the optical properties, which can be ascribed to a change on the molecular aggregation, was followed optically and with UV-Vis absorbance measurements, reported in **Figure 6.4**.

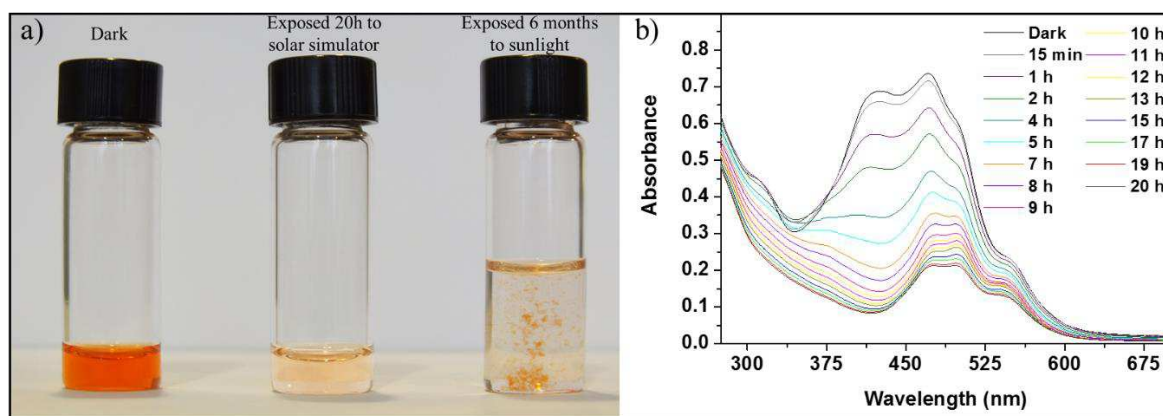


**Figure 6.4:** Evolution of PDI-4T solution's optical properties upon light exposure with white light (power density: 100 mW cm<sup>-2</sup>). a) Optical pictures. b) UV-Vis absorbance spectra.

To gain an insight into such aggregation process on a smaller scale, a microscopy study, as a function of the irradiation time, was performed. AFM imaging of drop cast films of the



solutions, after irradiation for few minutes, revealed the formation of small nanofibers with a length of few hundreds of nanometers which are randomly orientated on the SiO<sub>2</sub> surface (**Figure 6.5a**). Exposure to white light for about 10 h promotes the aggregation of the fibers into larger agglomerates (**Figure 6.5b-d**). In particular, from the SEM images in **Figure 6.5c-d**, it is possible to recognize the shape of the nanofibers inside the aggregates. Irradiation for 15 h leads to the formation of bigger bundles with a higher aspect ratio (**Figure 6.5e**), characterized by an average length of  $L \sim 17.1 \mu\text{m}$  and a width of  $W \sim 1.97 \mu\text{m}$ . Upon exposure of the solutions for more than 20 h, bundles of highly oriented ribbons are generated, appearing as macroscopic fibers networks, featuring a dendritic shape, a length of several millimeters and an average width of  $W \sim 1.65 \mu\text{m}$  (**Figure 6.5f-g**).

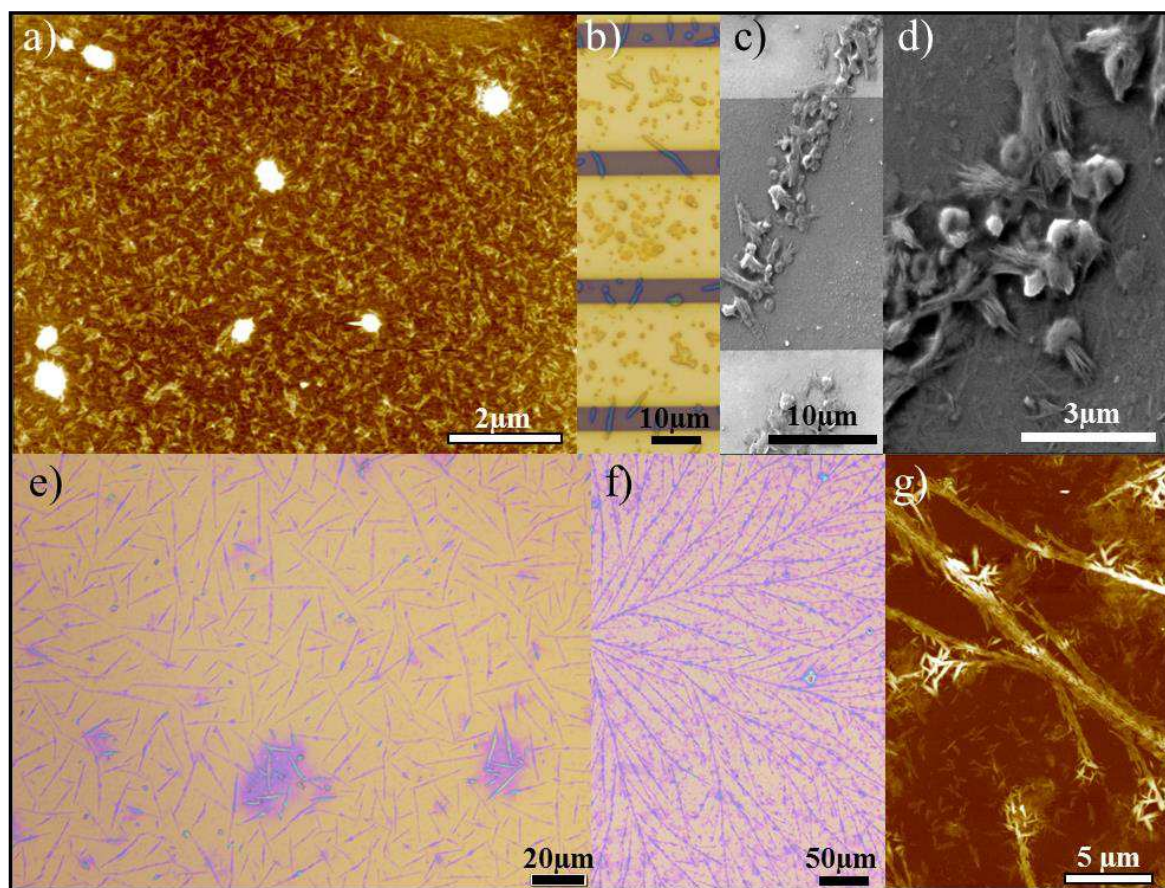


**Figure 6.5:** AFM, SEM and optical reflection images of drop cast PDI-4T solution upon different exposure times. a) Few minutes irradiation. (Image Z scale = 17 nm) b-d) 10 h irradiation. e) 15 h irradiation. f-g) 20 h irradiation. (AFM image Z scales = 110 nm).



Overall, the series of images shown in **Figure 6.5** provides for the first time a time-resolved evidence of the light-dependent evolution of the self-assembly: upon increase of the exposure time of the solution, the aggregation of the molecular building blocks into larger and larger fibers bundles is promoted. A deeper investigation on the structure of the aggregates with the AFM in the less coated areas of the samples, revealed the presence of laterally packed and intercoiled ribbons featuring a lengths of several micrometers (**Figure 6.6a**).

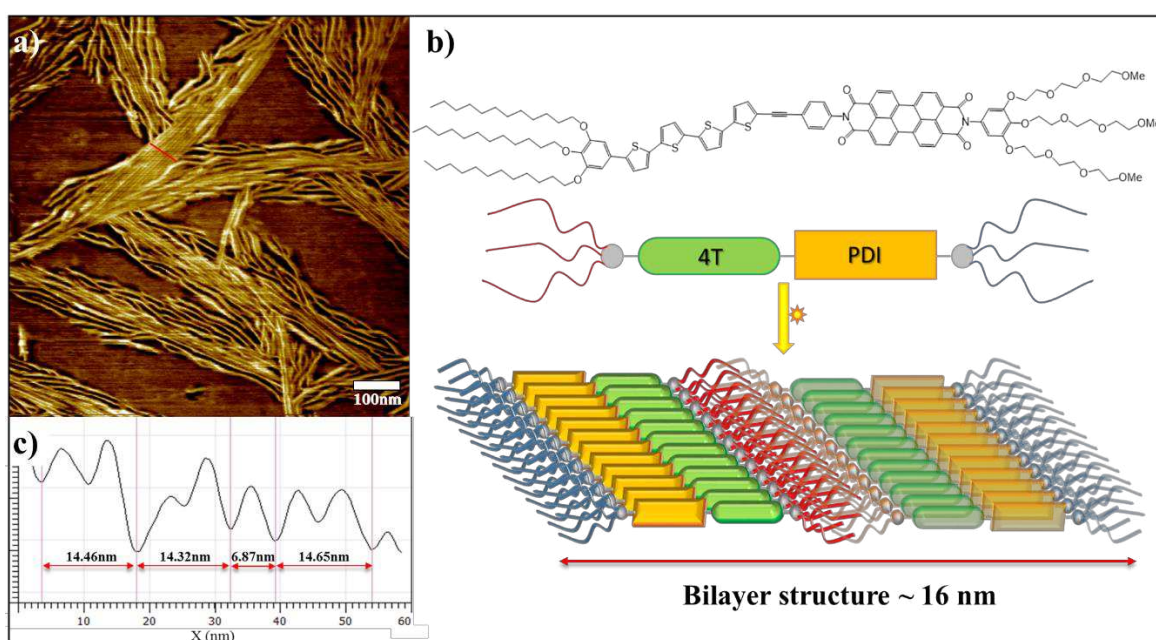


**Figure 6.6:** Insight on the supramolecular structure of PDI-4T fibers. a) AFM phase image showing layered features. b) Molecular structure and sketch of the supramolecular architecture. c) Cross section AFM profile showing the lateral size of the fibers.

From the cross section profiles in **Figure 6.6c**, it is possible to identify two different populations of ribbon widths, amounting to  $W \sim 7.0$  nm and  $W \sim 14.5$  nm. Being the contour length of the molecules, when the side chains adopt a fully elongated conformation, around 8 nm,<sup>19</sup> our result can be interpreted as an interdigitation of the alkyl substituents, belonging to adjacent ribbons, and eventual coiling of the side-groups. The 14.5 nm width suggests a supramolecular organization characterized by two laterally assembled molecules, in which all the hydrophobic side chains are in the middle of the structure, shielded from the water as shown in the schematic in **Figure 6.6b**. Interestingly, the use of water-based SIP turned out

to be the key to the fiber formation: irradiation of PDI-4T solutions in either THF,  $\text{CHCl}_3$ , *N,N*-dimethylformamide (DMF), acetone, ethanol, or isopropyl alcohol has not led to formation of fibrillary structures, even upon over 50 h light of irradiation. It is also worth of mention that the light irradiation, together with the effect of the polar water environment, allows to promote the self-assembly into fibrillary structures without involving the use of chlorinated solvents that, upon exposure to white light, form radicals which could be transferred to the molecules, promoting the self-assembly as reported by Moulin et al. in the case of light-induced self-assembly of triarylamine derivatives.<sup>21</sup> In our case the key role played by light irradiation in the fibers growth, likely involves electron transfer and electrostatic interactions, generated in the interaction between light and the donor-acceptor conjugated core of the dyads. However, X-ray photoelectron spectroscopy (XPS) analysis on PDI-4T drop-cast solutions before and after irradiation provided evidence of an increase of the S2p peak at 168.2 eV, being unambiguously assigned to oxidized sulfur atoms, from 4.31% up to 46.4%, demonstrating that an intense light exposure leads also to an oxidation of the thiophene rings in the molecule (**Figure 6.7**).

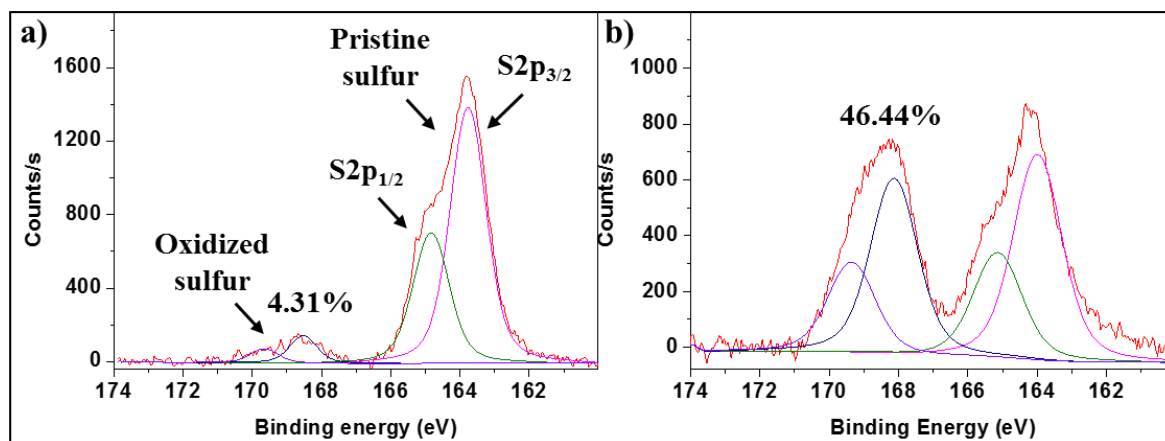


**Figure 6.7:** XPS spectra of PDI-4T drop cast solutions. a) Solution kept in dark for 6 months. b) Solution exposed to white light for 20 hours (power density = 100 mW/cm<sup>2</sup>).

To assess a structural insight into the geometry of the aggregates and into the molecule/molecule interactions, at the supramolecular level, grazing incidence X-ray diffraction (GIXRD) investigations of the fibers-containing samples were performed.

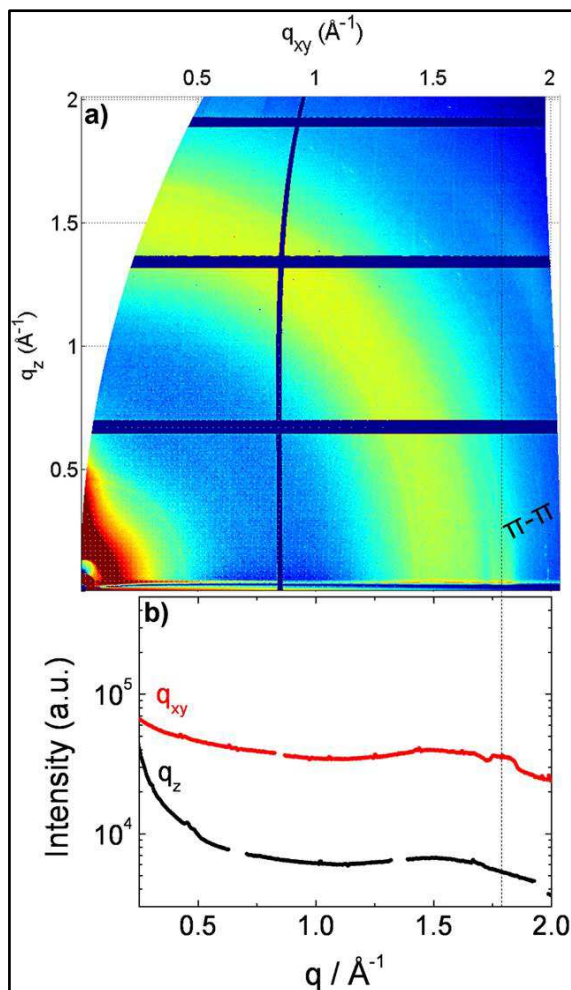


**Figure 6.8:** a) 2D-GIXRD pattern of PDI-4T bundles of fibers together with b) corresponding scattering intensity integrated along the out-of-plane ( $q_z$ ) and in-plane ( $q_{xy}$ ) directions.

The 2D X-ray pattern, reported in **Figure 6.8**, presents a main peak at position  $q_{xy} = 1.78 \text{ \AA}^{-1}$  which corresponds to a d-spacing of  $3.5 \text{ \AA}$ , typical distance for  $\pi$ - $\pi$  stacking. Since the peak is perturbed by the large footprint of the X-ray beam, a realistic estimation of the lateral dimension of the crystalline domains is not possible.<sup>22</sup> Being in the in-plane direction, this peak indicates that the dyad molecules adopt an edge-on orientation with respect to the basal plane of the substrate, in agreement with the proposed model in **Figure 6.6b**. Since the whole growth and the aggregation processes are performed in a strongly polar water environment, it is reasonable to imagine that the molecules within the fibers are oriented to expose the TEG hydrophilic side chains, while shielding the hydrophobic aliphatic ones. According to this model, the fibers should be fully decorated by TEG chains which

are known to be hygroscopic, as already discussed in the previous chapters, in other words, to be able of catching water molecules from the atmosphere. From the electrical point of view, such supramolecular nanofibers behave as electrical conductors and did not exhibit any field-effect when characterized in a three-terminal FET device configuration. By exploiting such electrical properties of the obtained fibrillary structures, it was possible to employ the measured electrical resistance to probe the behavior of such aggregates upon exposure to humidity. Such an exposure revealed a high sensitivity to the presence of water molecules in the atmosphere, confirming that the hydrophilic chains are in the external part of the ribbons, enabling dipole-dipole interactions and, in particular, hydrogen bonding with water molecules. These interactions are strong enough to align and compress the molecules

together inside the aggregates, decreasing the distance of the  $\pi$ - $\pi$  stacking, in accordance with XRD study reported for similar systems.<sup>23,24</sup> The decreasing  $\pi$ - $\pi$  distance, leads to an exponential increase of the charge transport through the fibers and thus of the conductivity of the self-assembled architectures. Therefore, the conductivity can be tuned with the relative humidity (RH) of the environment: thus our system can be employed as an electrical resistive type organic humidity sensor. Noteworthy, the adsorption and desorption of water on the fiber's surface is a fully reversible process. The response speed was measured by sending a pulsed flow of humid air over the sample during the application of a constant bias of 5 V. The results portrayed in **Figure 6.9b** show a response speed of about 26 ms with a good recovery time and an ultimate 100% reversibility. The calibration of the devices was carried out inside a chamber with a controlled atmosphere, in which the RH can be increased from 0% to 75% while performing the *in-situ* electrical measurement in real time using an *ad-hoc* custom PCB board (**Figure 6.9c**). **Figure 6.9a** displays the results of the calibration for two different channel lengths using the same applied voltage.

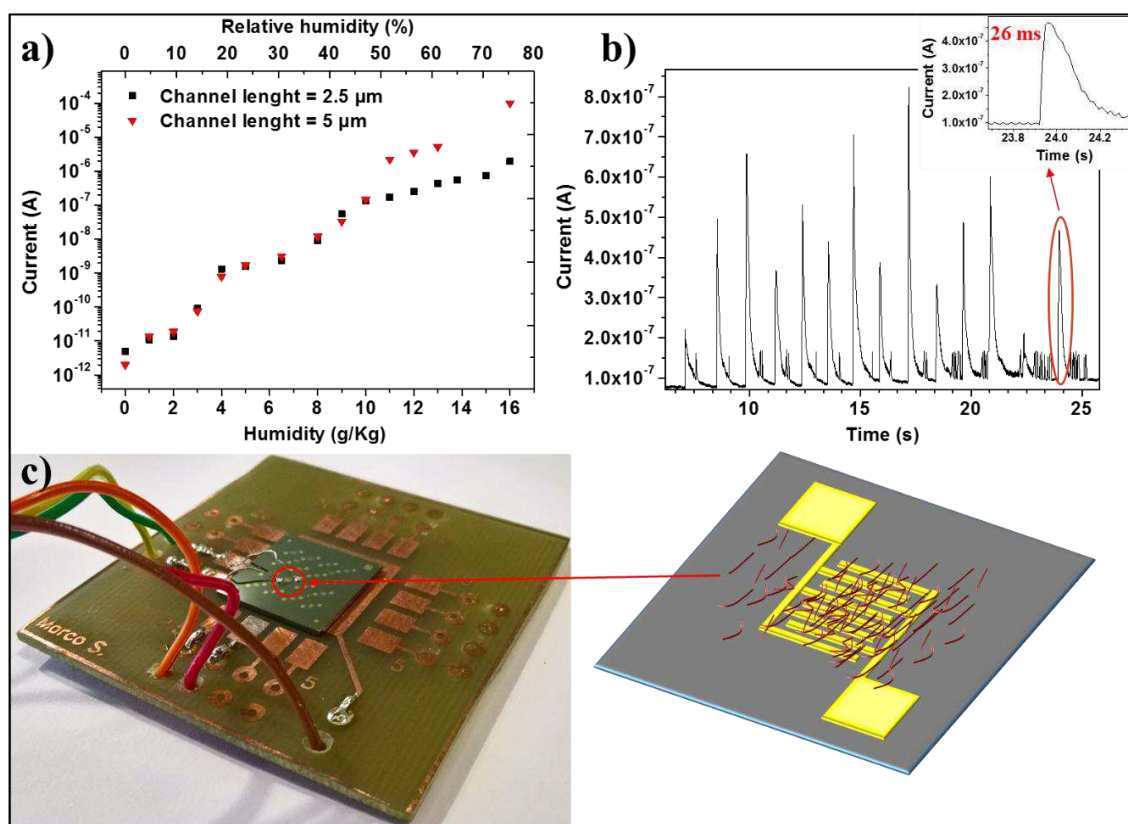


**Figure 6.9:** PDI-4T based electrical resistive humidity sensors (Applied bias = 5 V). a) Calibration of the devices within the range between 0 to 75% RH. b) Electrical response to short pulses of humid air. c) Picture of the custom setup used for *in-situ* electrical measurements.

The measurements reported in **Figure 6.9a** demonstrate that, when larger channel lengths are used, the sensitivity for higher humidity levels increases, as a result of the greater exposed surface area of the fibers between the gold contacts, that can interact with the water molecules.

The calibration plot in **Figure 6.9a** allowed to quantify the dependence of the measured current upon changes in the environmental humidity in the chamber, and revealed an exponential growth. The measured values of current range from a few pA, measured at RH  $\sim$  0%, up to tens of milliamps, measured at RH  $\sim$  75%, with an overall current variation exceeding seven orders of magnitude.

Interestingly, control experiments on such PDI-4T supramolecular nanofibers, revealed that the current response, observed and discussed above, is also strongly selective for water molecules. On this regard, the plots reported in **Figure 6.10**, portrays the electrical response of our PDI-4T based humidity sensors upon exposure to vapors from different solvents such as ethanol, methanol, and ethyl ether.

As revealed from such measurements, among the series of explored molecules, only methanol has been detected, resulting in an increased current passing through the fibers. However, the output signal in current changes has shown to be several (almost 3) orders of magnitude smaller and therefore negligible, compared to the one given by water under the same conditions. Such a finding can be justified by the sensing model provided and above discussed: water molecules features two  $-OH$  bonds and can provide two hydrogen atoms for the formation of hydrogen bonding, with the surrounding molecules. Moreover, water exhibits a small molecular size which allows it to diffuse within the TEG chains which decorates our 1D nanostructures. Upon absorption, water molecules can diffuse between the TEG chains, bridging them by mean of hydrogen bonding and providing a strong contribution in increasing the electrical current flowing through the fibers. On the other hand, ethanol and diethyl ether are too large to diffuse between the TEG chains and cannot provide any electrical change upon interaction with the PDI-4T nanofibers. In the case of methanol, its smaller size allows it to diffuse between the TEG, but the presence of just one hydrogen atom as a donor site for hydrogen bonding makes it less effective than water into bridging the chains, resulting in a smaller output signal upon interaction with the PDI-4T nanofibers.



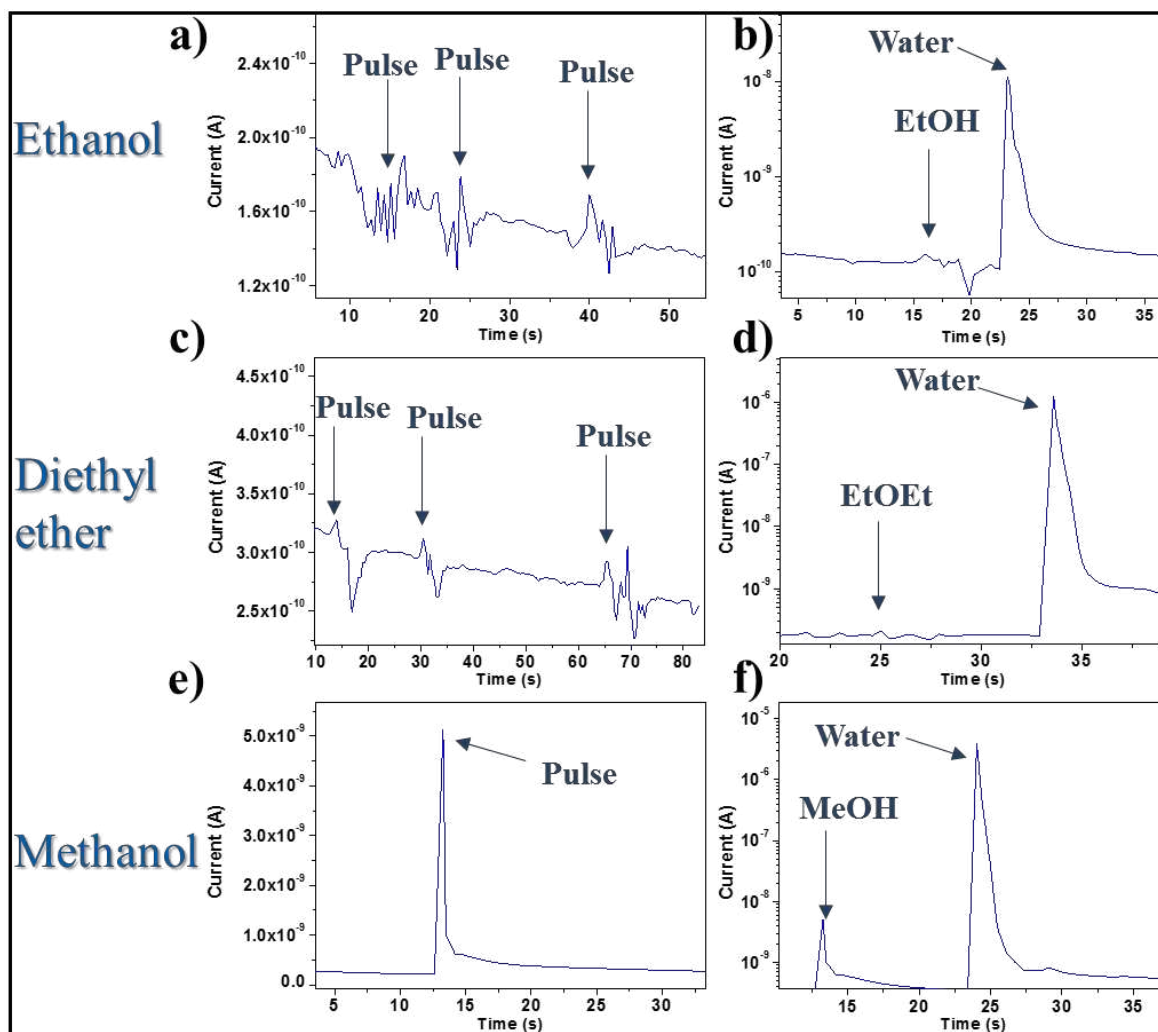


**Figure 6.10:** PDI-4T electrical response upon exposure to different solvent's vapors (Applied bias = 5 V; Channel length = 5  $\mu\text{m}$ ). a) Pulses of ethanol. b) Comparison between ethanol and water. c) Pulses of diethyl ether. d) Comparison between diethyl ether and water. e) Pulses of methanol. f) Comparison between methanol and water.

## 4 CONCLUSIONS

In conclusion, a novel approach, based on white light irradiation, acting as a remote controller for the self-assembly of amphiphilic D-A conjugated dyads into ordered structures, was developed and optimized. The joint effect of light irradiation and SIP in an environmentally friendly water solvent made it possible to form supramolecular nanoribbons, exhibiting phase segregated side chains. Upon tuning the exposure time, it was possible to control and tune the size of the aggregates, forming fibrillary bundles, which can

grow from few micrometers up to millimeter scale, featuring a dendritic structure. Such ultra-long 1D architectures possess an external shell exposing hydrophilic ethylene glycol moieties able to catch and reversibly absorb water molecules from the atmosphere. Upon absorption of water, the  $\pi$ - $\pi$  stacking distances between the aromatic cores of the dyads can be reversibly decreased. Such architectures, were therefore implemented in electrical devices and employed as active materials to build humidity sensors. The resulting PDI-4T-based resistive humidity sensor exhibited ultrafast response and extremely high sensitivity. To the best of our knowledge, the seven orders of magnitude change in current signal, by varying the RH from 0% to 75%, is the highest reported in literature for resistive humidity sensors based on organic molecules. Moreover, the reported response speed of 26 ms is in line with the best data recently reported on capacitive sensors based on graphene oxide continuous films exhibiting 30 ms response speed<sup>25</sup> and on resistive sensors integrating organic fibers which feature a 10 ms response speed, being the fastest ever reported.<sup>24</sup> As an additional figure of merit, the obtained PDI-4T humidity sensors have shown remarkable selectivity for water molecules compared to other polar solvent's vapor, which is a huge advantage compared to graphene or oxide based materials which, as explained in chapter 2.4, lack in selectivity.



## 5 REFERENCES

---

- 1 Hamley, I. W. *Introduction to Soft Matter: Synthetic and Biological Self-Assembling Materials*. (Wiley, 2007).
- 2 Yamamoto, Y. *et al.* Photoconductive coaxial nanotubes of molecularly connected electron donor and acceptor layers. *Science* **314**, 1761-1764, (2006).
- 3 Zhang, W. *et al.* Supramolecular linear heterojunction composed of graphite-like semiconducting nanotubular segments. *Science* **334**, 340-343, (2011).
- 4 Hill, J. P. *et al.* Self-assembled hexa-peri-hexabenzocoronene graphitic nanotube. *Science* **304**, 1481-1483, (2004).
- 5 Che, Y., Datar, A., Balakrishnan, K. & Zang, L. Ultralong nanobelts self-assembled from an asymmetric perylene tetracarboxylic diimide. *J Am Chem Soc* **129**, 7234-7235, (2007).
- 6 Zhang, X., Chen, Z. & Wu, F. Morphology Control of Fluorescent Nanoaggregates by Co-Self-Assembly of Wedge- and Dumbbell-Shaped Amphiphilic Perylene Bisimides. *J Am Chem Soc* **129**, 4886-4887, (2007).
- 7 Zhang, X., Rehm, S., Safont-Sempere, M. M. & Wurthner, F. Vesicular perylene dye nanocapsules as supramolecular fluorescent pH sensor systems. *Nat Chem* **1**, 623-629, (2009).
- 8 Sakurai, T. *et al.* Electron- or hole-transporting nature selected by side-chain-directed pi-stacking geometry: liquid crystalline fused metalloporphyrin dimers. *J Am Chem Soc* **133**, 6537-6540, (2011).
- 9 Sakurai, T. *et al.* Prominent electron transport property observed for triply fused metalloporphyrin dimer: directed columnar liquid crystalline assembly by amphiphilic molecular design. *J Am Chem Soc* **130**, 13812-13813, (2008).
- 10 Munoz, A., Illescas, B. M., Sanchez-Navarro, M., Rojo, J. & Martin, N. Nanorods versus nanovesicles from amphiphilic dendrofullerenes. *J Am Chem Soc* **133**, 16758-16761, (2011).
- 11 Hizume, Y. *et al.* Chiroselective assembly of a chiral porphyrin-fullerene dyad: photoconductive nanofiber with a top-class ambipolar charge-carrier mobility. *J Am Chem Soc* **132**, 6628-6629, (2010).
- 12 Nishizawa, T., Tajima, K. & Hashimoto, K. Supramolecular formation of fibrous nanostructure in donor-acceptor dyad film. *J Mater Chem* **17**, 2440-2445, (2007).
- 13 Huang, H. L. *et al.* Morphology Control of Nanofibril Donor-Acceptor Heterojunction To Achieve High Photoconductivity: Exploration of New Molecular Design Rule. *J Am Chem Soc* **135**, 16490-16496, (2013).
- 14 Pfattner, R. *et al.* Photo-induced intramolecular charge transfer in an ambipolar field-effect transistor based on a  $\pi$ -conjugated donor-acceptor dyad. *J Mater Chem C* **1**, 3985, (2013).
- 15 Chidichimo, G. & Filippelli, L. Organic Solar Cells: Problems and Perspectives. *Int J Photoenergy* **2010**, 1-11, (2010).
- 16 Ye, T., Singh, R., Butt, H. J., Floudas, G. & Keivanidis, P. E. Effect of local and global structural order on the performance of perylene diimide excimeric solar cells. *ACS Appl Mater Interfaces* **5**, 11844-11857, (2013).

- 17 Segura, J. L., Herrera, H. & Bäuerle, P. Oligothiophene-functionalized naphthalimides and perylene imides: design, synthesis and applications. *J Mater Chem* **22**, 8717, (2012).
- 18 Squillaci, M. A. *et al.* Self-Assembly of an Amphiphilic pi-Conjugated Dyad into Fibers: Ultrafast and Ultrasensitive Humidity Sensor. *Adv Mater* **27**, 3170-3174, (2015).
- 19 Li, W. S. *et al.* Use of side-chain incompatibility for tailoring long-range p/n heterojunctions: photoconductive nanofibers formed by self-assembly of an amphiphilic donor-acceptor dyad consisting of oligothiophene and perylenediimide. *Chem Asian J* **5**, 1566-1572, (2010).
- 20 Savage, R. C. *et al.* Integration of self-assembled discotic-based fibres into field-effect transistors: a comparison of preparation approaches. *J Mater Chem* **21**, 206-213, (2011).
- 21 Moulin, E. *et al.* The hierarchical self-assembly of charge nanocarriers: a highly cooperative process promoted by visible light. *Angew Chem Int Ed Engl* **49**, 6974-6978, (2010).
- 22 Smilgies, D. M. Scherrer grain-size analysis adapted to grazing-incidence scattering with area detectors. *J Appl Crystallogr* **42**, 1030-1034, (2009).
- 23 Bhattacharyya, A. *et al.* In-Situ GISAXS Study of Supramolecular Nanofibers having Ultrafast Humidity Sensitivity. *Sci Rep* **7**, 246-246, (2017).
- 24 Mogera, U., Sagade, A. A., George, S. J. & Kulkarni, G. U. Ultrafast response humidity sensor using supramolecular nanofibre and its application in monitoring breath humidity and flow. *Sci Rep* **4**, 4103, (2014).
- 25 Borini, S. *et al.* Ultrafast Graphene Oxide Humidity Sensors. *ACS Nano* **7**, 11166-11173, (2013).

# Chapter 7

## 2D laser reduced graphene oxide films for ozone sensing

### 1 INTRODUCTION

---

In this last experimental chapter the interest is shifted from the sensing of moisture to the detection of another gaseous compound, naturally present in the atmosphere, which in this case is also harmful for our health: ozone. Ozone sensors will be fabricated by using laser reduced graphene oxide (L-rGO) active materials, fabricated with a novel approach, starting from commercial GO solutions.

GO is a derivative of graphite in which oxygen containing groups are introduced within the lattice in order to facilitate the exfoliation of the bulk material into atomically thick monolayers, which are dispersible in water and polar solvents. The introduction of the oxygen containing groups dramatically improves the processability of such material compared to pristine graphene, at the expenses of the electrical and mechanical properties. As already discussed in chapter 2.4, numerous processes have been developed over the years to reduce graphene oxide as an alternative, cheap and up-scalable source of high quality graphene. Among all the reported techniques, this chapter will be focused into the study of the photo and, in particular, photo-thermal reduction processes of graphene oxide by means of high energy lasers. As compared with conventional thermal and chemical routes, photo-reduction of GO shows the distinct advantages of high efficiency, low cost, tunable reduction

degree, and flexible patterning with high spatial resolution. Even more important is the versatility for the fabrication and integration of graphene-based micro-devices.<sup>1</sup> So far, space confined laser reduction of GO has been reported with either short wavelength lasers such as extreme UV ( $\lambda = 46.9$  nm) or excimer<sup>2,3</sup> ( $\lambda = 248$  nm) sources, likely involving photo-chemical processes, with visible sources, such as Nd:YAG<sup>4,5</sup> ( $\lambda = 355$  nm) or diodes<sup>6,7</sup> ( $\lambda = 532, 663$  nm), involving both photo-chemical and photo-thermal processes, and even with pulsed IR sources such as femtosecond<sup>8</sup> ( $\lambda = 790$  nm) or picosecond<sup>9</sup> ( $\lambda = 1064$  nm) lasers, mostly involving photo-thermal reduction processes. The only limitation consists in the difficult integration of those patterned structures into electrical devices, due to the presence of the unused GO film surrounding the rGO areas.<sup>10</sup>

The project described in this chapter reports on the study and optimization of a novel technique, to produce and reduce ultra-uniform graphene oxide (GO) films, with controlled thickness and optoelectronic properties. Such films were reduced into high quality rGO by using a pulsed IR laser, directly patterning conductive path of rGO into an insulating matrix of GO. Our results show lowest volume resistivity of  $0.98\Omega/\text{sq}/\text{mil}$  and optical transmittance of 81% (at 550 nm) for laser reduced GO (L-rGO) layers. Additionally, we demonstrate a method for advancing rGO device fabrication by removing the unused GO films with diluted ammonia solutions. The obtained L-rGO films are then implemented as active material in electrical resistive sensors for the detection of few ppm of ozone in atmospheric environment.

## 2 EXPERIMENTAL

---

### 2.1 MATERIALS AND SAMPLES PREPARATION

The GO employed for this project is commercially available and was purchased from Graphenea in water dispersion (4 mg/ml). According to the manufacturer, the content of monolayer GO in the starting dispersions is >95%. The GO films with controlled thickness were prepared by spin-coating from water/ethanol solutions using a speed of 3000 rpm for 150 s with an acceleration of 1500 rpm/s. The optical characterizations were performed on quartz substrates, while the electrical ones are performed on thermally grown SiO<sub>2</sub>/Si n<sup>++</sup> substrates (230 ± 10) nm thick SiO<sub>2</sub> (Fraunhofer Institute for Photonic Microsystems IPMS, Dresden, Germany). All the substrates were sonicated in acetone (20 min), in isopropanol (20 min) and freshly cleaned with UV-ozone (10 min), prior use. Metal electrodes were deposited on the rGO patterned structures by thermal evaporation. An additional layer of Cr was evaporated as adhesion layer before Au evaporation to improve the adhesion between gold and rGO, increasing the mechanical resistance of the electrodes. GO reduction system consists of a motorized XYZ-stage with a sample chamber mounted on it and an optical setup that includes pulsed laser source and respective optical parts (**Figure 7.3a**). XYZ stage is operated by stepper motor controller Newport High-Performance Motion Controller XPS-Q4, allowing for single step of 10 nm in any horizontal direction. The teflon-made sample chamber has cylindrical shape and is designed to fit 2-inch wafer. It features a quartz window, flexible gas inlet and outlet pipes and a metallic sealing cover (**Figure 7.3b**). The sample chamber can be pressurized up to 1 bar with different types of gasses: air, forming gas (FOG = 5% H<sub>2</sub>, 95% N<sub>2</sub>) and nitrogen. High intensity light pulses are produced by Yb-doped fiber laser emitting at 1064 nm (FiberLast FLAST-Nano), focused in a spot of 8 μm. Typical pulse width and repetition rate are set to 70 ns and 90 kHz respectively. Maximum average laser power and peak power reach 10 W and 20 kW respectively. The electrical characterizations were performed by using a Keithley double channel source meter model 2636B connected to a probes station or to a custom made PCB board. The sheet resistance of the films was measured by employing a 4 micromanipulator probe station in a square

geometry by employing the Van Der Pauw technique<sup>11</sup>. The AFM images were recorded in intermittent contact mode using a Veeco/Bruker Dimension 3100 AFM, equipped with Nanoscope 4 controller and standard Bruker TESP-V2 tips, while the C-AFM images were recorded in contact mode using conductive Pt/Ir coated tips (Bruker SCM-PIC) with a Bruker Multimode V AFM, running with Nanoscope 5 controller. The XPS measurements were carried on using a Thermo Scientific K-Alpha X-ray photoelectron spectrometer with a chamber pressure of  $\sim 10^{-8}$  mbar and an Al anode as the X-ray source (X-ray radiation of 1486 eV). Spot sizes between 30  $\mu\text{m}$  and 400  $\mu\text{m}$  were used. The high-resolution spectra are an average of 60 scans. UV-Vis absorbance spectra were recorded using a JASCO V670 UV-Vis-NIR spectrophotometer. Optical and photoluminescence images were taken with an Olympus BX51 optical microscope equipped with an X-Cite series 120 fluorescence cube 37088 U-MWBS3 (excitation wavelength from 450 to 490 nm). Raman spectra were recorded in a Confocal Raman spectrometer (Renishaw inVia Reflex) using a laser excitation wavelength of 532 nm and power of  $\sim 0.6$  mW.

Ozone sensing experiments were performed in dedicated setup, which consists of an ozone generator, a sample exposure chamber, control and data acquisition equipment (**Figure 7.15a**). Ozone generator converts pressurized high purity oxygen into ozone by means of ultraviolet radiation. The latter is generated by an arc-discharge deuterium lamp (Hamamatsu L7293) mounted onto a reactor chamber in such a way that oxygen stream remains illuminated with lamps snout. The deuterium lamp produces continuous spectrum in the range 110-400 nm, part of which gets absorbed by the oxygen molecules and results in the formation of atomic oxygen (O) and ozone ( $\text{O}_3$ ). Molecular oxygen ( $\text{O}_2$ ) and ozone ( $\text{O}_3$ ) mixture then exists from the reactor chamber and enters in the sample chamber through a teflon pipe. The sample is mounted on FR4 printed circuit board (PCB) with a help of conductive silver paste, to ensure mechanical stability, electrical and thermal contact. Sample PCB has 20 W resistive heater on its bottom side and a temperature sensor located nearby the devices. This allows for rapid sample heating with the help of a temperature controller to desorb physisorbed gas molecules from L-rGO surface. Contact pads of L-rGO sensor under test are bonded with indium metal wires onto PCB pads for electrical connection with Keithley 2636 Source Meter.



### 3 RESULTS AND DISCUSSIONS

---

The commercial GO dispersion purchased from Graphenea consists in a stable dispersion of GO flakes, mostly monolayers ( $\sim 95\%$ ), featuring a lateral size ranging from 1 to 40  $\mu\text{m}$  and regular shape, as highlighted in **Figure 7.1**.

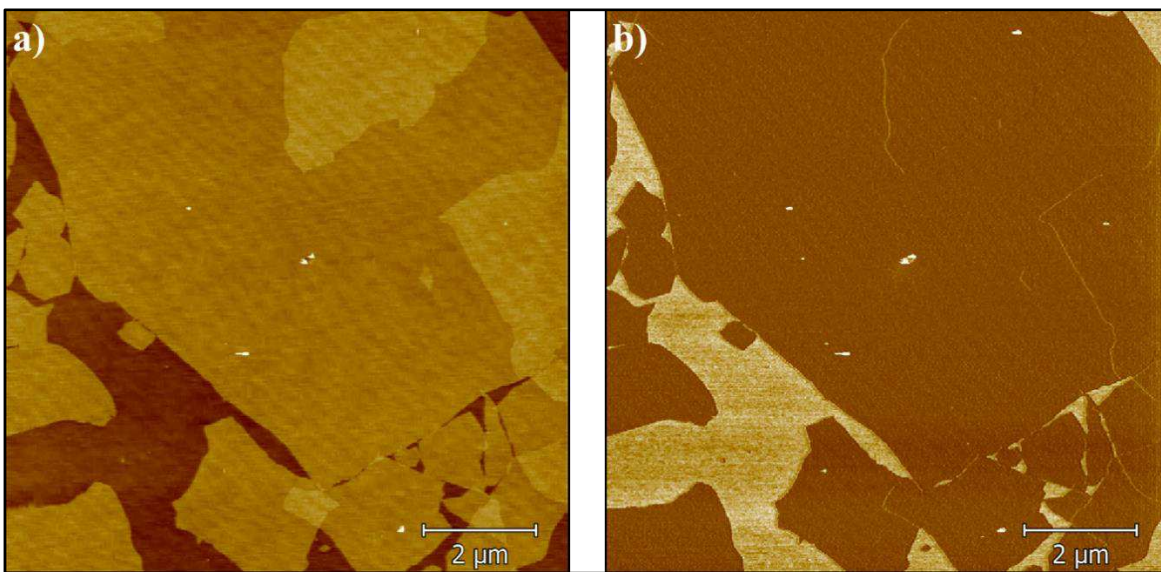


*Figure 7.1: AFM a) height (Z scale = 11 nm) and b) phase images of GO from Graphenea on SiO<sub>2</sub>.*

A procedure was optimized to obtain uniform and ultra-flat graphene oxide (GO) films over large areas (up to  $2.5 \times 2.5 \text{ cm}^2$ ) with controlled thickness. The key for the realization of such films was to dilute the commercial 4 mg/ml GO water solution with ethanol, up to 1:3 water/ethanol ratio, lowering the final concentration of GO solutions to 1 mg/ml. The dilution, followed by mild ultra-sonication, enables to achieve a higher amount of monolayers GO with respect to the starting solution, while the use of ethanol improves the uniformity of the produced films by increasing the wettability of the substrates and by lowering the boiling point of the solution, from  $100^\circ\text{C}$  (water) to  $78.1^\circ\text{C}$  (water/ethanol mixture).<sup>12</sup> Moreover, ethanol is not a good solvent for GO and it is not polar enough to solubilize back the GO flakes from dry films. This characteristic allows to perform multiple successive spin-coating depositions on the same substrate to increase the film's thickness



without modifying the morphology nor affecting the film underneath. Each spin-coating step increases the overall thickness of ca. 2 nm, allowing to finely control the thickness of the resulting films. The explored thickness ranges between  $2.8 \pm 0.4$  nm and  $17 \pm 1$  nm, obtained, respectively, with one and ten successive deposition steps (**Figure 7.2**).

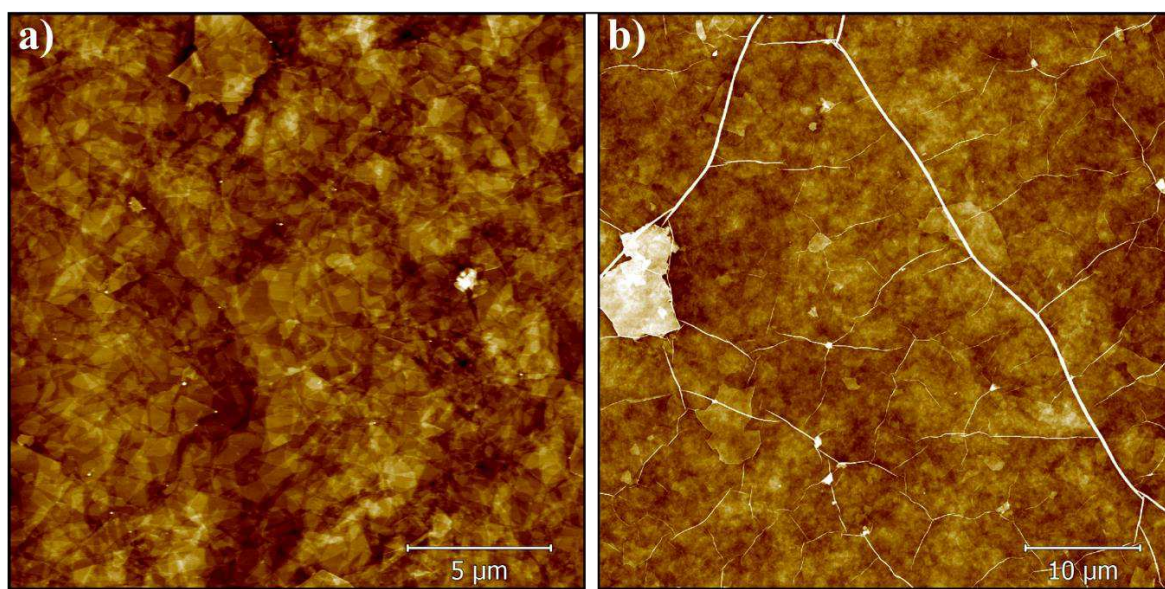


**Figure 7.2:** AFM topographical image of GO uniform films with different thickness. a) 3 nm thick film (image Z scale = 14 nm). b) 17 nm thick film (image Z scale = 60 nm).

From the morphological point of view, the two films reported in **Figure 7.2** show major differences: in the thin  $\sim 3$  nm film reported in **Figure 7.2a** it is still possible to recognize the shapes of the overlapping flakes and the film exhibits neither protrusion nor wrinkles, featuring a roughness of 1.4 nm. On the other hand, in the thick  $\sim 17$  nm thick film in **Figure 7.2b** it is not possible to identify the single flakes anymore because of the high overlapping, and the film presents wrinkles which cause an increased roughness up to  $\sim 8.2$  nm (4.3 nm excluding the wrinkles).

The GO films reduction was performed by placing the samples in a sample chamber, mounted on a XYZ stage, moving under an optical setup, which includes pulsed laser source and its focusing objective (**Figure 7.3a**). XY scans are operated by stepper motor controller, allowing for single step of 10 nm in any horizontal direction. The sample chamber is hermetically sealed with quartz window and provided with gas inlet and outlet pipes (**Figure**

**7.3b).** For the preliminary experiments, the sample chamber was pressurized up to 1 bar with different types of gasses: air, forming gas (FOG = 5% H<sub>2</sub>, 95% N<sub>2</sub>) and nitrogen.

High intensity light pulses are produced by Yb-doped fiber laser emitting at 1064 nm, employing a typical pulse width of 70 ns and repetition rate 90 kHz.

The laser spot, after being focused by the focusing objective, features a circular shape and a nominal diameter of  $\sim 8 \mu\text{m}$ , which cannot be modified by the user. Both sample position and laser power are controlled by the software and are sequenced according to the desired rGO pattern.

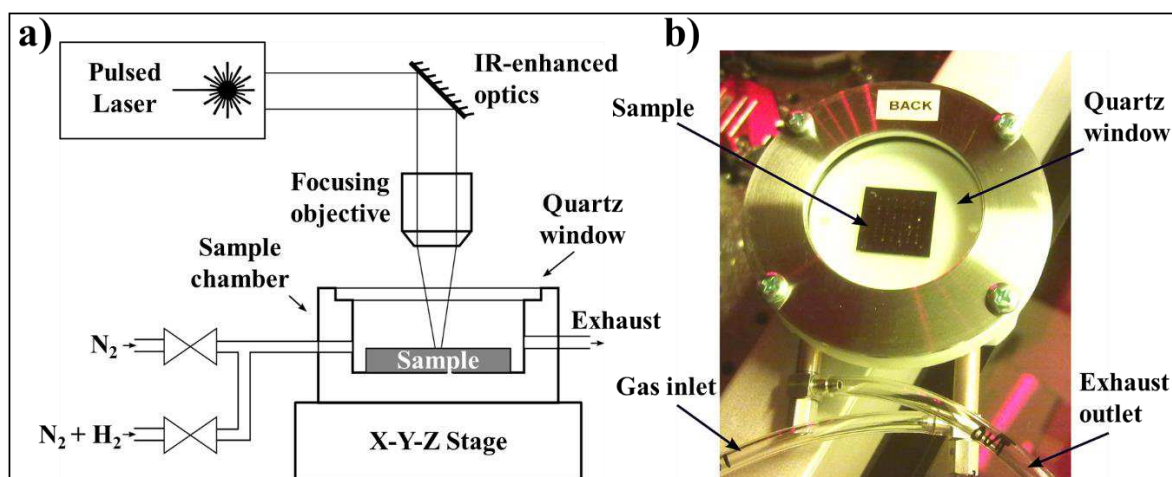


**Figure 7.3:** Laser writer setup used for the Laser assisted reduction of GO. a) Scheme of the setup. b) Optical picture of a sample inside the sample chamber.

The final electrical performances of the resulting L-rGO films are affected by several parameters, including power of the laser, overall exposure dose per spot, thickness of the starting GO film and nature of the atmosphere in which the reduction is performed. In order to optimize the performances and to find the best conditions for the laser reduction of GO, a systematic study was performed, by exploring different film's thickness, reduction atmosphere, laser's intensities, scan speeds and substrates. This study was performed by preparing series of films with different thickness on SiO<sub>2</sub> and quartz substrates and drawing patterns of 36 squared areas of  $400 \times 400 \mu\text{m}^2$  per substrate, under different conditions and using the layout reported in **Figure 7.4**.

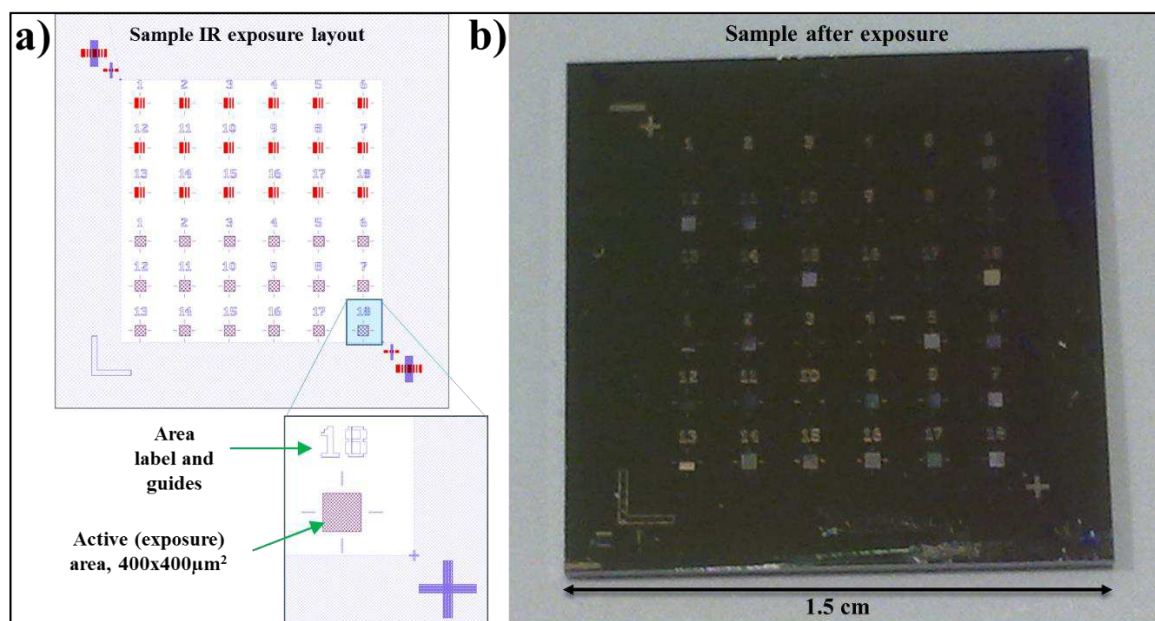


**Figure 7.4:** Layout for the systematic study of GO Laser reduction. a) Scheme of the layout. b) Optical picture of a sample series on SiO<sub>2</sub> after exposure.

The GO films were exposed to the laser by drawing, in a raster scan, 10 μm wide horizontal lines with a distance step of 5 μm between the centers of each line, meaning that each spot is exposed twice, to achieve a uniform exposure over the whole area.

Preliminary XPS characterizations were performed to study the evolution of the system, from the compositional point of view, upon laser exposure, by probing the core photoelectrons of the carbon atoms.

The evolution of carbon C1s peak, reported in **Figure 7.5**, showed that, by increasing the power density of the laser, there is an initial gradual decrease of the peaks around 287.5 eV and 289 eV, corresponding to the oxidized carbon atoms. Such evolution is also accompanied by a sharpening and a small shift of the peak around 286.6 eV, corresponding to the C-C sp<sup>2</sup> bond, meaning that the reduction process is occurring.<sup>13,14</sup>

By further increase of the power density the films start to be damaged and oxidized back, by the high energies employed for the process.

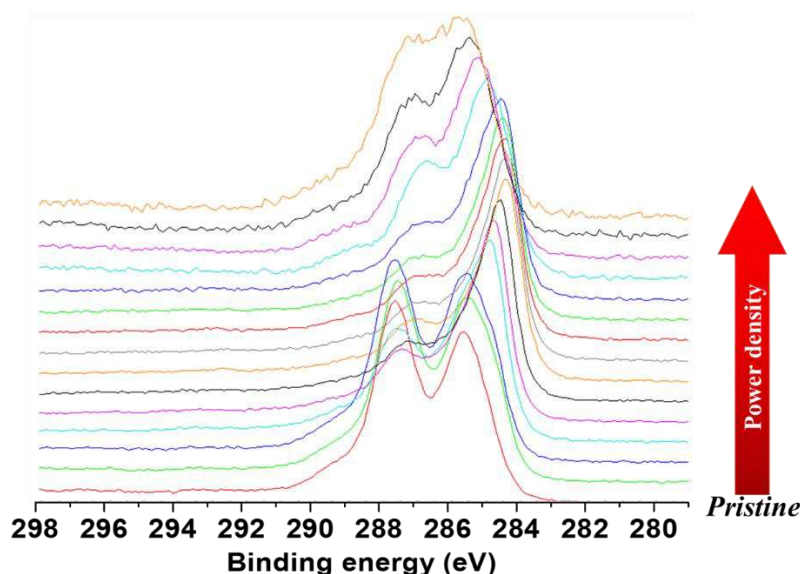


Figure 7.5: XPS C1s spectra of GO films exposed to IR laser at different power densities.

XPS characterization also allows to perform quantitative and qualitative analysis of the species covalently attached to carbon atoms. By performing a careful fitting of the peaks, it is then possible to gain an insight into the nature and the relative abundance of each oxygen containing group bonded to the carbon lattice. In such way, it is possible to differentiate between hydroxyl, carboxyl and carbonyl groups, from the different C1s binding energy each of this group provide to the electrons, within the carbon atom, to which they are connected (**Figure 7.6a**).

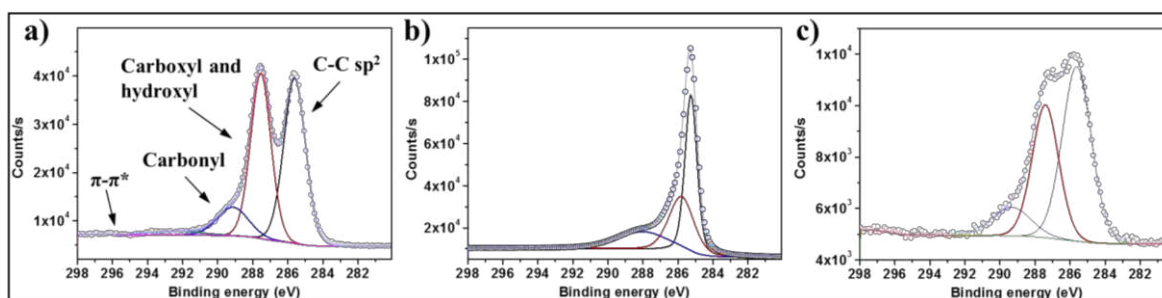


Figure 7.6: XPS C1s spectra of GO. a) Pristine. b) Optimally reduced. c) Damaged by too high power density.

By comparing the XPS C1s spectra of GO pristine, optimally reduced and damaged, respectively in **Figure 7.6a,b,c**, it is possible to see that the laser-induced, photo-thermal,



reaction is particularly effective for the removal of carboxyl and hydroxyl groups, but is not efficient for the removal of carbonyl groups. From the compositional point of view, the laser reduction appears to be more efficient than other reduction techniques such as the chemical approach, featuring a C-C  $sp^2$  component of the C1s spectra of  $\sim 75\%$ , comparable with the ones obtained by thermal reduction at high temperatures.<sup>15</sup>

In order to complement the XPS results, we have performed Raman spectroscopy, which is a standard and powerful tool for the characterization of carbon based materials, providing information about the carbon hybridization state.<sup>16</sup>

Similarly to the XPS experiments described above, Raman spectra were acquired in areas reduced by employing different laser powers in the same film. Representative results are shown in **Figure 7.7**. The Raman of the pristine GO, displayed in **Figure 7.7a**, shows the typical GO features, characterized by two main peaks at  $\sim 1350\text{ cm}^{-1}$  and  $\sim 1600\text{ cm}^{-1}$ , respectively named D and G peaks.<sup>17-19</sup> The presence of the G peak is associated with the in-plane stretching vibration of carbon atom pairs and can be observed for all carbon structures containing graphitic  $sp^2$  hybridization.<sup>20</sup> Instead, the D-peak is Raman forbidden in the absence of defects, and as such it is not observed in the Raman spectrum of perfect defect-less graphene. Its presence in GO stems from the  $sp^3$  carbon hybridization, created by the attachment of hydroxyl and epoxide groups, on the carbon basal plane. For low defective graphene, a common strategy to estimate the number of  $sp^3$  defects involves the study of the relative intensity of the D and G peaks.<sup>21</sup> However, this approach fails in heavily disordered GO,<sup>17,19</sup> since another defect-related peak, named D', falls in the same range of the G peak and overlaps with it, preventing a correct estimation of its intensity.

The Raman spectrum shown in **Figure 7.7b** was measured in an area reduced at higher laser power, corresponding to the optimum value, as found from the XPS analysis. Significant differences can be encountered in the two cases. First, the G peak becomes sharper and shifted at lower wavelength ( $1583\text{ cm}^{-1}$ ). At the same time, the D' peak can be clearly discerned as a shoulder to the more intense G peak. Even more interestingly, an intense peak appears at  $2696\text{ cm}^{-1}$ , which corresponds to the 2D peak commonly observed in pristine graphene. Such peak, which is the most intense in pristine graphene, has low intensity in GO, as it can be observed in **Figure 7.7a**, in which the 2D peak can be observed only as a modulation of a broad background. In the overall, the Raman features of our L-rGO resemble

more closely those of CVD graphene than those of the pristine GO. In particular, the 2D peak is typically not observed in thermally rGO,<sup>19</sup> and only very recently it was shown that it can be recovered through microwave assisted reduction.<sup>18</sup> In this regard, the presence of the 2D peak in the rGO spectrum is indicative of an extremely high degree of reduction, pointing out that our laser assisted approach is more effective than the conventional thermal treatment and comparable to the microwave assisted reduction.

Finally, the Raman spectrum shown in **Figure 7.7c** was measured in an area irradiated by even higher laser power. In this case, the intensity of the Raman peaks is extremely low, even if the parameters used for the acquisition of the spectrum are the same as those employed for **Figure 7.7b** and **c**. This finding indicates that the material has been damaged by the too-high laser power and the  $sp^2$  hybridization is almost destroyed, confirming the results of the previously discussed XPS characterization.

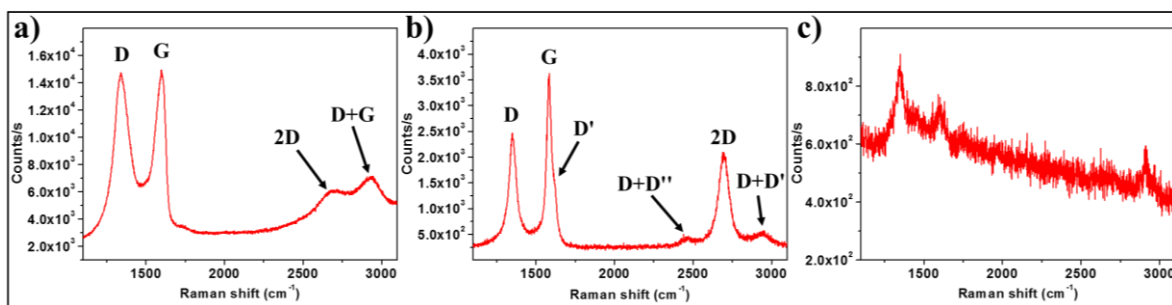


**Figure 7.7:** Raman spectra of GO. a) Pristine GO. b) Optimally reduced. c) Damaged by too high power density.

The information obtained with XPS and micro-Raman spectroscopy characterizations, were correlated with the electrical measurement of sheet resistance of the films. The sheet resistance is an electrical parameter to define the intrinsic resistance of 2D materials by excluding the contact resistance, through 4 probes (see chapter 3.2).

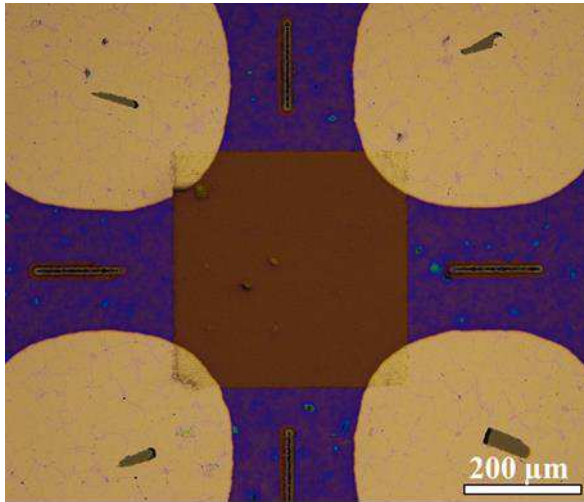


**Figure 7.8:** Optical micrograph of L-rGO with gold pads for electrical characterization.

The sheet resistance measurements were performed with the Van Der Pauw technique<sup>11</sup> by applying a constant current of 10  $\mu\text{A}$ . Test structures were fabricated by the deposition of four metallic contact pads at the corners of each square pattern. For that purpose, conventional photolithography methods are avoided as photoresist deposition, baking and stripping, may result in permanent deterioration of GO film. Therefore, metal evaporation (Cr/Au 3/60 nm) through precisely aligned *ad-hoc* stencil mask for each sample were realized (**Figure 7.8**).

**Figure 7.9** summarizes L-rGO sheet resistance data obtained with a sample featuring a starting GO film thickness of  $\sim 3$  nm. The data is obtained on the test structures processed at different gains and sample chamber atmosphere configurations.

Regardless of the sample chamber atmosphere, an identical qualitative behavior is observed. Firstly, significant drop of sheet resistance takes place within gain range of 25-35%. Secondly, sheet resistance remains nearly constant or increases slowly with increase of exposure dose in very wide energy range. Clearly, more than two times difference in sheet resistance is seen between oxygen free atmospheres ( $\text{N}_2$  and FOG) and air, indicating the importance of the former environments for better rGO quality.

At high exposure dose, sheet resistance increases dramatically. Rapid transition from insulating to conductive state is also seen in the work reported by Kymakis et al.<sup>22</sup> where fast monotonic decrease of rGO sheet resistance is observed upon increase of the exposure dose.<sup>22</sup>



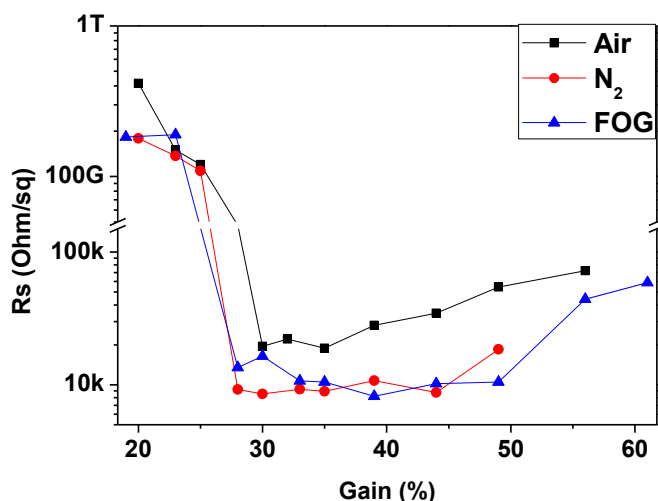


**Figure 7.9:** Sheet resistance for 2.8 nm thick GO film as a function of laser intensity (%) for three different atmospheres (FOG = 5% H<sub>2</sub>, 95% N<sub>2</sub>).

According to the plot in **Figure 7.9**, the best electrical properties, corresponding to a sheet resistance value of 8.5 kOhm/sq, are obtained in N<sub>2</sub> environment by using a gain of 30%. The gain is an arbitrary value of the laser intensity, given by the software, which cannot be directly converted into an actual power density.

By using a commercial power meter, especially designed for IR sources, and by performing a calibration of the actual output power, it was possible to convert the gain into energy values and, normalizing for the laser spot, into energy density.

**Figure 7.10** portrays the results of systematic studies on the sheet resistance performed on  $\sim 17 \pm 1$  nm thick GO, laser reduced by employing different energy per pulse and number of pulses per unit of area (e.g. different stage scan speed) under N<sub>2</sub> environment.

Such study aimed at finding the best dose to maximize the electrical conductance (e.g. the lowest sheet resistance) for such films.

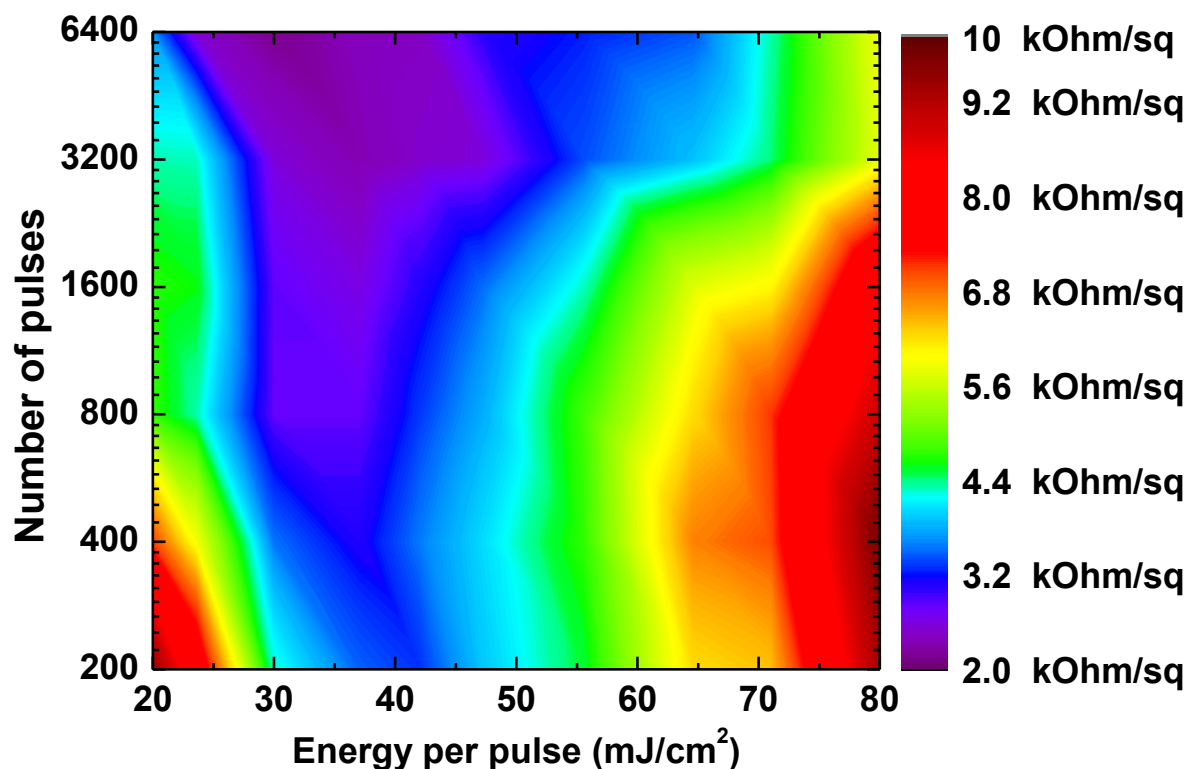


**Figure 7.10:** Effect of amount of pulses and energy per pulse on the sheet resistance of  $17 \pm 1$  nm thick L-rGO under  $N_2$  atmosphere.

From the color map in **Figure 7.10**, it is possible to see that the best performances, corresponding to a sheet resistance of 2.16 kOhm/sq (dark purple in the color map), can be obtained just within a very narrow combination of energies and amount of pulses per area. By combining such data with the other laser parameters (70 ns pulse width, 90 kHz frequency) and taking into account that each spot is exposed twice, because of the partial overlapping of the drawn lines, it was possible to find that the ideal exposure value, for the reduction of the 17 nm thick GO film, is  $216.7 \text{ J/cm}^2$ .

Interestingly, the same values of exposure dose have been found to be optimal regardless the substrates, allowing to pattern the same highly conductive areas also on transparent quartz substrates, meaning that the reduction process is not mediated by the absorbance or by the back-reflection given by the silicon substrates. Such optimized conditions have been used to reduce GO films with different thickness, allowing to find a parabolic relationship between film's thickness and sheet resistance (**Figure 7.11**), as expected for this kind of system.

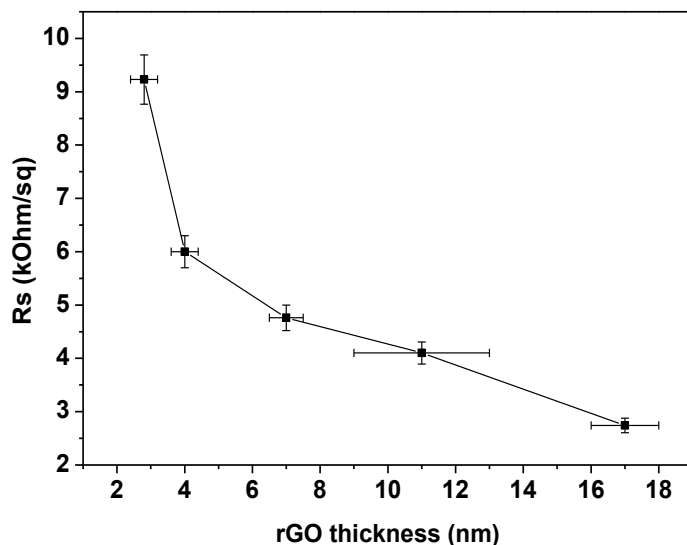


Figure 7.11: Relation between film's thickness and sheet resistance in L-rGO samples.

In order to get a better understanding in mechanism of GO reduction, L-rGO samples have been analyzed by conductive atomic force microscopy (C-AFM).

**Figure 7.12a** portrays AFM images which have been recorded at the corner between exposed and unexposed areas of a 2.8 nm thick film. Such scanned area was chosen to include both pristine (top right) and reduced (bottom left) GO portions within the same image. The unexposed area clearly displays the characteristic GO film pattern, exhibiting individual GO flakes randomly overlapping each other (**Figure 7.2a**). However, exposed region looks completely different, featuring no noticeable flake shapes but, instead, some circular structures. The corresponding current map, recorded by applying a constant bias of 50 mV to the rGO region while grounding the tip (**Figure 7.12b**), shows that the electrical current is strongly confined inside the exposed area.

As aforementioned, a careful look at the image reveals the presence of circular objects, featuring a lateral size of  $\sim 500$  nm, randomly scattered inside the rGO region and featuring higher conductivity compared to the background.

Taking into account the very high exposure dose applied in our experiments, it is reasonable to imagine that these round objects can be ascribed to peaks of laser intensity, suggesting a laser ablation-like photo-thermal process as main GO reduction mechanism in our experiments.

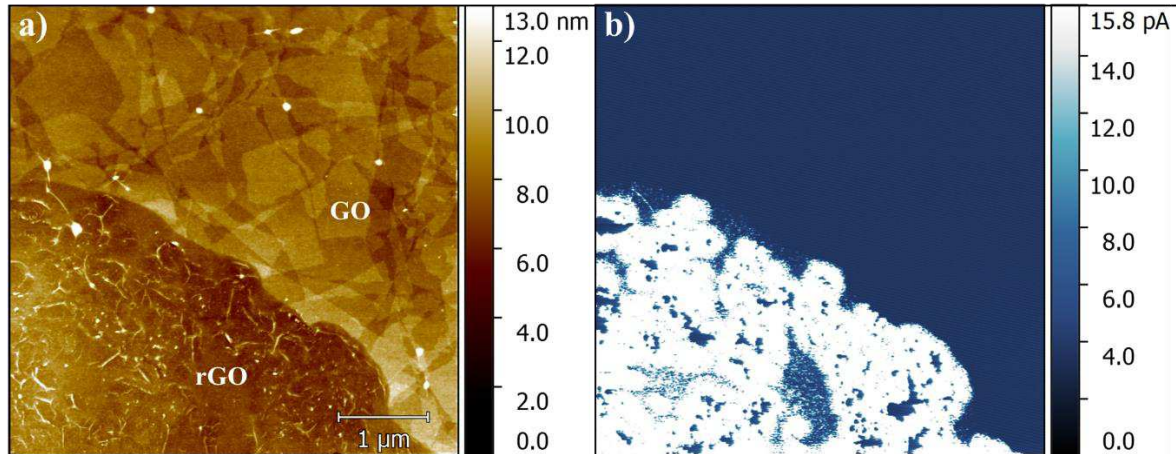


**Figure 7.12:** C-AFM characterization at the border between exposed and unexposed areas on 2.8 nm thick GO. a) Topography image. b) Electrical current map.

From the topography AFM image in **Figure 7.12a**, it is possible to observe the presence of a height step between GO and L-rGO areas, amounting to  $\sim 1.5$  nm. By considering an initial GO thickness of ca. 3 nm, such finding means that the reduction process likely involves an overall thickness loss of  $\sim 50$  %. This finding is in line with data reported on thickness measurements on single layer graphene and GO, showing a much larger thickness of the latter, given by the presence of the oxygen containing pending groups attached to the surface.<sup>23</sup>

Graphene and rGO are currently considered promising candidate materials for the fabrication of transparent and flexible electrodes as a replacement for the commonly used indium tin oxide (ITO) ones, which are expensive and brittle.<sup>24-26</sup>

Graphene and rGO feature wide range optical transmittance<sup>27</sup> and mechanical flexibility,<sup>28-30</sup> which are directly correlated with the amount of defects within the lattice. For such reason, it is fundamental to correlate the electrical properties achieved with the L-rGO with its optical transmittance.

In order to do it, a  $4 \times 4$  mm<sup>2</sup> wide window of rGO, reduced with the previously discussed optimized conditions and featuring a sheet resistance of  $2.51 \pm 0.12$  kΩ/sq, was drawn in the middle of a large area  $17 \pm 1$  nm thick GO film on quartz substrate (**Figure 7.13b**).

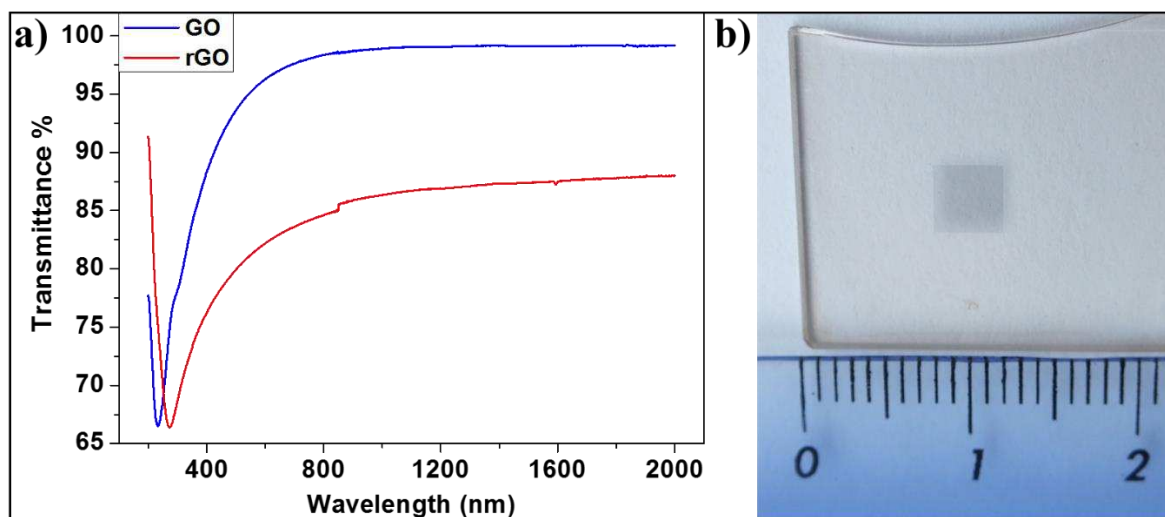


**Figure 7.13:** Optical properties of rGO. a) Comparison between the optical transmittance spectra of GO (unexposed area) and rGO (exposed area). b) Photograph of sample with 4x4mm<sup>2</sup> wide window of rGO drawn on a uniform 17 nm thick GO film on quartz substrate.

As displayed in **Figure 7.13**, pristine GO film features very high optical transmittance, as large as 95.2% at  $\lambda = 550$  nm, and exhibits a good optical contrast with the darker L-rGO part.

Reduced GO window is obviously less transparent, because of the restoration of the  $\pi$ -conjugated lattice,<sup>31,32</sup> but it still features a remarkably high optical transmittance, amounting to 81% at  $\lambda = 550$  nm with no absorbance peaks within the visible range.

A number of authors report on laser-reduction of graphene oxide followed by rGO-based device fabrication.<sup>10,33-35</sup> The main disadvantage of L-rGO device fabrication methods, reported up to date, is the presence of unused GO film surrounding the exposed L-rGO pattern. Unused GO film complicates and limits dramatically the device fabrication technology. Main issues, on this regard, are the absence of access to bare underneath substrate (e.g. Si/SiO<sub>2</sub>) and poor electrical contact of L-rGO devices with the measurement electrodes, due to bad metal adhesion to GO film and to mechanical weakness of such unused area of the film underneath the electrodes, which can be detached from the substrate, resulting in damages or disruption of the devices.

In this work we demonstrate also a simple and reliable workaround method to overcome such issues. The hydrophilic nature of graphene oxide suggests that it is possible to remove GO flakes by rinsing the films in water. However, this approach is not efficient and it only

works for freshly prepared GO films, failing for samples after 1 day drying. We found that unused GO parts can be successfully removed from the substrate by immersion into a weak basic (0.5% ammonia) water solution, with help of stirring, if necessary, to expose the underneath substrate before metallization of the devices (**Figure 7.14**).

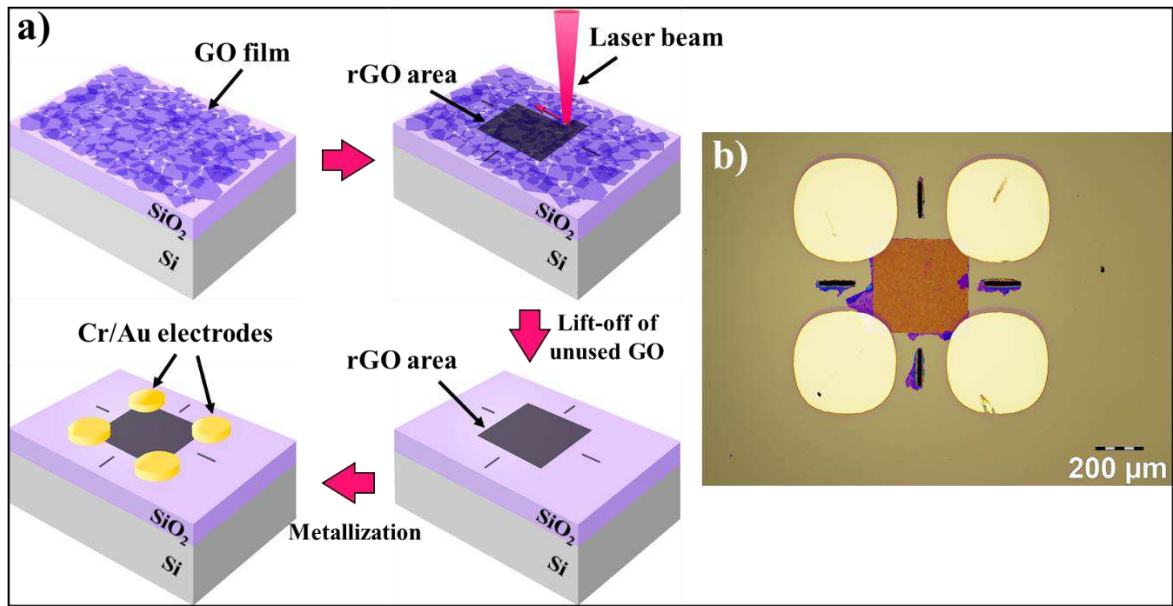


**Figure 7.14:** Optimized procedure for L-rGO devices fabrication. a) Flowchart of the processes. b) Optical micrograph of L-rGO device on clean SiO<sub>2</sub> substrate (no unused GO).

**Figure 7.15a** shows large scale rGO pattern, surrounded by free Si/SiO<sub>2</sub> substrate, as a result of the GO removal procedure described above. By employing such approach, it is possible to achieve narrow GO structures whose lateral dimensions are only limited by average GO flake size and laser reduction efficiency. As an example, **Figure 7.15b** shows ~ 10 μm rGO line with some cracks, due to lift-off of poorly reduced GO flakes. This method offers an opportunity of designing fine rGO structures within complex multilayer process.

An example application of this method is the fabrication of L-rGO devices for electrical resistive ozone sensing structures. As deeply discussed in chapter 2.4, graphene is a two-dimensional material featuring a large surface area and high conductivity, which is strongly dependent on the carrier concentration. Both properties make graphene a promising candidate for sensors that rely on charge transfer between graphene and physisorbed analytes. Graphene was found to become p-doped by the gas molecules such as H<sub>2</sub>O,<sup>36</sup>



$\text{NO}_2$ ,<sup>37</sup>  $\text{Br}_2$  and  $\text{I}_2$ <sup>38</sup> whereas n-type doping can be achieved by exposing graphene to  $\text{NH}_3$ ,<sup>37</sup>  $\text{CO}$ ,<sup>37</sup> alkali metals atoms.<sup>39</sup> Ozone, due to its structure, shows strong p-doping of graphene, as has been evidenced by Raman spectroscopy.<sup>40</sup> For making ozone sensitive structures, large size ( $600 \times 2000 \mu\text{m}^2$ ) rectangular L-rGO patterns were laser-written on  $\sim 17 \text{ nm}$  thick GO film, followed by unused GO removal step. After that, device metallization over the rGO patterns was realized by thermal evaporation of Cr/Au 3/60 nm via interdigitated electrodes stencil mask. Resulting ozone-sensor test structure is shown in **Figure 7.15c**.

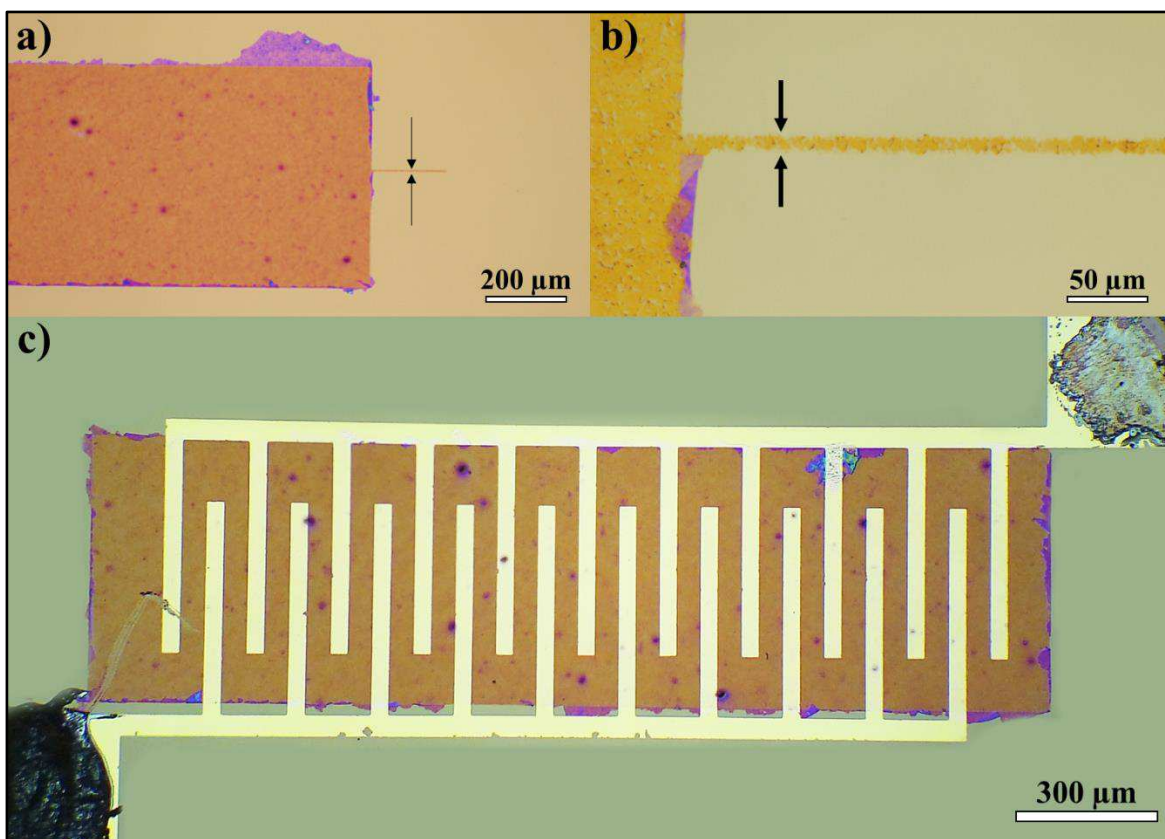


**Figure 7.15:** Optical micrograph of large area L-rGO structure for ozone sensing devices. a)  $600 \times 2000 \mu\text{m}^2$  L-rGO after unused GO removal shows the presence of GO residuals attached to the edges of the structure. b) Zoom-in showing a  $10 \mu\text{m}$  wide rGO line. c) Ozone sensor structure with interdigitated electrodes.

Ozone sensing experiments were performed in dedicated setup, which consists of an ozone generator, a sample exposure chamber, control and data acquisition equipment (**Figure 7.16a**). The obtained ozone sensor operation curve is illustrated in **Figure 7.16b**. Firstly, the sensor was conditioned several times by cycling to  $70^\circ \text{C}$  and back to room temperature in air atmosphere. After that, the test structure was turned on with DC bias of 10 mV. The



ignition of the ozone generator is well evidenced in a rapid increase of test structure conductivity. By turning on the heater, sample current drops due to desorption of some ozone molecules from L-rGO surface. Similar device operation concept has been reported for single wall carbon nanotubes network-based ozone sensors.<sup>41,42</sup> Such process was then repeated several times to ensure device functionality. The maximum change observed in the source-drain current amounts to 5.5% and corresponds to an ozone concentration of  $\sim 5$  ppm.

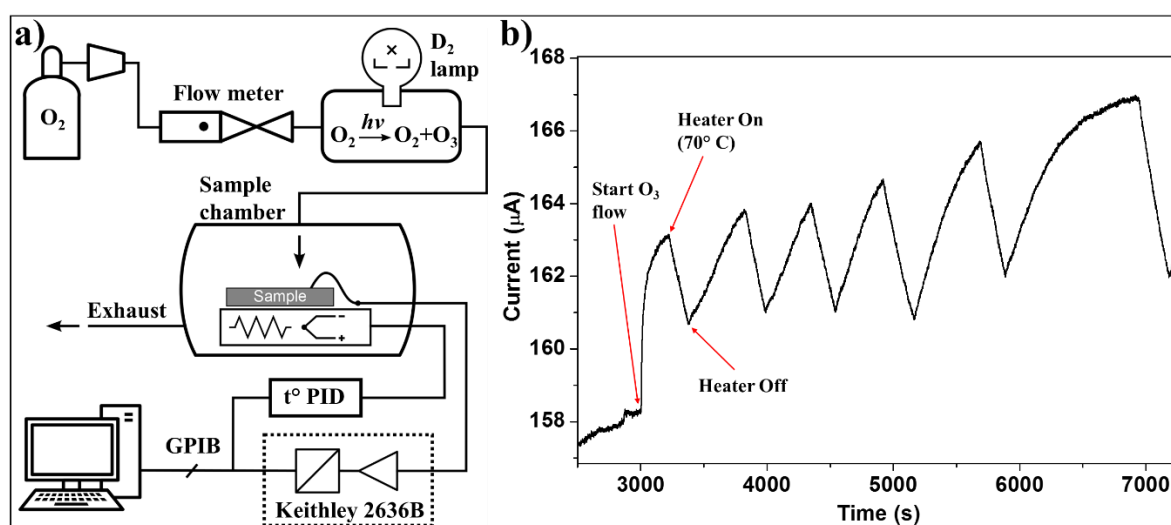


**Figure 7.16:** L-rGO ozone sensors test setup and results. a) Scheme of the used setup b) L-rGO electrical current response to absorption and desorption of ozone vs time under various cycles.

As displayed in **Figure 7.16b**, the developed L-rGO based ozone sensors exhibit high sensitivity and a linear response for very low ozone concentration, while approaching a saturation plateau around  $\sim 5$  ppm. This result is interesting and promising since, as deeply explained in chapter 1, ozone can be harmful for human health at concentration  $< 1$  ppm.

## 4 CONCLUSIONS

---

In this chapter it has been reported on a new approach to successfully produce and reduce highly uniform films of graphene oxide by means of high energy non-linear IR fiber laser. Such photo-thermal approach allows to pattern conducting reduced graphene oxide area with arbitrary shapes and enhanced optical and electrical properties. The devices fabricated with our optimized procedure feature lowest volume resistivity of  $0.98 \Omega/\text{sq}/\text{mil}$  at transmittance of 81% (at 550 nm), recorded on L-rGO films reduced in N<sub>2</sub> atmosphere.

To achieve such result and to find the best reduction conditions, a systematic study on the effect of reduction atmosphere, film's thickness and exposure dose, on the sample's characteristic (electrical, optical and compositional), has been performed. Additionally, a new technique to remove the unused GO film, after the patterning processes, has been developed, dramatically boosting the mechanical stability and the easiness of the devices fabrication processes. Finally these optimized structures of L-rGO has been employed, as active materials, to fabricate high performance electrical resistive ozone sensors, capable of detecting few ppm of ozone in atmospheric environment and conditions.

## 5 REFERENCES

---

- 1 Zhang, Y. L. *et al.* Photoreduction of Graphene Oxides: Methods, Properties, and Applications. *Adv Opt Mater* **2**, 10-28, (2014).
- 2 Petridis, C. *et al.* Post-fabrication, in situ laser reduction of graphene oxide devices. *Appl Phys Lett* **102**, (2013).
- 3 Sokolov, D. A., Rouleau, C. M., Geohegan, D. B. & Orlando, T. M. Excimer laser reduction and patterning of graphite oxide. *Carbon* **53**, 81-89, (2013).
- 4 Guo, L. *et al.* Two-beam-laser interference mediated reduction, patterning and nanostructuring of graphene oxide for the production of a flexible humidity sensing device. *Carbon* **50**, 1667-1673, (2012).
- 5 Wang, J. N. *et al.* Biomimetic graphene surfaces with superhydrophobicity and iridescence. *Chem Asian J* **7**, 301-304, (2012).
- 6 Zhou, Y. *et al.* Microstructuring of graphene oxide nanosheets using direct laser writing. *Adv Mater* **22**, 67-71, (2010).
- 7 Teoh, H. F., Tao, Y., Tok, E. S., Ho, G. W. & Sow, C. H. Direct laser-enabled graphene oxide-Reduced graphene oxide layered structures with micropatterning. *J Appl Phys* **112**, (2012).
- 8 Zhang, Y. L. *et al.* Direct imprinting of microcircuits on graphene oxides film by femtosecond laser reduction. *Nano Today* **5**, 15-20, (2010).
- 9 Trusovas, R. *et al.* Reduction of graphite oxide to graphene with laser irradiation. *Carbon* **52**, 574-582, (2013).
- 10 Zhou, Y. & Loh, K. P. Making patterns on graphene. *Adv Mater* **22**, 3615-3620, (2010).
- 11 Van Der Pauw, L. J. A method of measuring the resistivity and hall coefficient on lamellae of arbitrary shape. *Philips Tech Rev* **20**, 220, (1958).
- 12 Wade, J. & Merriman, R., W., Influence of water on the boiling point of ethyl alcohol at pressures above and below the atmospheric pressure. *J Chem Soc, Trans* **99**, 997-1011, (1911).
- 13 Some, S. *et al.* High-quality reduced graphene oxide by a dual-function chemical reduction and healing process. *Sci Rep* **3**, 1929, (2013).
- 14 Abdolhosseinzadeh, S., Asgharzadeh, H. & Seop Kim, H. Fast and fully-scalable synthesis of reduced graphene oxide. *Sci Rep* **5**, 10160, (2015).
- 15 Li, X. *et al.* Highly conducting graphene sheets and Langmuir-Blodgett films. *Nat Nanotechnol* **3**, 538-542, (2008).
- 16 Ferrari, A. C. & Robertson, J. Interpretation of Raman spectra of disordered and amorphous carbon. *Phys Rev B* **61**, 14095-14107, (2000).
- 17 King, A. A. *et al.* A New Raman Metric for the Characterisation of Graphene oxide and its Derivatives. *Sci Rep* **6**, 19491, (2016).
- 18 Voiry, D. *et al.* High-quality graphene via microwave reduction of solution-exfoliated graphene oxide. *Science* **353**, 1413-1416, (2016).
- 19 Yang, D. *et al.* Chemical analysis of graphene oxide films after heat and chemical treatments by X-ray photoelectron and Micro-Raman spectroscopy. *Carbon* **47**, 145-152, (2009).

- 20 Ferrari, A. C. & Basko, D. M. Raman spectroscopy as a versatile tool for studying the properties of graphene. *Nat Nanotechnol* **8**, 235-246, (2013).
- 21 Wang, Q. H. *et al.* Understanding and controlling the substrate effect on graphene electron-transfer chemistry via reactivity imprint lithography. *Nat Chem* **4**, 724-732, (2012).
- 22 Kymakis, E., Savva, K., Stylianakis, M. M., Fotakis, C. & Stratakis, E. Flexible Organic Photovoltaic Cells with In Situ Nonthermal Photoreduction of Spin-Coated Graphene Oxide Electrodes. *Adv Funct Mater* **23**, 2742-2749, (2013).
- 23 Schniepp, H. C. *et al.* Functionalized single graphene sheets derived from splitting graphite oxide. *J Phys Chem B* **110**, 8535-8539, (2006).
- 24 He, M., Jung, J. H., Qiu, F. & Lin, Z. Q. Graphene-based transparent flexible electrodes for polymer solar cells. *J Mater Chem C* **22**, 24254-24264, (2012).
- 25 Pang, S., Hernandez, Y., Feng, X. & Mullen, K. Graphene as transparent electrode material for organic electronics. *Adv Mater* **23**, 2779-2795, (2011).
- 26 Eda, G., Fanchini, G. & Chhowalla, M. Large-area ultrathin films of reduced graphene oxide as a transparent and flexible electronic material. *Nat Nanotechnol* **3**, 270-274, (2008).
- 27 Zheng, Q. B. *et al.* Transparent Conductive Films Consisting of Ultra large Graphene Sheets Produced by Langmuir-Blodgett Assembly. *ACS Nano* **5**, 6039-6051, (2011).
- 28 Lee, C., Wei, X. D., Kysar, J. W. & Hone, J. Measurement of the elastic properties and intrinsic strength of monolayer graphene. *Science* **321**, 385-388, (2008).
- 29 Trung, T. Q. *et al.* A Flexible Reduced Graphene Oxide Field-Effect Transistor for Ultrasensitive Strain Sensing. *Adv Funct Mater* **24**, 117-124, (2014).
- 30 Wang, M. *et al.* Large-Area, Conductive and Flexible Reduced Graphene Oxide (RGO) Membrane Fabricated by Electrophoretic Deposition (EPD). *ACS Appl Mater Interfaces* **6**, 1747-1753, (2014).
- 31 Becerril, H. A. *et al.* Evaluation of solution-processed reduced graphene oxide films as transparent conductors. *ACS Nano* **2**, 463-470, (2008).
- 32 Wang, X., Zhi, L. & Mullen, K. Transparent, conductive graphene electrodes for dye-sensitized solar cells. *Nano Lett* **8**, 323-327, (2008).
- 33 Yung, W. K. C., Li, G. J., Liem, H. M., Choy, H. S. & Cai, Z. X. Eye-friendly reduced graphene oxide circuits with nonlinear optical transparency on flexible poly(ethylene terephthalate) substrates. *J Mater Chem C* **3**, 11294-11299, (2015).
- 34 El-Kady, M. F., Strong, V., Dubin, S. & Kaner, R. B. Laser Scribing of High-Performance and Flexible Graphene-Based Electrochemical Capacitors. *Science* **335**, 1326-1330, (2012).
- 35 Strong, V. *et al.* Patterning and Electronic Tuning of Laser Scribed Graphene for Flexible All-Carbon Devices. *ACS Nano* **6**, 1395-1403, (2012).
- 36 Novoselov, K. S. *et al.* Electric field effect in atomically thin carbon films. *Science* **306**, 666-669, (2004).
- 37 Schedin, F. *et al.* Detection of individual gas molecules adsorbed on graphene. *Nat Mater* **6**, 652-655, (2007).
- 38 Jung, N. *et al.* Charge transfer chemical doping of few layer graphenes: charge distribution and band gap formation. *Nano Lett* **9**, 4133-4137, (2009).
- 39 Chen, J. H. *et al.* Charged-impurity scattering in graphene. *Nat Phys* **4**, 377-381, (2008).
- 40 Alzina, F. *et al.* Probing the electron-phonon coupling in ozone-doped graphene by Raman spectroscopy. *Phys Rev B* **82**, (2010).

- 41 Wongwiriyan, W. *et al.* Ultrasensitive ozone detection using single-walled carbon nanotube networks. *Jpn J Appl Phys* **45**, 3669-3671, (2006).
- 42 Park, Y. *et al.* Development of an ozone gas sensor using single-walled carbon nanotubes. *Sensor Actuat B-Chem* **140**, 407-411, (2009).

# Chapter 8

## Conclusions and outlooks

In summary, this thesis has been devoted to understanding and mastering the principles of supramolecular chemistry and nanotechnology and their synergic exploitation for the development of new gas sensing devices, with a special focus on the detection of water molecules.

We have demonstrated that well-engineered low-dimensional nanostructures, decorated with polyethylene glycol (PEG) can be exploited to harness supramolecular interactions between receptor sites and specific analytes. In particular, hydrogen bonding and dipole-dipole interactions between PEG derivative and water molecules in the atmosphere (moisture) have been employed to ultimately surpass the state-of-the-art performances of humidity sensing devices in different aspects, including sensitivity, selectivity and response speed.

PEG chains featuring different chain lengths and anchoring groups were used to decorate different organic or inorganic scaffolds exhibiting completely different characteristics and transduction mechanisms in sensing.

In the first experimental chapter (chapter 4), small gold nanoparticles (AuNPs) have been cross-linked with  $\sim 7$  nm long di-thiolated PEG linkers to form ordered 2D networks. In such two-dimensional arrays, the absorption of water molecules triggers the decoupling of the localized plasmon resonance between the nanoparticles resulting in a macroscopic color shift from blue to red which is complete within a few hundred milliseconds and is fully reversible. Such devices behave as colorimetric sensors and the amount of humidity is translated into an optical signal which can be easily detected by naked eyes and quantified by a

spectrophotometer. Since the optical readout is less technologically convenient than the electrical one, the same concept has been applied in chapter 5 to develop chemiresistive humidity sensors by employing shorter di-thiolated PEG chains, featuring nominal lengths between 1.5 and 2.2 nm. In this case the cross-link reaction is faster and leads to the formation of disordered 3D networks of AuNPs. The short linker chains ensure high mechanical resistance and, more importantly, electrical cross-talk between neighboring particles via direct tunneling. Since the tunneling current is strongly affected by the distance between the electrodes, small changes in the inter-particles distance due to absorption of water results in a dramatic change in current. The resulting devices features sensitivity of 32  $\Omega/\text{RH}(\%)$  (for 1.49 nm long linkers) and 678  $\Omega/\text{RH}(\%)$  (for 2.2 nm long linkers) in the range 0-70 % RH, which increase exponentially between 70% and 100 %, and a state-of-the-art response speed < 13 ms.

The presented AuNPs networks-based sensing devices features interesting performances, in terms of sensitivity and, in particular in terms of response speed but the non-specific water-PEG interactions given by the linear PEG chains employed and by the transduction mechanism causes a lack in selectivity, making the devices sensitive also to vapor of other polar solvents such as methanol or ethanol.

With the aim of boosting the performances of the above discussed sensing devices we moved from the nanoparticles networks, which are a mechanically robust scaffold, stabilized by strong covalent thiol-gold bonds, to fully supramolecular architectures in the configuration of 1D nanofibers. The structure of the building blocks has been engineered to trigger the self-assembly into supramolecular 1D structures in which the hydrophobic cores provide stabilization of the structure via  $\pi$ - $\pi$  stacking, allowing at the same time charge delocalization and transport while the surface is decorated by branched tetraethylene glycol, able to selectively interact with water molecules in the atmosphere. Absorption of water among the side chains provides alignment of the building block and decrease of the  $\pi$ - $\pi$  distance, resulting in a dramatic increase of the electrical current flowing through the fibers. Such devices showed unprecedented state-of-the-art sensitivity exhibiting an exponential change in current of 7 orders of magnitude in the range 0-75 % RH which is fully reversible and extremely fast (26 ms response). Moreover these supramolecular sensing devices exhibited also high selectivity, providing negligible output current changes when exposed to vapor of polar solvents such as methanol and ethanol.



Finally the last experimental chapter (chapter 7) reports on the use of reduced graphene oxide (rGO) as active material for the detection of a toxic gaseous molecule which is naturally present in the atmosphere: ozone. In particular, we have demonstrated that IR laser irradiation can be employed to reduce GO with high spatial resolution and that the resulting material can be used to detect ozone molecules in ambient atmosphere with a detection limit of few ppm. We demonstrated that our approach allows to achieve great control over every step of the fabrication processes of devices (I) by attaining a full control over the thickness and the morphology of the films by exploiting multiple spin-coating. (II) We can tune the reduction degree, by playing with the laser irradiation dose, defining spatially confined areas of highly conductive rGO on insulating GO matrixes. (III) We provide an efficient and reliable way to remove the unused GO after the reduction steps to expose the underneath substrate, making the metallization step and the device fabrication easier and more efficient. However, the application of such material as ozone sensor, reported in the last part of the project, represents mostly a proof-of-concept. Indeed the O<sub>3</sub>-GO interactions are purely electrostatic and feature a limited specificity because of the lack of use of optimized receptors, meaning that other p-dopant as, for example NO<sub>2</sub>, can be detected providing a similar output. Moreover the release of the absorbed O<sub>3</sub> is not spontaneous and must be triggered by increasing the film's temperature, as reported in literature for other carbon based materials such as carbon nanotubes.

So far, the supramolecular approach has been intensively studied and successfully exploited for the development of sensing devices targeting biological molecules or toxic metal ions in solutions while the application of such principles for the targeting of gaseous molecules has not been deeply investigated. This thesis aims to fill this gap clearly showing that the, supramolecular approach could be the key for the development of the new generation of gas sensing devices and that this versatile approach could be applied to different organic and inorganic scaffolds to meet any possible application requirement in terms of sensing performances as well as chemical and mechanical stability.

In the next future, the findings of this thesis can be exploited to extend our supramolecular approach to target different analytes by changing PEG chains with different receptors targeting specific analytes in the environment as well as in exhausted gases from machinery, industry or even from the human body. On this regard, for instance, the air exhaled from the mouth carries countless information regarding the health state of the human body and their

analysis represent already a powerful and non-invasive tool to detect several diseases or abnormal conditions. Increased concentrations of exhaled NO over the threshold of 50 ppb, for instance has been demonstrated to be caused by the presence of respiratory inflammations and asthma<sup>1</sup> while the presence of volatile organic compounds has been connected with the presence of pancreatic cancer.<sup>2</sup> The continuous monitoring of these and many other gaseous analytes could become crucial for an early diagnosis of many illnesses, saving thousands of lives and improving their quality. Our AuNPs 3D networks can be functionalized with receptors engineered to target such analytes. By taking advantage of the robustness, of the nanoscopic size and of the extremely low energy consumption of such devices it could be possible to implant them directly on the back surface of the teeth to regularly monitor the presence and the concentration of each of the different gaseous constituents at the same time.

On the other hand, in a closer future, our 2D AuNPs based colorimetric sensors could be implemented in contact lenses to provide useful information on the hydration level just by looking at their color, helping to prevent inflammation and possible diseases connected to a poor hydration. On a more fundamental view, such hybrid materials represent the first example reported on solid state dynamic assemblies of nanostructures in which is possible to couple and decouple the localized surface plasmon resonance in a controlled and fully reversible manner, employing humidity as external controller. Deeper and more focused studies on such architectures could be employed to gain a deeper insight on the effective distance of the phenomena linked to the near-field and to improve our knowledge on the field of plasmonics.

Our work on 1D supramolecular nanofibers clearly highlighted the potentials of the supramolecular approach for gas sensing and the possible future applications of such materials are only limited by the imagination of the organic chemists synthesizing the molecular building blocks. Apart from sensing, such materials can find applications as semiconductors for nano-scaled transistors in logic gates with tunable characteristics by modification of the cores and side chains materials but also in photovoltaics, where self-assembled molecular dyads provides unprecedented contact area for bulk heterojunctions.

Regarding the reduced graphene oxide it may find application in the next generation of electronic devices such as light emitting diodes and solar cells, where transparent electrodes are needed. Despite rGO electrical performances are still not comparable with the ones of

ITO and FTO, its mechanical resistance and flexibility make it the most promising candidate in the field of flexible electronics, where the more performing and brittle oxides-based materials cannot be employed. However, the main short-term challenge for graphene and its related materials is to gain control over the functional groups attached on their surface. The development of reliable functionalization techniques for graphene, GO and rGO could allow the development of selective and cost-effective sensors for several different analytes and, from a more general point of view, could pave the way towards the development of (multi-)functional materials with controlled and triggered characteristics for applications in various fields of electronics.

Overall, there is a great technological potential towards the use of low-dimensional functional nanostructures decorated with the receptors of ad-hoc analytes for the realization of highly selective, sensitive, fully reversible and fast sensor which can be printed on flexible supports, towards wearable sensing devices.

- 1 Pijnenburg, M. W. H. & De Jongste, J. C. Exhaled nitric oxide in childhood asthma: a review. *Clin Exp Allergy* **38**, 246-259, (2008).
- 2 Brodie, B. A. *et al.* Non-invasive exhaled breath volatile organic compound analysis for the diagnosis of pancreatic cancer. *Br J Surg* **104**, 37-37, (2017).

## CLOSING REMARKS

---

All the images displayed in this thesis are original and were designed by the author (Marco A. Squillaci) specifically for this manuscript (this statement obviously is not applied for literature data in which is clearly indicated the source reference within the caption).

All the experimental data reported in this thesis were performed and collected by the author, except from the following:

- **Chapter 4:** The DDA simulations on the optical behavior of 2D AuNPs networks, exposed to different humid environments, were performed by Dr. Cyriaque Genet and Dr. Xiaolan Zhong from the group of Prof. Thomas W. Ebbesen.
- **Chapter 5:** The low temperature electrical measurements on 3D networks of AuNPs, to assess information on the charge transport mechanism in such system, were performed by Marc-Antoine Stoeckel (PhD student in the same Nanochemistry group of Prof. Paolo Samorì)
- **Chapter 6:** The synthesis of the PDI-4T building block to grow the 1D supramolecular nanofibers was performed by Dr. Yulian Zaganyarski, former PhD student in the group of Prof. Klaus Müllen. The Synchrotron GIXRD measurements, to assess information over the molecular arrangements between the building block within the fibers, were performed by Dr. Laura Ferlauto (Former PhD student in Nanochemistry group and in Bologna CNR in the group of Dr. Silvia Milita).
- **Chapter 7:** The studies of the GO laser reduction on its electrical properties were performed in collaboration with Dr. Alexander V. Klekachev, former Post-Doc in Nanochemistry group. He also build and programmed the setup for the production and the detection of ozone. Raman measurements on the Lr-GO were performed with Dr. Marco Gobbi, Post-Doc in Nanochemistry group.

All the original projects reported in this manuscript were designed and developed by Marco A. Squillaci and Prof. Paolo Samorì.

## ACKNOWLEDGEMENTS

---

It seems like just few weeks ago, but 42 month have already passed since my first day in Strasbourg at the Institut de Science et d'Ingénierie Supramoléculaires. These years have been both amazing and tough and taught me a lot from the professional as well as personal point of view.

I am indebted to Prof. Paolo Samorì for accepting me as a PhD student even though his group was already full. He gave me the freedom to pursue my own ideas and to develop my project in autonomy, allowing me to make my own mistakes and to learn from them. His confidence and his suggestions made me a better scientist and pushed me to overcome my limits day by day.

My gratitude goes also to the members of my PhD jury: Prof. Stellacci, Prof. Stemmer and Dr. Rogez, for accepting to be the referees of my PhD defense and for the time they have dedicated to read my thesis.

I would like to thank the “Nanochemistry people”, starting from Corinne, for her endless patience and her precious help in these years. The Italian community: Agostino, Marco Carroli, Marco Gobbi, Sara, Emanuele, Matilde, Alessandro, Simone and the already far away Thomas and Maria for all the time spent together, the beers and the laughs. A special mention goes to Chiara Musumeci, who kindly welcomed me in the group, teaching me what I know on the atomic force microscopy and putting me on the “right trails” for my research, and to Laura Ferlau(n)to who made me feel home in Strasbourg during the first six months of this adventure (which would have been awful without you!).

Of course I cannot forget the non-Italian part of the group, starting with Tim and Marc-Antoine for their help with the French translation and their delicious dinners. I also thank Dr. Alexander Klekachev for all the time spent in office and in lab, for the death metal songs at 2 AM and for everything he taught me. Thanks to all past and current members: Artur, Lei, Nicolas, Fanny, Yifan, Chang-Bo (Jean le bon), Lili, Mohamed, Oliver and all the others (I am sure I am forgetting someone).

It has been a privilege to be part the Marie Curie ITN network “SYNCHRONICS” which allowed me to grow professionally, to travel across Europe and, most important, to meet wonderful people.

Finally I want to thank all the people who shared most of their life with me: my actual family who always supported me, even after my decision to live abroad, and my chosen family, my whole-life-friends: Walter, Alessio, Simone, Eugenio, Damiano, Serena (This is already the third thesis in which I acknowledge you!).

As is usually the case for scientific publications, the last person to be named is the most important and the one who deserves the highest acknowledgement. Valentina, the one who makes me laugh, makes me think, drives me crazy... in one word, the one who makes me feel alive. Thanks for what you have done in the last 8+2 years, this thesis is also yours. Ti amo.

## PUBLICATIONS IN INTERNATIONAL JOURNALS

---

- 17) **M. A. Squillaci**, A. Cipriani, G. Carminati, M. Melucci, P. Samorì, “Supramolecular nanofibers of engineered oligothiophene for chemiresistive humidity sensing”. Manuscript in preparation.
- 16) **M. A. Squillaci**, C. Genet, X. Zhong, T. W. Ebbesen, P. Samorì, “Facile fabrication of 2D humidity sensing dynamic plasmonic superlattices of cross-linked gold nanoparticles”. Manuscript in preparation
- 15) **M. A. Squillaci**, M.-A. Stoeckel, P. Samorì, “3D porous networks of gold nanoparticles as robust micro-sized electrical resistive humidity sensors”. Manuscript in preparation
- 14) **M. A. Squillaci**, A. V. Klekachev, M. Gobbi, P. Samorì, “Laser-reduced graphene oxide for ozone sensing applications”. Manuscript in preparation.
- 13) T. Leydecker, **M. A. Squillaci**, F. Liscio, E. Orgiu, P. Samorì, “Precise control of ambipolarity of solution processed semiconductor films through blending of polymers”. Manuscript in preparation.
- 12) **M. A. Squillaci**, G. Markiewicz, A. Walczak, A. Ciesielski, A. R. Stefankiewicz, P. Samorì, “Self-organization of amino-acid-derived NDI assemblies into a nanofibrillar superstructure with humidity sensitive n-type semi-conducting properties”. Manuscript submitted.
- 11) M. Campitiello, **M. A. Squillaci**, A. Ciesielski, P. Samorì, S. Masiero, “Self-assembly of ferrocenyl functionalized lipophilic guanosines into cation-free stacked G-quartet wires”. Manuscript submitted.
- 10) L. Zhang, S. Li, X. Zhong, **M. A. Squillaci**, E. Orgiu, P. Samorì, “Supramolecular self-assembly in sub-micron electrocyclic cavity: fabrication of heat reversible  $\pi$ -gel memristor”. Manuscript submitted
- 9) S. Yang, A. G. Ricciardulli, S. Liu, R. Dong, M. R. Lohe, A. Becker, **M. A. Squillaci**, P. Samorì, K. Müllen, X. Feng, "Ultrafast Delamination of Graphite into High-Quality Graphene Using Alternating Currents", *Angew. Chem. Int. Ed.*, 2017, 56, 6669–6675.
- 8) M. Gobbi, S. Bonacchi, J. X. Lian, Y. Liu, X.-Y. Wang, M.-A. Stoeckel, **M. A. Squillaci**, G. D’Avino, A. Narita, K. Müllen, X. Feng, Y. Olivier, D. Beljonne, P. Samorì, E. Orgiu, "Periodic potentials in hybrid van der Waals heterostructures formed by supramolecular lattices on graphene", *Nat. Commun.*, 2017, 8, 14767.
- 7) **M. A. Squillaci**, F. Qiu, A. Aliprandi, F. Zhang, X. Feng, P. Samorì, "Direct Patterning of Organic Functional Polymers through Conventional Photolithography and Noninvasive Cross-Link Agents", *Adv. Mater.*, 2016, 28, 5249–5254.



- 6) S. Haar, M. El Gemayel, Y. Shin, G. Melinte, **M. A. Squillaci**, O. Ersen, C. Casiraghi, A. Ciesielski, P. Samorì, "Enhancing the Liquid-Phase Exfoliation of Graphene in Organic Solvents upon Addition of n-Octylbenzene", *Sci. Rep.*, 2015, 5, 16684.
- 5) B. Dinesh, **M. A. Squillaci**, C. Ménard-Moyon, P. Samorì, A. Bianco, "Self-assembly of diphenylalanine backbone homologues and their combination with functionalized carbon nanotubes", *Nanoscale*, 2015, 7, 15873–15879.
- 4) R. Kurapati, J. Russier, **M. A. Squillaci**, E. Treossi, C. Ménard-Moyon, A. Esaú Del Rio-Castillo, E. Vazquez, P. Samorì, V. Palermo, A. Bianco, "Dispersibility-Dependent Biodegradation of Graphene Oxide by Myeloperoxidase", *Small*, 2015, 11, 3985–3994.
- 3) **M. A. Squillaci**, L. Ferlauto, Y. Zagranyarski, S. Milita, K. Müllen, P. Samorì, "Self-Assembly of an Amphiphilic  $\pi$ -Conjugated Dyad into Fibers: Ultrafast and Ultrasensitive Humidity Sensor", *Adv. Mater.*, 2015, 27, 3170–3174.
- 2) E. Orgiu, **M. A. Squillaci**, W. Reka, K. Börjesson, F. Liscio, L. Zhang, P. Samorì, "The dramatic effect of the annealing temperature and dielectric functionalization on the electron mobility of indene-C60 bis-adduct thin films", *Chem. Commun.*, 2015, 51, 5414–5417.
- 1) V. Torrisi, **M. A. Squillaci**, F. Ruffino, I. Crupi, M.G. Grimaldi and G. Marletta (2014). Schottky barrier height tuning by Hybrid organic-inorganic multilayers. *MRS Proceedings*, 1660, mrsf13-1660-tt05-07 doi:10.1557/opl.2014.396.

## AWARDS

---

**European Material Research Society (E-MRS) Spring meeting 2017 Graduate Student Award** In recognition of an outstanding contribution in the **Symposium L: *New materials for organic electronics: from synthesis to processing, characterization and device physics.***

## CONTRIBUTIONS IN INTERNATIONAL CONFERENCES

---

### ORAL COMMUNICATIONS

6) “Photolithographic direct patterning of organic polymers with novel and non-invasive cross-link agents”

**M. A. Squillaci**, F. Qiu, A. Aliprandi, F. Zhang, X. Feng, P. Samorì

**European Material Research Society (E-MRS) Spring meeting 2017 – Symposium L:** 22-26<sup>th</sup> May 2017 – Strasbourg, France.

5) “Micro-sized humidity sensors with porous 3D networks of gold nanospheres”

**M. A. Squillaci**, M.-A. Stoeckel, P. Samorì

**European Material Research Society (E-MRS) Spring meeting 2017 – Symposium R:** 22-26<sup>th</sup> May 2017 – Strasbourg, France.

4) “Supramolecular engineering of low dimensional humidity sensing materials”

**M. A. Squillaci**, P. Samorì

**ISIS Young scientist seminar:** 19<sup>th</sup> January 2017- Institut de Science et d’Ingénierie Supramoléculaires (I.S.I.S.), Strasbourg, France.

3) “Light-induced self-assembly of an amphiphilic  $\pi$ -conjugated dyad into fibers with controlled size and sensing properties”

**M. A. Squillaci**, L. Ferlauto, Y. Zaganyarski, S. Milita, K. Müllen, P. Samorì

**European Optical Society Annual Meeting (EOSAM) 2016** 26-30<sup>th</sup> September 2016 – Berlin, Germany.

2) “3D porous networks of gold nanoparticles as robust micro-sized electrical resistive humidity sensors”

**M. A. Squillaci**, M.-A. Stoeckel, P. Samorì

**European Material Research Society (E-MRS) Fall meeting 2016 – Symposium D:** 19-22<sup>nd</sup> September 2016 – Warsaw, Poland

1) “Self-assembly of an amphiphilic  $\pi$ -conjugated dyad into fibers: ultrafast and ultrasensitive humidity sensors”

**M. A. Squillaci**, L. Ferlauto, Y. Zaganyarski, S. Milita, K. Müllen, P. Samorì

**European Material Research Society (E-MRS) Fall meeting 2016 – Symposium H: 19-22<sup>nd</sup> September 2016 – Warsaw, Poland**

## **POSTER PRESENTATIONS**

**3) “Self-Assembly of an Amphiphilic  $\pi$ -Conjugated Dyad into Fibers: Ultrafast and Ultrasensitive Humidity Sensor”**

**M. A. Squillaci**, L. Ferlauto, Y. Zaganyarski, S. Milita, K. Müllen, P. Samorì

**13<sup>th</sup> European Conference on Molecular Electronics (ECME 2015) 1-5<sup>th</sup> September 2015 -Strasbourg, France.**

**2) “In-situ space confined laser assisted reduction of graphene oxide films”**

**M. A. Squillaci**, A. V. Klekachev, S. Berciaud, O. Fenwick, P. Samorì

**Graphene Nanotubes annual meeting (GDRI 2014) 21-25<sup>th</sup> September 2014 - Strasbourg, France.**

**1) “Growing supramolecular fibers using light-induced electron transfer as main driving force”**

**M. A. Squillaci**, L. Chen, K. Müllen, P. Samorì

**7<sup>th</sup> International Conference on Molecular Electronics (ElecMoL 2014) 24-29<sup>th</sup> August 2014 - Strasbourg, France.**



# Supramolecular Engineering of Optoelectronic Sensing Devices

## Résumé

Cette thèse explore l'utilisation des principes de la chimie supramoléculaire afin de fabriquer des dispositifs senseurs de gaz novateurs et à haute performance, avec une lecture (opto)-électronique. Parmi les différentes sections, divers échafaudages tels que des réseaux hybrides bi- et tridimensionnels de particules d'or et des nanofibres supramoléculaires sont utilisés comme matériaux actifs pour la détection quantitative de l'humidité. Au sein de la dernière section, des couches 2D d'oxyde de graphène sont fabriquées par exposition à un laser IR, puis comme validation de principe, exploitées comme matériau actif pour la détection d'ozone à une concentration ppm. Chacun des échafauds présentés est basé sur un mécanisme de transduction différent, mais dans tous les cas, les interactions entre récepteurs et analytes sont basés sur des liaisons dynamiques non covalentes.

Mots-clés : Capteurs d'humidité, Capteurs d'ozone, interactions non-covalentes, Nanoparticules d'or, Nano-fibres supramoléculaires, Oxyde de graphène

## Résumé en anglais

This thesis explores the use of supramolecular chemistry principles to fabricate novel and high performances gas sensing devices, featuring (opto)-electronic readouts. Within the different sections, diverse scaffolds such as 2D and 3D hybrid networks of gold nanoparticles and 1D supramolecular nanofibers are exploited as active materials for the quantitative detection of environmental humidity. In the last section, 2D layers of reduced graphene oxide are fabricated by IR laser exposure and, as a proof-of-concept application, they are exploited as active materials for the detection of ozone in ppm concentration. Each of the presented scaffolds rely on a different transduction mechanism but, in all the cases, the interactions between the receptors and the analytes are based on dynamic non-covalent bonds.

Keywords : Humidity sensors, Ozone sensors, Non-covalent interactions, Gold nanoparticles, Supramolecular nanofibers, Graphene oxide